

STABILIZING ALKALI METAL ELECTRODEPOSITION VIA
NANOSTRUCTURED HYBRID ELECTROLYTE AND INTERPHASE DESIGN
FOR RECHARGEABLE METAL BASED BATTERIES

A Dissertation

Presented to the Faculty of the Graduate School

of Cornell University

In Partial Fulfillment of the Requirements for the Degree of

Doctor of Philosophy

by

Zhengyuan Tu

May, 2018

© 2018 Zhengyuan Tu

STABILIZING ALKALI METAL ELECTRODEPOSITION VIA
NANOSTRUCTURED HYBRID ELECTROLYTE AND INTERPHASE DESIGN
FOR RECHARGEABLE METAL BASED BATTERIES

Zhengyuan Tu, Ph. D.

Cornell University 2018

Abstract

Significant advances in the amount of electrical energy that can be stored in electrochemical cells, such as rechargeable batteries require the adoption of high energy metallic anodes including Li, Na, Al, Zn, etc. Such anodes introduce significant technical challenges because they are known to form rough electrodeposits, loosely termed dendrites, during the device operation. This produces irreversible active material (electrode and electrolyte) losses during normal cell operation and poses safety concerns because the dendrites can proliferate in the inter-electrode space, shorting the cell internally. Though a similar phenomenon has been investigated in the more conventional context of metal electroplating, more complex effects can dominate in a battery configuration especially at current densities below the limiting current and in cells where the metal anodes undergo chemical reactions with electrolyte components. In this thesis, a comprehensive materials strategy involving structural and interfacial engineering is pursued to stabilize lithium metal electrodeposition. The strategy is based on guidelines defined by a theoretical linear stability analysis of metal electrodeposition in structured electrolytes. The origin of the deposition instability is revealed to involve fundamental features of electrolytes and interfaces near metal anodes, which lead to electro-convective, morphological and chemical

instability. I show that the first two instabilities can be addressed by using a nanostructured polymer/ceramic hybrid electrolyte, which exhibits high conductivity, high modulus and the ability to rectify ion transport through confinement. The well-defined nanoporous structure of the electrolytes also confine the length scale of the electrodeposit, which allows surface tension and other weaker forces at the interface to flatten rough electrodeposits, promoting dendrite-free operation. The chemical instability poses a more serious challenge because it is intrinsic to the chemistry of the electrode and electrolyte components; any exposure of one to the other can in principle drive a reaction cascade that ends in unconstrained growth in the cell impedance and premature failure. I show that this challenge can be overcome by the careful design of solid electrolyte interphases (SEIs) that regulate mass transport of reactive electrolyte ingredients and at the same time are able to flex to accommodate volume expansion of the anode. A significant finding is that these features can be realized using electrolyte additives designed to selectively break-down in-situ to form SEI with explicit composition set by the chemistry of the additive. A particularly important example are additives that break down to form halogen salts, which exhibit low surface diffusion barriers and fast interfacial transport. Such materials are shown to be highly effective in improving battery cycle lifetime. A second category of SEI explored in the study are so-called artificial SEI formed by pretreating the metallic electrode with polymers, metals, and metal oxide precursors prior to cell assembly.

BIOGRAPHICAL SKETCH

Zhengyuan was born in Nanchang, Jiangxi, China, where he enjoyed a happy childhood with his warm family. After receiving the bachelor degree in Polymer Science and Engineering from Chu-Kochen honor college in Zhejiang University, he continued to pursue his MS and PhD degree in Department of Materials Science and Engineering at Cornell University. His research has been focused on designing nanostructured composite materials and solid-liquid interphase for high energy batteries.

Dedicated to my family and friends

ACKNOWLEDGMENTS

At first, I would like to express my sincere gratefulness for the constant guidance and kind support from my committee chair, Prof. Lynden A. Archer, throughout my five-year Ph.D. program. He has always encouraged and motivated me for the research and offered invaluable suggestions regarding both academia and life.

I also sincerely thank my other two committee members. Prof. Ulrich B. Wiesner always offers his excellent insights on the big picture of the research, which inspires me to think at a high dimension. Prof. Lena F. Kourkoutis has provided tremendous support through our collaboration on using advanced microscopic technology to interrogate battery materials. I have also found her course very attractive and helpful.

Many thanks to my colleagues and collaborators across Cornell. Special thanks go to Yingying Lu, Jennifer Schaefer, and Samanvaya Srivistava, who have kindly offered selfless help when I firstly joined the group. I have particularly enjoyed working with Snehashis Choudhury, Lin Ma, and Shuya Wei, who have provided me with many ideas and supports. I am also grateful for the opportunity to work with Michael J. Zachman, who is a reliable microscopist with top-notch skills. Equal gratitude goes to all kind people who have helped me in any manner.

All my research cannot be smoothly performed without the support from dedicated staff in the MSE and CBE departments, CNET, CCMR, CNF, and NMR facility in Colorado School of Mines.

Last but not the least, I would like to thank my parents for their constant support and love, and my friends who have made my life at Cornell joyful and memorable.

TABLE OF CONTENTS

ABSTRACT	III
BIOGRAPHICAL SKETCH.....	V
DEDICATION	VI
ACKNOWLEDGMENTS	VII
CHAPTER 1	1
INTRODUCTION	1
CHAPTER 2	24
NANOSTRUCTURED HYBRID POLYMER/CERAMIC COMPOSITE ELECTROLYTE FOR LITHIUM METAL RECHARGEABLE BATTERIES	24
2.1 Abstract	25
2.2 Introduction	25
2.3 Experimental Section.....	30
2.4 Results and discussion	34
Reference	63
CHAPTER 3	68
EFFECT OF NANOPOROUS STRUCTURE ON THE STABILITY OF LITHIUM ELECTRODEPOSITION	68
3.1 Abstract	69
3.2 Introduction	69
3.3 Experimental Section.....	72
3.4 Results and discussion	74
Reference	112
CHAPTER 4	117
STABILIZING LITHIUM ELECTRODEPOSITION USING LIQUID ELECTROLYTE ADDITIVES AND NANOSTRUCTURED HYBRID ELECTROLYTES	117
4.1 Abstract	118
4.2 Introduction	118
4.3 Experimental Section.....	123
4.4 Results and discussion	134
Reference	152
CHAPTER 5	157
DESIGNING ARTIFICIAL SOLID-ELECTROLYTE INTERPHASES FOR SINGLE-ION AND HIGH-EFFICIENCY TRANSPORT IN BATTERIES	157

5.1 Abstract	158
5.2 Introduction	158
5.3 Experimental Section.....	162
5.4 Results and discussion	167
Reference	199
CHAPTER 6	207
SOLID-SOLID INTERPHASES FOR HYBRID RECHARGEABLE BATTERY ANODES	
.....	207
6.1 Abstract	208
6.2 Introduction	208
6.3 Experimental Section.....	212
6.4 Results and discussion	215
Reference	251
CHAPTER 7	258
STABILIZING PROTIC AND APROTIC LIQUID ELECTROLYTES AND LI METAL	
ELECTRODES USING ULTRATHIN ARTIFICIAL SOLID ELECTROLYTE	
INTERPHASES	258
7.1 Abstract	259
7.2 Introduction	259
7.3 Experimental Section.....	262
7.4 Results and discussion	263
Reference	284

CHAPTER 1

INTRODUCTION

Partially reproduced from *Nature Energy* 1 (2016): 16114.

Partially reproduced from *Accounts of chemical research* 48. 11 (2015): 2947

1.1 Lithium battery-based energy storage technology

Secondary or rechargeable batteries represent critical energy storage technologies for contemporary portable devices, electrical transportation, and grid¹⁻³. Prior to 1990, lead-acid battery, nickel-cadmium battery and nickel-metal hydride batteries have been widely used in energy applications. However, due to the limited energy density and voltage output, those conventional batteries were outperformed by lithium ion batteries (LIBs) which readily offer a two-fold increase in terms of both gravimetric and volumetric energy density (**Figure 1.1**)⁴. Since the first launch of LIBs, they have been quickly replacing conventional rechargeable batteries and taking up the market till today.

The success in LIB technology has been understood to be built on three key scientific achievements. A first is the discovery and optimization of lithium ion intercalation in a number of materials⁵⁻⁷. In contrast to a typical reaction which alters the chemistry and structure of a material before/after lithiation, intercalation is essentially a reversible process that maintains the original material structure except introducing a small volume expansion (usually < 30%). For example, layered graphite is known to be able to accommodate lithium ions between graphene layers with a maximum lithium storage capacity of 360 mAh g⁻¹ in the form of LiC₆, which makes it ideal as the battery anode. Equivalent or similar structures have also been found in cathode materials that allow reversible lithium ion storage. The list includes layered LiMO₂, M = Co, Mn, Ni, Al etc.

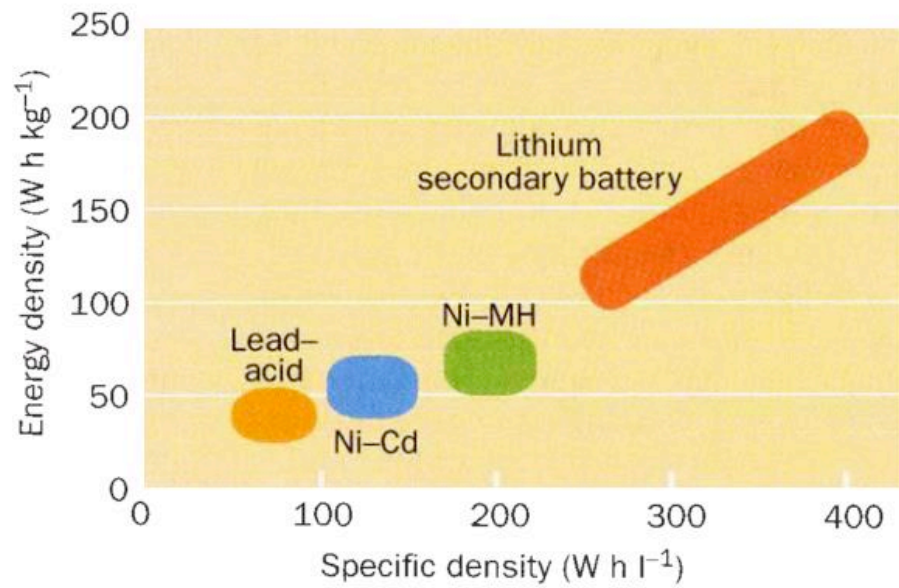


Figure 1.1. A comparison of the energy density and the specific density among lead acid (yellow), Ni-Cd (blue), Ni-Metal hybrid (green) and lithium secondary battery (red). Adapted with permission⁴. Copyright (1995), Nature Publishing Group.

and their mixtures, Olivine LiFePO_4 , and spinel lithium titanate ($\text{Li}_4\text{Ti}_5\text{O}_{12}$), $\text{LiMn}_{1.5}\text{Ni}_{0.5}\text{O}_{4-\delta}$, and so on. The second finding that enables LIBs involves the application of non-aqueous solvents in electrolytes, such as carbonates, ethers, esters, etc⁸. The most critical advantage of many aprotic solvents is the broadened electrochemical stability window compared with their aqueous alternatives, meaning the battery can be operated at a high voltage without decomposing the electrolyte. However, typical aprotic solvents can still suffer from the intrinsic thermodynamic instability when the voltage is scanned below 1.5 V (vs Li/Li^+), which needs to be addressed by the third achievement related to the designed solid electrolyte interphase (SEI)^{6, 9}. SEI usually refers to a naturally formed semi-solid interphase from the decomposition of the electrolyte on the electrode surface. Current understanding recognizes SEI as an inorganic/polymeric composite layer with a finite thickness of tens of nanometers, which conducts ions yet not electrons so that further decomposition of the electrolyte can be prevented. A well-defined SEI is critical for achieving high round-trip efficiency and the long-term performance of the battery. Details will be discussed in later sections.

Built on these key findings, LIBs have been rapidly developed over two decades with primary efforts focused on optimization of electrode structure, electrolyte formula, and so-called SEI additives, which facilitate the formation of SEI with desirable properties. The state-of-art LIBs typically provide an energy density of 250 – 300 Wh/kg and 500 – 600 Wh/L, at a cycling rate of about 1C (1C-rate means 1 hour for charge or

discharge) and with an output voltage $> 3.4 \text{ V}^{10-11}$. Though such battery performance satisfies many current applications, it gradually cannot keep pace with the increasing energy demand from advanced devices, especially the electrification of transportation (ground vehicles, drones, airplanes, etc.). A recent goal set by United States Advanced Battery Consortium (USABC) and Battery500 consortium is targeting advanced battery packs with an energy density of 500 W/kg, which requires strides in the progress of energy storage technologies offering high energy, high efficiency and long lifespan. Despite the performance LIBs can in principle still be improved by developing high voltage (4.5-5V) liquid, composite or even solid electrolyte¹²⁻¹³, only incremental achievements have been obtained so far. More revolutionary reformation involves replacing the graphite-based anode with other anodes such as Si, Sn or elemental Li which provide at least ten-time higher specific capacity than the carbonaceous anodes¹⁴⁻¹⁵ (**Figure 1.2**). Particularly, Li metal has received extensive attentions not only due to its high energy, but also the potential to be paired with advanced high energy, yet non-lithiated cathodes including metal fluorides (CuF_2 , FeF_3 , etc.), sulfur, O_2 , and CO_2 to form lithium metal batteries (LMBs)¹⁶⁻¹⁷. Unlike the lithium intercalation in a LIB, the operation of LMB involves electrodeposition/plating of metallic lithium anode based on the direct redox reaction of lithium ion to/from lithium metal, which introduces several instability and safety issues¹⁰. Thus, it is imperative to develop materials and configurations to enable stable and safe batteries with metallic lithium incorporated.

1.2 Mechanism of lithium batteries

Before diving into the detail of lithium electrodeposition in a battery, it would be helpful to understand how batteries operate in general³ (**Figure 1.3**). A typical battery consists of three key components: anode, cathode and the electrolyte. As mentioned earlier, the former two components store energy by either intercalation or conversion mechanism based on the materials structure. Upon charging, ions can migrate from the cathode to anode under the electric field, and the reversed process occurs during the discharge. The shuttling of ions is achieved in an ion-conductive electrolyte, which typically comprises of one or mixed aprotic solvents (ethylene carbonate, dimethylcarbonate, propylene carbonate, dioxane, glymes, etc.) doped with binary lithium salt (typically lithium hexafluorophosphate (LiPF_6), lithium bis(trifluoromethanesulfonyl)imide (LiTFSI), lithium bis(oxalato)borate (LiBOB), etc.)¹⁹. Liquid electrolytes require to be infused into a solid separator, usually an electronically insulating, porous membrane, to prevent the electric contact of the two electrodes²⁰. Some solid-state or semi-solid-state materials can also conduct ions by ion hopping or diffusion through vacancies and thus can serve both as the electrolyte and separator²¹⁻²². In either case, the ion mobility in the bulk electrolyte

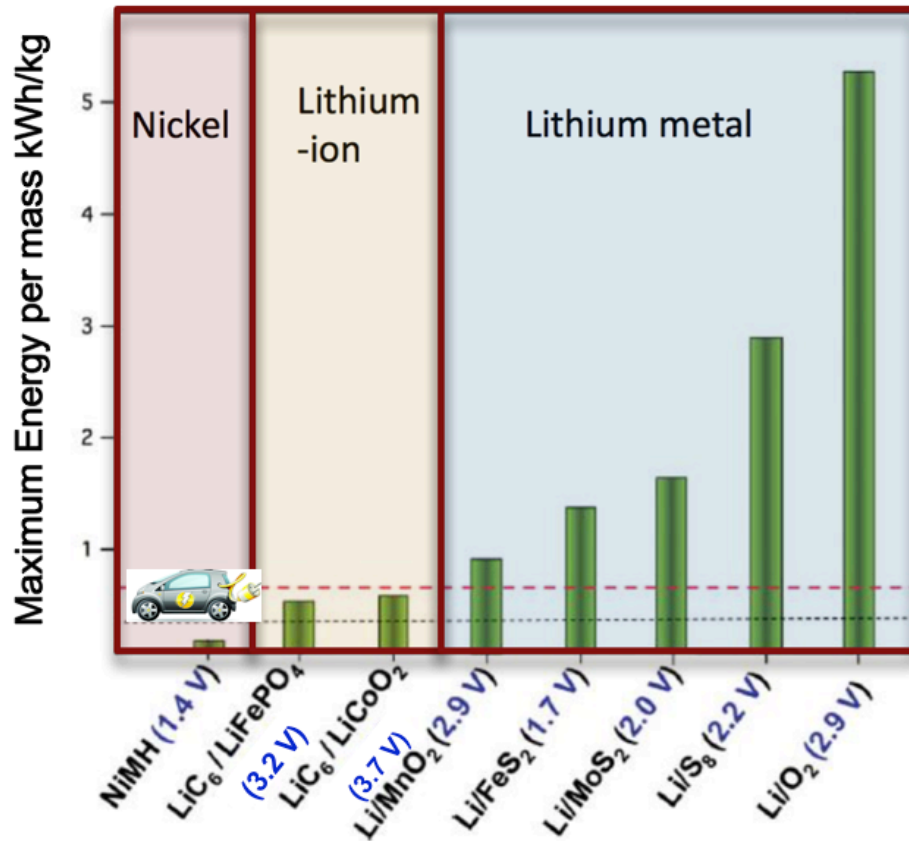


Figure 1.2. theoretical specific energy and nominal voltage for various Li based rechargeable batteries. Red line and black line are long term and short term targets, respectively. Blue line is the target for HEVs. Reproduced with permission¹⁸. Copyright (2012) Wiley.

as well as the charge/mass transfer between heterogeneous phases will largely determine the reversibility and energy of the battery system.

1.3 Lithium electrodeposition in a battery

The incorporation of metallic lithium in a battery can in principle significantly improve the energy density without changing the battery operation protocol and mechanism, yet it invokes safety concern arising from the rough lithium electrodeposition or the so-called dendrite formation²³⁻²⁴. Recharging a LMB requires electrodeposition of lithium onto a metal substrate (or on lithium itself), a process that is fundamentally unstable. At low current densities, the concentration of electric field lines and preferential transport of ions to rough regions on the electrode surface produce the morphological instability loosely termed dendrites^{10, 25}. Meanwhile, at high current densities, depletion of anions in the electrolyte near the anode creates a space charge that drives a hydrodynamic instability termed electroconvection²⁶. This electroconvection draws ions away from regions surrounding a growing dendrite and focuses them on the dendrite tip, enhancing dendrite growth. Thus, for quite fundamental physical reasons, recharge of a LMB at either low or high currents produces rough and dendritic deposition of the metal. One should note that because of the small voltage difference (<300 mV) for lithium ions to intercalate into versus deposit onto a graphitic carbon electrode², uneven

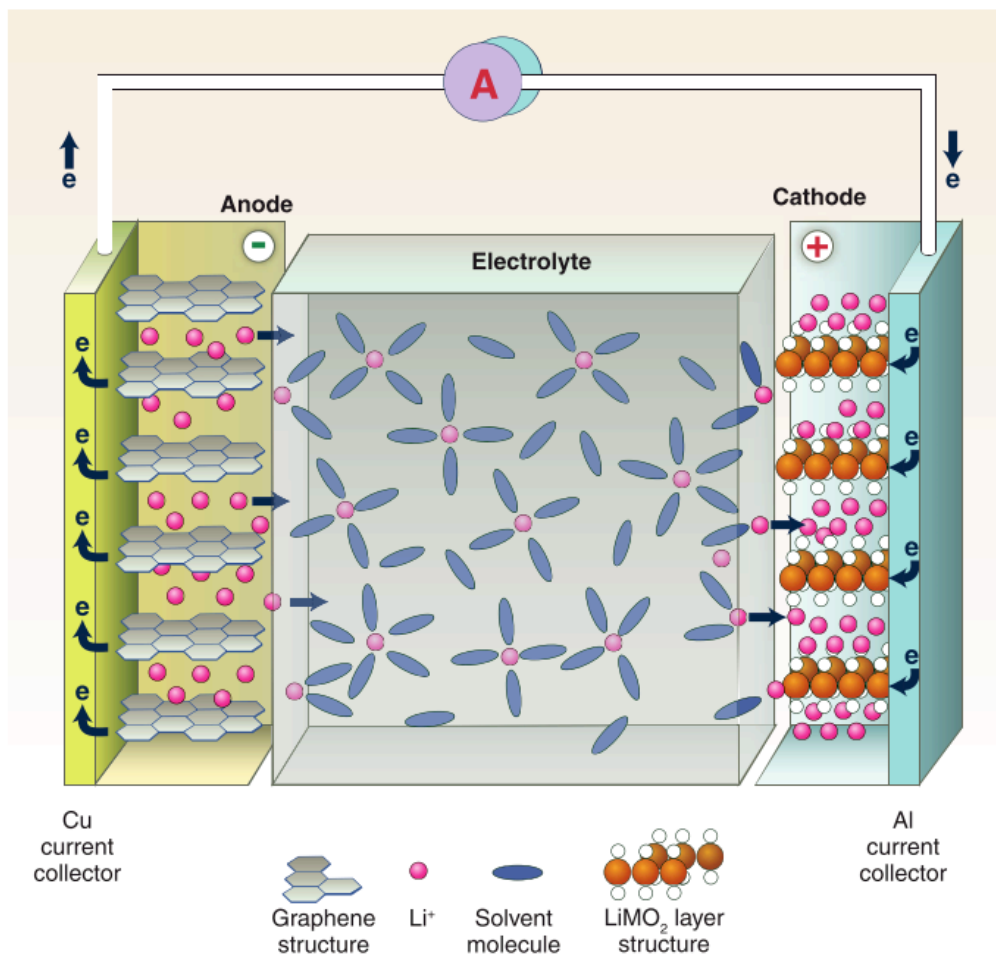


Figure 1.3 A schematic description of the general structure of lithium ion battery.

Adapted with permission³. Copyright (2011) AAAS Publishing

electrodeposition of lithium dendrites can also occur in a too quickly charged LIB and sets limits on “fast-charging” technology for LIBs in transportation. In other words, a too quickly charged LIB, or a LIB charged at too low temperature, may despite their lower energy storage capacity, fail by similar catastrophic processes as a LMB.

In fact, similar uneven electrodeposition of metals has long been observed in other fields such as electroplating of Zn, Cu, Ag, etc. Conventional wisdom considers the process as a competition between ion migration under the electric field and the diffusion by concentration gradient, especially when the current density (J) approaches the limiting value beyond which diffusion is unable to replenish ions depleted from regions in an electrolyte by electromigration²⁷⁻²⁸. Transport processes in dilute electrolytes that lead to space-charge formation have been shown to nucleate dendrites

at the Sand’s time²⁹ $\tau_s = \frac{\pi D(nF)^2 C_o^2}{4J^2 t_a^2}$, which scales inversely as the anion transference number squared. Thus, the nucleation of dendrites may be delayed—in principle, indefinitely—in electrolytes for which the anion transference number is zero or in which a supporting electrolyte is present in high concentration.

While modification of ion transport can suppress dendrites, they cannot eliminate them in liquid electrolytes. Monroe and Newman³⁰⁻³¹ introduced the idea that dendrite growth may be stopped completely using a mechanically strong separator. By evaluating the effect of elastic deformation of the electrode and separator on the deposition reaction kinetics, the authors found that non-uniform Li deposition is

completely arrested when the condition $G > 1.8G_{\text{Li}}$ is met. Here G and G_{Li} are, respectively, the shear modulus of the separator and Li-metal. This condition is met for $G \approx 6$ GPa at room temperature, but could be achieved at much lower separator modulus as one approaches the melting temperature ($T = 180.5$ °C) of Li. To our knowledge, only one study has attempted to evaluate this prediction quantitatively³². The guidance provided by the Monroe and Newman analysis is nonetheless intuitive, which has fueled the common perception that a solid-state electrolyte separator with high modulus is a requirement for practical room-temperature LMBs.

For a lithium metal electrode, an additional complexity comes in along with the effect from the ion transport and electrolyte/separator mechanics, which involves the surface of the electrode or the interphase between the electrode/electrolyte. This factor has been more or less neglected in other metals, but must be considered in reactive metals such as lithium which is prone to react with the electrolyte either chemically or electrochemically. Earlier work shows that none of the commonly used liquid electrolytes are stable in contact with Li-metal and all form a resistive passivation layer that is heterogeneous and unstable³³. Significant effort has been placed on creating artificial SEIs, either designed ex situ or formed in situ by additives that limit exposure of the Li anode to the electrolyte. Recent joint density functional theoretical (JDFT)

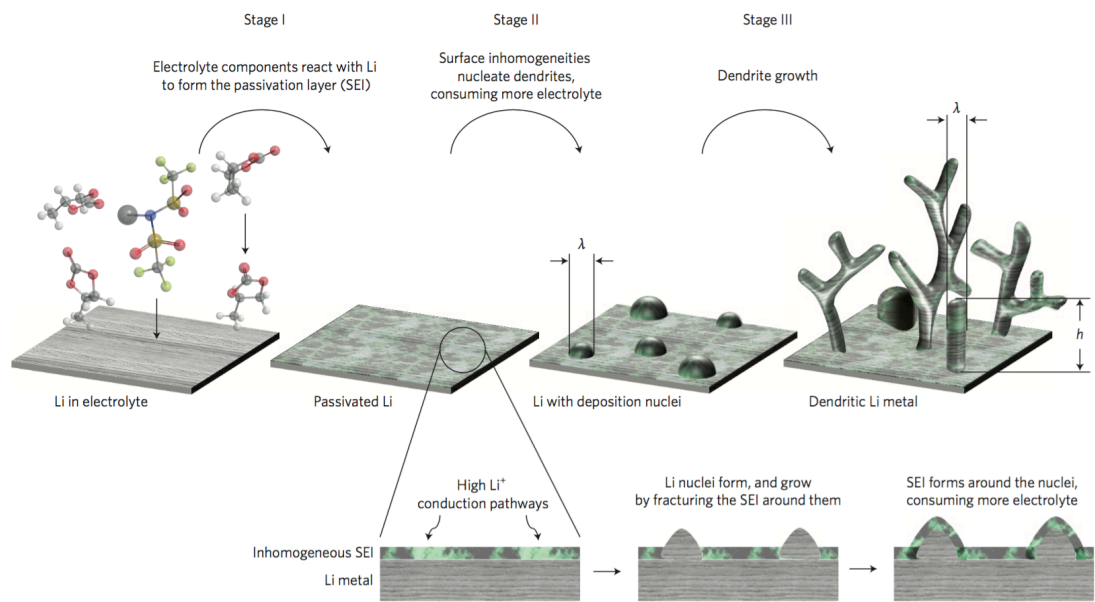


Figure 1.4. Schematic illustration of the evolution dendrites and the origin of instability. Reproduced with permission¹⁰. Copyright (2017) Nature Publishing Group

calculations³⁴ show that a cleverly engineered SEI can not only control Li surface reactivity, but also may alter transport and surface tension. In particular, the calculated energy barriers for Li⁺ diffusion at the anode (E_a) are substantially lower in a SEI composed of halide salts (for example: LiBr, $E_a \approx 0.03$ eV; LiF, $E_a \approx 0.16$ eV), compared with Li₂CO₃ ($E_a \approx 0.24$ eV), which forms naturally when aprotic solvents react with Li. An important achievement of the JDFT analysis is that it explains why electrodes based on Mg, which have low surface diffusion barriers and high surface energies, do not form dendrites.

1.4 Understanding the origin of instability

Thus, the three factors including electroconvective-induced dendrite growth, mechanical weakness, and preferable surface chemistry can in principle work in tandem to cause lithium electrodeposition instability. Starting from a linear stability analysis, we came up with a family of strategies to suppress dendrite proliferation governed by a simulation-derived phase diagram, as shown in **Figure 1.5**. The diagram defines the stability and instability of electrodeposition in white and gray regions, respectively, which are divided by well-defined boundaries. Straightforwardly, stable electrodeposition can be achieved with sufficiently high modulus, a result in agreement with previous theoretical and experimental work. Even when the modulus is low, it is still possible to stably electrodeposit lithium given other preferable conditions. To better understand the phase

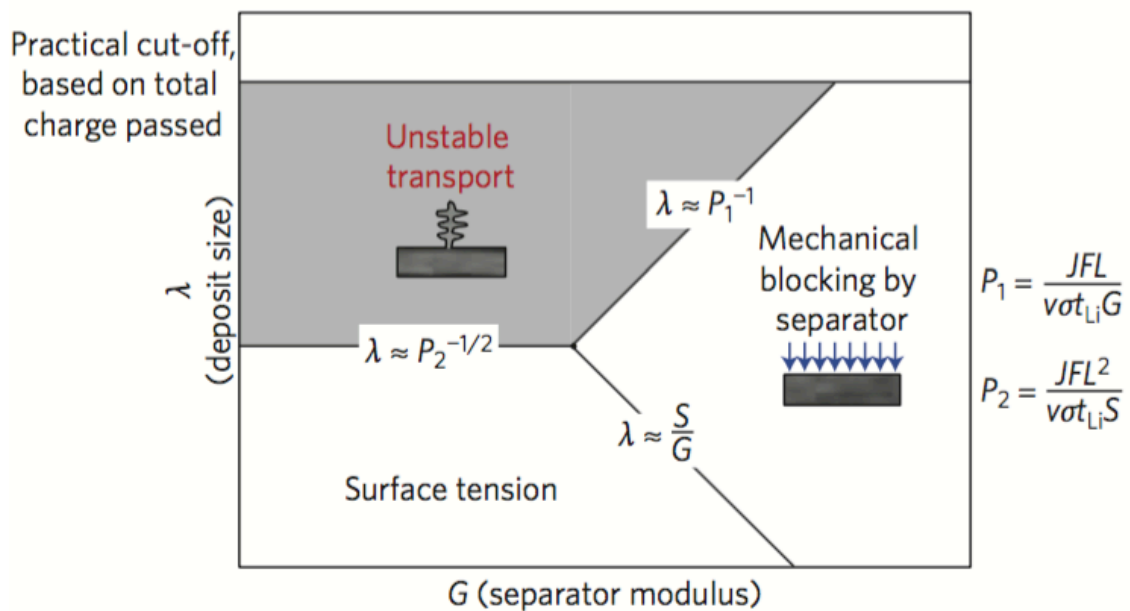


Figure 1.5. Stability phase diagram from the linear stability analysis. Reproduced with permission¹⁰. Copyright (2017) Nature Publishing Group

diagram, we identify the following five variables that determine the stability of deposition at the Li anode: t_{Li} , σ , J , G , and S . The first three variables (t_{Li} , σ , J) control transport processes in the electrolyte, the fourth accounts for the effects of electrolyte separator mechanics on kinetics of the deposition reaction, and the final term captures the effect of the surface tension. S is the most straightforward of these variables to manipulate in a battery, but the most difficult to measure accurately because it depends on properties of the SEI, such as its thickness, structure, stiffness, and diffusivity of Li^+ in the SEI. These five variables can be used in conjunction with the molar volume of Li-metal (v) to write down two dimensionless groups, $P_1 = JFL / v\sigma t_{Li}G$ and $P_2 = JFL^2 / v\sigma t_{Li}S$, which determine the current density-scaled growth rate ξ / J of a Li dendrite nucleate of size λ as shown in Fig. 1. Here, F is Faraday's constant and L is the electrolyte separator thickness. A recent detailed analysis, leads to an analytical relationship between ξ / J , λ , P_1 , and P_2 of the form:

$$\frac{\xi}{J} = \frac{v}{F} \frac{2\pi}{\lambda} \left[1 - \frac{2\pi L}{\lambda P_1} - \left(\frac{2\pi}{\lambda} \right)^2 \frac{L^2}{P_2} \right]$$

Thus, it is clear that to move the boundary between the gray and white region towards more stable electrodeposition ($\xi \leq 0$), smaller P_1 and P_2 values are required and thus the preferable material properties embedded in the two dimensionless groups become apparent. The size of P_1 reflects the balance between destabilizing influences of transport and the stabilizing effect of separator mechanics, while P_2 balances transport with surface tension. The condition $\xi / J = 0$ can also be achieved for a critical deposit size λ_{cr} , which is the smallest nucleate size that can be stably deposited. This result

implies that if a well-defined nanostructure is applied to guide electrodeposition with length scale smaller than the λ_{cr} , the electrodeposition should be stable at the given condition.

1.5 Goals and Methods

Inspired by the theoretical framework, my Ph.D. projects are thus focused on two aspects. The first involves exploring the effect of nanostructure hybrid electrolyte/separator with pore size comparable to the critical deposit size for achieving stability of lithium electrodeposition. A model system with nanoporous ceramic and polymer have been studied in the context of lithium battery or lithium electrodeposition system. This class of materials and configurations significantly alleviate the dendrite growth of lithium and prevent the potential battery short-circuit. However, the side reaction between the lithium and the electrolyte can still occur, which asks for my second research focus: careful design of electrode/electrolyte interphase protection. It is found that many materials ranging from halide salt additives, single-ion conductive polymer, ceramic, or even metals could in principle promote efficient lithium plating/stripping. The bifurcated research directions can also be integrated to achieve a synergetic effect, which could provide information for the development of high energy lithium or other metal-based rechargeable batteries.

1.6 Outline of the dissertation

Chapter 2: This chapter will focus on a family of hybrid electrolyte separator based on nanoporous Al_2O_3 and PVDF-HFP lamellar support. The sandwich structure

provides a good combination of high modulus and toughness. After imbibing with the liquid electrolyte, a high ionic conductivity at room temperature can also be obtained, meaning ions can move freely in the nanostructured material. While the nanopores allow swift ion transportation, they can effectively prevent the penetration of oversized dendrite. As a result, dendrite free battery operation can be achieved at moderately high current density and very large overall capacity.

Chapter 3: To further investigate the effect of pore size on electrodeposition of lithium, this chapter will focus on a reformed design of the battery configuration which allows direct interaction between the nanoporous structure with the lithium electrodeposits on the surface. Systematic studies on the pore size effect of the ion transport and deposition stability are then conducted. By using NMR and electrochemical analyzer, a strong lithium transference number dependence on the pore size and concentration are observed, which is in agreement with the theoretical prediction based on the ion-double layer interaction. Lithium electrodeposition is found to be related to the pore dimension, a result also found in track-etched polymer membranes with similar straight nanoporous structure.

Chapter 4: A class of lithium halogen salts (LiF, LiCl, LiBr, etc.) has been studied as electrolyte additives in the aprotic electrolyte for stabilizing lithium electrodeposition. It is found that with limited amount of halogen salts, flat electrodeposition can be achieved which significantly improves the battery lifetime. The result is in good agreement with joint density function theory (JDFT) that predicts a low diffusion

barrier of ion movement on these halogen salts compared with other lithium salts. The result underscores the need to carefully tune the surface property of the electrode by introducing robust and dendrite-inhibiting chemicals.

Chapter 5: To engineer the electrode/electrolyte interphase with better protection, a fluorinated, single-ion conducting polymer is used as an artificial SEI coating on the lithium metal anode. The coating can be readily prepared by solvent casting, which provides a flexible thickness ranging from 100 nm to 10 μm . The electrochemical properties such as the interfacial impedance can also be systemically changed with various coating thicknesses. The high bulk conductivity, high transference number and electrochemical stability of the electrolyte can be simultaneously obtained by such surface protection. A synergistic effect can be found when the nanoporous Al_2O_3 is also employed, which maximally provides dendrite prevention ability and electrochemical stability. Very recently, a related project enlightens the feasibility of the polymer coating on the cathode, as an interlayer to prevent the electrolyte oxidation at high voltage. The result enables the first adoption of highly efficient yet unstable electrolyte at a voltage $> 4.3\text{V}$.

Chapter 6: In this chapter, we report a family of electrochemically active artificial SEI which is composed of transition metal nanoparticles such as Sn or In. Unlike the conventional SEI which merely serves as an ionic conductive layer, the metal-SEI can store lithium ions in addition to the lithium plating, providing a hybrid energy storage model. The metal SEI can be prepared through facile ion exchange in the electrolyte, a

drop-in process for large-scale manufacturing. Resultant protected lithium electrodes exhibit a 5-fold drop of the interfacial impedance and thus higher capacity in terms of battery performance. The structural and chemical information have been carefully studied using a combination of techniques including XRD, cryo-FIB-SEM, cyclic voltammetry and XPS. The result supports the hypothesis on the hybrid storage electrode and further explains the improved lithium plating/stripping lifetime without short-circuiting.

Chapter 7: As a class of artificial SEI parallel to what has been discussed previously, a nanometer-thick Al_2O_3 coating prepared by atomic layer deposition (ALD) provides pin-hole free protection for the electrode. We found that simply by engineering the electrode surface, the electrochemical stability of the electrolyte can be largely improved due to the prevented decomposition occurring near the electrode. The ALD coating further allows efficient lithium plating/stripping over extensive cycling. Post-mortem cryo-FIB-SEM images reveal a solid, dense lithium deposit in contrast to the typical loose and dendritic structure. The ALD coating enables a proof-of-concept battery configuration where the lithium is stored in the cathode initially, and then in situ formed as a metallic lithium anode during the first cycle. The concept is closely related to the anode-free lithium metal battery, in which high energy density and safety are simultaneously achieved by limiting the amount of lithium in the cell.

1. Tarascon, J. M.; Armand, M., Issues and challenges facing rechargeable lithium batteries. *Nature* **2001**, *414* (6861), 359-367.
2. Armand, M.; Tarascon, J. M., Building better batteries. *Nature* **2008**, *451* (7179), 652-657.
3. Dunn, B.; Kamath, H.; Tarascon, J.-M., Electrical energy storage for the grid: a battery of choices. *Science* **2011**, *334* (6058), 928-935.
4. Scrosati, B., Battery technology-challenge of portable power. *Nature* **1995**, *373* (6515), 557-558.
5. Bruce, P. G.; Scrosati, B.; Tarascon, J. M., Nanomaterials for rechargeable lithium batteries. *Angew. Chem. Int. Ed.* **2008**, *47* (16), 2930-2946.
6. Yoshino, A., The Birth of the Lithium-Ion Battery. *Angewandte Chemie-International Edition* **2012**, *51* (24), 5798-5800.
7. Whittingham, M. S., Electrical energy storage and intercalation chemistry. *Science* **1976**, *192* (4244), 1126-1127.
8. Xu, K., Nonaqueous liquid electrolytes for lithium-based rechargeable batteries. *Chem. Rev.* **2004**, *104* (10), 4303-4418.
9. Goodenough, J. B.; Kim, Y., Challenges for rechargeable Li batteries. *Chem. Mater.* **2009**, *22* (3), 587-603.
10. Tikekar, M. D.; Choudhury, S.; Tu, Z.; Archer, L. A., Design principles for electrolytes and interfaces for stable lithium-metal batteries. *Nature Energy* **2016**, *1*, 16114.

11. Pang, Q.; Liang, X.; Kwok, C. Y.; Nazar, L. F., Advances in lithium–sulfur batteries based on multifunctional cathodes and electrolytes. *Nature Energy* **2016**, *1*, 16132.
12. Manthiram, A.; Yu, X.; Wang, S., Lithium battery chemistries enabled by solid-state electrolytes. *Nature Reviews Materials* **2017**, *2*, 16103.
13. Deng, S.; Xiao, B.; Wang, B.; Li, X.; Kaliyappan, K.; Zhao, Y.; Lushington, A.; Li, R.; Sham, T.-K.; Wang, H.; Sun, X., New insight into atomic-scale engineering of electrode surface for long-life and safe high voltage lithium ion cathodes. *Nano Energy* **2017**, *38*, 19-27.
14. Besenhard, J.; Yang, J.; Winter, M., Will advanced lithium-alloy anodes have a chance in lithium-ion batteries? *J. Power Sources* **1997**, *68* (1), 87-90.
15. Lin, D.; Liu, Y.; Cui, Y., Reviving the lithium metal anode for high-energy batteries. *Nature Nanotechnology* **2017**, *12* (3), 194-206.
16. Aurbach, D.; McCloskey, B. D.; Nazar, L. F.; Bruce, P. G., Advances in understanding mechanisms underpinning lithium–air batteries. *Nature Energy* **2016**, *1*, 16128.
17. Ma, L.; Hendrickson, K. E.; Wei, S.; Archer, L. A., Nanomaterials: Science and applications in the lithium–sulfur battery. *Nano Today* **2015**, *10* (3), 315-338.
18. Lu, Y.; Das, S. K.; Moganty, S. S.; Archer, L. A., Ionic Liquid-Nanoparticle Hybrid Electrolytes and their Application in Secondary Lithium-Metal Batteries. *Adv. Mater.* **2012**, *24* (32), 4430-4435.

19. Schaefer, J. L.; Lu, Y.; Moganty, S. S.; Agarwal, P.; Jayaprakash, N.; Archer, L. A., Electrolytes for high-energy lithium batteries. *Applied Nanoscience* **2012**, *2* (2), 91-109.
20. Arora, P.; Zhang, Z., Battery separators. *Chem. Rev.* **2004**, *104* (10), 4419-4462.
21. Agrawal, R. C.; Pandey, G. P., Solid polymer electrolytes: materials designing and all-solid-state battery applications: an overview. *Journal of Physics D-Applied Physics* **2008**, *41* (22).
22. Quartarone, E.; Mustarelli, P., Electrolytes for solid-state lithium rechargeable batteries: recent advances and perspectives. *Chem. Soc. Rev.* **2011**, *40* (5), 2525-2540.
23. Brissot, C.; Rosso, M.; Chazalviel, J. N.; Lascaud, S., Dendritic growth mechanisms in lithium/polymer cells. *J. Power Sources* **1999**, *81*, 925-929.
24. Li, Z.; Huang, J.; Yann Liaw, B.; Metzler, V.; Zhang, J., A review of lithium deposition in lithium-ion and lithium metal secondary batteries. *J. Power Sources* **2014**, *254*, 168-182.
25. Tikekar, M. D.; Archer, L. A.; Koch, D. L., Stabilizing electrodeposition in elastic solid electrolytes containing immobilized anions. *Science Advances* **2016**, *2* (7), e1600320.
26. Fleury, V.; Chazalviel, J.-N.; Rosso, M., Coupling of drift, diffusion, and electroconvection, in the vicinity of growing electrodeposits. *Physical Review E* **1993**, *48* (2), 1279.
27. Han, J.-H.; Khoo, E.; Bai, P.; Bazant, M. Z., Over-limiting current and control of dendritic growth by surface conduction in nanopores. *Scientific reports* **2014**, *4*.

28. Rosso, M.; Gobron, T.; Brissot, C.; Chazalviel, J.-N.; Lascaud, S., Onset of dendritic growth in lithium/polymer cells. *J. Power Sources* **2001**, *97*, 804-806.
29. Sand, H. J., On the Concentration at the Electrodes in a Solution, with special reference to the Liberation of Hydrogen by Electrolysis of a Mixture of Copper Sulphate and Sulphuric Acid. *Proceedings of the Physical Society of London* **1899**, *17* (1), 496.
30. Monroe, C.; Newman, J., The impact of elastic deformation on deposition kinetics at lithium/polymer interfaces. *J. Electrochem. Soc.* **2005**, *152* (2), A396-A404.
31. Monroe, C.; Newman, J., The effect of interfacial deformation on electrodeposition kinetics. *J. Electrochem. Soc.* **2004**, *151* (6), A880-A886.
32. Stone, G.; Mullin, S.; Teran, A.; Hallinan, D.; Minor, A.; Hexemer, A.; Balsara, N., Resolution of the modulus versus adhesion dilemma in solid polymer electrolytes for rechargeable lithium metal batteries. *J. Electrochem. Soc.* **2012**, *159* (3), A222-A227.
33. Aurbach, D.; Zinigrad, E.; Cohen, Y.; Teller, H., A short review of failure mechanisms of lithium metal and lithiated graphite anodes in liquid electrolyte solutions. *Solid state ionics* **2002**, *148* (3), 405-416.
34. Ozhabes, Y.; Gunceler, D.; Arias, T., Stability and surface diffusion at lithium-electrolyte interphases with connections to dendrite suppression. *arXiv preprint arXiv:1504.05799* **2015**.

CHAPTER 2

NANOSTRUCTURED HYBRID POLYMER/CERAMIC COMPOSITE ELECTROLYTE FOR LITHIUM METAL RECHARGEABLE BATTERIES

Reproduced from *Advanced Energy Materials* 4. 2 (2014)

Reproduced from *Small* 11. 22 (2015): 2631

2.1 Abstract

A nanoporous composite material that offers the unique combination of high room-temperature ionic conductivity and high mechanical modulus is reported. When used as the separator/electrolyte in lithium batteries employing metallic lithium as anode, the material displays unprecedented cycling stability and excellent ability to prevent premature cell failure by dendrite-induced short circuits

2.2 Introduction

Advances in materials that enable high-energy and safe electrochemical storage are understood to be a critical next step for portable electronic devices and for electric vehicles. Progress in both fields requires high-density, reliable and safe storage of electrical energy. Rechargeable lithium ion batteries (LIB), due to their high energy density, low internal resistance and minimal memory effects, are currently the most attractive storage technology¹⁻⁴, they are expected to dominate the marketplace for the foreseeable future. Two well-known drawbacks of current LIB technology stem from the carbonaceous material used to host lithium in the anode. First, the 6/1 C/Li molar ratio in the anode lowers the anode specific capacity by more than one order of magnitude: from 3860 mAh g⁻¹ to around 360 mAh g⁻¹⁵. It also limits the choice of cathode to relatively low capacity, lithiated compounds, such as lithiated metal oxides, phosphates, and silicates, and presents a barrier to usage of novel, high-storage capacity cathode chemistries based on un-lithiated materials including oxygen, sulfur, and carbon dioxide⁶⁻⁷. A second, less appreciated drawback arises from the small difference in potential that separates lithium insertion into the host and lithium plating

onto the host.^[8] Thus, either an overcharged or too quickly charged lithium ion battery can become a lithium metal battery (LMB), wherein the deposited metallic lithium provides the primary storage material in the anode. This means that notorious safety issues associated with non-uniform electrodeposition on metallic lithium anodes, dendrite formation and potential for catastrophic cell failure by internal short circuits⁸, which are normally associated with LMBs, are also an important concern for LIBs.

Development of electrolyte and separator platforms that permit safe and reliable cycling of lithium batteries that utilize metallic lithium anodes provide a potential solution to both of these problems, and is thus an important scientific undertaking. A key requirement of such an electrolyte/separator would be the ability to suppress or eliminate uneven electrodeposition of Li and/or to retard subsequent dendrite formation and proliferation during repeated charge-discharge cycles⁹. Several strategies have been proposed in the older literature for suppressing/managing lithium dendrite growth in LMBs. The list includes electrode coatings that prevent dendrite-induced short-circuits¹⁰; introducing so-called solid electrolyte interface (SEI) additives into the electrolyte, which facilitate electrodeposition of Li¹¹, application of external pressure on the lithium metal electrode to “flatten” the electrode/electrolyte interface¹². Mechanical blocking using solid or solid-like electrolytes with sufficiently high modulus to prevent growth of any formed dendrites¹³⁻¹⁴ has good theoretical support from the model of Monroe and Newman, which shows that an electrolyte with shear modulus around two times that of lithium metal can prevent dendrite growth in a LMB¹⁵. Unfortunately, the most commonly used electrolyte materials that present sufficiently high mechanical moduli, including polymers and ceramics, are

insufficiently conductive and/or too brittle to be used in practical room-temperature LMBs.

Recently, new approaches have become available to retard lithium dendrite growth and proliferation in secondary batteries. Self-suspended suspensions of polyethylene glycol (PEG) functionalized nanoparticles have for example been shown to undergo a jamming transition, leading to formation of a nanoporous network of a lithium conductive PEG phase, mechanically reinforced by a silica nanoparticle network¹⁶⁻¹⁷. While the confinement of PEG in the nanopores leads to moderate enhancements in Li transference number, the room temperature ionic conductivities of the jammed materials are not high. By blending similar silica nanoparticles tethered with an ionic liquid (IL) in a conventional propylene carbonate (PC) - lithium bis(trifluoromethanesulfonyl) imide (LiTFSI) electrolyte, Lu et al. showed that high room-temperature ionic conductivities can be achieved in such hybrids. And, when used as the electrolytes in LMBs, the IL-nanoparticle hybrid electrolytes lead to as much as a ten-fold increase in cell lifetime¹⁸. The authors explained their observation in terms of the space charge mechanism proposed by Chazaviel¹⁹. Specifically, it was argued that because the anion (TFSI) is the same for both the nanoparticle-tethered IL and for the electrolyte salt, the IL-tethered particles provide a reservoir of TFSI throughout the electrolyte that neutralizes development of the space charge. More recently an elegant, self-healing approach has been proposed for dendrite prevention through mixing small amounts of salts based on Cesium ions with a lithium salt-based electrolyte²⁰. This method has so far shown promising ability to prevent lithium dendrite formation in post-mortem studies of lithium electrodes, but it has been

insufficiently studied to determine its applicability to LMBs cycled at moderate and high current densities.

In this communication we report a model nanoporous separator/electrolyte configuration that facilitates both high mechanical moduli and facile ion transport at room temperature. The separator is created by laminating a nanoporous γ -Al₂O₃ sheet with a high pore density between macroporous poly(vinylidene fluoride-co-hexafluoropropylene) (PVDF-HFP) polymer layers to create a sandwich-type composite structure (**Figure 2.1**). The obtained composite separator exhibits remarkably improved toughness, in comparison to nanoporous alumina, and readily imbibes an electrolyte based on 1M LiTFSI in PC to produce an electrolyte/separator material with room-temperature ionic conductivity above 1 mS cm⁻¹ and mechanical modulus of at least 0.5 GPa at room temperature. To our knowledge the reported materials are among the first to exhibit this attractive combination of mechanical and ion transport properties at room temperature.

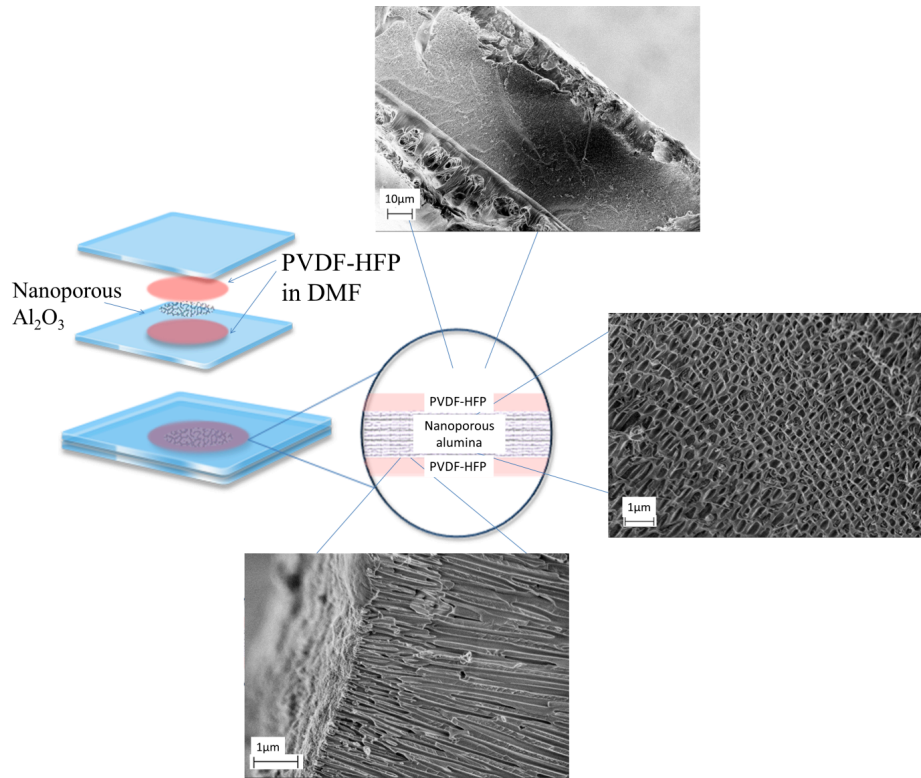


Figure 2.1. Middle and left: Schematic of the structure and preparation method of PVDF-HFP/Al₂O₃ separator. SEM pictures of the PVDF-HFP/Al₂O₃ with 100 nm nanopores: top, cross-section of the composite; right, cross-section of the internal alumina layer; bottom, boundary between alumina and polymer.

2.3 Experimental Section

For nanoporous hybrid electrolyte/separator

Polyvinylidene fluoride hexafluoropropylene (PVDF-HFP, supplied by Sigma Aldrich.) was dissolved in N, N-dimethylformamide (DMF, supplied by Sigma Aldrich) at 10 wt% concentration. The viscous solution was poured onto a clean glass plate, covered by nanoporous alumina membrane (Whatman Anodisc[®] 25 with 20 nm, 100 nm, and 200 nm pore sizes, supplied by Fisher). The surface flatness and overall laminate membrane thickness (around 0.8 mm) were controlled using a doctor blade technique. The glass plate with materials on top was immersed in a water bath at room temperature. The formed solid composite separator was completely dehydrated in vacuum. To prepare the electrolyte -separator, the composite separator was soaked in 1M lithium bis(trifluoromethanesulfonyl)imide (LiTFSI)/ propylene carbonate (PC) solution for at least 24 hours. The symmetric lithium coin cells and the Li/LTO coin cells (both 2032 type) were prepared under argon protection (glove box, MBraun. Labmaster). The symmetric lithium/lithium coin cells have Li/(PVDF-HFP/Al₂O₃/LiTFSI/PC)/Li structure, while the Li/LTO coin cells have Li/(PVDF-HFP/Al₂O₃/LiTFSI/PC)/LTO structure. The LTO electrode is composed of 10% PVDF binder, 10% carbon black, and 80% LTO. A small amount of N-methylpyrrolidone (NMP) was used as solvent for homogenizing all components. The resultant slurry was coated on a copper plate and rigorously dried. Because the laminated PVDF-HFP/Al₂O₃/LiTFSI/PC electrolyte-separators hosts large amounts of liquid electrolyte that wets LTO well, it is assumed that activation of the LTO

electrode occurs almost immediately after contacting with the electrolyte-separator and none of the usual electrochemical activation processes were used in the current experiments.

Scanning electron microscopy (LEO-1550-FESEM) was used to characterize the laminated structure in the composite separator. The separator was cut in liquid nitrogen to achieve clean edges. The sample was placed vertically on a SEM stub for cross-section observation. The SEM images were obtained under 3 kV voltages with aperture size of 30 μm . Mechanical properties of the separator/electrolyte materials were characterized using dynamic mechanical analysis (DMA-Q800) in the temperature range from -130 $^{\circ}\text{C}$ to 150 $^{\circ}\text{C}$. A heating rate of 10 $^{\circ}\text{C min}^{-1}$ and frequency of 1 Hz were employed for these measurements. Atomic force microscopy (AFM, Asylum-MFP-3D-Bio-AFM) was used to indirectly measure the modulus of the unlaminated Al_2O_3 film. The force mode was chosen to obtain the force plot against the indent depth. Conductivity and impedance were measured against frequency using a Novocontrol N40 broadband dielectric spectroscopy at different temperature from -5 $^{\circ}\text{C}$ to 100 $^{\circ}\text{C}$. The lithium plate/strip experiment and galvanostatic charge/discharge experiment were performed on a Neware CT-3008 battery tester. The plate-strip experiment was performed with symmetric lithium coin cells under different current density (0.02, 0.05, 0.1, and 0.2 mA cm^{-2}). The coin cells harvested after the plate-strip experiment were taken apart in a glove box and the separator/electrolytes dried in the vacuum chamber of the glove box and stored for SEM analysis. The galvanostatic experiment was performed under different

charging/discharging rate (0.315, 0.630, and 1.575 mA cm⁻², which corresponds to 1C, 2C and 5C, respectively).

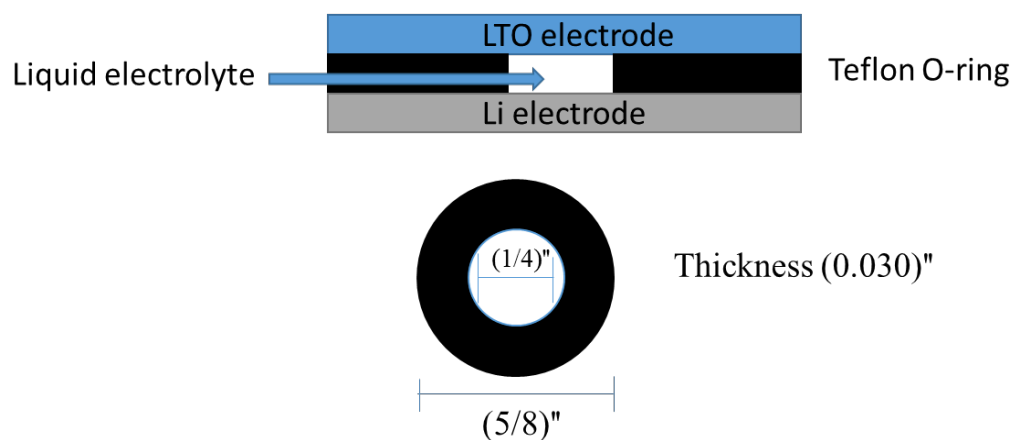
For thick LTO model cell:

Lithium metal foils with 0.35 mm thickness were purchased from Sigma Aldrich. Lithium titanate oxide (Li₄Ti₅O₁₂) nanopowders (Sigma-Aldrich, particle size < 200nm), Super P carbon black, and polyvinylidene fluoride (PVDF, Sigma-Aldrich, Molecular Weight ~ 520k) were pre-mixed in a mortar and then transferred for thorough ball milling. The resultant Li₄Ti₅O₁₂ powders were portioned based on a predetermined weight. A hydraulic press was used to compress Li₄Ti₅O₁₂ powders at 20000 kPa for 5 mins. The obtained Li₄Ti₅O₁₂ plates were carefully transferred and stored in an argon-filled glove box (Mbraun).

Al₂O₃ based polymer/ceramic composite separators were prepared as reported.^[33, 34] Briefly, nanoporous Al₂O₃ (Whatman) and (Poly(vinylidene fluoride-hexafluoropropylene) (PVDF-HFP) were composited through phase-separation method. The resultant polymer/ceramic composites were soaked in propylene carbonate (PC) with 1M bis(trifluoromethane)sulfonimide lithium salt (LiTFSI) for over 24 hours in argon atmosphere.

To test the battery performance, the above mentioned materials were assembled in CR2032 coin cells. The Li₄Ti₅O₁₂ plates were used as cathodes and lithium foils were used as anodes. The composite polymer/ceramic composite membranes imbibed with liquid electrolyte were placed in between two electrodes as separators. For comparison,

a type of home-made Teflon rings were used as spacers in coin cells with no separator as a control group (**Scheme 2.1**).



Scheme 2.1. The configuration of lithium coin cell with Teflon O-ring instead of separator.

The galvanostatic cycling tests of coin cells were conducted on Neware battery test systems. The surface information of $\text{Li}_4\text{Ti}_5\text{O}_{12}$, lithium foil and separator were obtained using SEM (LEO-1550-FESEM) and Bruker Energy Dispersive Spectrometer (EDS). XRD (Scintag-Theta-Theta-X-Ray-Diffraction) technique was used to characterize the structure of the $\text{Li}_4\text{Ti}_5\text{O}_{12}$ electrode. A Novocontrol broadband dielectric spectrometer was used to gather impedance spectra of coin cells at a temperature range from -5 to 100 °C.

2.4 Results and discussion

The nanoporous $\gamma\text{-Al}_2\text{O}_3$ is prepared by voltage-controlled anodic oxidation of metallic aluminum²¹⁻²², and it is possible to precisely manipulate the pore dimensions through the processing voltage. PVDF-HFP/ $\gamma\text{-Al}_2\text{O}_3$ separators were prepared using a phase separation method described in the Experimental Section. The resultant composite films were immersed in a 1M LiTFSI/PC solution to form the electrolyte-separator used for electrochemical studies. The scanning electron micrograph (**Figure 2.1**) shows the material possesses a tri-layer, laminated structure in which the top and the bottom layers are PVDF-HFP and the middle layer is alumina comprised of a dense, uniform distribution of nanometer-sized pores. Before compositing with PVDF-HFP, the porous alumina is extremely brittle which makes it difficult to handle. The macroporous PVDF-HFP coating produced by the phase separation procedure provides exceptionally high levels of mechanical reinforcement for the alumina, without infiltrating its pores. This configuration results in a composite film with dramatically higher mechanical flexibility, high mechanical modulus, and room

temperature conductivity approaching that of the liquid LiTFSI/PC electrolyte hosted in the open pores of the PVDF-HFP/Al₂O₃ laminate.

The shear mechanical modulus is both intuitively and based on theory considered an important physical property for assessing the ability of an electrolyte/separator to impede lithium dendrite growth in a LMB. Because of its brittleness, the mechanical modulus of the unlaminated nanoporous alumina cannot be characterized using normal mechanical testing methods. We instead employ an atomic force microscopy (AFM) approach to first obtain a load-displacement curve (see **Figure 2.2**), and by applying Oliver and Pharr's method²³, subsequently deduce the reduced elastic modulus to be around 500 MPa. This value is substantially lower than the theoretical modulus for bulk Al₂O₃ and somewhat lower than expected even if one factors in the nanoporous nature of the material²⁴. It suggests that even the very small strains applied in the AFM measurement may cause some amount of brittle failure of the unlaminated material. This situation is quite different for the PVDF-HFP/Al₂O₃ composite film, which can be subjected to orders of magnitude larger mechanical deformations without showing any evidence of mechanical failure. **Figure 2.3a** reports the elastic/storage modulus of PVDF-HFP/Al₂O₃ separator film measured using dynamical mechanical analysis of a bulk specimen over a broad range of temperature (-130 °C to 150 °C). The pore size of the Al₂O₃ is varied from 20 nm to 200 nm and the Figure also presents data for the macroporous PVDF-HFP copolymer film without the nanoporous Al₂O₃ interlayer, for comparison. It is apparent that irrespective of the measurement temperature, the elastic modulus for the PVDF-HFP/Al₂O₃ is about one order of magnitude higher than that of the PVDF-HFP and exhibits at most a weak dependence on the nanopore dimensions.

At room temperature, the elastic modulus is close to 0.4 GPa for the composite material with the largest Al₂O₃ pore dimension. In every case, the elastic modulus decreases gradually with increasing temperature, which is attributed to the broad glass transition region for the highly random PVDF-HFP copolymer²⁵. After soaking the PVDF-HFP/Al₂O₃ separators in a 1M LiTFSI/PC electrolyte the materials become even tougher, but slippery, which makes it difficult to measure their mechanical modulus. Based on several repeat experiments we conclude that the storage modulus of a composite film based on Al₂O₃ is at least 0.15 GPa (see Figure S4).

Figure 2.3b reports the conductivity of PVDF-HFP/Al₂O₃/LiTFSI/PC electrolyte-separator with different pore sizes for temperatures ranging from -5 °C to 100 °C. The DC conductivity is determined from AC measurements by the method proposed by Jonscher²⁶. A typical AC conductivity vs. frequency profile is provided in the supporting materials section. The conductivity of PVDF-HFP/Al₂O₃/LiTFSI/PC electrolytes with 100 and 200 nm pore sizes are over 1×10^{-3} S cm⁻¹ at room temperature, which is close to that of the LiTFSI/PC liquid electrolyte. Such high conductivity is attributed to the unrestricted movement of LiTFSI in liquid PC hosted in the pores of the separator. Materials based on Al₂O₃ with smaller, 20 nm pores shows slightly lower conductivity (8×10^{-4} S cm⁻¹) at room temperature, which may be evidence that the decreased pore size to some extent hinders ion transport. The solid lines through the data are fitted using the Arrhenius equation $\sigma = Ae^{-E_a/RT}$ (see **Figure 2.4**). The deviations between theory and data in the low temperature region are attributed to the broad glass transition temperature of PVDF-HFP. The activation

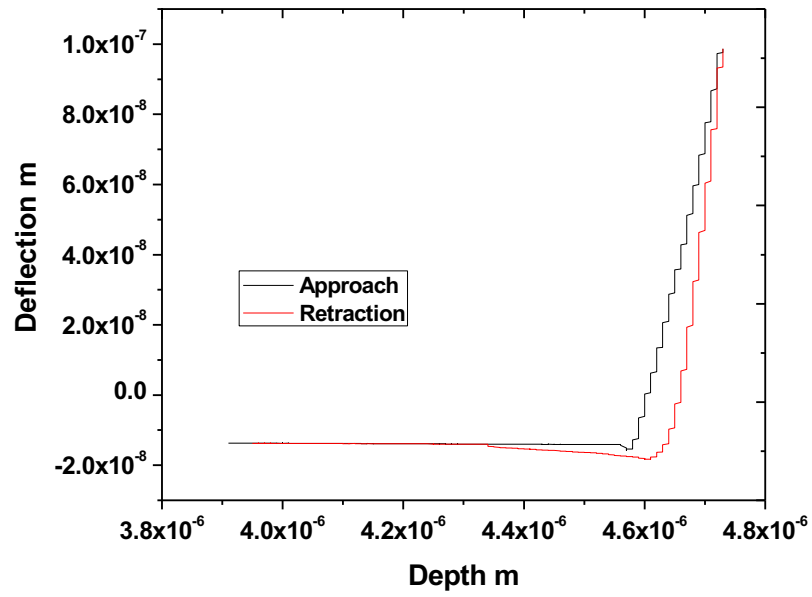


Figure 2.2. A typical force plot from AFM measurement to study the modulus of brittle nanoporous Al_2O_3 .

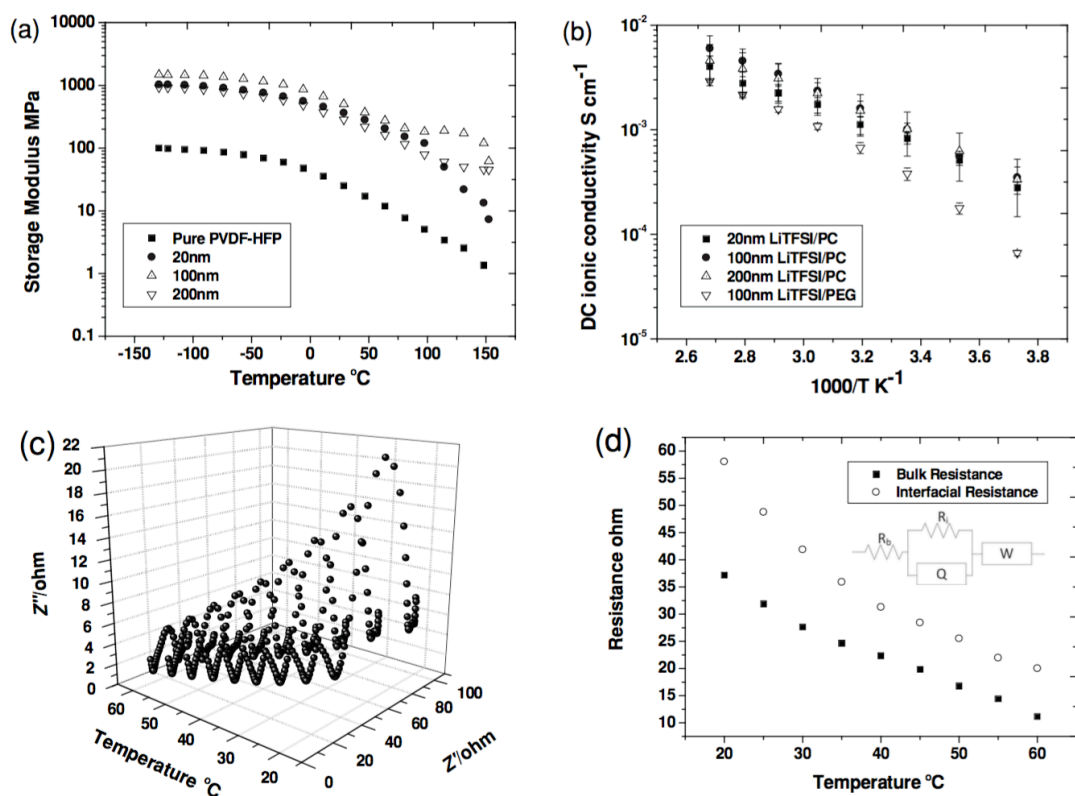


Figure 2.3. (a) Storage modulus of PVDF-HFP/Al₂O₃ separators with various pore sizes and pure PVDF-HFP as a function of temperature. (b) DC ionic conductivity of PVDF-HFP/Al₂O₃ separators with various pore sizes after immersing in LiTFSI/PC and separators with 100 nm pores in LiTFSI/PEG. (c) Impedance spectra of PVDF-HFP/100 nm Al₂O₃/LiTFSI/PC against temperature. (d) Bulk resistance and interfacial resistance of the composite in (c) against temperature, analyzed using the equivalent circuit as inset.

energy obtained from the fits is provided in **Table 2.1** in the supporting materials section. The activation energy values are evidently all close to consensus values for LiTFSI/PC, implying that for the pore dimensions studied, the pores are large enough that the PVDF-HFP/Al₂O₃ serves essentially as a host for the liquid LiTFSI/PC electrolyte.

In addition to facilitating good ion transport in bulk, a suitable electrolyte for a LMB must also present low barriers for injection and removal of Li ions at the electrode/electrolyte interface. **Figure 2.3c** reports impedance spectra of a PVDF-HFP/Al₂O₃/LiTFSI/PC material based on Al₂O₃ with 100 nm nanopores measured in a symmetric lithium coin cell as a function of temperature. By fitting the results to the equivalent circuit model depicted in the inset to **Figure 2.3d**, both the bulk and interfacial resistance can be obtained (**Table 2.2**). It is apparent that both the interfacial and bulk resistances at 25 °C are low (48.8 Ω and 31.9 Ω, respectively) and as expected decrease with increasing temperature. The higher interfacial resistance compared with the bulk resistance shows that the main obstacle for ion conduction is the interfacial diffusion. The corresponding room-temperature bulk and interfacial resistances for the electrolyte-separators based on Al₂O₃ with 20 nm and 200 nm nanopores are, respectively, 9.5 Ω, 51.2 Ω, 60.6 Ω and 82.0 Ω. (see **Table 2.2**). It means that for the range of pore dimensions studied, the materials are good candidates for application in batteries.

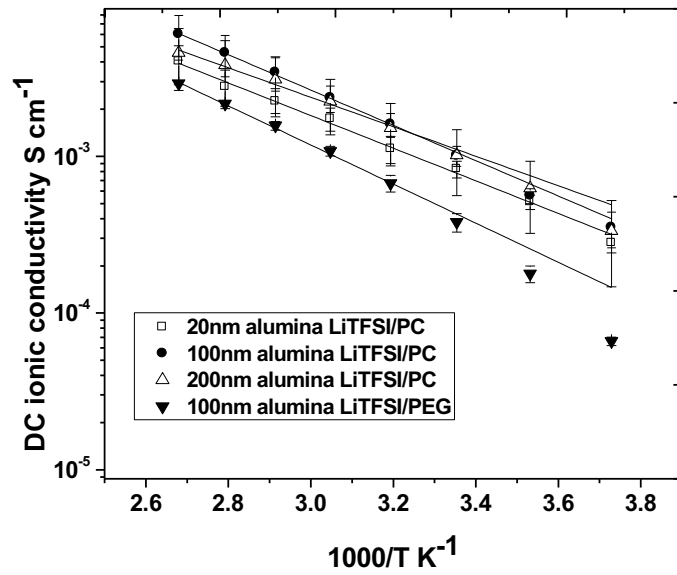


Figure 2.4. DC ionic conductivity of PVDF-HFP/ Al_2O_3 separator with various pore sizes after immersing in LiTFSI/PC and separator with 100 nm pores in LiTFSI/PEG. The solid lines are Arrhenius fits of the data.

Table 2.1. DC ionic conductivity of each system in **Figure 2.4** at room temperature, and activation energy derived from Arrhenius fits.

Sample description #	Conductivity at 25°C [S cm ⁻¹]	Activation Energy Ea [eV]
20 nm Al ₂ O ₃ /LiTFSI/PC	8.30E-4	0.20674 ± 0.00968
100 nm Al ₂ O ₃ /LiTFSI/PC	1.01E-3	0.22375 ± 0.00684
200 nm Al ₂ O ₃ /LiTFSI/PC	1.07E-3	0.18680 ± 0.00712
100 nm Al ₂ O ₃ /LiTFSI/PEG	3.80E-4	0.24762 ± 0.01585

Table 2.2. Bulk and interfacial resistance for composites with various pore diameters.

Temperature °C	Bulk Resistance	Interfacial Resistance	Bulk Resistance	Interfacial Resistance	Bulk Resistance	Interfacial Resistance
	20 nm [ohm]		100 nm [ohm]		200 nm [ohm]	
20	10.77 ± 0.28	65.69 ± 1.85	37.20 ± 0.75	58.03 ± 1.46	72.78 ± 0.83	111.40 ± 1.34
25	9.49 ± 0.24	51.20 ± 1.38	31.88 ± 0.69	48.78 ± 1.29	60.60 ± 0.66	82.00 ± 0.92
30	8.52 ± 0.20	40.94 ± 1.05	27.63 ± 0.57	41.86 ± 1.02	50.77 ± 0.49	62.40 ± 0.68
35	7.91 ± 0.18	32.52 ± 0.79	24.64 ± 0.50	35.93 ± 0.83	43.09 ± 0.40	47.90 ± 0.54
40	7.41 ± 0.15	26.01 ± 0.60	22.35 ± 0.45	31.32 ± 0.72	36.28 ± 0.39	35.70 ± 0.50
45	6.87 ± 0.13	20.18 ± 0.45	19.83 ± 0.50	28.43 ± 0.74	30.00 ± 0.39	25.93 ± 0.46
50	6.32 ± 0.12	16.14 ± 0.36	16.79 ± 1.82	25.52 ± 2.24	24.05 ± 0.21	18.75 ± 0.27
55	5.75 ± 0.11	12.65 ± 0.28	14.44 ± 0.92	21.99 ± 1.14	19.64 ± 0.18	13.69 ± 0.22
60	5.21 ± 0.10	10.00 ± 0.22	11.17 ± 1.41	20.04 ± 1.60	16.11 ± 0.16	10.29 ± 0.20

To assess the stability of our PVDF-HFP/Al₂O₃/LiTFSI/PC electrolyte-separators in batteries employing metallic lithium anodes, we performed electrochemical cycling of a Li/Li₄Ti₅O₁₂(LTO) cell utilizing a laminated material based on Al₂O₃ with 100 nm pores as both the separator and electrolyte. This cell configuration was chosen because of the well-known, stable electrochemical cycling of Li/LTO cells in conventional electrolytes at both low and high rates. It therefore allows the new separator/electrolyte materials to be evaluated at high current densities and over large numbers of charge-discharge cycles to establish their performance limits²⁷.

Figure 2.5a and **2.5b** report the capacity and Coulombic efficiency as a function of cycle number at a fixed current density of 0.315 mA cm⁻² (1C) and 1.575 mA cm⁻² (5C). The experiment is also taken at 0.630 mA cm⁻² (2C) (**Figure 2.6**). It is apparent from this Figure that apart from a small amount of capacity fading over the first few cycles, the cells exhibit stable, high-efficiency cycling over at least 1100 charge/discharge cycles, with no evidence of short circuiting and with a capacity approaching the theoretical maximum (175 mAh g⁻¹) for LTO. Scrutiny of **Figure 2.5a** and **2.5b** shows that the initial capacity fading is accompanied by as rapid a decrease of the Coulombic efficiency from above 100% to stable values close to 100% for more than 1000 cycles. We therefore attribute the initial fading and the excess discharge to electrolyte decomposition and formation of the solid electrolyte interface during the first few cycles, as well as to unwanted side reactions, which further cause electrolyte decomposition²⁸. **Figure 2.5c** and **2.5d** report the galvanostatic charge-discharge profiles after the 1st, 100th, and 1000th cycles at a fixed current density of 0.315 mA

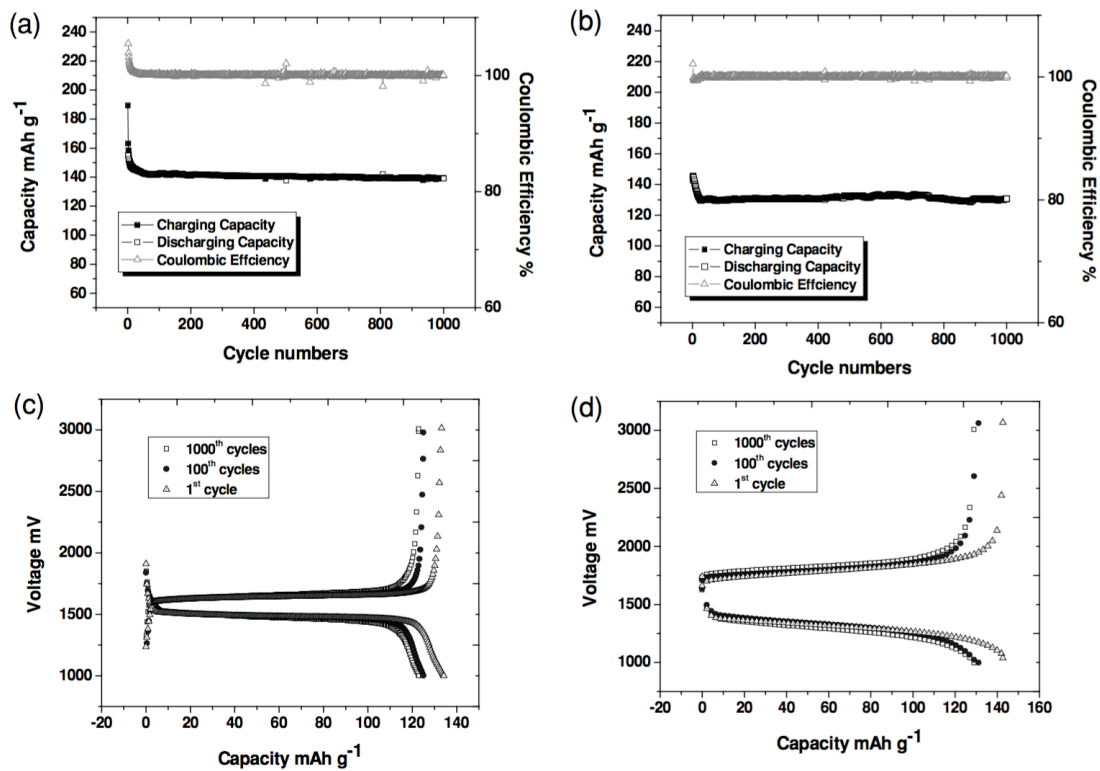


Figure 2.5. Galvanostatic charging/discharging plots for Li/(PVDF-HFP/100 nm Al₂O₃/LiTFSI/PC)/LTO cells under: (a) 0.315 mA cm⁻² (1C) and (b) 1.575 mA cm⁻² (5C). Discharge and charge voltage profiles versus capacity for 1st, 100th, and 1000th cycle for (c) 0.315 mA cm⁻² (1C); (d) 1.575 mA cm⁻² (5C).

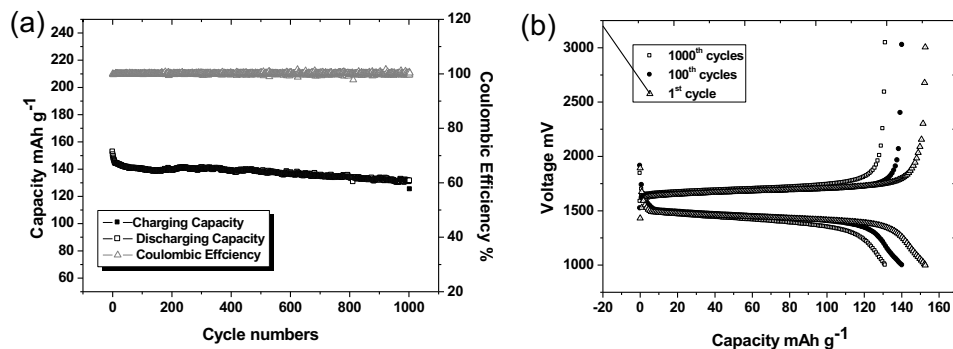


Figure 2.6. (a) Galvanostatic charging/discharging plot for Li/(PVDF-HFP/100 nm Al₂O₃/LiTFSI/PC)/LTO cell under 0.630 mA cm⁻² (2C). (b) Voltage as a function of capacity for 1st, 100th, and 1000th cycle for (a). 0.315 cm⁻² (1C) and 1.575 mA cm⁻² (5C). It is apparent that the voltage plateau, round-trip efficiency, and capacity retention are all quite high.

To further evaluate the performance of the PVDF-HFP/Al₂O₃/LiTFSI/PC electrolyte in LMBs, we employed a cyclic lithium plate/strip electrochemical procedure in a symmetric lithium cell to characterize performance over extended periods of time. Because the capacity of the cathode/anode is not limited by the finite capacity of the LTO host used for the experiments reported in **Figure 2.6**, much larger amounts of lithium can be moved between electrodes within each cycle, which increases the chances of cell failure by dendrite-induced short circuits. In the present experiments a fixed protocol was used wherein cells were periodically charged for 3 hours and discharged for 3 hours at a range of current densities. Formation of a short circuit in this configuration produces an internal path for current flow in the electrolyte, which lowers the internal resistance and causes the measured voltage to drop. Thus, by monitoring the voltage versus time during these strip/plate cyclic experiments, it is possible to identify the onset of short-circuiting from the voltage drop. **Figure 2.8a** depicts the time-dependent voltage profile for a cell based on the electrolyte-separators containing Al₂O₃ with 100 nm pores, cycled for up to 1000 hours under a constant current density of 0.2 mA cm⁻². **Figure 2.8b** reports results from similar measurements, except without the nanoporous Al₂O₃ layer in the separator. The sudden drop observed in the peak-to-peak voltage amplitude in **Figure 2.8b** is attributed to cell failure by dendrite-induced short circuits. A variety of hypotheses have been presented in the literature for why these dendrites form^{19, 29-30}, and proliferate to the point that they lead to cell failure^{15, 19}. Although these results shed no new light on the dendrite nucleation processes, they clearly show that the pore configuration and mechanics of the electrolytes-separators employed are important impediments to dendrite proliferation.

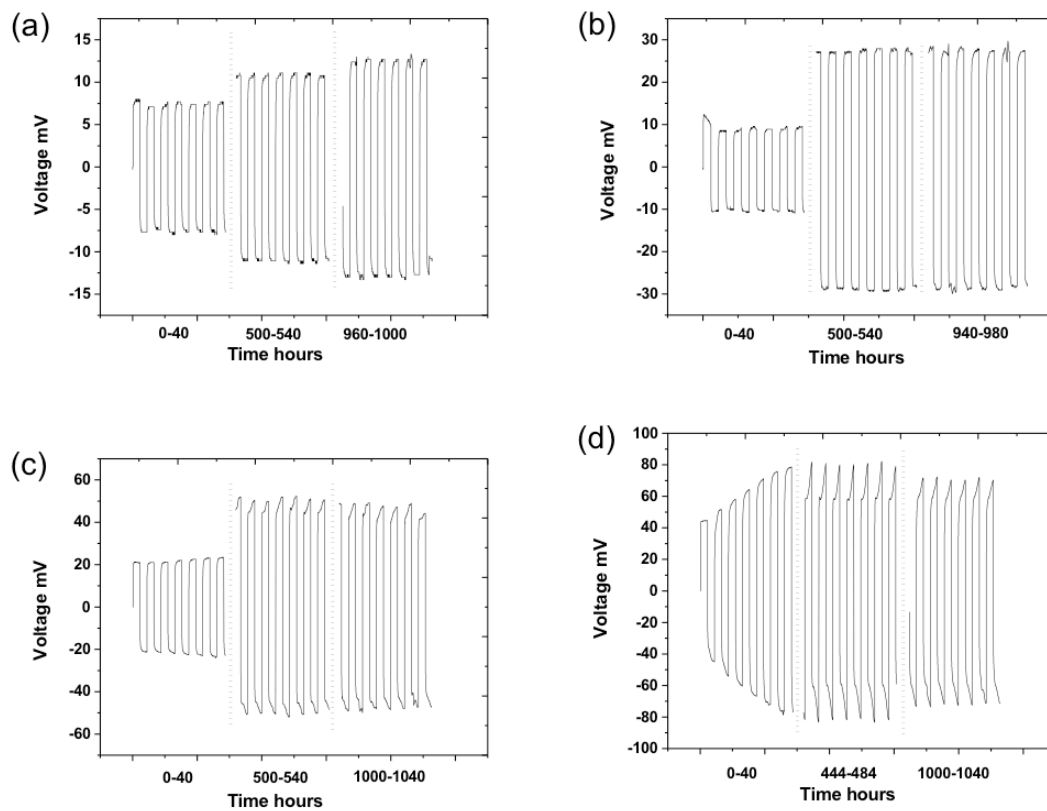


Figure 2.7. Voltage profiles for lithium plating/stripping experiment as a function of time for symmetric lithium coin cell with PVDF-HFP/100 nm Al₂O₃/LiTFSI/PC under (a) 0.02 mA cm⁻²; (b) 0.05 mA cm⁻²; (c) 0.1 mA cm⁻²; (d) 0.2 mA cm⁻²

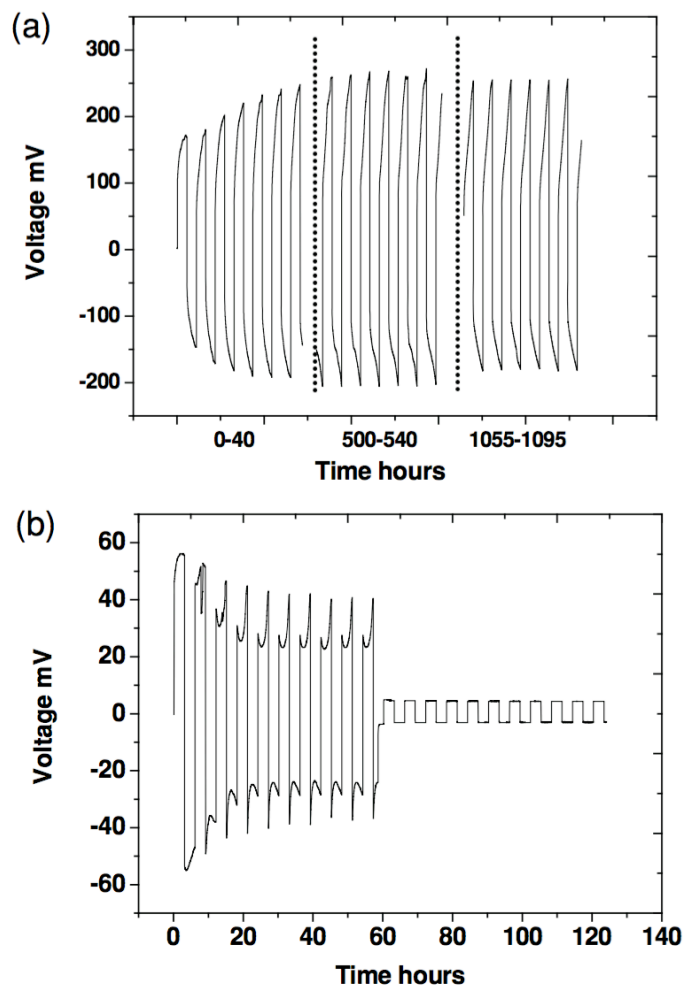


Figure 2.8. Voltage profiles for lithium plating/stripping experiment as a function of time for symmetric lithium coin cell cycled at a fixed current density of 0.2 mA cm^{-2} using: (a) PVDF-HFP/100 nm Al_2O_3 /LITFSI/PC and (b) PVDF-HFP/LiTFSI/PC as separators/electrolytes. The thickness for both separator samples is around 0.8 mm.

In particular, it is seen that while cells based on the PVDF-HFP/LiTFSI/PC fail by short circuiting after as little as 60 hours of operation at 0.2 mA cm^{-2} , cells based on the PVDF-HFP/ Al_2O_3 /LiTFSI/PC electrolyte exhibit stable voltage profiles even after 1000 hours of operation. Considering the modulus of PVDF-HFP/ Al_2O_3 is almost ten times higher than that of PVDF-HFP itself, this result is consistent with Monroe and Newman's analysis.^[15] Results from similar measurements using PVDF-HFP/ Al_2O_3 /LiTFSI/PC electrolyte-separators at both lower and higher current densities are provided in the supporting materials section (**Figure 2.7**). It is apparent from these experiments that the materials are quite effective in stabilizing the cells against failure by short circuiting.

In the field of dendrite study two tests, known as polarization and lithium plating stripping, are recognized as important measurements to evaluate the battery lifetime. The former involves applying single direction DC current to symmetric lithium batteries with two lithium metal electrodes^{19, 29}. Lithium ions will thus be continuously deposited from one electrode to the other. The latter requires the cycling of symmetric lithium batteries which plates and strips lithium ions repeatedly³¹. The lifetime of batteries can be read from voltage/time profile where the sudden drop of the voltage means the occurrence of the short circuit. Although polarization and plating/stripping experiment intuitively demonstrate the battery lifetime, their running conditions are far cry from that of a practical battery where the operation voltage range is much higher. Many studies have used cells with lithium metal anodes against lithium compound cathodes (e.g. LiFePO_4 , $\text{Li}_4\text{Ti}_5\text{O}_{12}$, etc.) to evaluate the battery performance³²⁻³³. However, these cathodes are generally skinny thus the total capacity of the cathodes

are two orders of magnitude lower than that of the lithium due to lack of active materials. Even though dendrites are forming and consequently growing, it is likely they are not long enough to connect electrodes and further fail the battery. In other words, not enough lithium ions are driven during the experiment so that the dendrite formation/growth cannot be comprehensively studied.

Thus, we report a model full-cell LMB with PVDF-HFP/Al₂O₃ laminates infused with liquids as the separator/electrolyte, and a cathode with comparable capacity as the lithium anode. The concept is demonstrated using Li₄Ti₅O₁₂ as the “cathode” material due to its satisfying energy density and stable electrochemical performance. Such a cell configuration simultaneously combines the advantage of polarization, lithium plating/stripping and galvanostatic cycling tests while eschews their weakness. It provides a mechanism rigorously evaluating performance and lifetime of rechargeable batteries based on lithium metal anodes that are most akin to practical batteries. To our best knowledge, it is the first time that a model LMB full cell is demonstrated to present stable electrochemical performance as well as satisfactory lifetime under close-to-real conditions.

Figure 2.9a illustrates the fabrication process of the Li₄Ti₅O₁₂ electrode and the configuration of lithium coin cells used in the study, as also described in the experimental section. The loading of the active material, Li₄Ti₅O₁₂, in the cathode has been optimized to achieve near balance in the charge storage capacity of the two electrodes; which is not the case in previous works³⁴⁻³⁵. After compression, Li₄Ti₅O₁₂ electrodes show moderate mechanical integrity for coin cell assembly. **Figure 2.9b** presents the scanning electron microscope (SEM) pictures of Li₄Ti₅O₁₂ electrode

surfaces, which shows a macroscopically flat surface can be readily obtained. At small length scales, $\text{Li}_4\text{Ti}_5\text{O}_{12}$ takes the form of nanoparticles with diameters around 150 nm. The high surface area of the $\text{Li}_4\text{Ti}_5\text{O}_{12}$ nanoparticles is able to offer good ion-exchange ability³⁶. Energy-dispersive X-ray spectroscopy (EDS) elemental mapping shows a uniform distribution of Ti and C, meaning $\text{Li}_4\text{Ti}_5\text{O}_{12}$ nanoparticles are homogeneously covered by conductive carbon. **Figure 2.9c** reports the X-ray diffraction (XRD) profile of the $\text{Li}_4\text{Ti}_5\text{O}_{12}$ electrode. The characteristic diffraction peaks appear at the identical positions as the standard $\text{Li}_4\text{Ti}_5\text{O}_{12}$ material³⁷, which indicates that the crystal structure of $\text{Li}_4\text{Ti}_5\text{O}_{12}$ electrodes remains unchanged during physical compressing process. We have further assembled CR2032 coin cells using above-mentioned $\text{Li}_4\text{Ti}_5\text{O}_{12}$ electrodes against lithium foils as counter electrodes, with PVDF-HFP/ Al_2O_3 membranes soaked with 1M LiTFSI/PC as separators. The coin cells are expected to have high energy density due to the balanced capacity between two electrodes. For comparison, coin cells using the same electrodes but without separators are also assembled. Specifically, a Teflon O-ring is placed between electrodes and the electrolyte is stored in the cavity.

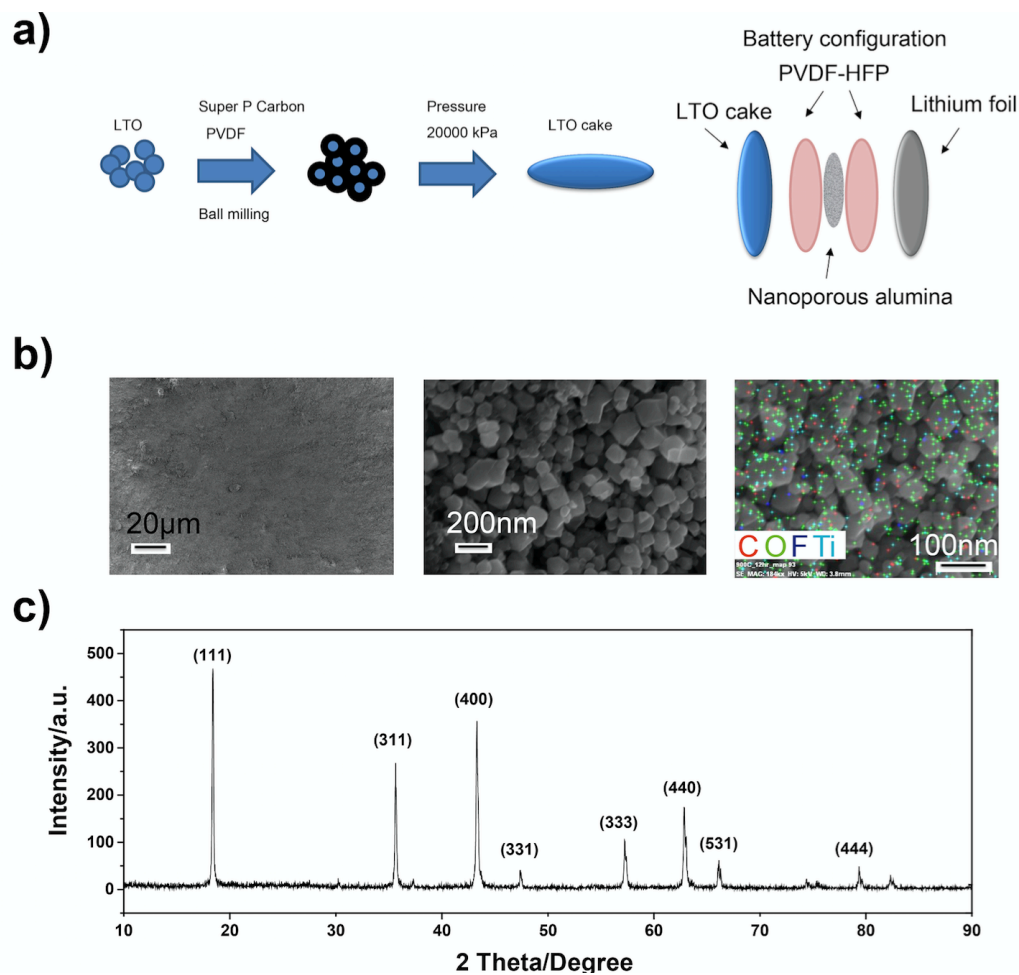


Figure 2.9. a) The preparation process of the $\text{Li}_4\text{Ti}_5\text{O}_{12}$ electrode and an illustration of cell assembly. b) SEM pictures of the $\text{Li}_4\text{Ti}_5\text{O}_{12}$ electrode surface at low magnification (left) and high magnification (middle); elemental mapping of the $\text{Li}_4\text{Ti}_5\text{O}_{12}$ electrode surface showing C, O, F, and Ti signals (right). c) XRD profile of the $\text{Li}_4\text{Ti}_5\text{O}_{12}$ electrode.

Galvanostatic cycling experiments from 1V to 3V have been conducted to evaluate the electrochemical performance and lifetime of coin cells under practical operation voltage. **Figure 2.10a** compares the time-dependent voltage profiles of coin cells with or without PVDF-HFP/Al₂O₃ separators cycled at 0.2 mA cm⁻². It is observed coin cell without PVDF-HFP/Al₂O₃ survives the first discharge cycle but cannot be re-charged. Such short lifetime could be attributed to the uneven deposition of lithium on the anode that in fact diminishes the available deposition area (**Figure 2.11** and **2.12**). Thus the dendrite proliferates rapidly at the tips due to the enhanced electric field. On the contrary, the presence of PVDF-HFP/Al₂O₃ separator allows stable battery operation for 1000 hours with only negligible capacity fading. Note that the capacity of Li₄Ti₅O₁₂ cathode is comparable to that of the lithium anode, each charging/discharging process takes nearly 75 hours. The voltage-capacity profile is reported in **Figure 2.10b**. Flat plateaus are observed during charging both initially and after 680 hours. Similar plateaus also present during discharging but with slightly lowering trend, which might result from limited diffusion in thick Li₄Ti₅O₁₂ electrode. At first cycle, both charge and discharge specific capacity are close to 140 mAh g⁻¹, which only slightly decrease after 750 hours. Thus it is proved the PVDF-HFP/Al₂O₃ separators are able to effectively stabilize the long-term operation of LMBs under practical condition where high voltage and massive ion transportation are involved.

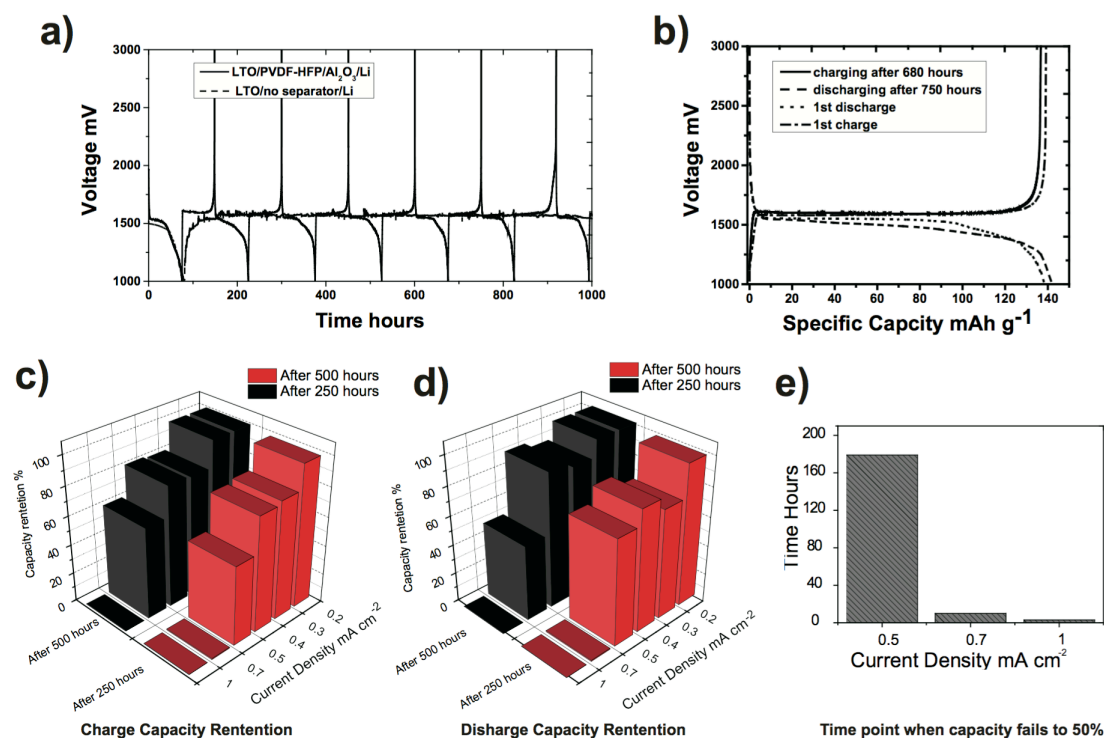


Figure 2.10. a) Voltage profiles Li/Li₄Ti₅O₁₂ coin cells with (black) and without (red) PVDF-HFP/Al₂O₃ laminated separator cycled at 0.2 mA cm⁻². b) Voltage/capacity profiles of Li/Li₄Ti₅O₁₂ coin cells with PVDF-HFP/Al₂O₃ separator as in a). c) Charge capacity retention of Li/Li₄Ti₅O₁₂ coin cells with PVDF-HFP/Al₂O₃ separator cycled at various current densities after 250 h (black) and 500 h (red). d) Discharge capacity retention of Li/Li₄Ti₅O₁₂ coin cells with PVDF-HFP/Al₂O₃ separator cycled at various current densities after 250 h (black) and 500 h (red). e) Time points after which the discharge capacity of Li/Li₄Ti₅O₁₂ coin cells with PVDF-HFP/Al₂O₃ separator drop to 50% of initial capacities when the current densities are 0.5, 0.7, and 1 mA cm⁻².

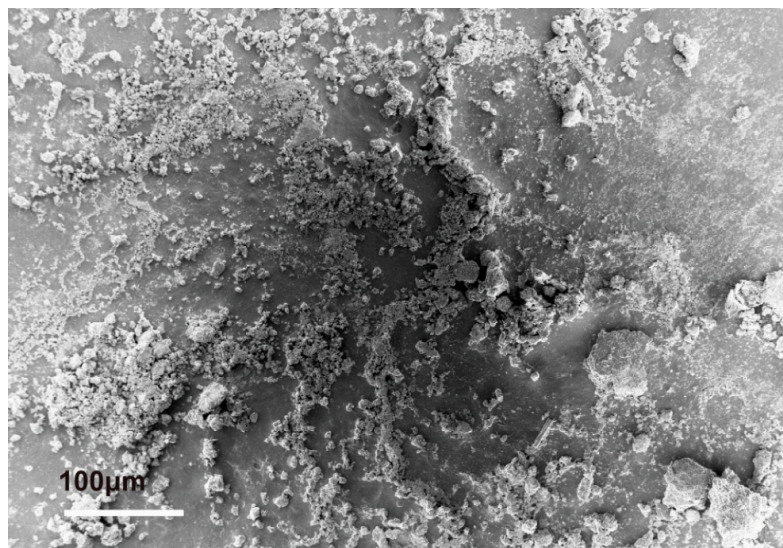


Figure 2.11. SEM picture of lithium metal surface harvested from coin cell without separator after 1st discharge and during consequent charging



Figure 2.12. SEM picture of pristine lithium metal surface

To further evaluate the battery performance at various current densities, similar galvanostatic cycling tests at 0.3, 0.4, 0.5, 0.7 and 1 mA cm⁻² have also been conducted. **Figure 2.10c** and **2.10d** respectively show the charge capacity and discharge capacity retention after 250 and 500 hours. As expected, batteries show gradually decreased capacity retention with increasing current density even though batteries are not short-circuit. The faded capacity is likely due to the limited ions diffusion in electrodes. For high current density at 0.7 and 1 mA cm⁻², the capacity fades to almost zero before 250 hours. **Figure 2.10e** compares the time points when discharge capacities of coin cells tested at 0.5, 0.7 and 1 mA cm⁻² decrease to half of the initial capacities. More efforts are being invested to improve the ion transportation efficiency in both electrolyte/separator interface and electrode.

Impedance spectra can provide insightful information about both bulk and interfacial resistance, which is helpful to understand ion transportation through the electrolyte and electrodes. **Figure 2.14a** reports the temperature-dependent impedance spectra of Li/Li₄Ti₅O₁₂ coin cells with PVDF-HFP/Al₂O₃ separator tested at 0.4 mA cm⁻² after 1000 hours cycling. The impedance decreases drastically with increasing temperature from -5 °C to 100 °C. At room temperature, the interfacial resistance reaches over 1500 ohms even though the bulk resistance remain low. The surprisingly high interfacial resistance does not emerge before or at the initial stage of the test (**Figure 2.13**). **Figure 2.14b** compares the room temperature impedance spectra of the Li/Li₄Ti₅O₁₂ coin cells before the test, after 100 hours test and after 1000 hours test, respectively. It is observed that bulk resistances of the coin cells remain low at all three stages, meaning little change of conductivity in electrolyte and electrodes.

However, the interfacial resistance at first decreases after 100 hours, and then increases largely at the end. One possible explanation is that at the initial stage of the battery operation, the electrolyte/electrode interface is gradually wetted by the electrolyte, which results in a decrease of interfacial resistance. The latter huge interfacial resistance could be attributed to the solid state interface (SEI) layer formation on the lithium surface, diffusion barrier in the electrode and even electrolyte decomposition³⁸⁻³⁹. It also explains the fading of the capacity and lowered efficiency after long battery operation at high current densities.

Post-mortem studies have been conducted on faded Li/Li₄Ti₅O₁₂ coin cells to further understand the battery performance and dendrite proliferation. Li anodes and separators are harvested after disassembling the coin cells and carefully transferred for SEM observation. The cross-section of the nanoporous Al₂O₃ separator is shown in **Figure 2.14c I**, indicating intact nanochannels and no dendrite penetration. **Figure 2.14c II** shows the lithium anode surface after battery cycling for 1000 hours. No mossy electrodeposits are observed even though the surface morphology is moderately changed after long-term continuous striping/plating at high voltage (**Figure 2.15**). EDS spectra and elemental mapping are also presented in **Figure 2.14c**. The dominant signals of oxygen, fluorine and carbon mainly come from the LiTFSI salt and the solvent.

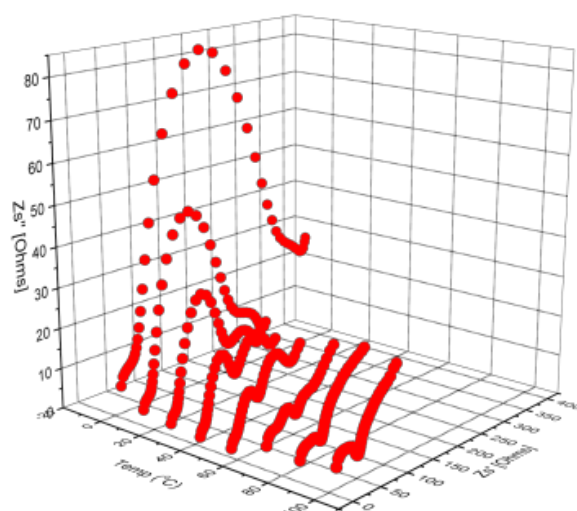
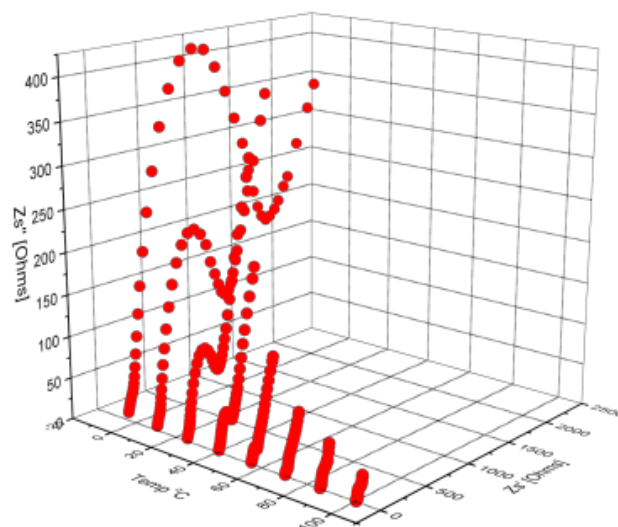


Figure 2.13. Temperature-dependent impedance spectra of pristine Li/Li₄Ti₅O₁₂ coin cells with PVDF-HFP/Al₂O₃ (left), and Li/Li₄Ti₅O₁₂ coin cells with PVDF-HFP/Al₂O₃ after 100 hours operation.

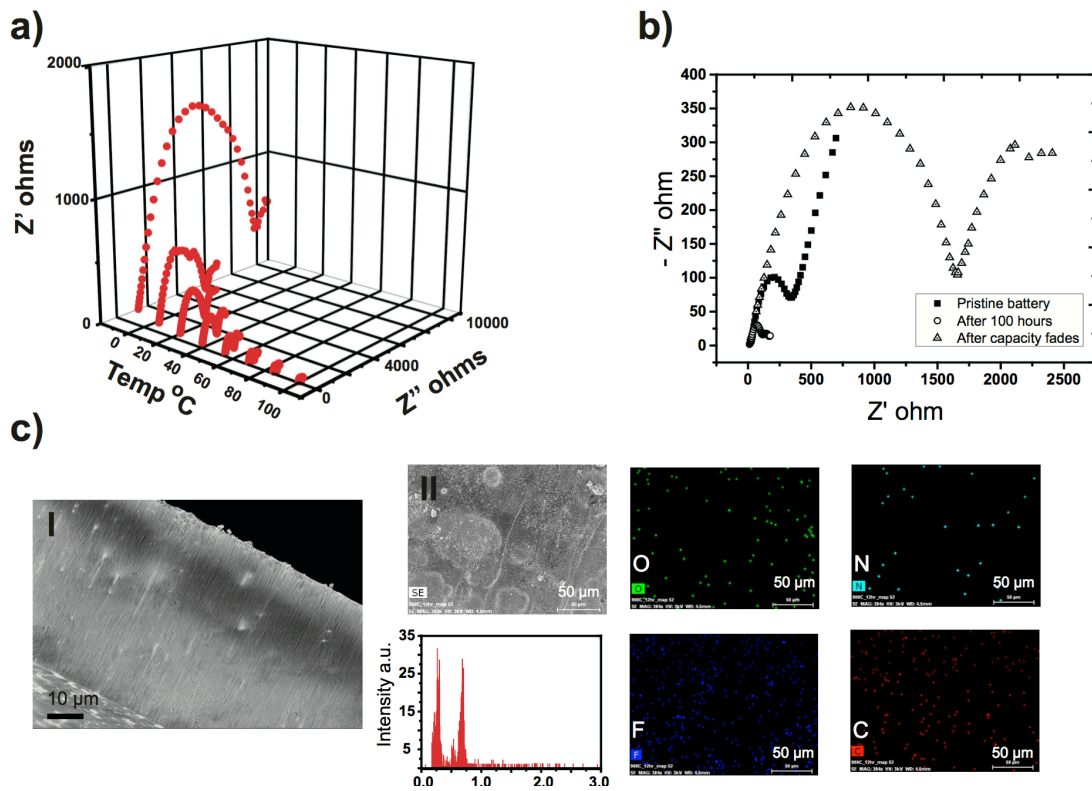


Figure 2.14. a) Temperature-dependent impedance spectra of Li/Li₄Ti₅O₁₂ coin cells with PVDF–HFP/Al₂O₃ after cycled for 1000 h. b) Room temperature impedance spectra of Li/Li₄Ti₅O₁₂ coin cells with PVDF–HFP/Al₂O₃ before test (black), after 100 h test (red), and after 1000 h test (blue). c) I) SEM picture of the cross-section of PVDF–HFP/Al₂O₃ separator harvested from coin cells cycled for 1000 h; II) SEM of the lithium anode surface harvested from coin cells cycled for 1000 h with EDS spectra and elemental mappings.

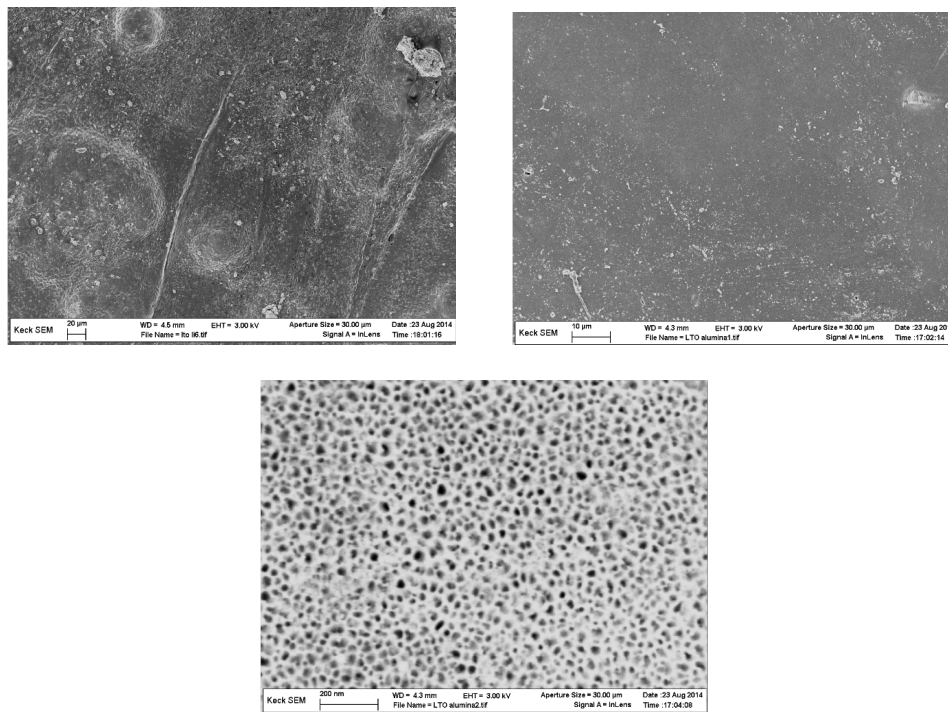


Figure 2.15. SEM pictures of lithium metal surface (left), separator surface (middle), and Al₂O₃ surface (right) after 1000 hours operation. All samples are harvested from coin cell by disassembling. Separator surface is covered by PVDF-HFP while at some sites Al₂O₃ is exposed by carefully removing PVDF-HFP.

In summary, we report a nanoporous electrolyte-separator comprised of laminated PVDF-HFP/Al₂O₃ composite membranes infused with a conventional low-volatility, liquid electrolyte. The materials are shown to be stable against metallic lithium and exhibit good toughness, high mechanical modulus, high ionic conductivity, and low interfacial impedances at room temperature. Using Li/LTO cells we show that the materials allow for exceptional, stable cycling performances for more than 1000 charge/discharge cycles. In symmetric lithium/lithium cells, the PVDF-HFP/Al₂O₃ membranes exhibit more than 1000 hours of stable operation at current densities ranging from 0.02 to 0.2 mA cm⁻². These last results are substantial improvements over symmetric cells based on PVDF-HFP without the Al₂O₃ inter-layer, but soaked in the same liquid electrolyte; these cells fail in as little as 60 hours when cycled at 0.2 mA cm⁻².

High-energy electrochemical cells in which a Li₄Ti₅O₁₂ cathode with a high mass loading of active material balances the high energy of the metallic lithium cathode are demonstrated for the first time. Long-term galvanostatic cycling of cells at moderate current density show ultra-stable battery operation and no signs of dendrite growth over extended cycling. Post-mortem SEM and EDS analysis of the electrodes confirm the stability of electrodeposition in the nanoporous electrodes. We further explore the impedance spectra of coin cells at different stages of cycling. The increased interfacial resistance after 1000 hours may result in the capacity fading at high current densities. These results point towards new approaches to construct next-generation high energy and safe LMBs.

Reference

1. Bruce, P. G.; Scrosati, B.; Tarascon, J. M., Nanomaterials for rechargeable lithium batteries. *Angew. Chem. Int. Ed.* **2008**, *47* (16), 2930-2946.
2. Dunn, B.; Kamath, H.; Tarascon, J.-M., Electrical energy storage for the grid: a battery of choices. *Science* **2011**, *334* (6058), 928-935.
3. Dresselhaus, M.; Thomas, I.; GRÄTZEL, M.; STEELE, B. C.; HEINZEL, A.; SCHLAPBACH, L.; ZÜTTEL, A.; TARASCON, J.; Armand, M., Materials for clean energy. *Nature* **2001**, *414*, 332-337.
4. Aricò, A. S.; Bruce, P.; Scrosati, B.; Tarascon, J.-M.; Van Schalkwijk, W., Nanostructured materials for advanced energy conversion and storage devices. *Nature materials* **2005**, *4* (5), 366-377.
5. Tarascon, J. M.; Armand, M., Issues and challenges facing rechargeable lithium batteries. *Nature* **2001**, *414* (6861), 359-367.
6. Bruce, P. G.; Freunberger, S. A.; Hardwick, L. J.; Tarascon, J.-M., Li-O₂ and Li-S batteries with high energy storage. *Nature materials* **2012**, *11* (1), 19.
7. Xu, S.; Das, S. K.; Archer, L. A., The Li-CO₂ battery: a novel method for CO₂ capture and utilization. *RSC Advances* **2013**, *3* (18), 6656-6660.
8. Armand, M.; Tarascon, J. M., Building better batteries. *Nature* **2008**, *451* (7179), 652-657.
9. Scrosati, B., Battery technology-challenge of portable power. *Nature* **1995**, *373* (6515), 557-558.

10. Umeda, G. A.; Menke, E.; Richard, M.; Stamm, K. L.; Wudl, F.; Dunn, B., Protection of lithium metal surfaces using tetraethoxysilane. *J. Mater. Chem.* **2011**, *21* (5), 1593-1599.
11. Shiraishi, S.; Kanamura, K.; Takehara, Z. i., Surface Condition Changes in Lithium Metal Deposited in Nonaqueous Electrolyte Containing HF by Dissolution-Deposition Cycles. *J. Electrochem. Soc.* **1999**, *146* (5), 1633-1639.
12. Gireaud, L.; Grugeon, S.; Laruelle, S.; Yrieix, B.; Tarascon, J. M., Lithium metal stripping/plating mechanisms studies: A metallurgical approach. *Electrochem. Commun.* **2006**, *8* (10), 1639-1649.
13. Stephan, A. M., Review on gel polymer electrolytes for lithium batteries. *Eur. Polym. J.* **2006**, *42* (1), 21-42.
14. Meyer, W. H., Polymer electrolytes for lithium-ion batteries. *Adv. Mater.* **1998**, *10* (6), 439-448.
15. Monroe, C.; Newman, J., The impact of elastic deformation on deposition kinetics at lithium/polymer interfaces. *J. Electrochem. Soc.* **2005**, *152* (2), A396-A404.
16. Nugent, J. L.; Moganty, S. S.; Archer, L. A., Nanoscale organic hybrid electrolytes. *Adv. Mater.* **2010**, *22* (33), 3677-3680.
17. Schaefer, J. L.; Lu, Y.; Moganty, S. S.; Agarwal, P.; Jayaprakash, N.; Archer, L. A., Electrolytes for high-energy lithium batteries. *Applied Nanoscience* **2012**, *2* (2), 91-109.
18. Lu, Y.; Das, S. K.; Moganty, S. S.; Archer, L. A., Ionic Liquid-Nanoparticle Hybrid Electrolytes and their Application in Secondary Lithium-Metal Batteries. *Adv. Mater.* **2012**, *24* (32), 4430-4435.

19. Brissot, C.; Rosso, M.; Chazalviel, J. N.; Lascaud, S., Dendritic growth mechanisms in lithium/polymer cells. *J. Power Sources* **1999**, *81*, 925-929.
20. Ding, F.; Xu, W.; Graff, G. L.; Zhang, J.; Sushko, M. L.; Chen, X. L.; Shao, Y. Y.; Engelhard, M. H.; Nie, Z. M.; Xiao, J.; Liu, X. J.; Sushko, P. V.; Liu, J.; Zhang, J. G., Dendrite-Free Lithium Deposition via Self-Healing Electrostatic Shield Mechanism. *J. Am. Chem. Soc.* **2013**, *135* (11), 4450-4456.
21. Diggle, J. W.; Downie, T. C.; Goulding, C., Anodic oxide films on aluminum. *Chem. Rev.* **1969**, *69* (3), 365-405.
22. O'sullivan, J.; Wood, G. In *The morphology and mechanism of formation of porous anodic films on aluminium*, Proceedings of the Royal Society of London A: Mathematical, Physical and Engineering Sciences, The Royal Society: 1970; pp 511-543.
23. Oliver, W. C.; Pharr, G. M., An improved technique for determining hardness and elastic modulus using load and displacement sensing indentation experiments. *J. Mater. Res.* **1992**, *7* (6), 1564-1583.
24. Xia, Z.; Riestler, L.; Sheldon, B.; Curtin, W.; Liang, J.; Yin, A.; Xu, J., Mechanical properties of highly ordered nanoporous anodic alumina membranes. *Rev. Adv. Mater. Sci* **2004**, *6* (2), 131-139.
25. Abbrent, S.; Plestil, J.; Hlavata, D.; Lindgren, J.; Tegenfeldt, J.; Wendsjö, Å., Crystallinity and morphology of PVdF-HFP-based gel electrolytes. *Polymer* **2001**, *42* (4), 1407-1416.
26. Jonscher, A. K., The universal dielectric response. *Nature* **1977**, *267*, 673-679.

27. Armstrong, G.; Armstrong, A. R.; Bruce, P. G.; Reale, P.; Scrosati, B., TiO₂ (B) Nanowires as an Improved Anode Material for Lithium-Ion Batteries Containing LiFePO₄ or LiNi_{0.5}Mn_{1.5}O₄ Cathodes and a Polymer Electrolyte. *Adv. Mater.* **2006**, *18* (19), 2597-2600.
28. Arora, P.; White, R. E.; Doyle, M., Capacity fade mechanisms and side reactions in lithium-ion batteries. *J. Electrochem. Soc.* **1998**, *145* (10), 3647-3667.
29. Rosso, M.; Gobron, T.; Brissot, C.; Chazalviel, J.-N.; Lascaud, S., Onset of dendritic growth in lithium/polymer cells. *J. Power Sources* **2001**, *97*, 804-806.
30. Stone, G.; Mullin, S.; Teran, A.; Hallinan, D.; Minor, A.; Hexemer, A.; Balsara, N., Resolution of the modulus versus adhesion dilemma in solid polymer electrolytes for rechargeable lithium metal batteries. *J. Electrochem. Soc.* **2012**, *159* (3), A222-A227.
31. Hallinan, D. T.; Mullin, S. A.; Stone, G. M.; Balsara, N. P., Lithium metal stability in batteries with block copolymer electrolytes. *J. Electrochem. Soc.* **2013**, *160* (3), A464-A470.
32. Yi, T.-F.; Jiang, L.-J.; Shu, J.; Yue, C.-B.; Zhu, R.-S.; Qiao, H.-B., Recent development and application of Li₄Ti₅O₁₂ as anode material of lithium ion battery. *J. Phys. Chem. Solids* **2010**, *71* (9), 1236-1242.
33. Yuan, L.-X.; Wang, Z.-H.; Zhang, W.-X.; Hu, X.-L.; Chen, J.-T.; Huang, Y.-H.; Goodenough, J. B., Development and challenges of LiFePO₄ cathode material for lithium-ion batteries. *Energy Environ. Sci.* **2011**, *4* (2), 269-284.

34. Tu, Z.; Kambe, Y.; Lu, Y.; Archer, L. A., Nanoporous Polymer-Ceramic Composite Electrolytes for Lithium Metal Batteries. *Advanced Energy Materials* **2014**, *4* (2).
35. Lu, Y.; Tu, Z.; Archer, L. A., Stable lithium electrodeposition in liquid and nanoporous solid electrolytes. *Nature materials* **2014**.
36. Tang, Y.; Yang, L.; Fang, S.; Qiu, Z., Li₄Ti₅O₁₂ hollow microspheres assembled by nanosheets as an anode material for high-rate lithium ion batteries. *Electrochim. Acta* **2009**, *54* (26), 6244-6249.
37. Prakash, A.; Manikandan, P.; Ramesha, K.; Sathiya, M.; Tarascon, J.; Shukla, A., Solution-combustion synthesized nanocrystalline Li₄Ti₅O₁₂ as high-rate performance Li-ion battery anode. *Chem. Mater.* **2010**, *22* (9), 2857-2863.
38. Liu, J.; Song, K.; van Aken, P. A.; Maier, J.; Yu, Y., Self-supported Li₄Ti₅O₁₂-C nanotube arrays as high-rate and long-life anode materials for flexible Li-ion batteries. *Nano Lett.* **2014**, *14* (5), 2597-2603.
39. Thevenin, J.; Muller, R., Impedance of lithium electrodes in a propylene carbonate electrolyte. *J. Electrochem. Soc.* **1987**, *134* (2), 273-280.

CHAPTER 3

EFFECT OF NANOPOROUS STRUCTURE ON THE STABILITY OF LITHIUM ELECTRODEPOSITION

Reproduced from *Advanced Energy Materials* 7. 8 (2017)

3.1 Abstract

Successful strategies for stabilizing electrodeposition of reactive metals, including lithium, sodium, and aluminum are a requirement for safe, high-energy electrochemical storage technologies that utilize these metals as anodes. Unstable deposition produces high-surface area dendritic structures at the anode/electrolyte interface, which causes premature cell failure by complex physical and chemical processes that have presented formidable barriers to progress. Here we report that hybrid electrolytes created by infusing conventional liquid electrolytes into nanoporous membranes provide exceptional ability to stabilize Li. Electrochemical cells based on γ -Al₂O₃ ceramics with pore diameters below a cut-off value above 200 nm exhibit long-term stability even at a current density of 3mA cm⁻². The effect is not limited to ceramics; similar large enhancements in stability are observed for polypropylene membranes with less monodisperse pores below 450nm. We critically assess these findings using theories for ion rectification and electrodeposition reactions in porous solids and show that the source of stable electrodeposition in nanoporous electrolytes is fundamental.

3.2 Introduction

Research aimed at overcoming science and technology barriers associated with performance and safety limitations of high-energy rechargeable batteries has emerged as a requirement for large-scale electrification of transportation¹⁻⁴. It is now known, for example, that replacing the carbon-based anode in today's lithium-ion batteries with metallic lithium would lead to a ten-fold increase in the amount of charge stored

(from 360 mAh g⁻¹ to 3860 mAh g⁻¹) per unit mass of the battery anode. Such lithium metal batteries (LMB) are also promising for a variety of other reasons. The most important is that they enable the use of high-energy unlithiated materials, such as sulfur, oxygen, and carbon dioxide⁵⁻⁶ as the active species in the cathode. This raises the prospect of multiple battery platforms that offer large improvements in specific energy (SE) on either a mass or volumetric basis considering the electrode materials only (e.g. SE_{Li-S} = 2.5 kWh kg⁻¹ or 2.8 kWh L⁻¹; SE_{Li-O₂} = 12 kWh kg⁻¹; SE_{Li-O₂/CO₂} = 10.5 kWh kg⁻¹), relative to today's state-of-the-art Li-ion technology (SE_{Li-ion} = 0.5 kWh kg⁻¹).

Unregulated, rough/dendritic lithium electrodeposition during charging is now understood to be the main hurdle to practical LMBs that can be operated stably and safely over the thousands of charge-discharge cycles required for applications in transportation⁷⁻⁸. Several recent studies, including a few excellent reviews⁹⁻¹², summarize the physico-chemical factors that produce unstable Li deposition and discuss possible strategies to prevent Li dendrite formation and stabilize LMBs during cell recharge. Previously, we reported that a family of nanoporous γ -Al₂O₃/polymer laminate membranes able to imbibe large amounts of liquid electrolyte in their pores break the conventional modulus-ionic conductivity tradeoff that had previously prohibited solutions based on solid electrolytes. The membranes were also reported to exhibit impressive ability to retard Li dendrite proliferation in Li/Li symmetric as well as Li/Li₄Ti₅O₁₂ half cells¹³⁻¹⁴.

A recent theoretical study of Li electrodeposition in elastic media suggests that aside from their high mechanical modulus and high ionic conductivity, there are at least two fundamental reasons why nanoporous ceramic membranes may stabilize the anode in a LMB. First, the channels constrain dendrite nucleate sizes below critical dimensions where surface tension alone can completely stabilize electrodeposition at the Li-metal/electrolyte interface¹⁵. Second, nanochannels with charged walls can effectively regulate fluid flow or rectify ion transport in the electrolyte, reducing the driving force for electroconvection and dendrite formation¹⁶. The latter effect is well known in biological and microsystems studies where it is thought to play important roles in the selectivity of ion channels.^[10] The analysis reported by Jorne¹⁷ is to our knowledge among the first to consider the influence of pore geometry on ion migration in charged nanopores. This analysis shows that when pore sizes in a membrane with charged walls approach nanometer length-scales, electro-osmotic flow becomes pronounced and significantly retards diffusion of ions with the same sign as the charge on the membrane wall, rectifying the ionic current when an electric field is present¹⁸⁻²⁰. Empirical studies of aqueous copper solutions in nanoporous Al₂O₃ show that while ions interact strongly with the nano-channel surface, surface conduction dominates over electro-osmotic flow under over-limiting current¹⁶.

Herein, we report on the transport properties, ion rectification attributes, and lithium-anode stabilization mechanisms of nanoporous γ -Al₂O₃ membranes (**Figure 3.1a**) infused with liquid electrolytes. Our focus is on model Al₂O₃ membranes with regular, straight pores with mean pore diameters in the range 20 nm to 300 nm. This focus is

motivated by a recent theoretical analysis of the stability of electrodeposition in elastic solids^{9,21}. Under typical electrolyte and cell operating conditions used in a LMB, this analysis predicts a transition from stable to unstable deposition when the size λ of deposit nucleates exceed a critical value $\lambda_{cr} \approx 200$ nm. By systematically varying the pore size of Al₂O₃ membranes in the selected range we are able to evaluate this prediction in some detail and at the same time provide broader insights about ion transport in electrolytes confined in nanopores with charged walls.

3.3 Experimental Section

Nanoporous Al₂O₃ membranes with pore sizes 20 nm, 50 nm, 100 nm, 150 nm, 200 nm, 300 nm and a thickness of 60 μ m were prepared by anodization¹³. Polypropylene separators with various pore sizes were purchased from Sterlitech Inc. Electrolytes were prepared by dissolving bis(trifluoromethane)sulfonimide lithium salt (LiTFSI) in dioxolane: dimethoxyethane (DOL:DME, v/v = 1:1) and stored in the argon-filled glovebox (MBraun, Labmaster) in the presence of molecular sieve and lithium metal for removing trace amounts of moisture. CR2032 coin cells were also fabricated in the glovebox with the cell configuration described in **Figure 3.1c**, using glass fiber as separator with/without Al₂O₃. The Al₂O₃ is placed as its top side with accurate pore sizes in direct contact with the lithium. symmetric coin cells, two lithium foils (Alfa Aesar) were used as working and counter electrodes. For Coulombic efficiency tests, a stainless steel disk was used as the counter-electrode, and 1% LiNO₃ was added in 1M LiTFSI DOL:DOE to stabilize the lithium surface on the stainless steel. For full cells, lithium foil was paired with either lithium iron phosphate (LiFePO₄) or lithium nickel

cobalt aluminum oxide ($\text{LiNi}_{0.8}\text{Co}_{0.15}\text{Al}_{0.05}\text{O}_2$) with 1 M LiPF_6 in EC:DEC as the electrolyte. Electrodes were prepared through a typical slurry coating method. Briefly, active materials were mixed with Super P carbon and PVDF binder with NMP as the disperser at a ratio of 8:1:1. After being thoroughly ball milled, the homogeneous slurry was coated on aluminum foil using a doctor blade, and then dried in vacuum oven at 60°C , followed by heating at 100°C overnight. Cathodes were stored in the glovebox before cell assembly.

Post-mortem analysis of the morphology of Al_2O_3 membranes were performed on a Leo 1550 Keck Field Emission Scanning Electron Microscopy (FESEM) and FEI Strata 400 Focused Ion Beam (FIB) fitted with a Quorum PP3010T Cryo-FIB/SEM Preparation System. Upon opening the coin cell, the sample was immediately plunged into slush nitrogen and subsequently maintained -165°C in the cryo-FIB. This minimized both reactions with air during transfer into the cryo-FIB, and lithium redeposition while milling, respectively. The sample remained under liquid nitrogen or in vacuum for the duration of the experiment. Temperature-dependent conductivity measurements were carried out using a Novocontrol dielectric/impedance spectrometer in the frequency range from 10^7 Hz to 10^{-1} Hz and a temperature range of -25°C to 45°C . Lithium transference numbers were measured by combined impedance and polarization experiments using a Solartron battery workstation. Briefly, the first impedance spectra were measured followed by a small constant voltage charging until the steady state. Then the steady state impedance was measured immediately afterward, and the Bruce-Vincent procedure used to calculate the Li^+ transference number.

Self-diffusivity of the solvent and ions was studied by pulsed-field gradient (PFG) NMR on a Bruker AVANCEIII 400 MHz spectrometer with a 5 mm z-gradient probe. All the diffusion experiments were performed at room temperature. The radio frequency pulse width was calibrated for each sample to obtain maximal signal intensity. The ^1H , ^7Li , and ^{19}F self-diffusion coefficients were measured using a PFG stimulated echo sequence. The gradient was varied in 16 steps from 2% to 95% of the maximum gradient strength, 1000 G cm^{-1} . The diffusion time was set to 20 ms and the duration of each gradient pulse is 1 ms. Liquid and semi-solid samples were filled into NMR tube at the same height to avoid the influence of convection. Galvanostatic cycling was performed on Neware CT-3008 battery testers at room temperature. Li - LFP cells were galvanostatically cycled between 3.8 and 2.5V, and Li - NCA cells were firstly charged to 4.1 or 4.3 V at constant current. Cells were then held at a predetermined voltage for 120 mins and discharged to 3 V galvanostatically.

3.4 Results and discussion

Al_2O_3 membranes prepared by anodizing highly pure aluminum are known to spontaneously form individual, straight nanochannels throughout the bulk membrane²²⁻²³. The straight, non-tortuous pore paths make these materials good model systems for studying the effect of pore confinement on Li metal electrodeposition and ion transport. The diameter and interpore distance of Al_2O_3 membranes can also be finely tuned at the nanoscale through the choice of electrolyte and anodizing voltage

used to prepare the materials. In this study, Al_2O_3 membranes with pore sizes ranging from 20 nm to 300 nm were used (see SEM images shown in **Figure 3.1b**). For electrochemical studies, membranes were assembled in the tri-layer configuration depicted in **Figure 3.1c**, wherein a conventional glass fiber membrane is sandwiched between two identical layers of Al_2O_3 . This arrangement allows membranes to be created with good mechanical toughness that are able to withstand coin cell assembly and disassembly. Upon closing the cell with pressure, the soft lithium can be deformed and tightly contact the membrane. While we previously reported that polymer laminating layers applied to the membrane surface may also be utilized for this purpose¹³, advantages of the current arrangement include its simplicity and the fact that the nanoporous membrane makes direct, conformal contact with the Li metal electrode. The latter feature facilitates better control of the size of any dendrite nucleate formed at the interface. The glass fiber matrix is also readily wetted by liquid electrolytes employed in the study.

Figure 3.2a reports temperature-dependent ionic conductivity measured in symmetric (Li/Li) CR2032 type coin cells at temperatures in the range $-25\text{ }^\circ\text{C}$ to $45\text{ }^\circ\text{C}$. Nanoporous Al_2O_3 with various pore sizes were used in the study, and in every case the pores were filled with the liquid electrolyte 1 M LiTFSI DOL:DME (1:1). The temperature range used for the study was selected to ensure that no phase changes occur in the electrolyte solvent during the measurements. It is apparent from the figure that the Al_2O_3 membranes exhibit DC ionic conductivity above $1 \times 10^{-3}\text{ S cm}^{-1}$ at all

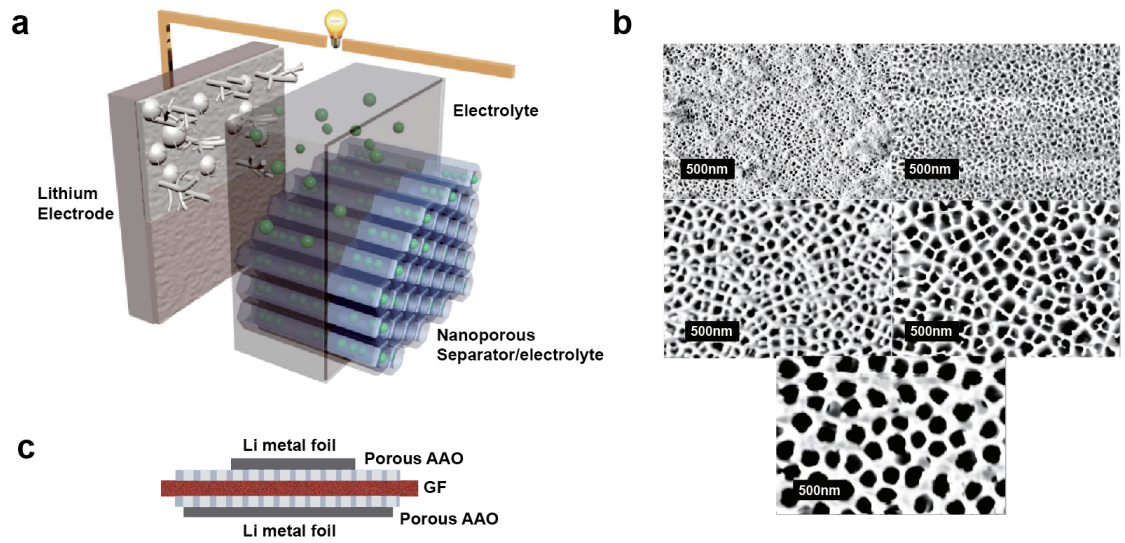


Figure 3.1. a) Illustration of nanoporous Al₂O₃ and its application as the hybrid electrolyte for stable lithium metal battery. b) FE-SEM images of Al₂O₃ membranes with various pore sizes, from 20 nm to 200 nm. The scale bars represent 500 nm. c) Scheme of coin cell configuration, in which two Al₂O₃ membranes sandwich a glass fiber matrix, placed between two lithium metal foils.

temperatures, close to that of the membrane-free bulk liquid electrolyte. A slight decrease of conductivity is nonetheless observed for the Al_2O_3 membranes with the smallest pore sizes. The solid lines in **Figure 3.2a** represent Vogel-Fulcher-Tammann fits of the measured temperature-dependent conductivity data; the activation energy deduced from the fits are reported in **Figure 3.3**. Comparison of the results for the membranes and membrane-free electrolyte systems clearly show that there is a reduction in activation energy when Al_2O_3 is present. This observation is conventionally attributed to electro-osmotic flow-facilitated ion transport in the charged pores, which is known to be pronounced when liquids are confined in narrow pores¹⁸. An alternative possibility is that less thermally driven electrostatic interactions between ions and the channel walls facilitate conduction. This means ions can hop along cylinder channels to augment conventional diffusive transport in the liquid medium contained in the channels¹⁶.

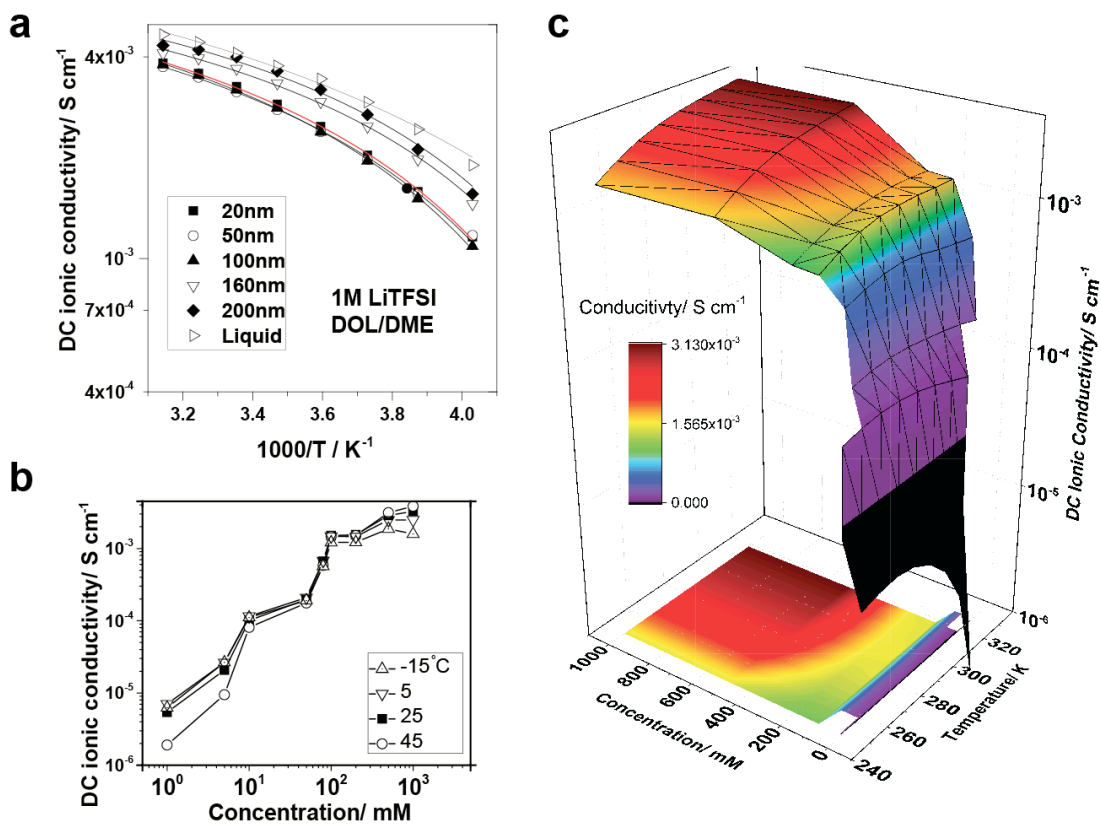


Figure 3.2. a) Temperature-dependent DC ionic conductivity of Al_2O_3 /1 M LiTFSI DOL:DME with different pore sizes. b) Concentration-dependent DC ionic conductivity of 20 nm pore-size Al_2O_3 / LiTFSI DOL:DME at various temperatures. c) Heat map representing the dependence of both temperature and concentration on the DC ionic conductivity for 20 nm pore-size Al_2O_3 /LiTFSI DOL:DME systems.

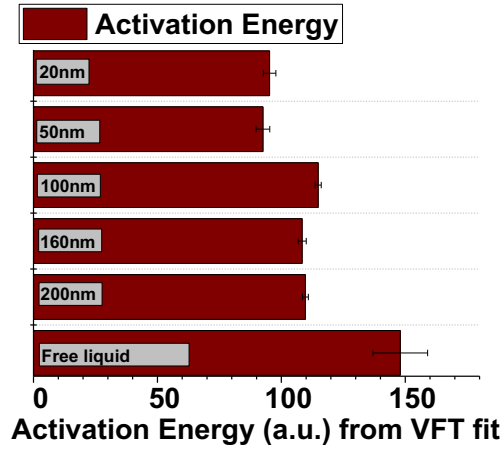


Figure 3.3. Activation energy (a.u.) derived from the VFT fitting of the temperature – dependent ionic conductivity of 1M LiTFSI DOL:DME in different Al₂O₃ separators and as liquid.

Figure 3.2b reports the effect of salt concentration (c) on the DC ionic conductivity of 20 nm pore-size Al_2O_3 membranes infused with electrolytes containing LiTFSI salt with a range (1 mM to 1 M) of concentration. As expected, conductivity increases as the salt concentration rises. At low salt concentrations, the relationship between salt concentration and DC conductivity is modestly stronger than linear, whereas at high salt concentration ($c > 100\text{mM}$) it is sublinear. The initial rise can be attributed to the increase in concentration of dissociable ions in solution, while the sub-linear regime reflects competition between increased number of ions and decreased ion mobility as a result of stronger viscous friction when the salt concentration is high²⁴. Further increase of the concentration lowers conductivity as the slow-down in ion motion due to higher electrolyte viscosity begins to dominate the contribution from increased number of charge carriers. A more comprehensive illustration of the concentration and temperature dependent conductivity is depicted as a heat map in **Figure 3.2c**. A typical Arrhenius-like strong temperature dependence of conductivity is observed at high salt concentrations, whereas at lower salt concentrations ($c < 100 \text{ mM}$) the conductivity becomes nearly temperature independent — an unusual result for a liquid electrolyte. We suspect that at these salt concentrations, ions migrate through the membranes by different, interface-dominated processes than in a bulk liquid electrolyte. Specifically, we hypothesize that at low salt concentration, dissociated salt in the electrolyte is localized in the Debye layer near the membrane pore walls; the Li-ions move in response to an external field by some combination of electromigration and site-to-site hopping along the charged pore walls.

Typically, liquid electrolytes, in which a lithium salt is mixed with an aprotic liquid solvent, are characterized by small cationic transference numbers, $t_{Li^+} < 0.5$. Higher t_{Li^+} can be obtained in polymeric, ceramic, or nanoparticle-based electrolytes, in which the anions are immobilized to a stationary or slow-moving support²⁵⁻²⁷. **Figure 3.5a** reports the lithium transference number for LiTFSI in DOL:DME at salt concentrations from 1 mM to 1000 mM in electrolytes with/without the nanoporous Al₂O₃ membranes. All measurements were performed using a previously reported electrochemical method²⁸, which utilizes the formula, $t_{Li^+} = \frac{I_{ss}(\Delta V - I_o R_o)}{I_o(\Delta V - I_{ss} R_{ss})}$, to estimate t_{Li^+} from impedance measurements and steady-state polarization data. I_{ss} and I_o represent the steady state and initial current, respectively, V is the applied constant voltage, R_o is the initial charge transfer resistance, and R_{ss} is the steady state charge transfer resistance. For the membrane-free liquid electrolyte, a slight increase of t_{Li^+} is observed at low salt concentration, in agreement with previous theoretical and experimental studies²⁹⁻³⁰. In contrast, at low salt concentration, a large increase of t_{Li^+} is observed for the membrane-based electrolytes relative to the free liquid, reflected by a sharper increase of t_{Li^+} at lower c than observed for the Al₂O₃ membrane-free liquid. A t_{Li^+} value as high as 0.9 is measured at a LiTFSI concentration of 50 mM in 20 nm pore-size Al₂O₃. The high t_{Li^+} can also be straightforwardly observed from the ratio between steady state current and initial current (**Figure 3.4**), meaning that the effect is not an artifact of the analysis used to deduce t_{Li^+} from the experimental data. In contrast, at high salt concentration ($c > 100$ mM), the membranes appear to have little, if any, effect on t_{Li^+} .

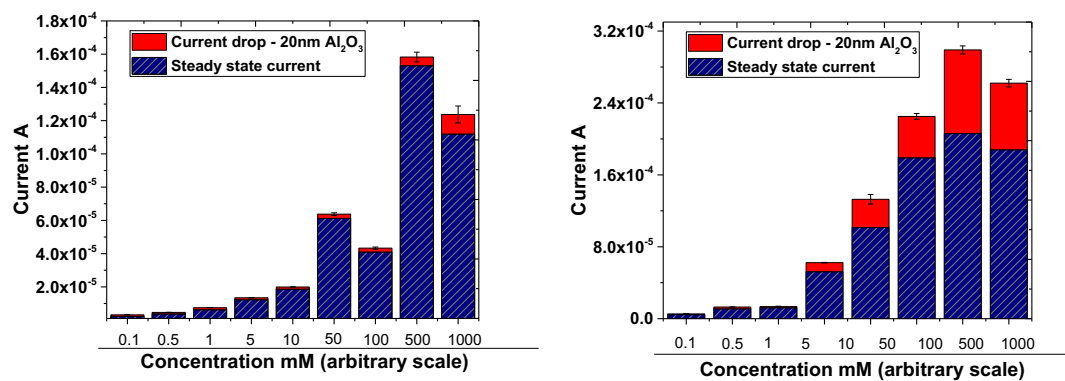


Figure 3.4. Current drop from the beginning of the polarization experiment to stable voltage region, indicated by the red bar. The blue bar represents the current at the steady state.

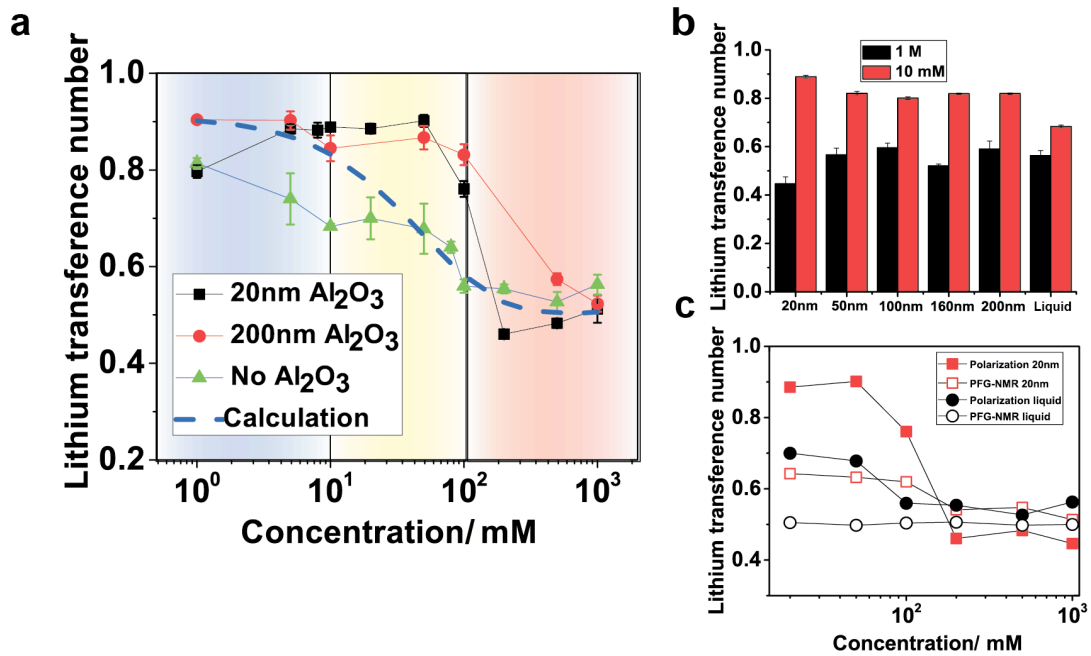


Figure 3.5. a) Lithium transference number measured by the electrochemical method for coin cells with 20 nm pore-size Al₂O₃, 200 nm pore-size Al₂O₃, and no Al₂O₃ cases, at LiTFSI/DOL:DME concentrations from 1 mM to 1 M. b) Lithium transference number measured for coin cells with 20, 50, 100, 160, 200 nm pore-size Al₂O₃ and glass fiber separator at concentration of 10 mM and 1 M LiTFSI/DOL:DME. c) Comparison of the lithium transference number determined from the electrochemical method and diffusional method for free liquid and 20 nm pore-size Al₂O₃.

Our findings for the smallest pore diameters are consistent with expectations from the analysis of Jorne¹⁷; namely, at lower salt content the Debye screening length is large ($\lambda_D \approx 2-3$ nm) and the length scale associated with electro-osmotic flow in the membrane pores ($4-5 \lambda_D$) is of the same order of magnitude as the pore dimension. In this limit, this theory predicts that a liquid electrolyte constrained in a porous medium with even modest surface charge can function as an ion rectifier (ie. impeding transport of ions with the same charge as the pore surface), yielding high t_{Li+} , which is consistent with what we observe. The results reported in **Figure 3.5b** show, however, that at the same salt concentration, the ion-rectifying effect is largely insensitive to the membrane pore size; it is just as strong for membranes with 20 nm pores as in those with 200 nm pores. This result challenges the simple physical explanation provided by Jorne's analysis (as the dashed line in **Figure 3.5a** which deviates from experimental data at intermediate c range). One may instead argue that the ion rectifying effect observed here may originate from the same surface migration/hopping process hypothesized earlier to be the source of the temperature-independent ionic conductivity observed in electrolytes with $c < 100$ mM.

Lithium transference number t_{Li+} calculation can be performed based on the previous work proposed by Jorne¹⁷, with modification to fit this system. The equation as follows is used to estimate the lithium transference number:

$$t_{Li+} = \frac{F^2 z_i u_i c_i + \frac{q^2 \left(\frac{r_0}{\lambda}\right)}{\mu \left(\frac{r_0}{\lambda}\right)} \left[1 - \frac{I_0 \left(\frac{r_0}{\lambda}\right) I_2 \left(\frac{r_0}{\lambda}\right)}{I_1^2 \left(\frac{r_0}{\lambda}\right)} \right]}{\kappa_{avg} + \frac{q^2 \left(\frac{r_0}{\lambda}\right)}{\mu \left(\frac{r_0}{\lambda}\right)} \left[1 - \frac{I_0 \left(\frac{r_0}{\lambda}\right) I_2 \left(\frac{r_0}{\lambda}\right)}{I_1^2 \left(\frac{r_0}{\lambda}\right)} \right]}$$

in which, F is Faraday constant, z is the charge of the specie, u is the ion mobility, c is the disassociated ion concentration, κ is the overall ionic conductivity, q is the surface charge density, μ is the viscosity of the electrolyte, I_0 , I_1 , and I_2 are modified Bessel function of zero, 1st, and 2nd order, respectively. r_0 is the radius of the channel, λ is the Debye length which is given as the following equation, and plotted as **Figure 3.6**:

$$\lambda = \left(\frac{\varepsilon k T}{e^2 N_A 2 C} \right)^{1/2}$$

in which, ε is the permittivity of the electrolyte, k is the Boltzmann constant, C is the concentration of the electrolyte.

The change of the viscosity from 1 mM to 1 M is small, which is assumed to be linear. The conductivity and mobility are extrapolated from experimental value with polynomial fitting. Surface charge density is obtained from the previous work, and fractioned based on the square root of dielectric constant ratio of the solvent used in this study and the one in the literature³¹. Values are normalized with the experimental data for the high concentrations. The raw data directly from the equation are plotted as **Figure 3.7** with different surface charge values when the concentration is 1 mM.

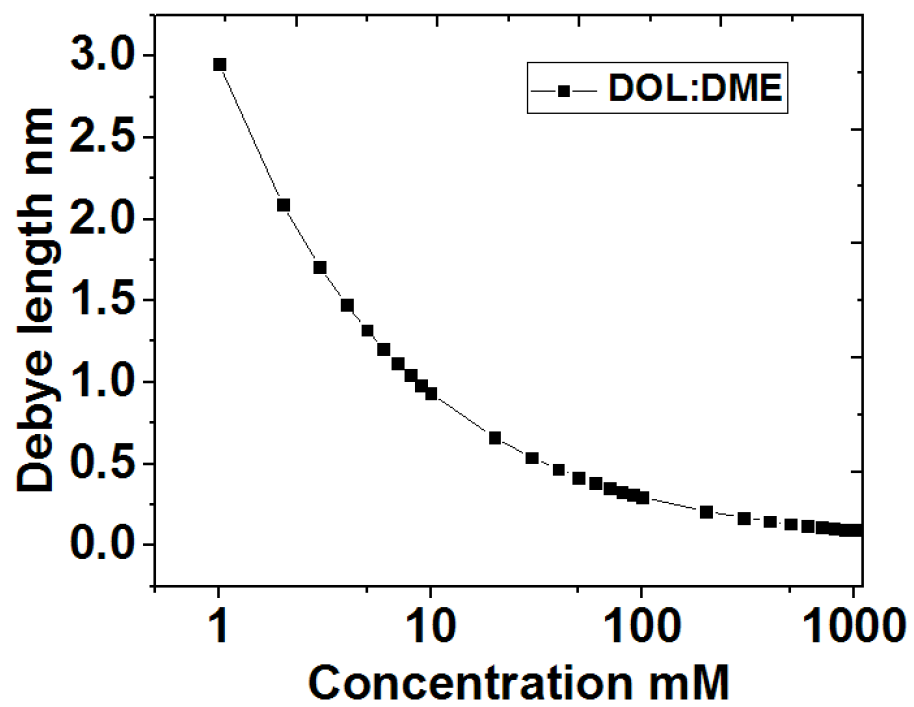


Figure 3.6. Debye length vs. concentration for DOL:DME electrolyte

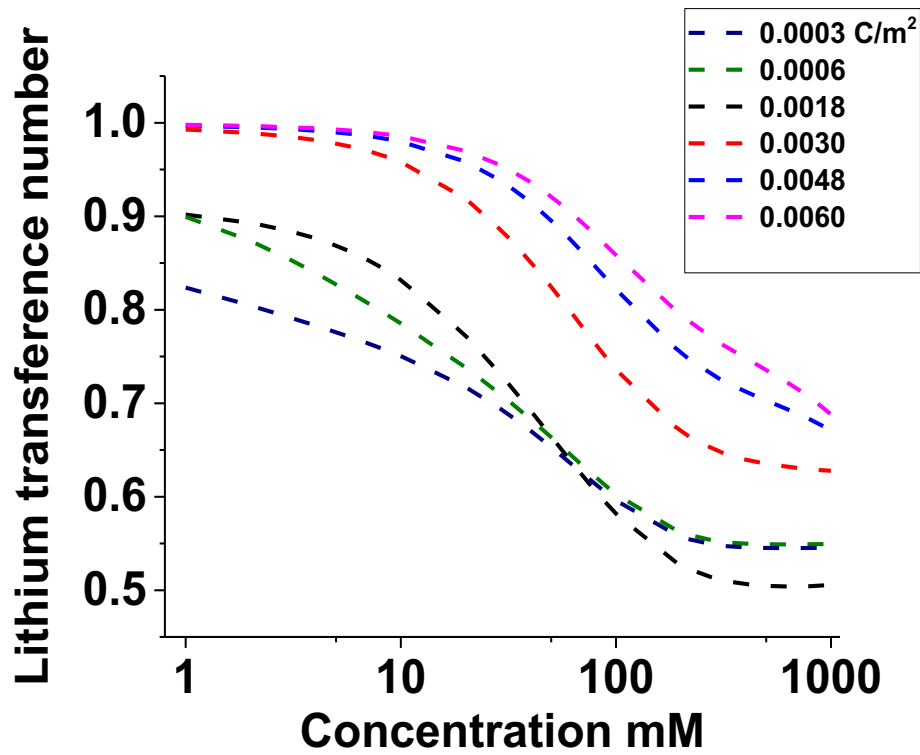


Figure 3.7. Lithium transference number derived from theory against lithium salt concentration. Data represent different surface charge densities when the salt concentration is 1 mM.

Pulsed field gradient – nuclear magnetic resonance (PFG-NMR) was used as a secondary tool for characterizing the diffusivity D_+ of Li^+ and fluorine-containing (presumed to be the diffusivity D_- of TFSI anions) species in the same LiTFSI/DOL:DME electrolyte. From these measurements, t_{Li^+} can be simply obtained by the equation, $t_{\text{Li}^+} = \frac{D_+}{D_+ + D_-}$. **Figure 3.5c** compares t_{Li^+} values measured using the two methods for membrane-free liquid electrolytes and electrolyte with the presence of nanoporous Al_2O_3 , with LiTFSI concentration in the range $20 \text{ mM} \leq c \leq 1 \text{ M}$. The figure shows that the t_{Li^+} values of free liquid deduced from PFG are a nearly constant ~ 0.5 , irrespective of c . This means that the self-diffusivity of the cation and anion remains more or less the same as both increase with decreasing c . The overall diffusivity of the solvent also increases by a factor of around 2 (from $1.3 \times 10^{-9} \text{ m}^2 \text{ s}^{-1}$ to $2.5 \times 10^{-9} \text{ m}^2 \text{ s}^{-1}$) when the salt concentration decreases from 1 M to 20 mM, as shown in **Figure 3.8**. This behavior can be explained in terms of the reduction in electrolyte viscosity as c is lowered. The t_{Li^+} for the electrolyte in nanoporous Al_2O_3 measured using the same method shows a modest increase of t_{Li^+} upon reduction of the salt concentration, but the change is clearly not as pronounced as that seen in t_{Li^+} measured electrochemically. Similar discrepancies between t_{Li^+} values deduced from electrochemical and diffusion measurements have been reported in many literature studies, particularly when the conductivity of the electrolyte is low³². In most electrolytes this is likely due to the dominance of undissociated ion pairs, ion clusters or electrostatically coupled ions, which would compromise the ability of PFG-NMR to

differentiate between mobile Li^+ and TFSI anions, as assumed in calculating t_{Li^+} from the measured diffusivity.

To better understand these processes, impedance spectroscopy was used to quantify the temperature-dependent bulk and interface resistance in symmetric cells with 1 M and 10 mM LiTFSI DOL:DME infused in a 20 nm pore-size Al_2O_3 membrane. The resultant Nyquist plots are reported in **Figure 3.11a** and **Figure 3.9**. The bulk and interface resistances obtained by fitting the plots using the equivalent circuit model illustrated as **Figure 3.10** are provided in **Table 3.1**. The small resistance value measured at room temperature (13.55 ohm for 1 M) indicates that ion transport occurs virtually uninhibited in the nanoporous Al_2O_3 membrane. As expected, the Nyquist semicircles shrink exponentially with increasing temperature at both concentrations. A detailed look at interfacial resistance (**Figure 3.11d**) shows its monotonic increase with temperature at all concentrations. Fitting the interfacial resistance data to the Arrhenius model suggests the conduction of ions through the interface is a thermally activated process, with almost invariant activation energy. **Figure 3.11b** and **3.11c** compare the impedance spectra of Al_2O_3 with 20 nm, 50 nm, and 100 nm pore sizes with those measured in the membrane-free liquid electrolyte, at LiTFSI concentrations of 10 mM and 1 M, respectively, in DOL:DME.

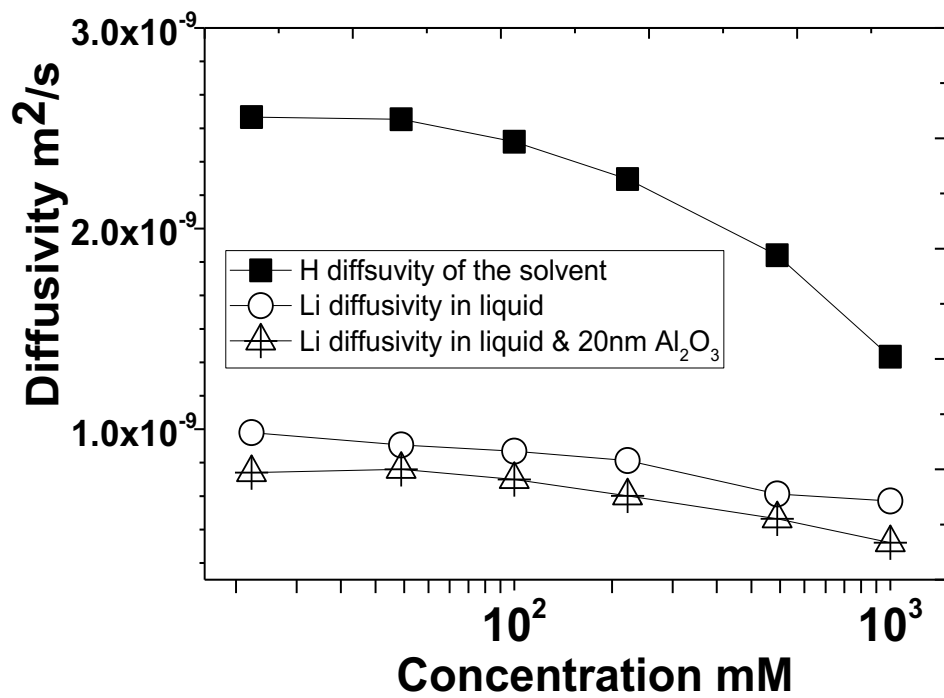


Figure 3.8. Diffusivity of the solvent and lithium species from LiTFSI/DOL:DME systems with concentrations from 20 mM to 1000 mM measured using PFG-NMR.

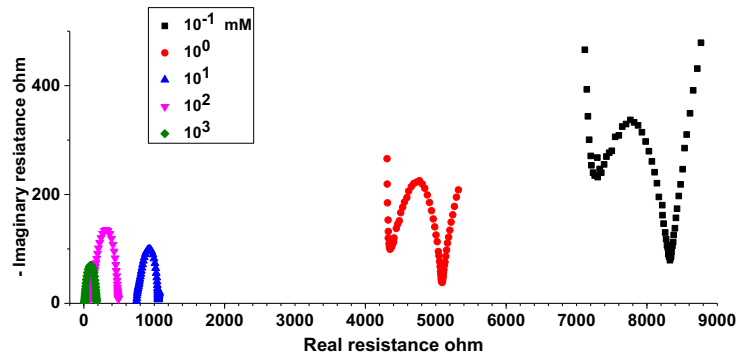


Figure 3.9. Typical impedance spectra of coin cells having 20 nm pore-size Al_2O_3 imbided with different concentrations of LiTFSI DOL:DME. Data are measured at room temperature.

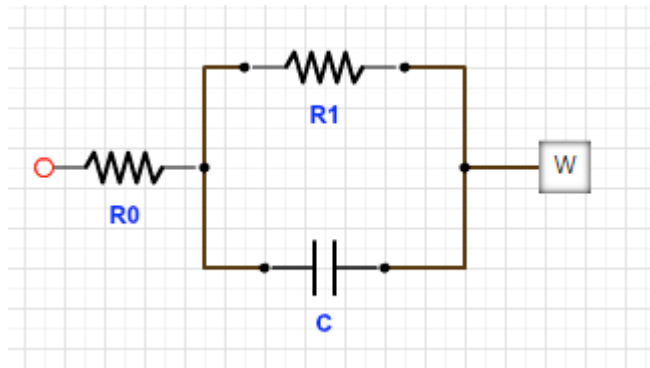


Figure 3.10. Equivalent circuit model for fitting impedance spectra. R_0 is attributed to the bulk resistor and R_1 is the interfacial resistor. Capacitor C is replaced by a constant phase element. W represents a Warburg element.

Table 3.1. Bulk and Interfacial resistance fitted from the equivalent circuit model shown in **Figure 3.11a** for 1 M and 10 mM LiTFSI DOL:DME in 20 nm pore-size Al₂O₃.

T/K	Ω/ohm Bulk 1M	T/K	Ω/ohm Bulk 10 mM	T/K	Ω/ohm Interfacial 1M	T/K	Ω/ohm Interfacial 10mM
258.15	57.14	258.15	177	258.15	1363	258.15	19070
268.15	34.42	268.15	169.4	268.15	517.8	268.15	5876
278.15	23.66	278.15	169.4	278.15	235.4	278.15	1915
288.15	17.55	288.15	176	288.15	118.8	288.15	702.9
298.15	13.55	298.15	187.1	298.15	64.96	298.15	292.1
308.15	10.61	308.15	209.7	308.15	38.52	308.15	144.6
318.15	8.636	318.15	232.3	318.15	21.81	318.15	84.58

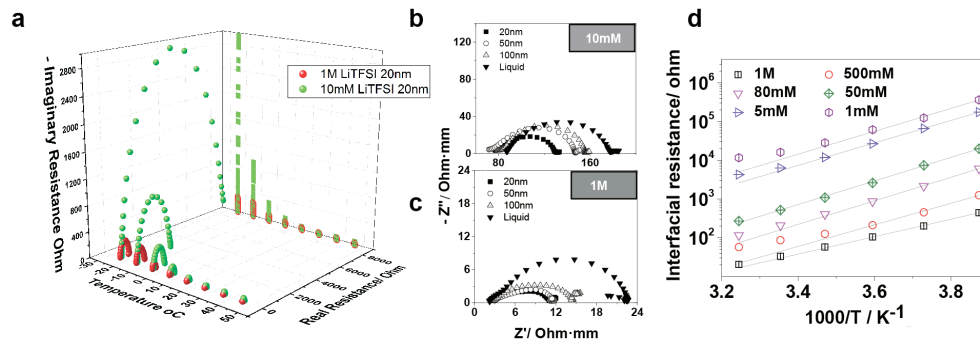


Figure 3.11. a) Temperature-dependent impedance spectra of 20 nm pore-size $\text{Al}_2\text{O}_3/\text{LiTFSI DOL:DME}$ at 1M (red) and 10 mM (green). b) Comparison of room-temperature impedance spectra for different $\text{Al}_2\text{O}_3/\text{LiTFSI DOL:DME}$ at 10 mM and c) 1 M. d) Interfacial resistance of coin cells with 20 nm pore-size $\text{Al}_2\text{O}_3/\text{LiTFSI DOL:DME}$ at various temperatures and concentrations

Comparison of the results for the Al_2O_3 membrane-based and membrane-free cells shows that in all cases, only a single arc is observed. This normally indicates that no secondary interphases are formed when the nanoporous Al_2O_3 membranes are introduced to the cells. A negligible difference in bulk resistance is observed for all pore sizes, indicating liquid-like ion transport in the electrolyte. In contrast, the interfacial resistance shows an obvious pore size dependence, which increases as the pore size approaches micrometer length scales. The interfacial resistance is also lower in cells that utilize Al_2O_3 membranes, compared with those that use the free liquid electrolyte. We attribute this behavior to the effect of the nanostructured Al_2O_3 protecting the Li-metal surface from the liquid electrolyte, and hence from the resistive SEI formed in regions of the metal surface that are in direct contact with the liquid electrolyte¹⁵. A similar large decrease in interfacial impedance at Li-metal electrodes was observed when halide salt additives were precipitated on the surface of Li-metal electrodes³³.

A suitable separator for LMBs must also be able to suppress Li dendrite proliferation and stabilize deposition. As discussed in the introduction, there are at least two mechanisms (ion rectification and mechanically constraining the nucleate size) by which nanoporous Al_2O_3 membranes infiltrated with a liquid electrolyte might suppress dendrite growth in a LMB. The results in the previous section show that preventing direct contact between the liquid electrolyte and the Li-metal surface in regions where the solid Al_2O_3 framework contacts the Li-metal may also provide a mechanism for preserving fast interfacial ion transport, which would stabilize Li

deposition as well. The salt concentration in the electrolyte provides a straightforward methodology to isolate and understand the roles played by the first two mechanisms.

We performed galvanostatic lithium cycling experiments in which a predetermined amount of lithium metal is sequentially stripped from one electrode and plated on another in a two-electrode symmetric Li/Li cell by passing a fixed current for a predetermined time. The stability of the deposition can be deduced from the voltage profile. At a low LiTFSI concentration (10 mM), where t_{Li^+} is high, the voltage profiles reported in **Figure 3.12** show that Li/Li cells based on Al_2O_3 membranes with 20 nm pore size cycle stably at low (0.071 mA cm^{-2}) to moderate (0.1 mA cm^{-2}) current density, with no sign of short circuiting for more than 1000-hours of battery operation. Unfortunately, the poor conductivity of the electrolytes causes the voltage to diverge in these membranes, which limits their utility for practical LMBs, where stable operation at current densities of at least 1 mA cm^{-2} is desired.

Figures 3.13a, b and c report voltage profiles for electrolytes based on 20 nm pore-size Al_2O_3 membranes infiltrated with 1M LiTFSI DOL:DME. These electrolytes have higher conductivity, but t_{Li^+} is comparable to the liquid electrolyte. It is seen from the figure that Li/Li cells with this electrolyte design can be cycled at current densities one order of magnitude or larger ($1 - 3 \text{ mA cm}^{-2}$). The peak-to-peak voltages are stable for more than 1500 hours of operation, the most impressive long-term cycling performance reported so far for a LMB. Slight increase of the overpotential is observed at the highest current density, which largely comes from the thickened SEI layse after extensive cycling, but the overall voltage profile remains stable. **Figure 3.14** compares the voltage profiles obtained for symmetric lithium cells with a range of

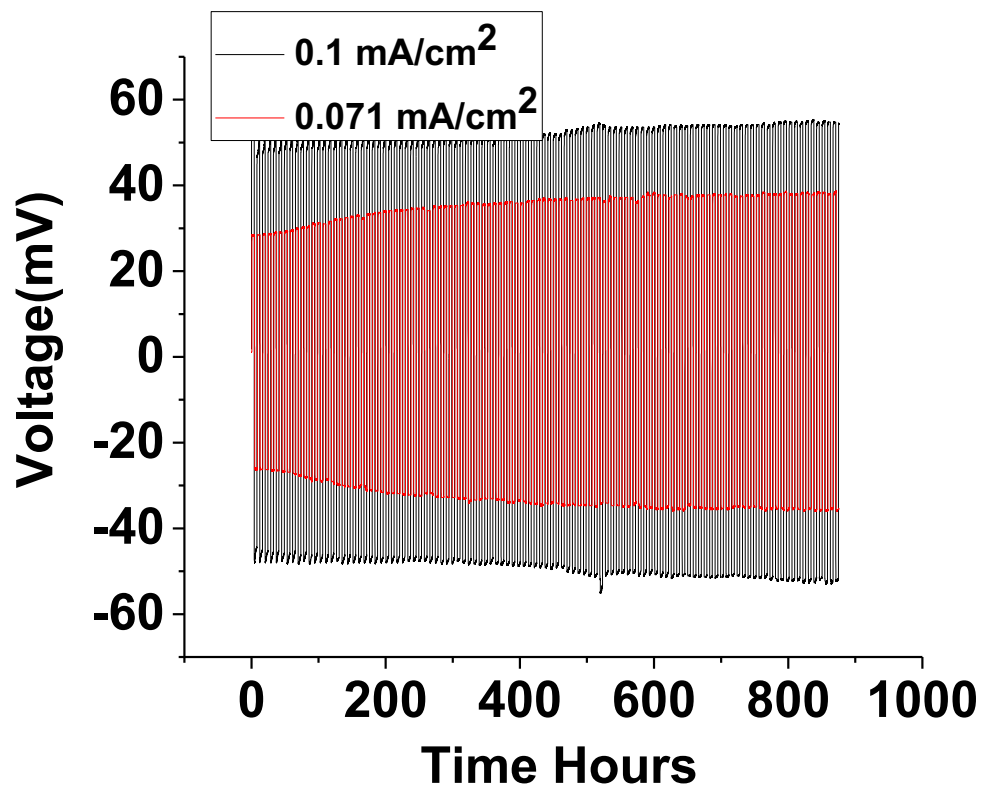


Figure 3.12. Lithium plating stripping experiments on coin cells with 20 nm pore-size Al_2O_3 imbibed with 10 mM LiTFSI DOL:DME

Al_2O_3 pore diameters that were each cycled at 3 mA cm^{-2} over a period of 250 hours. More unstable voltage profiles are clearly seen when the pore diameter increases, with large fluctuations apparent in electrolytes based on Al_2O_3 membranes with 300nm diameter pores. This observation is confirmed by the voltage profiles observed from long-term cycling of the same cells (see **figure 3.15**), where it is seen that cells based on larger membrane pore diameters exhibit the least ability to sustain stable cell operation. It is seen however, that even after 1500 operating hours (ie. 5400 C cm^{-2} charge passed, which is to our knowledge the longest operating lifetime of a LMB reported in a liquid electrolyte), in no case are the dendrites able to completely short-circuit the cells. In contrast, if the Al_2O_3 membrane is replaced with a glass fiber membrane (average pore diameter $\approx 2 \mu\text{m}$) a clear short-circuit event is observed in less than 160 hours of operation, even at a much lower current density of 1 mA cm^{-2} (**Figure 3.13a** red lines), underscoring the importance of the membrane architecture in stabilizing the cells. Our findings are in qualitative agreement with the conclusions presented in reference 34 that under normal cell running conditions, there exists a critical membrane pore diameter above which deposition of Li is unstable to dendrite formation. Our findings also show that of the materials studied, the 20 nm pore-size Al_2O_3 is most effective in protecting the Li metal surface, and as such is preferred. As significant, however, is the fact that our results clearly show that even without ion rectification the membranes are exceptionally effective in stabilizing operation of a LMB.

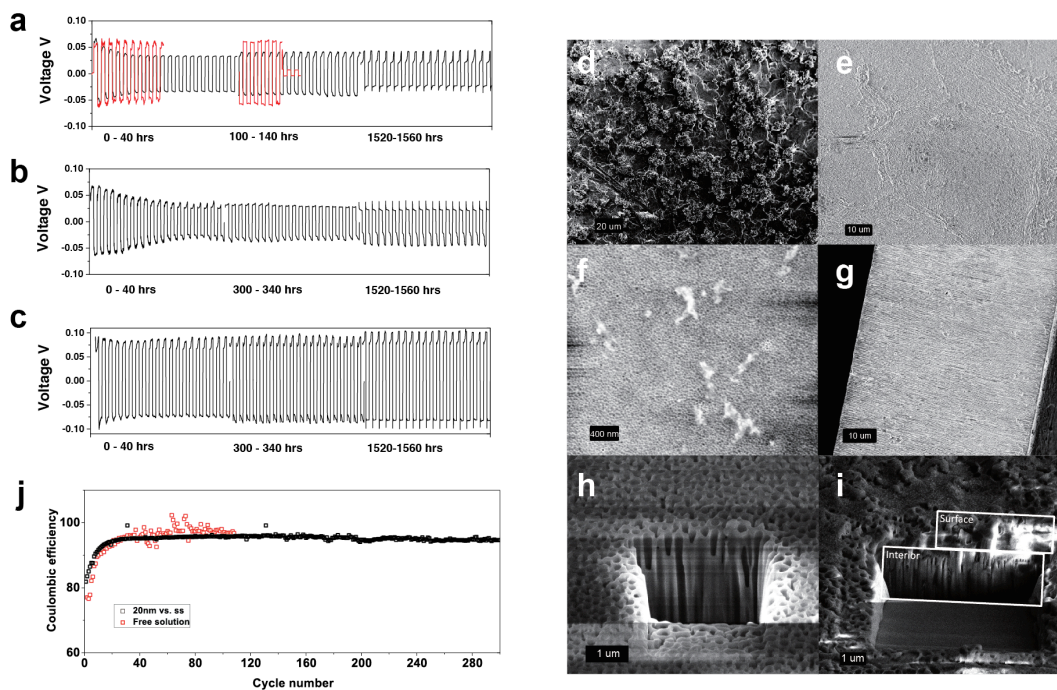


Figure 3.13. a) Lithium plating/stripping experiment for symmetric coin cells with 20 nm pore-size Al_2O_3 / 1M LiTFSI DOL:DME at the current density of 1 mA cm^{-2} for 1 hour per charge/discharge; the red line represents the same experiment for coin cells without Al_2O_3 . b) Above mentioned experiment for 20 nm pore-size Al_2O_3 / 1M LiTFSI DOL:DME at the current density of 1.5 mA cm^{-2} for 1 hour per charge/discharge, and c) 3 mA cm^{-2} for 1 hour per charge/discharge. d) SEM image of lithium surface after 100 hours plating/stripping at 1 mA cm^{-2} , e) of lithium surface stabilized by Al_2O_3 after the same experiment, f) of 20 nm pore-size Al_2O_3 surface facing the electrode, and g) of Al_2O_3 cross-section after the same experiment. h) Surface and cross-section, milled by cryo-FIB, of the electrolyte side of the 200 nm pore-size Al_2O_3 after 100 hours plating/stripping. i) Surface and cross-section, milled by cryo-FIB, of the 200 nm pore-size lithium electrode side of the Al_2O_3 . j) Coulombic efficiency of 1M LiTFSI/DOL:DME with and without 20 nm pore-size Al_2O_3 at the current density of 0.5 mA cm^{-2} .

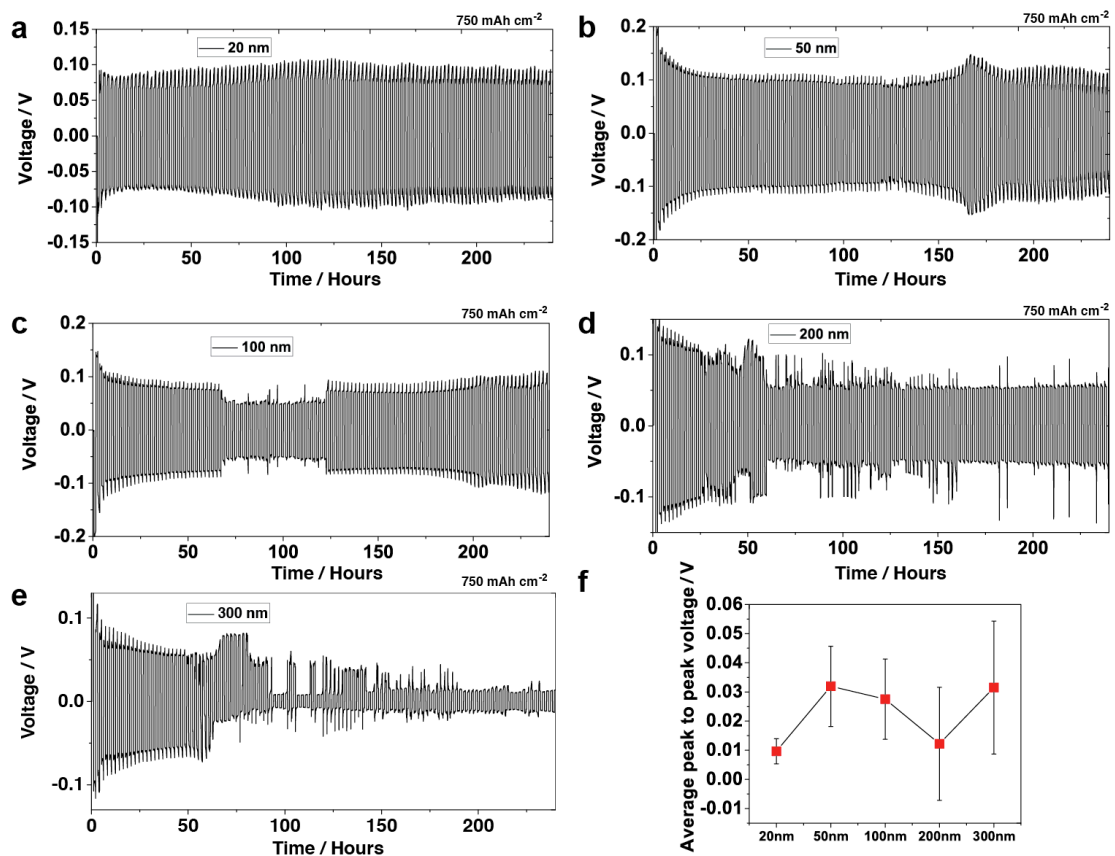


Figure 3.14. Voltage profile from galvanostatic cycling of symmetric Li/Al₂O₃/Li cells at 3 mA/cm² with varying Al₂O₃ membrane pore diameter: a) 20 nm, b) 50 nm, c) 100 nm, d) 200 nm, and e) 300 nm. f) Average peak-to-peak voltages determined from profiles from a) to e).

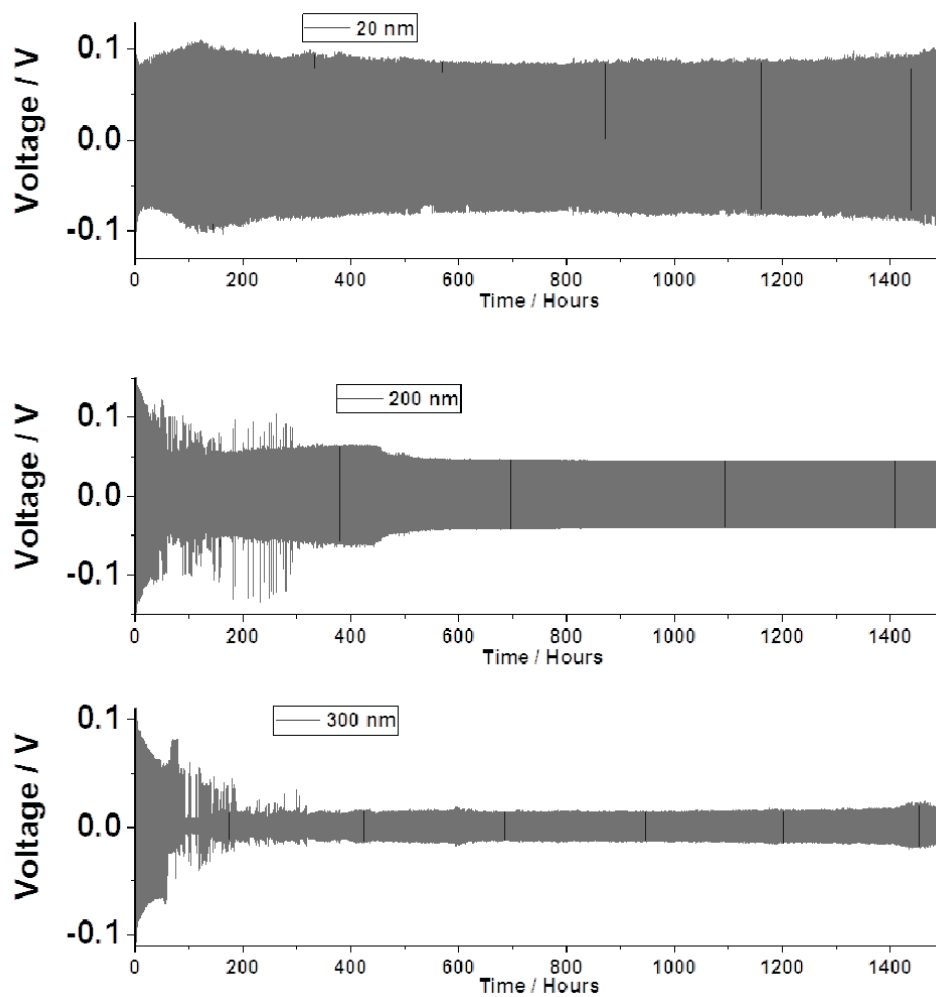


Figure 3.15. Voltage profiles from long-term galvanostatic cycling of symmetric Li/Al₂O₃/Li cells at 3 mA/cm² with varying Al₂O₃ membrane pore diameter: a) 20 nm, b) 200 nm, and c) 300 nm.

In order to evaluate the generality of our findings, we investigated the effect of membrane pore size on the stability of Li electrodeposition in the context of other membrane materials and electrolyte chemistries. Results reported in **Figure 3.16** show that effect of pore diameter of commercially available polypropylene (PP) membranes on electrodeposition. For these studies membranes with pore diameters in the range 100 nm to 10 μm and nearly constant porosity were infused with a liquid electrolyte comprised of 1 M LiPF_6 in EC:DEC and evaluated in Li/Li symmetric cells at a fixed current density of 2 mA/cm^2 . It is apparent from **Figures 3.16** and **3.17**, that more than a 10-fold increase in cell operational lifetime (from < 50 hours at 10 μm to over 500 hours at 100 nm), but that the transition towards increased instability with increased pore diameter is not as abrupt as for the nanoporous Al_2O_3 membranes. We attribute this difference to the greater polydispersity in pore diameters of the PP membranes.

A closer inspection of the voltage profiles in **Figures 3.13a, b** and **c** show that the peak-to-peak voltage remains relatively constant during long-term cycling. This implies that the electrolyte is able to form a compact, stable SEI that resists the volume strain at the electrolyte/electrode interface during cycling. Such voltage profiles differ from what was observed in our previous work for Al_2O_3 membrane electrolytes infused with carbonate liquid electrolytes, for which the peak-to-peak voltage gradually increases as a result of build-up of interfacial impedance³⁴. Post-mortem studies (**Figure 3.13d - i**) confirm the smoothness of the lithium surface after plating/stripping, as opposed to the rough lithium surface observed in the membrane-free systems. The Al_2O_3 membrane itself remains intact even after cell disassembly,

and SEM images of the cross-section show no evidence of dendrite penetration or breaking. Cryo-focused ion beam milling was employed to explore the internal structure of the Al_2O_3 . A cross-section of the nanoporous Al_2O_3 was exposed by milling to a depth of 5-10 μm from the surface, revealing a nanotube-like structure with no dendrites visually evident in the pores.

Figure 3.13j shows that in addition to improving LMB life time, the nanoporous Al_2O_3 membranes also improve the reversibility of the lithium deposition process. The Coulombic efficiency provides an indicator of this reversibility and was measured using a coin cell where a lithium metal anode was cycled against a stainless steel current collector used as the cathode. A fixed amount of charge was passed each cycle, depositing a predetermined amount of lithium on the stainless steel. The process was subsequently reversed to determine the recoverable charge. **Figure 3.13j** and **figure 3.18** report the Coulombic efficiency (CE) of coin cells with/without the nanoporous Al_2O_3 membranes. It is obvious from these results that the nanoporous Al_2O_3 helps to improve the efficiency up to 95% for nearly 300 cycles, whereas the free liquid in glass fiber yields an unstable Coulombic efficiency over 40 cycles, likely due to the irregular porous structure and protonated group on the glass fiber. We attribute the high Coulombic efficiency to the effectiveness of the membranes in limiting dendrite formation, which constrains parasitic reaction between the lithium metal and liquid electrolyte, reducing the loss of lithium³⁵.

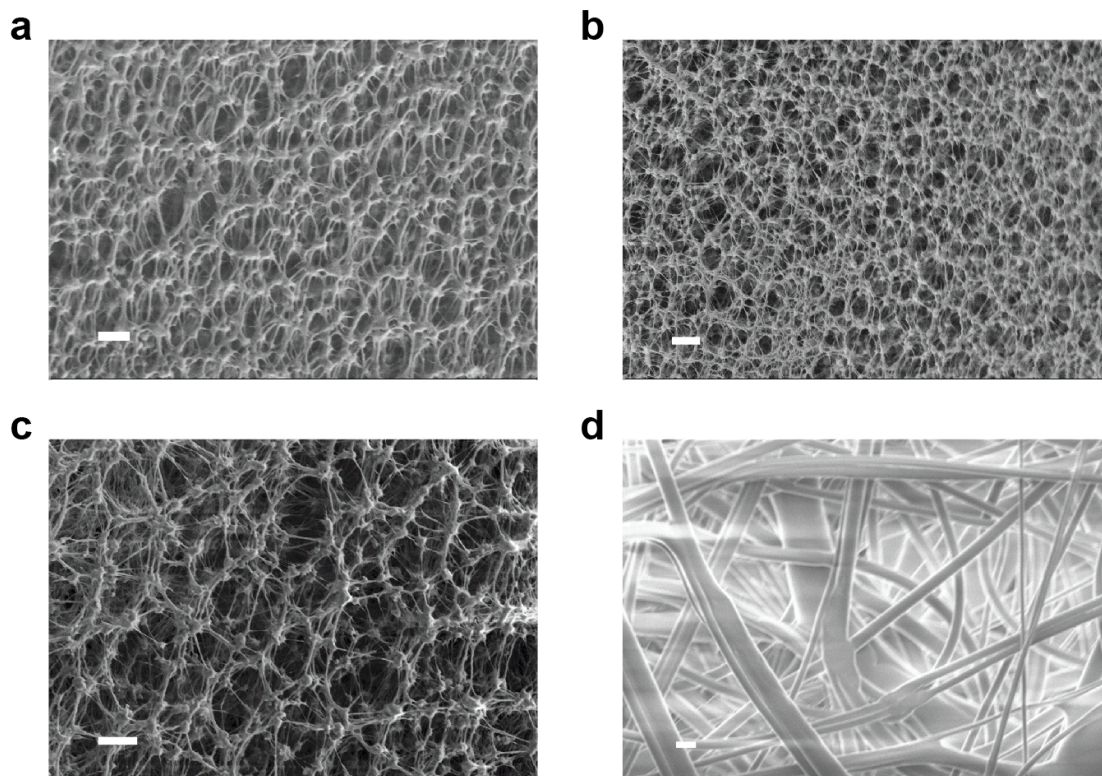


Figure 3.16. SEM images of polypropylene membranes with a) 100 nm, b) 200 nm, c) 450 nm, and d) 10 μm . The scaling bar is 2 μm .

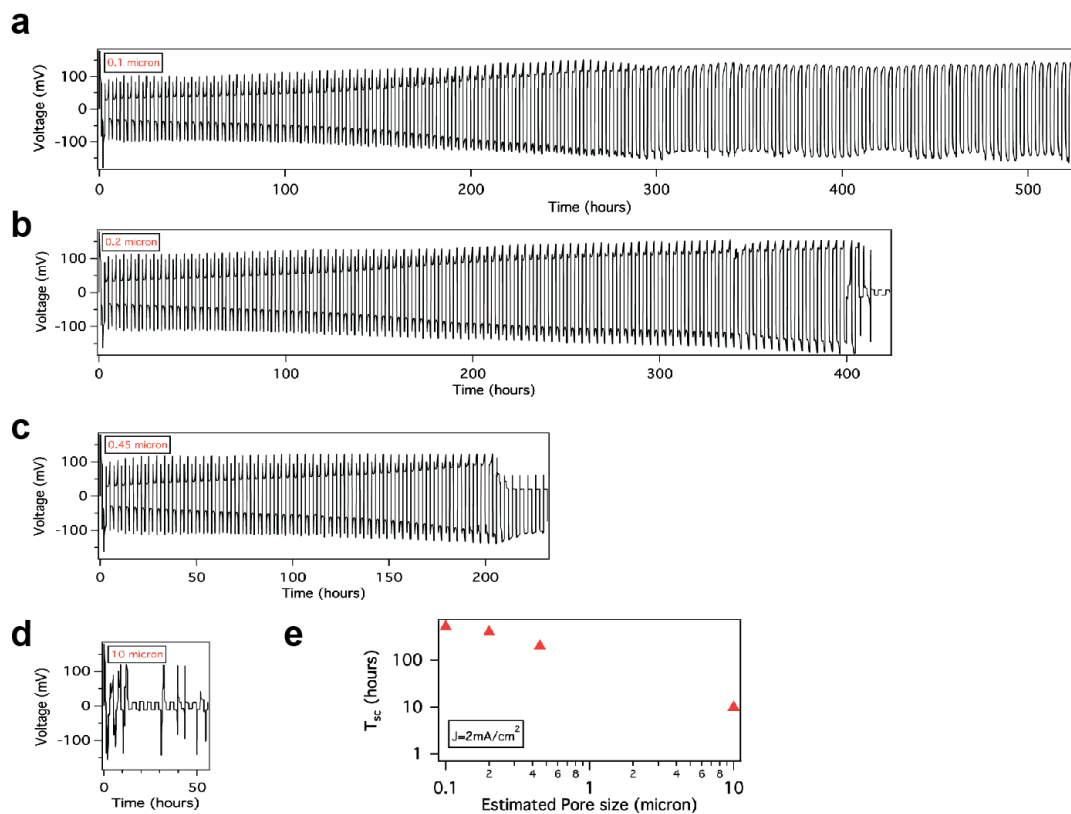


Figure 3.17. 1-hour lithium plating stripping experiments on porous polypropylene membranes with a) 100 nm, b) 200 nm, c) 450 nm, and d) 10 μm at the current density of 2 mA cm^{-2} . e) Short-circuit time vs. pore size.

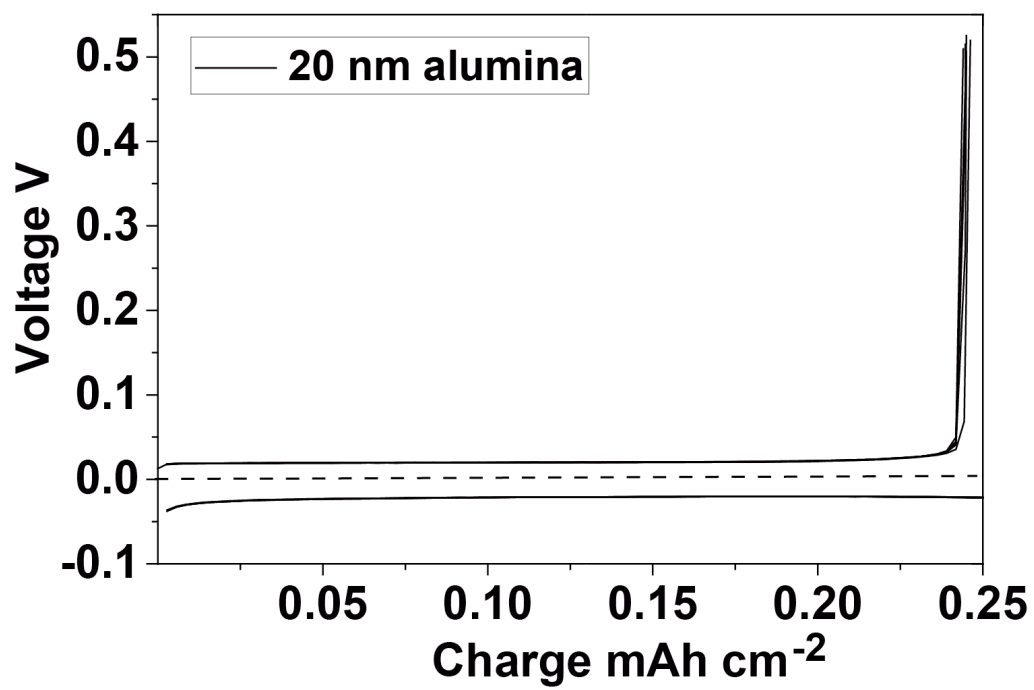


Figure 3.18. Voltage vs. capacity profile for Coulombic efficiency test.

To further evaluate the nanoporous Al_2O_3 membranes, we studied their performance in full electrochemical cells, in which a lithium metal anode is paired with one of two conventional cathodes: lithium iron phosphate (LiFePO_4 (LFP)), or lithium nickel cobalt aluminum oxide ($\text{LiNi}_{0.8}\text{Co}_{0.15}\text{Al}_{0.05}\text{O}_2$ (NCA)). Unlike the symmetric cells in which the voltage remains low over the cell lifetime, LFP and NCA provide the opportunity to evaluate the compatibility of Li-metal, nanoporous Al_2O_3 , and liquid electrolytes, under higher-voltage conditions. **Figure 3.19a** shows the galvanostatic cycling of Li/ Al_2O_3 /LFP battery under the 1C, with the inset depicting voltage profile of milestone cycles. For these measurements, a typical slurry coating process was used to prepare the electrode sheet at a mass loading of 2-3 mg cm^{-2} . An initial specific capacity of 125 mAh g^{-1} was observed after the first few activation cycles, with stable operation observed for over 120 cycles. Low over-potential during charge/discharge indicates a small resistance, which minimizes ohmic loss. Even when commercial LFP electrode is used, on which mass loading is as high as 15 mg cm^{-2} , the Li/ Al_2O_3 /LFP cells exhibit satisfactory C - rate compatibility. A decrease of the specific capacity from 145 mAh g^{-1} to 90 mAh g^{-1} when the C - rate ramps from 0.05 C to 0.8 C has been observed (**Figure 3.19b**). The result can be attributed to the increased overpotential caused by slow ion transport in the thick electrode. Nanoporous Al_2O_3 is also compatible with a high voltage NCA cathode, as shown in **Figure 3.19c** and **d**. Stable battery performance with specific capacity greater than 120 mAh g^{-1} can be achieved at various C rates by a combination of constant current and constant voltage charge up to 4.1V, followed by constant current discharge to 3 V. If cells are charged to 4.3V, a larger capacity of 140 mAh g^{-1} can be observed with only moderately

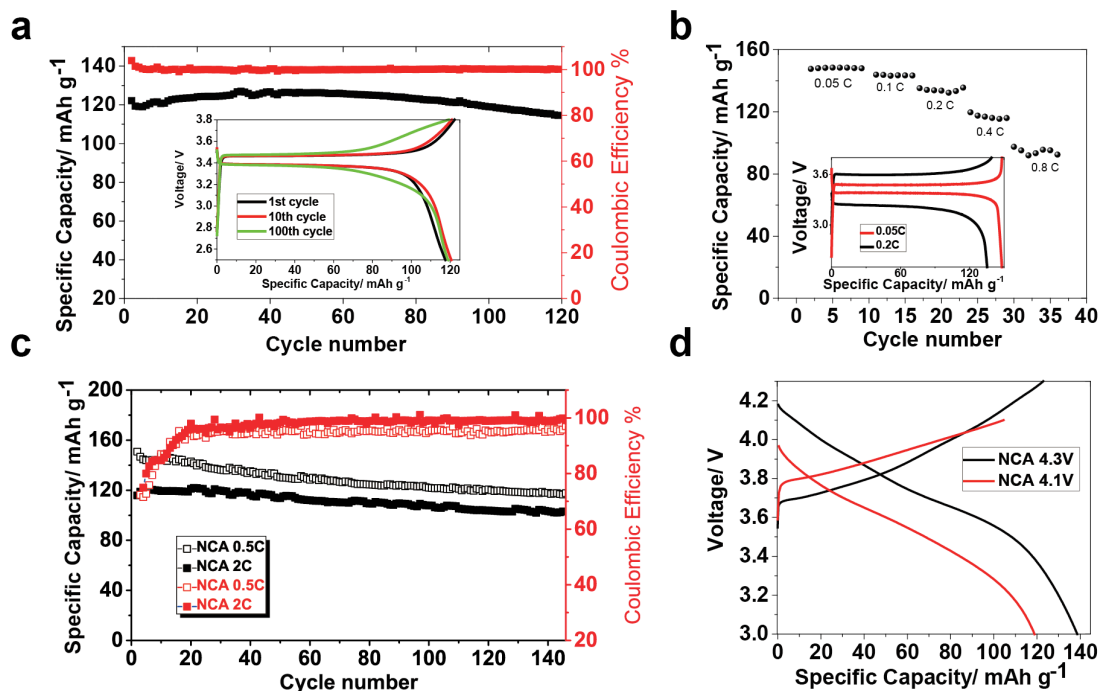


Figure 3.19. a) Galvanostatic cycling of Li - thin LiFePO₄ battery with 20 nm pore-size Al₂O₃/1 M LiPF₆ EC:DEC cycled at 1C; the inset shows the voltage profile at milestone cycles. b) Li - thick LiFePO₄ battery with 20 nm pore-size Al₂O₃/1 M LiPF₆ EC:DEC cycled at various C rates; the inset compares the voltage profiles at 0.05 C and 0.2 C. c) Galvanostatic cycling of Li - NCA battery with 20 nm pore-size Al₂O₃/1 M LiPF₆ EC:DEC cycled at various C rates charged up to 4.1V. d) Voltage profile of Li - NCA battery with 20 nm pore-size Al₂O₃/1 M LiPF₆ EC:DEC charged up to 4.1V and 4.3V at 2 C, respectively. The constant voltage charging process for Li - NCA batteries is not shown.

increased capacity fading after 140 cycles. A more demanding test has been performed by adopting high loading NCA electrode (20 mg cm^{-2}) with 20 nm pore-size Al_2O_3 , as shown in **Figure 3.20**. It is apparent from these results that these cells can be stably operated at 0.5 C with Coulombic efficiency close to unity, while at the same time yielding a high specific capacity over 100 cycles. The results from these tests imply that nanoporous Al_2O_3 infused with a preferred liquid electrolyte can be readily deployed as a nanostructured electrolyte system for room-temperature lithium metal battery.

In summary, we have systematically investigated a family of nanostructured electrolytes created by infusing nanoporous Al_2O_3 membranes with conventional salt-in-liquid electrolytes. Conductivity measurements of electrolytes with nanopore dimensions ranging from 20 nm to 200 nm reveal liquid-like ionic conductivities, but lower activation energies compared to an analogous bulk liquid electrolyte. Impedance measurements indicate that that source of this observation is a lower interfacial resistance. These measurements together show that interactions between ions in the electrolyte and the nanopores play an important role in setting the overall conductivity of liquid electrolytes infused in the membrane pores. The lithium transference number of the electrolytes is also studied by means of electrochemical and PFG-NMR analysis. We find that liquid electrolytes confined in nanopores exhibit a high lithium transference number at low and moderate salt concentrations, in qualitative agreement with previously proposed theory, but the effect is apparent even at nanopore sizes well above the Debye screening length for the electrolyte. The lithium transference number, measured by electrochemical and NMR methods, do not agree, implying a significant

interfacial contribution in the selective ion transport observed in the nanochannels. The application of the nanostructured electrolytes to lithium metal batteries shows that, regardless of the nanopore size, they stabilize deposition of Li. At a current density of 3 mA cm^{-2} , the highest studied, symmetric Li/Li cells containing the nanoporous Al_2O_3 -based electrolytes show no sign of short-circuiting, as confirmed by electrochemical and post-mortem SEM and cryo-FIB observation. Our results therefore provide a means for understanding how membranes based on nanoporous solids may be used to stabilize LMB operation by decoupling the effects of ion transport and mechanical pore-size limitations on dendrite nucleate size. The compatibility of nanoporous Al_2O_3 with lithium metal batteries is further evaluated in lithium cells employing conventional intercalating cathodes (LFP and NCA). Stable cycling performance is achieved with high specific capacity under various C rates, with no sign of cell failure by dendrite-induced short-circuiting.

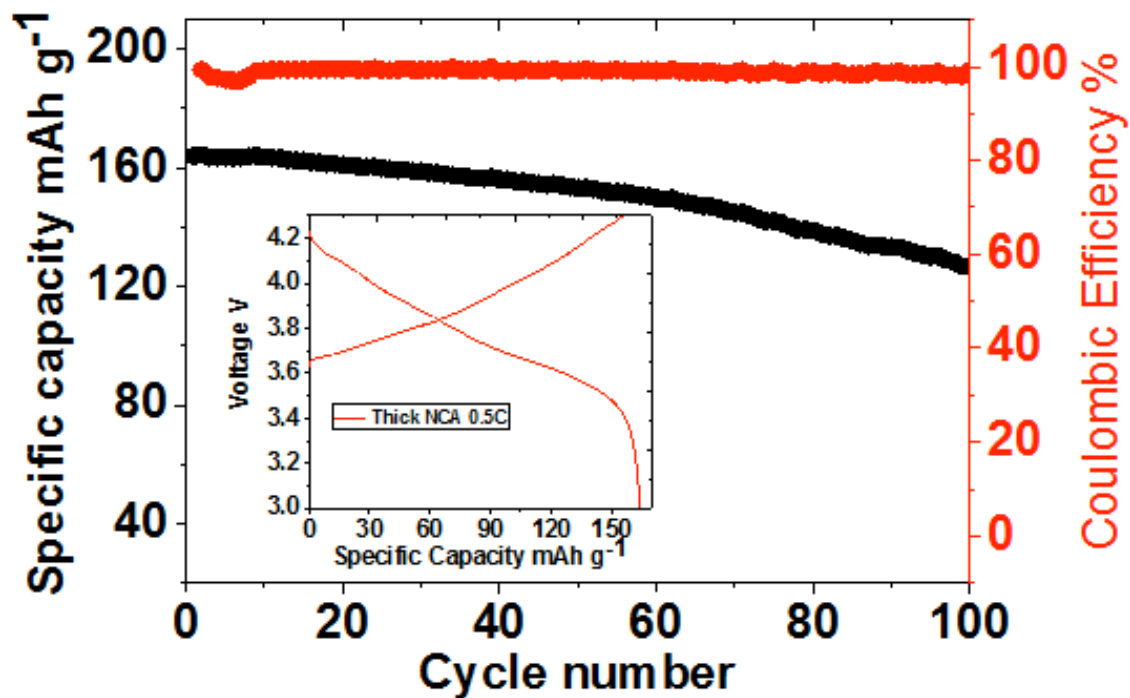


Figure 3.20. Galvanostatic cycling of Li/Al₂O₃ with 1M LiPF₆ EC:DEC/thick NCA operated at 0.5 C. The total capacity of the cell reaches 3 mAh cm⁻². The inset of the figure shows the voltage profile of the 1st cycle. The cut-off voltage is 4.3 V.

Reference

1. Tarascon, J. M.; Armand, M., Issues and challenges facing rechargeable lithium batteries. *Nature* **2001**, *414* (6861), 359-367.
2. Armand, M.; Tarascon, J. M., Building better batteries. *Nature* **2008**, *451* (7179), 652-657.
3. Yoshino, A., The Birth of the Lithium-Ion Battery. *Angewandte Chemie-International Edition* **2012**, *51* (24), 5798-5800.
4. Bruce, P. G., Energy storage beyond the horizon: Rechargeable lithium batteries. *Solid State Ionics* **2008**, *179* (21-26), 752-760.
5. Xu, S.; Das, S. K.; Archer, L. A., The Li-CO₂ battery: a novel method for CO₂ capture and utilization. *RSC Advances* **2013**, *3* (18), 6656-6660.
6. Ma, L.; Hendrickson, K. E.; Wei, S.; Archer, L. A., Nanomaterials: Science and applications in the lithium-sulfur battery. *Nano Today* **2015**, *10* (3), 315-338.
7. Chazalviel, J. N., Electrochemical Aspects of the Generation of Ramified Metallic Electrodeposits. *Phys. Rev. A* **1990**, *42* (12), 7355-7367.
8. Rosso, M.; Gobron, T.; Brissot, C.; Chazalviel, J.-N.; Lascaud, S., Onset of dendritic growth in lithium/polymer cells. *J. Power Sources* **2001**, *97*, 804-806.
9. Tikekar, M. D.; Choudhury, S.; Tu, Z.; Archer, L. A., Design principles for electrolytes and interfaces for stable lithium-metal batteries. *Nature Energy* **2016**, *1*, 16114.

10. Xu, W.; Wang, J. L.; Ding, F.; Chen, X. L.; Nasybutin, E.; Zhang, Y. H.; Zhang, J. G., Lithium metal anodes for rechargeable batteries. *Energy Environ. Sci.* **2014**, *7* (2), 513-537.
11. Tu, Z.; Nath, P.; Lu, Y.; Tikekar, M. D.; Archer, L. A., Nanostructured electrolytes for stable lithium electrodeposition in secondary batteries. *Acc. Chem. Res.* **2015**, *48* (11), 2947-2956.
12. Cheng, X. B.; Zhang, R.; Zhao, C. Z.; Wei, F.; Zhang, J. G.; Zhang, Q., A review of solid electrolyte interphases on lithium metal anode. *Advanced Science* **2015**.
13. Tu, Z.; Kambe, Y.; Lu, Y.; Archer, L. A., Nanoporous Polymer-Ceramic Composite Electrolytes for Lithium Metal Batteries. *Advanced Energy Materials* **2014**, *4* (2).
14. Tu, Z.; Lu, Y.; Archer, L., A Dendrite-Free Lithium Metal Battery Model Based on Nanoporous Polymer/Ceramic Composite Electrolytes and High-Energy Electrodes. *Small* **2015**.
15. Tikekar, M. D.; Archer, L. A.; Koch, D. L., Stability Analysis of Electrodeposition across a Structured Electrolyte with Immobilized Anions. *J. Electrochem. Soc.* **2014**, *161* (6), A847-A855.
16. Han, J.-H.; Khoo, E.; Bai, P.; Bazant, M. Z., Over-limiting current and control of dendritic growth by surface conduction in nanopores. *Scientific reports* **2014**, *4*.
17. Jorne, J., Transference number approaching unity in nanocomposite electrolytes. *Nano Lett.* **2006**, *6* (12), 2973-2976.

18. Chen, W.; Yuan, J.-H.; Xia, X.-H., Characterization and manipulation of the electroosmotic flow in porous anodic alumina membranes. *Anal. Chem.* **2005**, *77* (24), 8102-8108.
19. Siwy, Z.; Heins, E.; Harrell, C. C.; Kohli, P.; Martin, C. R., Conical-nanotube ion-current rectifiers: the role of surface charge. *J. Am. Chem. Soc.* **2004**, *126* (35), 10850-10851.
20. White, H. S.; Bund, A., Ion current rectification at nanopores in glass membranes. *Langmuir* **2008**, *24* (5), 2212-2218.
21. Tikekar, M. D.; Archer, L. A.; Koch, D. L., Stabilizing electrodeposition in elastic solid electrolytes containing immobilized anions. *Science Advances* **2016**, *2* (7), e1600320.
22. Diggle, J. W.; Downie, T. C.; Goulding, C., Anodic oxide films on aluminum. *Chem. Rev.* **1969**, *69* (3), 365-405.
23. O'sullivan, J.; Wood, G. In *The morphology and mechanism of formation of porous anodic films on aluminium*, Proceedings of the Royal Society of London A: Mathematical, Physical and Engineering Sciences, The Royal Society: 1970; pp 511-543.
24. Suo, L. M.; Hu, Y. S.; Li, H.; Armand, M.; Chen, L. Q., A new class of Solvent-in-Salt electrolyte for high-energy rechargeable metallic lithium batteries. *Nature Communications* **2013**, *4*.
25. Lu, Y.; Tikekar, M.; Mohanty, R.; Hendrickson, K.; Ma, L.; Archer, L. A., Stable Cycling of Lithium Metal Batteries Using High Transference Number Electrolytes. *Advanced Energy Materials* **2015**.

26. Schaefer, J. L.; Yanga, D. A.; Archer, L. A., High Lithium Transference Number Electrolytes via Creation of 3-Dimensional, Charged, Nanoporous Networks from Dense Functionalized Nanoparticle Composites. *Chem. Mater.* **2013**, *25* (6), 834-839.
27. Agrawal, R. C.; Pandey, G. P., Solid polymer electrolytes: materials designing and all-solid-state battery applications: an overview. *Journal of Physics D-Applied Physics* **2008**, *41* (22).
28. Evans, J.; Vincent, C. A.; Bruce, P. G., Electrochemical measurement of transference numbers in polymer electrolytes. *Polymer* **1987**, *28* (13), 2324-2328.
29. Stokes, R., The Variation of Transference Numbers with Concentration. *J. Am. Chem. Soc.* **1954**, *76* (7), 1988-1990.
30. Kay, R. L.; Dye, J. L., The Determination of the Electrophoretic Contribution to Conductance from the Concentration Dependence of Transference Numbers. *Proceedings of the National Academy of Sciences* **1963**, *49* (1), 5-11.
31. Sprycha, R., Electrical double layer at alumina/electrolyte interface: I. Surface charge and zeta potential. *J. Colloid Interface Sci.* **1989**, *127* (1), 1-11.
32. Dai, H.; Zawodzinski, T. A., The dependence of lithium transference numbers on temperature, salt concentration and anion type in poly (vinylidene fluoride)-hexafluoropropylene copolymer-based gel electrolytes. *J. Electroanal. Chem.* **1998**, *459* (1), 111-119.
33. Lu, Y.; Tu, Z.; Archer, L. A., Stable lithium electrodeposition in liquid and nanoporous solid electrolytes. *Nature materials* **2014**.

34. Lu, Y.; Korf, K.; Kambe, Y.; Tu, Z.; Archer, L. A., Ionic-Liquid–Nanoparticle Hybrid Electrolytes: Applications in Lithium Metal Batteries. *Angew. Chem. Int. Ed.* **2014**, *53* (2), 488-492.
35. Choudhury, S.; Mangal, R.; Agrawal, A.; Archer, L. A., A highly reversible room-temperature lithium metal battery based on crosslinked hairy nanoparticles. *Nature communications* **2015**, *6*.

CHAPTER 4

STABILIZING LITHIUM ELECTRODEPOSITION USING LIQUID ELECTROLYTE ADDITIVES AND NANOSTRUCTURED HYBRID ELECTROLYTES

Reproduced from *Nature materials* 13. 10 (2014): 961

4.1 Abstract

Rechargeable lithium, sodium, and aluminum metal-based batteries are among the most versatile platforms for high-energy, cost-effective electrochemical energy storage. Non-uniform metal deposition and dendrite formation on the negative electrode during repeated cycles of charge and discharge are major hurdles to commercialization of energy storage devices based on each of these chemistries. A long-held view is that unstable electrodeposition is a consequence of inherent characteristics of these metals and their inability to form uniform electrodeposits on surfaces with inevitable defects. We report on electrodeposition of lithium in simple liquid electrolytes and in nanoporous solids infused with liquid electrolytes. We find that simple liquid electrolytes reinforced with halogenated salt blends exhibit stable long-term cycling at room temperature, often with no signs of deposition instabilities over hundreds of cycles of charge and discharge and thousands of operating hours. We rationalize these observations with the help of surface energy data for the electrolyte/lithium interface and impedance analysis of the interface during different stages of cell operation. Our findings provide support for an important recent theoretical prediction that the surface mobility of lithium is significantly enhanced in the presence of lithium halide salts.

4.2 Introduction

High energy and safe electrochemical storage are critical components in multiple emerging fields of technology where portability is a requirement for performance and large-scale deployment. From advanced robotics, autonomous aircraft, to hybrid electric vehicles, the number of technologies demanding advanced electrochemical storage solutions is rising. The rechargeable lithium ion battery (LIB) has received

considerable attention because of its high operating voltages, low internal resistance and minimal memory effects¹⁻⁷. Unfortunately LIBs are currently operating close to their theoretical performance limits due to the relatively low capacity of the anode LiC_6 and the lithiated cathode materials (LiCoO_2 and LiFePO_4) in widespread use. It has long been understood that a rechargeable lithium metal battery (LMB), which eschewed the use of a carbon host at the anode can lead to as much as a ten-fold improvement in anode storage capacity (from 360 mAh g^{-1} to 3860 mAh g^{-1}) and would open up opportunities for high energy un-lithiated cathode materials such as sulfur and oxygen, among others⁸⁻¹⁰. Together, these advances would lead to rechargeable batteries with step-change improvements in storage capacity relative to today's state of the art LIBs.

A grand challenge in the field concerns the development of electrolytes, electrode, and battery systems configurations that prevent uneven electrodeposition of lithium and other metal anodes, and thereby eliminate dendrites at the nucleation step¹. It is understood that without significant breakthroughs in this area, the promise of LMBs, as well as of storage platforms based on more earth abundant metals such as Na and Al metal cannot be realized. Specifically, after repeated cycles of charge and discharge growing metal dendrites can bridge the inter-electrode space, producing internal short circuits in the cell. In a volatile electrolyte, ohmic heat generated by these shorts may lead to thermal runaway and catastrophic cell failure, which places obvious safety and performance limitations on the cells. The ohmic heat generated during a short-circuit may also locally melt dendrites to create regions of "orphaned" or electrically disconnected metal that results in a steady decrease in storage capacity as a battery is

cycled. Lithium-ion batteries (LiB) are designed to remove these risks by hosting the lithium in a conductive carbon host at the anode. However, the small potential difference that separates lithium insertion into versus plating onto carbon can potentially lead to similar failure modes in an overcharged or too quickly charged LiB. Thus, the need for materials that prevent non-uniform electrodeposition of metals such as Li is also implicit in new fast charging LIB technology targeted for electric-drive vehicles.

Researchers have for decades considered many approaches to stabilize lithium electrodeposition on metallic anodes¹¹⁻²⁵. Of these approaches, all solid-state batteries based on solid, ceramic electrolytes are considered by far the most promising, both from the perspective of their inherent safety and from theory, which indicate that a ceramic electrolyte with modulus above the shear modulus of the metallic anode can prevent dendrites from crossing the inter-electrode space. A persistent, vexing problem with ceramic electrolytes is that their room-temperature ionic conductivity rarely reaches levels commonplace in liquid electrolytes and required for normal battery operation. This problem can to some extent be managed by reducing the thickness of the solid electrolyte or by operating the batteries at elevated temperature. However these changes reveal other, more serious shortcomings, which have been most clearly demonstrated in studies of high-temperature sodium metal cells²⁶⁻²⁷. In these cells it was found that even at temperatures where the sodium anode is a low-modulus liquid and a high-modulus, solid sodium-beta-alumina ceramic is used as the electrolyte, metal dendrites form at the electrode/electrolyte interface and ultimately proliferate through stress and corrosion-induced cracks in the ceramic. More recent

studies by Tu *et al.*¹⁴ suggest that the need for high operating temperatures can be removed by making use of nanoporous ceramics that host a low-volatility and electrochemically stable liquid electrolyte in the pores. The authors report that these electrolytes provide a combination of solid-like mechanical modulus and liquid-like bulk and interfacial conductivities at room temperature. And, when employed in LMBs, they substantially increase the lifetime of cells cycled at low and moderate current densities, but postmortem inspection of the surface of the porous ceramic host reveal that, as in the case of the bulk ceramics, dendrites are still able to nucleate and proliferate on the surface, but appear unable to penetrate through the pores of the porous material.

A longstanding puzzle in the field is that secondary batteries based on some metals (e.g. Mg) show no evidence of electrode instability and dendrite formation under deposition conditions where dendrites form and proliferate in others, such as Li²⁸. At low surface deposition rates, thermodynamic and surface forces determine whether electrodeposited atoms preferentially form the low dimensionality, fiber-like structures, which lead to dendrites, or whether they form higher dimensional crystalline phases. Whereas at the intermediate and high surface deposition rates common in batteries, the mobility of atoms at the interface determines whether smooth or rough electrodeposits are created. Density functional theoretical analysis of Mg and Li electrodeposits at a vacuum metal interface reveal that Mg-Mg bonds are on average 0.18 eV stronger compared to a Li-Li²⁹. This means that under the same deposition conditions, the probability of a lower dimension, fiber-like Mg deposit spontaneously transforming to a higher-dimension crystal is more than 1000 times higher than that for the

corresponding transition in lithium. In electrolytes, these differences are only slightly altered by the interfacial tension, which is orders of magnitude lower, perhaps explaining why Li surfaces are more prone to nucleate dendrites irrespective of the electrolyte. A surprising and heretofore unexplored prediction from recent joint density functional theoretical (JDFT) calculations by Arias and co-workers³⁰ is that the presence of halide anions, particularly fluorides, in an electrolyte produce as much as a 0.13 eV reduction in the activation energy barrier for Li diffusion at an electrolyte-lithium metal electrode interface. If correct, this means that it should be possible to increase the surface diffusivity by more than two orders of magnitude, which may lead to large improvements in the stability of Li electrodeposition and dendrite suppression in simple liquid electrolytes.

We herein report on the stability of lithium electrodeposition in common liquid electrolytes reinforced with halogenated lithium salts. Remarkably, we find that consistent with expectations from the JDFT calculations, premature cell failure by dendrite growth and proliferation can be essentially eliminated in plate-strip type experiments even at high operating current densities. In more aggressive, high-rate polarization experiments, we find levels of dendrite suppression in room temperature liquid electrolytes that are superior to all previous reports from elevated temperature studies of polymer and other solid-state electrolytes long thought to be essential for developing reliable LMBs. Experimental characterization of the interfacial tension and impedance at the electrolyte-lithium metal interface confirm that the interfacial

mobility is a strong decreasing function of halogenated lithium salt and is the most likely source of the improved stability of Li electrodeposits in liquids.

4.3 Experimental Section

Methods

Pre-determined quantities of lithium halide salts and LiTFSI (LiPF_6) were dissolved in propylene carbonate (PC) and ethylene carbonate (EC)/diethylene carbonate (DEC) (1:1 (v:v) EC:DEC) electrolyte mixtures. The total lithium salt concentration was kept constant at 1 M. The mole fraction of LiF relative to total lithium salt was varied from 0.1-100%. To prepare the anhydrous solution, LiTFSI, LiPF_6 , LiF, PC, EC and DEC were dried rigorously by previous reported method^{12-13, 31} (Also see supplementary information).

Composite nanoporous alumina membranes were prepared using our previously reported approach¹⁴. Briefly, nanoporous alumina membranes were soaked in Polyvinylidene fluoride hexafluoropropylene (PVDF-HFP)/DMF solution. Then a phase separation approach was adopted to prepare sandwich-type alumina/PVDF-HFP membranes. These membranes were further immersed in previously described LiF+LiTFSI/PC electrolyte for at least 24 hours. The coin cell configuration for alumina membrane assembly is displayed in **Scheme 4.1**.

The thinner $\text{Li}_4\text{Ti}_5\text{O}_{12}$ (LTO) electrodes were composed of 80% of LTO, 10% of carbon black, and 10% of PVDF binder. A pre-determined amount of N – methylpyrrolidone (NMP) was added as solvent and the resultant slurry was thoroughly mixed. Following procedure involves using a doctor blade to coat slurry on

a clean copper sheet and it's rigorously dried in vacuum oven. The thicker $\text{Li}_4\text{Ti}_5\text{O}_{12}$ (LTO) electrodes (64 microns in thickness) used in the half-cell battery experiments were provided by the U.S. Department of Energy's (DOE) Cell Fabrication Facility, Argonne National Laboratory and used as received.

Symmetric lithium metal coin cells (2032 type, **Scheme 4.2**) were used for dielectric spectroscopy, impedance spectroscopy, cycling voltammetry, galvanostatic polarization and cycling measurements. Ionic conductivities were measured by Novocontrol N40 broadband dielectric spectrometer. The galvanostatic polarization and cycling measurements were conducted using Neware CT-3008 battery tester. Impedance spectra were measured as a function of frequency by a step heating procedure using impedance spectrometer. Cells were disassembled and the lithium metal electrodes harvested and rinsed with PC before analyzed by scanning electron microscopy (SEM, LEO1550-FESEM).

The contact angles were measured at room temperature using a Ramé-hart, Inc. Model 100-00-115 goniometer. The lithium foil was placed in a transparent environmental chamber with a rubber seal on the top. A single drop of the test liquid was placed on the substrate via a microliter syringe though the seal. The contact angle was determined six times at different positions and the average values reported.

Sample Preparation

Electrolytes: A rigorous, multi-step drying protocol was used to avoid contamination of the electrolytes by residual moisture. To prepare the anhydrous solution, LiTFSI was first dried at 110 °C for 4 hours and then at 170 °C for 3 days under vacuum.

Propylene carbonate (PC) was kept on 3 Å molecular sieves for at least one week and subsequently stored in an Argon-filled glovebox, MBraun Labmaster.. Ethylene carbonate (EC) was dissolved in diethyl carbonate (DEC) (1:1 v:v ratio) and kept on 3 Å sieves for at least one week and also stored in the glovebox. Pre-determined amounts of LiF+LiTFSI (LiF+LiPF₆) in PC (EC:DEC) was then prepared in an argon-filled glovebox.

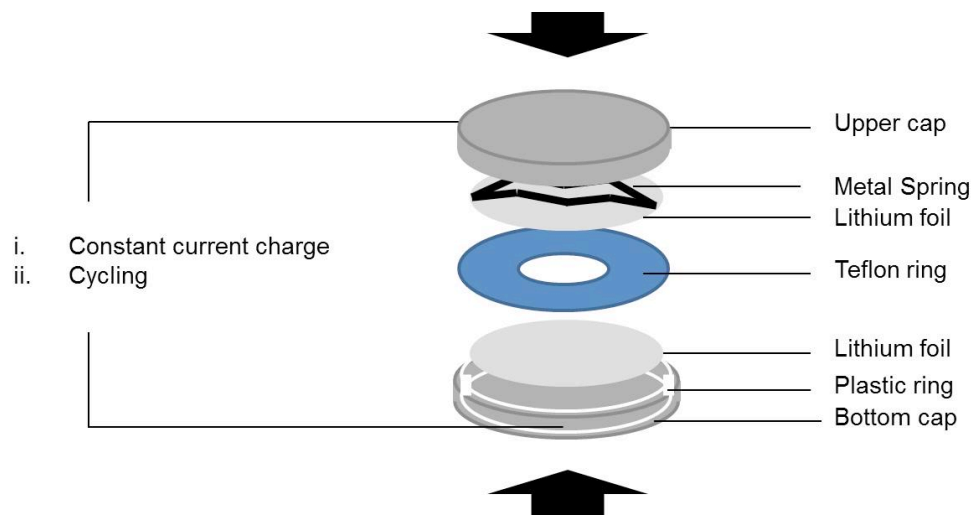
Nanoporous alumina membranes: alumina membrane filters, Whatman Anodisc 13 with 20nm pores size, were purchased from Fisher. Polyvinylidene fluoride hexafluoropropylene (PVDF-HFP, purchased from Sigma Aldrich.) was dissolved in N, N -dimethylformamide (DMF, supplied from Sigma Aldrich) at 10 wt% concentration. The viscous PVDF/DMF solution was casted on a clean glass cover slip, covered by the alumina membranes. The plate as well as the materials, were immersed in a DI water bath for 10 seconds, and a second glass cover slip was placed on top of the PVDF coated membrane to control the thickness and surface smoothness. The resultant laminated membranes were kept in a water bath overnight before being carefully sectioned to a desired size. Composite membranes produced in this manner were transferred into a bath of dry propylene carbonate (PC), which is periodically refreshed. The membranes were further rigorously dried in 1M LiTFSI/PC solution in glovebox (MBraun) under argon protection using a combination of lithium metal ingots and molecular sieves. The as prepared laminated alumina membranes were subsequently immersed for at least 24 hours in a 30mol% LiF+LiTFSI/PC solution containing 1M Li⁺.

Cell Assembly: Symmetric lithium-lithium coin cell (CR2032 type) were assembled in an Argon filled glove box. To avoid any cracking of the laminated alumina membrane during the coin cell assembly, the cell configuration shown in **Scheme 4.1** was employed. Briefly, a disc-shaped piece of lithium foil with comparable diameter as the laminated separator was placed at the bottom of the cell while a second smaller piece of lithium foil was applied to the top. This configuration is advantageous because it protects against accidental contact of the lithium electrodes during cell assembly and protects the laminated membrane from cracking when subjected to perpendicular stress during the final stages of cell assembly.

A more detailed configuration of the symmetric lithium cells used to study the liquid electrolytes is provided in **Scheme 4.2**. Briefly, a Polytetrafluoroethylene (Teflon) ring is used as a separator. The outer diameter is $(5/8)$ ", inner diameter is $(1/4)$ ", and the thickness is (0.030) ". The thickness of the lithium metal (Alfa Aesar) is 0.75mm. In assembling the cell, one side of the lithium metal is attached onto the Teflon ring, which creates an effective sample holder with a sealed bottom. Sufficient liquid electrolyte is slowly charged into the Teflon hole to avoid entrainment of bubbles, and the other lithium foil is carefully placed onto the other side of the separator. In this cell configuration, the liquid electrolyte in the empty space between the two electrodes provides the only barrier to lithium electrodeposits growing and proliferating in the inter-electrode space and short-circuiting the cell. Relative to lithium metal, the Teflon separator is a rigid material so the distance between the two lithium electrodes can be taken to be constant. The time for the dendrite propagation is then only related to the growth velocity.



Scheme 4.1. Cartoon of the specific configuration used for the Li/nanoporous membrane/Li coin cells. Two gray plates are lithium foils while the white one designates the laminated membrane.



Scheme 4.2. The configuration of symmetric lithium cells used in galvanostatic polarization and galvanostatic cycling measurements.

Sample characterization

Polarization Experiments: Eight cells with the same electrolyte composition were prepared and the time-dependent voltage characterized at a fixed current density. At the beginning of the test, the cell was first aged for one day and rested at zero volts for 10mins. The short-circuit time was determined as the time at which the steady voltage dropped discontinuously. In all cases this drop was clean and easy to detect. Data collected for the eight cells was averaged to determine the average short-circuit time vs. current density plotted in **Figure 4.5**. The error bars in the figure are standard deviations from the average value recorded in each 8-cell sample set and are generally in the range of 8-10%. To measure the impedances at the three important stages of cell operation - before polarization, at steady state, and after cell short-circuit, cells polarized under the same conditions were terminated after 10mins rest, after the time-dependent voltage reaches steady-state and after a clear drop-off of the voltage is observed. Three cells were collected at each stage for impedance measurements. A fixed frequency range of 10^6 to 10^{-1} Hz. was used for the impedance measurements.

Measuring ionic conductivity of the electrolytes: The ionic conductivity of all electrolytes was measured using frequency-domain dielectric relaxation measurements in the range 10^7 to 10^{-1} Hz using a Novocontrol Broadband dielectric spectrometer. The temperature was ramped in a step profile to achieve data at -5, 10, 25, 40, 55, 70, 85 °C. The DC conductivity is extracted from the ionic conductivity vs. frequency plot at each temperature. DC ionic conductivities of LiF+LiTFSI/PC with various LiF mole fractions were measured in cells using liquid electrolytes soaked in a

macroporous glass fiber separator as well as in cells using nanoporous Al₂O₃ infused with liquid electrolyte. **Figure 4.1a** reports the conductivity versus temperature of LiF+LiTFSI/PC soaked in glass fiber separators. The glass fiber separators were assembled in symmetric lithium coin cells for the conductivity measurement. **Figure 4.1b** shows the conductivity versus temperature of LiF+LiTFSI/PC soaked in alumina/PVDF separator. The alumina based separators were loaded between two copper plates for conductivity test.

The continuous lines through the data in **Figure 4.1a** are obtained by fitting the experimental results to the Vogel-Fulcher-Tammann (VFT) formula, $\sigma = A \exp(-B/(T-T_0))$, where B is the effective activation energy barrier, in the units of absolute temperature; T and T_0 are the measurement and reference temperatures, respectively; and A is a pre-exponential factor which equals to the ionic conductivity in the high-temperature limit. The equation fits the data over the range of temperature and lithium fluoride content studied⁴⁻⁶. The short-circuit time vs. current density by galvanostatic polarization measurement is fitted by the following power law function⁷⁻¹⁰: $T_{SC} = CJ^{-m}$. The parameter C is related to the diffusion coefficient of ions, mobile ion concentration, anion transport number, and ion mobility⁸⁻¹⁰. Values of all of these parameters are presented in **Table S2**.

Galvanostatic cycling experiments: For the galvanostatic cycling test, the cell was initially charged at a fixed current density for 90mins, and then discharged at the same current density for 180mins, followed with charging 180mins to continue the cycling.

Characterizing the Interfacial Energy at the electrode/electrolyte interface: The contact angle of each liquid electrolyte on the surface of clean lithium metal was measured

using a goniometer in an argon-filled enclosure. Analysis of the contact angle data by Young's equation and Zisman approach¹¹⁻¹³ can be used to determine the surface energy as follows:

$$\gamma_L \cos \theta = \gamma_S - \gamma_{SL} \quad (1)$$

$$\cos \theta = 1 - b(\gamma_L - \gamma_C) \quad (2)$$

Where γ_L is the experimentally determined surface energy (surface tension) of the liquid (electrolyte), θ is the contact angle, γ_S is the surface energy of the solid (lithium: 0.52 J m^{-2}), γ_{SL} is the solid/liquid interfacial energy, b is the slope of the regression line and γ_C is the critical surface tension when $\cos \theta = 1$. The two parameters b and γ_C are calculated from (2) using γ_L values from the literature and the measured θ for pure PC and DMC. The variation of γ_C in electrolytes with different concentrations of LiF was obtained from the regression line (**Figure 4.2**). γ_{SL} were then calculated from (1). Note that the deviations of the measurements and Zisman calculation may apply but the results in terms of the L-S surface energy change very small due to the large lithium surface energy compared with that of a liquid electrolyte. Results from this method are displayed in Table S1.

Table 4.1. Contact angles, liquid electrolyte surface tensions (γ_L), lithium surface energy (γ_S) and solid/liquid interfacial energies (γ_{SL}) of various electrolyte compositions.

Sample	θ (°)	$\cos \theta$	Electrolyte surface tension($N m^{-1}$)	Liquid-solid surface energy($J m^{-2}$)
Pure PC	23.0	0.92	0.0448	0.479
Pure DMC	7.3	0.99	0.0291	0.491
PC/1M LiTFSI	22.0	0.93	0.0426	0.480
5 mol% LiF	19.5	0.94	0.0403	0.482
10 mol% LiF	18.5	0.95	0.0381	0.484
30 mol% LiF	16.0	0.96	0.0358	0.486
50 mol% LiF	15.0	0.97	0.0336	0.487
Li: $0.52 J m^{-2}$; PC: $0.045 N m^{-1}$; DMC: $0.0286 N m^{-1}$				

Table 4.2. VFT fitting parameters and scaling exponent by power law fitting. The fittings of these two equations were conducted by Origin 8.0.

Sample	VFT: $\sigma = A \exp(-B/(T - T_0))$			$T_{SC} = AJ^{-m}$
	$A(S/cm)$	$B(K)$	$T_0(K)$	m
0.1 mol% LiF	0.081±0.0029	461±12	162±2.1	-
1 mol% LiF	0.079±0.0011	485±5.1	156±0.88	-
3 mol% LiF	0.035±0.0028	291±22	188±4.9	-
5 mol% LiF	-	-	-	1.42
10 mol% LiF	0.0033±0.0085	365±8.1	168±1.7	1.53
30 mol% LiF	0.0061±0.00097	127±32	215±12	1.70
100 mol% LiF	0.00052±0.000030	506±21	138±3.8	
30 mol% LiF @ 70°C	-	-	-	0.60
30 mol% LiCl	-	-	-	1.36
30 mol% LiBr	-	-	-	2.10
30 mol% LiI	-	-	-	1.27

4.4 Results and discussion

Electrolytes containing 1 M Li⁺ cations were studied in two configurations: (i) In liquid form; and (ii) as liquids infused in nanoporous solids. Electrolytes employed in both situations were created by blending pre-determined amounts of halogenated lithium salts and lithium bis(trifluoromethanesulfonyl)imide (LiTFSI) in a low volatility propylene carbonate (PC) liquid host. To explore consequences of our observations on lifetime of lithium metal batteries, we also performed a small number of studies using blends of lithium fluoride (LiF) and lithium hexafluorophosphate (LiPF₆) in a 50/50 blend of ethylene carbonate (EC) and diethylene carbonate (EC:DEC). Because the most impressive enhancements in interfacial mobility predicted by JDFT are for electrolytes containing LiF, this first communication will focus on these materials. **Figure 4.1a** reports the DC conductivity for LiF+LiTFSI/PC as a function of LiF mole fraction in the electrolytes. It is apparent that at low LiF concentrations, DC conductivities close to the measured values for a LiTFSI/PC liquid electrolyte control are found. At LiF concentrations above 3 mol percent, the conductivity falls with increasing LiF content and the shape of the conductivity-versus-temperature profiles are seen to become flatter, but for all compositions studied, room-temperature conductivity well above 10⁻³ S cm⁻¹ are observed. A lower bulk electrolyte ionic conductivity upon addition of LiF is consistent with expectations based on the reduced dissociation of the salt, relative to LiTFSI, and consequent lower population of mobile ions in solution. The inset to the figure shows the effect of LiF on the wettability/contact angle (right axis) and surface energy (left axis) of the electrolyte with a lithium metal surface (see supplemental information **Figure 4.2** &

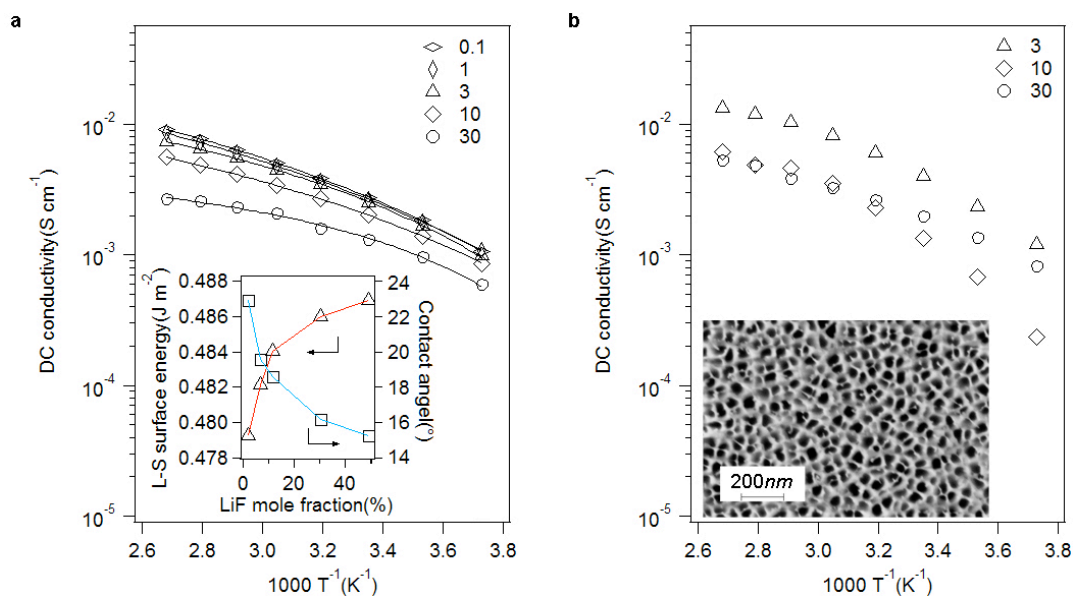


Figure 4.1. DC ionic conductivity of LiF+LiTFSI/PC with various LiF mole fractions as a function of temperature. a, Without alumina/PVDF membrane. The electrolyte is placed in a home-made Teflon O-ring (**Scheme 4.2**) without presence of any separator. The solid lines are Vogel-Fulcher-Tammann (VFT) fits for the temperature-dependent ionic conductivity. The parameters from the VFT fitting are shown in **Table 4.2**. The inset shows the liquid-solid surface energy and contact angle as a function of LiF mole fraction. b, With alumina/PVDF membrane. The SEM image shows the nanostructure of the alumina membrane with pore diameter around 40nm.

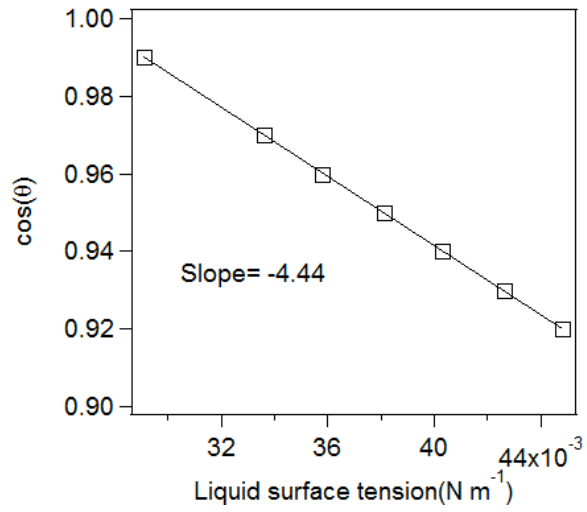


Figure 4.2 Zisman's plot for LiF+LiTFSI/PC, PC, DMC on lithium metal surface. Based on Zisman approach, the contact angle of different liquids on the same surface is linearly dependent on the liquid surface tension.

Table 4.1). The measurements were performed using a contact angle goniometer with lithium sample enclosed in a home-made argon-filled chamber. It is apparent from the figure that addition of LiF causes a non-monotonic decrease in contact angle and a commensurate rise in interfacial energy. Later, we will show that electrodeposition of lithium metal in these electrolytes produce isolated mushroom-like structures of diameter around 40 μm . The increase in surface energy produced upon addition of LiF to the electrolytes are therefore many orders of magnitude lower than the differences in bonding energy between Mg-Mg and Li-Li atoms to significantly change the tendency of Li to form lower dimensional dendritic structures.

Figure 4.1b reports the DC conductivity for nanoporous solid electrolytes created by infusing LiF+LiTFSI/PC into nanoporous $\text{Al}_2\text{O}_3/\text{PVDF}$ monoliths (see lower inset) with a nominal pore diameter of 40nm. The detailed preparation protocols for these electrolytes are provided in the supplementary materials section. It is apparent from **Figure 4.1b** that while the effect of LiF composition on conductivity is more complex than for the liquid electrolytes, over the range of LiF compositions studied the electrolytes again exhibit room-temperature conductivities above $10^{-3} \text{ S cm}^{-1}$; underscoring their suitability as room-temperature electrolytes for lithium batteries. Electrochemical stability of LiF-containing electrolytes was characterized by cyclic voltammetry and the results reported in the supplementary materials section (**Figure 4.3**). With 30mol% LiF, the width of electrochemical stability window is observed to increase measurably. The peak in the voltammogram at around 4.1 V vs. Li/Li^+ in the first cycle is in fact consistent with formation of a passivation film on the electrode that protects the electrolyte.

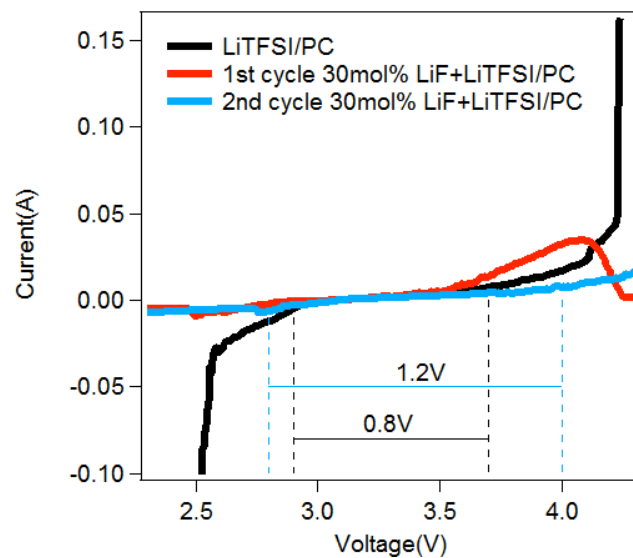


Figure 4.3. Electrochemical stability window from cyclic voltammetry measurements for 1M LiTFSI/PC and 30mol% LiF+LiTFSI/PC at a rate of 0.5 mV s^{-1} . The measurements were conducted in symmetric lithium cells.

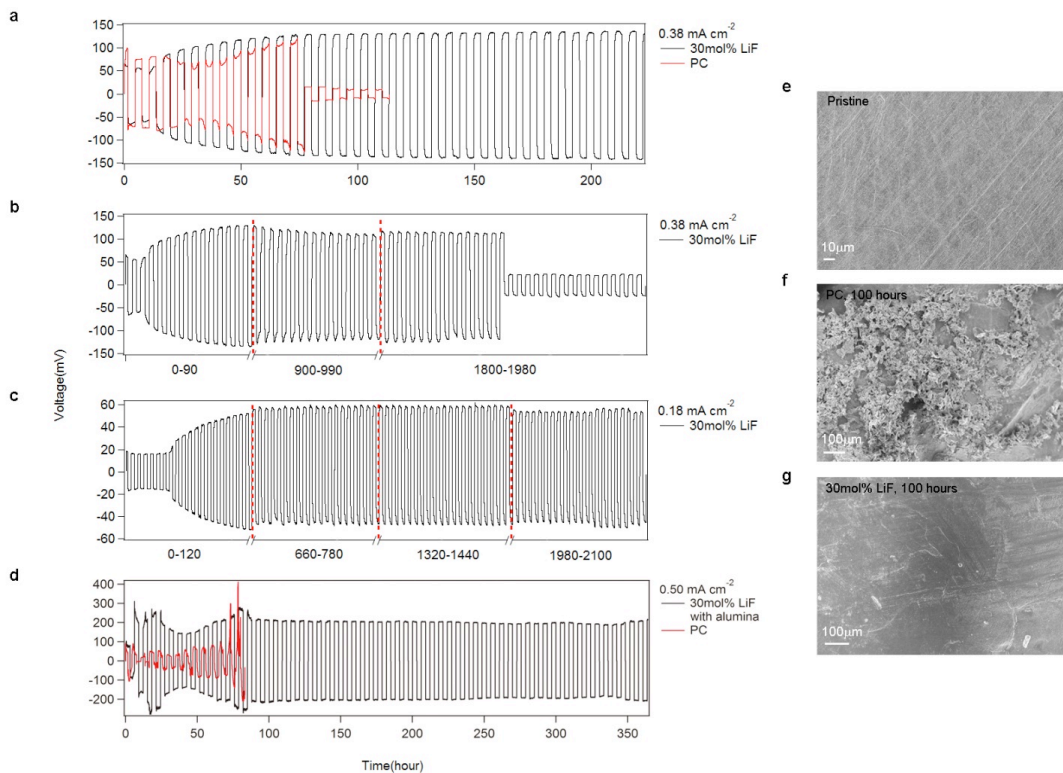


Figure 4.4. Voltage versus time for a symmetric lithium cell with each half cycle lasts 3 hours. a, Initial voltage profiles of 30mol% LiF+LiTFSI/PC (black) and LiTFSI/PC (red) electrolytes at a current density of 0.38mA cm^{-2} . b, Voltage profile of 30mol% LiF+LiTFSI/PC electrolyte at a current density of 0.38mA cm^{-2} before observing cell short-circuits. c, Typical voltage profile for LiF+LiTFSI/PC electrolytes at lower current densities (less than 0.2mA cm^{-2}). d, Initial voltage profiles of 30mol% LiF+LiTFSI/PC (black) and LiTFSI/PC (red) electrolytes with alumina/PVDF membrane at a current density of 0.50mA cm^{-2} . The initial voltage disturbance is due to the electrolyte consumption and SEI layer formation. The voltage reaches a stable plateau after 80 hours and lasts for over 350 hours. Such stable performance at high current density originate from two factors: 1) the LiF additive stabilizes the lithium deposition and forms a flat surface, which are in favor of steady battery usage; 2) the high modulus of alumina separator prevents the dendrite proliferation and avoids the short-circuit. SEM analyses: e, Pristine lithium anode before galvanostatic cycling. f, Lithium anode in contact with LiTFSI/PC electrolyte after 100-hour cycling at 0.38mA cm^{-2} . g, Lithium anode in contact with 30mol% LiF+LiTFSI/PC electrolyte after 100-hour cycling at 0.38mA cm^{-2} .

We investigated electrodeposition of Li in the liquid and nanoporous LiF+LiTFSI/PC based electrolytes using galvanostatic cycling of Li|LiF+LiTFSI/PC|Li symmetric lithium cells in which the lithium stripping/plating process is cycled over three-hour charge and discharge intervals designed to mimic operation in a LMB. The cells are configured to ensure that during each three-hour period sufficient lithium is transported between electrodes to create a dendrite bridge in the inter-electrode space to short-circuit the cells. The cells also do not include a separator and, once formed, the only resistance to dendrites bridging the inter-electrode spacing is provided by the intervening liquid electrolyte. Figure 4.4a compares the voltage profiles observed in symmetric cells containing electrolytes with and without LiF at a fixed, high current density of 0.38 mA cm^{-2} .

The figure shows that cells that do not contain LiF in the electrolyte exhibit a large and irreversible drop in voltage consistent with catastrophic failure by a dendrite-induced short-circuit, in as little as 75 hours of operation (i.e. less than 13 cycles of charge and discharge). In contrast, cells containing 30 mol% LiF in the electrolyte cycle stably for more than 1800 hours (300 cycles of charge and discharge) before succumbing to failure in the same manner. This nearly 25-fold enhancement in cell lifetime achieved upon addition of LiF to a liquid electrolyte is considerably higher than any previous report for cells in which solid polymers¹⁸, composites^{12,13,15} and other mechanical agents are used to protect lithium metal electrodes against premature failure by dendrite-induced shorts. It is also significant that the current experiments are performed at substantially higher current densities than those reported for solid polymer or ceramic electrolytes and at room temperature. **Figure 4.4c** reports voltage

profiles for cycling experiments performed at comparable current densities as in previous studies using polymers and other mechanical agents. Remarkably, even after 2100 hours of continuous operation, the cell shows no evidence of failure. **Figure 4.4d** reports a similar result for cells based on nanoporous membranes infused with liquid electrolytes, but cycled at a very high current density of 0.5 mA cm^{-2} . While cells with the control LiTFSI/PC electrolyte are seen to quickly fail, those containing LiF in the electrolyte settle down over a period of around 75 hours and cycle stably for more than 350 hours.

Figures 2e-g are scanning electron micrographs of the lithium metal electrode surface before cycling (**e**), after 100 hours of cycling in a LiTFSI/PC control electrolyte (**f**), and after 100 hours of cycling in a LiF+LiTFSI/PC electrolyte containing 30 mol% LiF (**g**). It is evident from the figure that the improved lifetimes of the cells containing LiF coincides with the observation of virtually pristine Li metal electrodes after extended cycling.

Unidirectional galvanostatic polarization of symmetric lithium cells provides a convenient, accelerated-testing scheme for assessing the stability of lithium metal electrodes during electrodeposition. In this approach, lithium is continuously stripped from one electrode and plated on the other until the cell fails by consumption of all of the lithium or as a result of a dendrite-induced short-circuit. A constant current density is applied to the cell and the corresponding voltage profile is obtained as a function of time (**Figure 4a**). The time (T_{sc}) at which a sharp drop-off in the potential is observed provides an estimate for its lifetime. Because there is no pause in the deposition, as occurs when the direction of the current is reversed in the cyclic plate-strip experiment

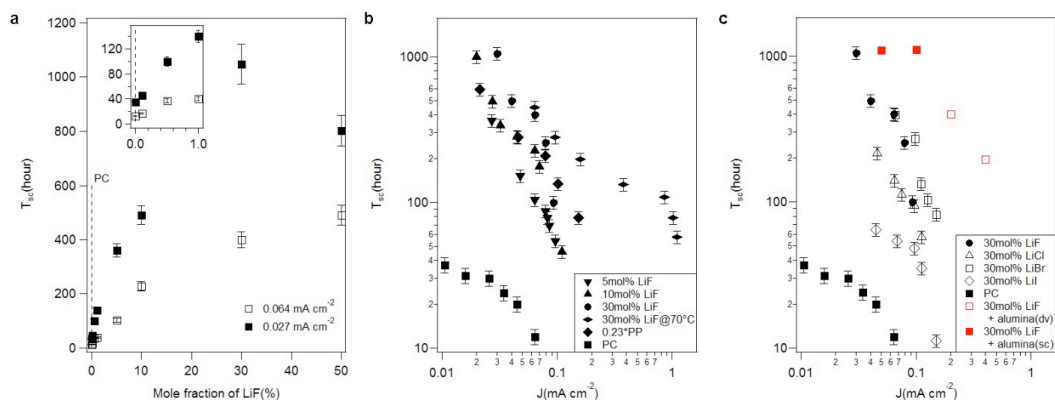


Figure 4.5. Short-circuit time T_{sc} from galvanostatic polarization measurements for symmetric lithium cells. a, T_{sc} as a function of LiF mole fraction at 0.027mA cm^{-2} , 0.064mA cm^{-2} . b, T_{sc} as a function of current density J for various LiF concentrations and for PP-TFSI. c, T_{sc} as a function of current density J for different lithium halides with 30mol % of the halide. The red markers are used to represent results for cells based on nanoporous alumina/PVDF membranes infused with LiF+LiTFSI/PC electrolytes. The filled red symbols indicate the cells that short-circuit while the open red symbols represent the ones that diverge instead of short. Measurements were conducted at room temperature unless indicated.

discussed in the last section, there is no opportunity for defects produced by instability in one deposition cycle to heal before they nucleate dendrites that ultimately short circuit the cell. Consequently, cell failure by dendrite-induced short circuits are observed on timescales as much as one order of magnitude lower than for the plate-strip cycling measurements^{12,24,25}.

Figure 4.5a reports measured T_{sc} values as a function of LiF concentration in the electrolyte at two current densities. Consistent with the observations reported in the previous section, the figure shows that addition of LiF to a LiTFSI/PC electrolyte produces large increases in cell lifetime. The top inset shows that addition of as little as 1mol% LiF produces more than a three-fold enhancement in cell lifetime at both low (0.027 mA cm^{-2}) and moderate (0.064 mA cm^{-2}) current densities. The figure further shows that at a higher LiF contents the relationship between T_{sc} and LiF composition in the electrolyte is nonlinear. At 30 mol % LiF, it is seen that more than a 30-fold enhancement in cell lifetime is achieved at either current density, confirming the earlier observations based on cyclic plate-strip experiments. The ability of LiF salt to extend cell lifetime seems to reach its maximum level at around 30mol% LiF. For higher LiF mole fraction (50mol% LiF), there is a decrease of T_{sc} , which might be attributed to the low DC conductivity or low mobile ion concentration. It is also difficult to polarize the cell at relatively high current density for the same reason²³.

Figure 4.5b studies the effect of current density, J , and temperature on T_{sc} for electrolytes containing varying concentrations of LiF, including a PC electrolyte containing 23 vol% of the ionic-liquid methy-3-propylpiperidinium (PP) TFSI known for its exceptional ability to facilitate stable electrodeposition of lithium^{11,12}. It is clear

from the figure that both in terms of the variation of T_{sc} with J and the enhancements in lifetime achieved relative to the electrolyte without additives, the LiF-based electrolytes with around 30 mol % LiF perform at least as well as those containing PP TFSI. As previously reported for electrolytes containing PP TFSI, T_{sc} exhibits a power-law dependence on J , $T_{sc} \sim J^m$, over a wide range of current densities^{13,24,25}. Power law exponents m obtained from the data are provided in **Table 4.2** and show no noticeable dependence on LiF composition. It is also apparent from the figure that at 70 °C electrolytes containing LiF exhibit T_{sc} values with little sensitivity to J over a range of current densities, allowing these electrolytes to achieve 100-fold or more enhancements in cell lifetime, relative to the control electrolyte at 25 °C. **Figure 4.5c** nicely shows that LiF is not unique and that other halogenated lithium salts, especially LiBr, are able to significantly extend lifetime of lithium metal electrodes. **Figure 4.5c** further shows that T_{sc} values measured using nanoporous electrolytes¹⁴ (also see **Figure S7**) containing LiF are substantially higher than those measured in any of the other systems and are virtually independent of J . The two open red symbols are results for cells where no short-circuiting was observed, but in which the voltage diverged as a result of all of the lithium in the stripping electrode being plated on the other electrode without creating dendrite-induced short circuiting. It is remarkable that these cells show no evidence of short-circuiting at high current densities normally inaccessible in galvanostatic polarization experiments in symmetric Li cells. Post-mortem SEM analysis for these cells are provided as supplementary **Figure 4.7**.

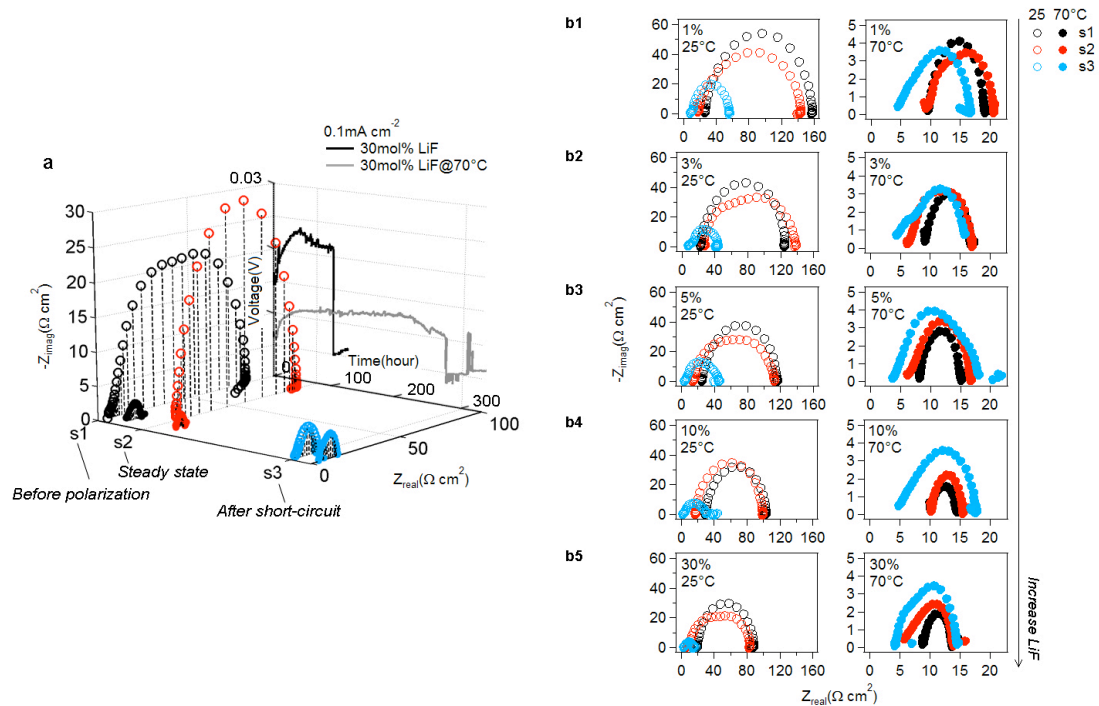


Figure 4.6. Voltage profile at a fixed current density, impedance spectra of the three stages (s1: before polarization, s2: steady state, s3: after short-circuit) at 25°C and 70°C. a, Voltage profiles and impedance spectra at 0.1 mA cm^{-2} for 30 mol% LiF+LiTFSI/PC electrolyte. b, Impedance spectra for 1 mol%, 3 mol%, 5 mol%, 10 mol% and 30 mol% LiF+LiTFSI/PC electrolytes.

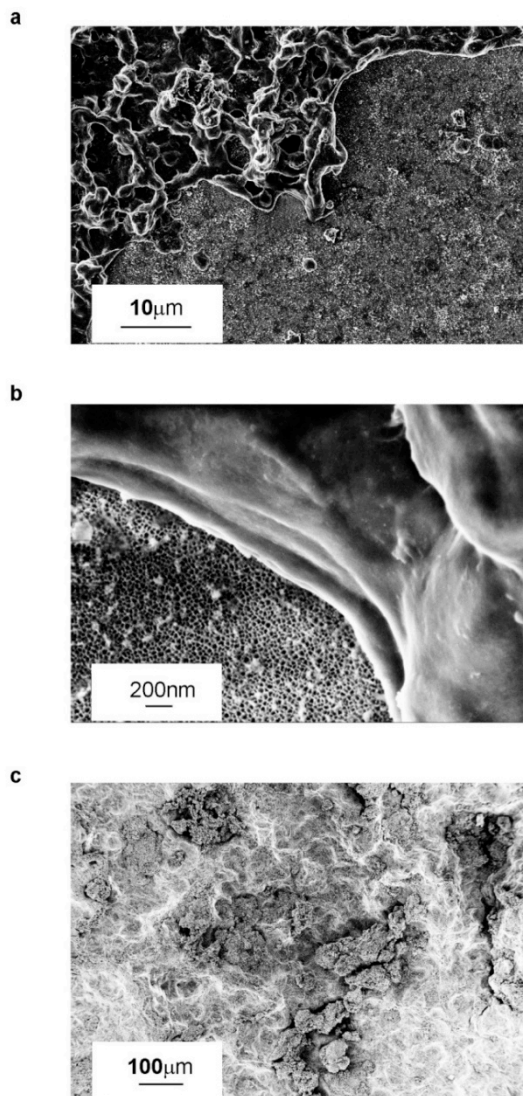


Figure 4.7. SEM analysis of alumina/PVDF separator and lithium substrate after 400 hours lithium plating/stripping test at 0.5 mA cm^{-2} . a, Alumina/PVDF separator with lithium metal on one side. b, Zoom in picture of a. c, Morphology of lithium surface.

Analysis of the electrode-electrolyte interface at different stages of polarization provides additional insight into the role played by LiF. Impedance spectroscopy is a frequency-domain technique that allows the complex resistance or impedance in all components of a cell (electrode, electrolyte, and their interfaces) to be determined as a function of temperature. Impedance spectra of the symmetric lithium cells before unidirectional galvanostatic polarization, at steady state, and after cell failure were collected and typical results are reported in **Figures 4.6a,b**. Measurements were performed at 25°C and 70°C to characterize the effect of temperature. It is readily apparent from the figure that the interfacial impedance (related to the width of the curves) drops noticeably at the point of short-circuiting. Note that it is not possible to fit the impedance spectra by an equivalent circuit model because the surface is no longer uniform once the dendrite starts to form. **Figure 4.6a** compares the impedances of the three stages for 30mol% LiF+LiTFSI/PC electrolyte at 25°C and 70°C. Both the bulk (related to the lower intercept of the spectra) and interfacial impedances decrease sharply with only a 45°C temperature increase.

Figure 4.6b displays the impedance spectra for 1mol%, 3mol%, 5mol%, and 10mol% and 30mol% LiF + LiTFSI/PC electrolytes individually. At 25°C, the bulk and interfacial impedances is seen to change slightly after the onset of polarization, but as already noted drops substantially after the cell short-circuits. Electrolytes with higher LiF mole fraction have comparable bulk, but measurably lower interfacial impedances at all stages. It suggests that LiF has the ability to enhance the lithium ion diffusion primarily at the electrode/electrolyte interface. When operating at 70°C, spectra at all three stages exhibit similar bulk and interfacial impedances between 5 and 15 $\Omega \text{ cm}^2$

with negligible dependence of electrolyte composition. It indicates that the impedance is so small that the magnitude is almost similar to that of the short-circuited cell, which consistent with expectations based on the JDFT calculation, leads to much larger enhancements in cell lifetime. In general, the lowered impedance created by LiF leads to the extension of the cell lifetime, and the sharply reduced impedance by temperature explains the tremendous enhancement of cell lifetime at high temperature because lithium ions can easily migrate and plate on the negative electrode.

To further evaluate the suitability of LiF-added electrolytes in LMBs, more commonly used electrolytes comprised 1:1 (v:v) EC:DEC with and without LiF were investigated at room temperature using Li/Li₄Ti₅O₁₂ (LTO) half-cell. LTO is a no-strain material commercially utilized in electric vehicles and is capable of cycling at both low and high rates for consecutive charge and discharges³². In practice, even commercial LTO spinel powder yields a well-defined discharge plateau at 1.55V in carbonate electrolytes, and a discharge capacity close to the theoretical capacities (175 mAh g⁻¹) when accommodating lithium and negligible round-trip IR losses³³. To characterize the effect of LiF on performance of Li/LTO half-cell, thin LTO (15 microns of active material) and thick LTO (64 microns of the active material) were studied in an accelerated procedure employing a very high current density of 2.0 mA cm⁻² (1C). For cells based on the thick LTO electrode, an activation process at 0.1C for 10 cycles was employed prior to the higher current density experiments. A two-hour charge/discharge protocol allows enough lithium to be transported during each cycle to create dendrites that are large enough to short-circuit the cells based on the thick

electrode, whereas those based on the more common thin electrodes do not allow sufficient lithium transport to create a dendrite that spans the inter-electrode space.

Figure 4.8(a1-b1) show the voltage profiles obtained using the thin electrodes with and without LiF additive. Unlike the symmetric cells where the current is fixed and the voltage left unconstrained, the voltage range and current are fixed in these experiments. The onset of failure as a result of formation of dendrite shorts or regions of disconnected lithium is then expected to show up in the lifetime or capacity of the cells. It is apparent from **Figure 4.8(a1)** that addition of LiF to the electrolytes increases the discharge capacity, but otherwise does not alter the cycling performance of the cells. The blow-up charge and discharge curves in **Figures 4.8(a2)** and **Figures 4.8(b2)** show that the round-trip IR losses in both cells are quite minimal, as expected for LTO. The corresponding results for the thick electrodes are reported in **Figures 4.8c,d**. It is apparent from the voltage profiles in **Figure 4.8(c1)** and **Figure 4.8(d1)** that whereas little change in the Li-F containing electrolytes not only increases the accessible discharge capacity, but substantially improves the cycling stability of the cells. This latter feature is consistent with what one might expect from the earlier observations based on symmetric Li-Li cells which show that Li-F improves the stability of electrodeposition.

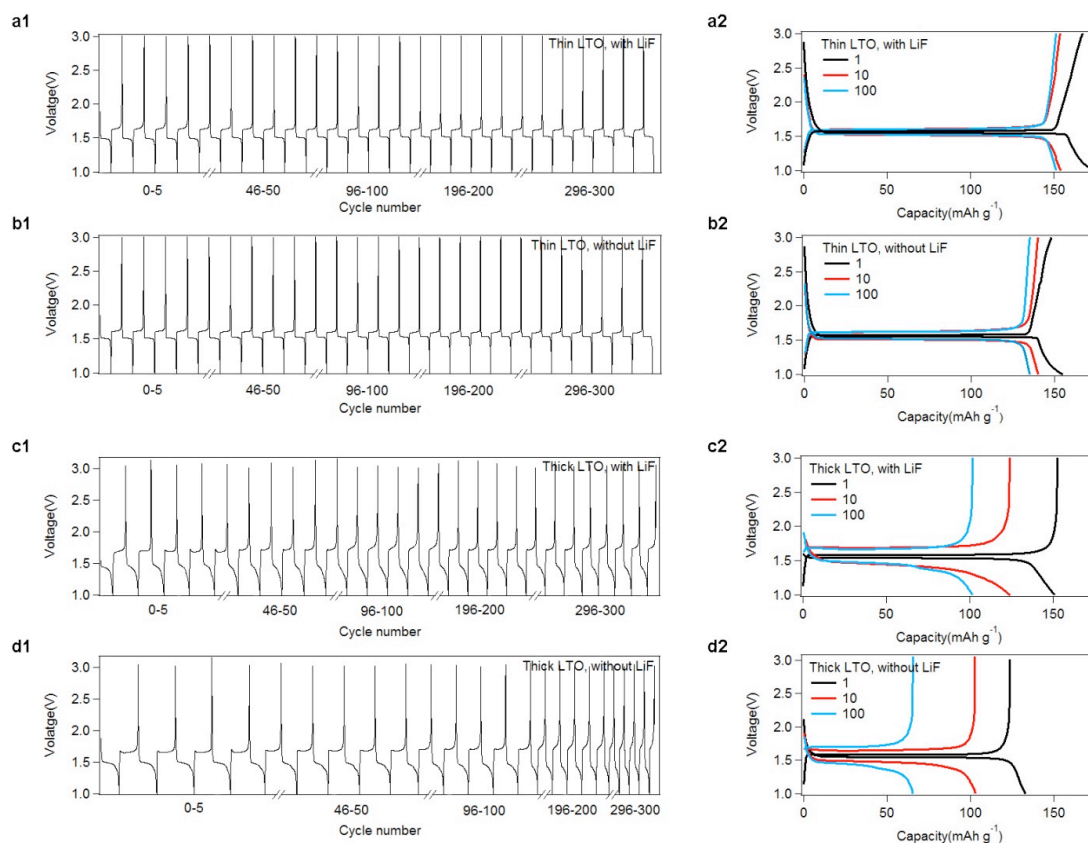


Figure 4.8. Charge-discharge characteristics of Li/Li₄Ti₅O₁₂ (Li/LTO) with 30mol% LiF+LiTFSI/EC:DEC and LiTFSI/EC:DEC electrolytes at room temperature. Thin LTO electrode: Voltage vs. time profile for the first 5 cycles, 46-50 cycles, 96-100 cycles, 196-200 cycles and 296-300 cycles at 1C rate (0.18 mA cm⁻²) with LiF (**a1**) and without LiF (**b1**). About 0.88μm lithium (charge passed=0.65C cm⁻², about 2.2μm LTO is reacted) is transported from one electrode to the other in each half cycle. Initial, 10th, 100th charge-discharge profiles with LiF (**a2**) and without LiF (**b2**). Thick LTO electrode: Voltage vs. time profile for the first 5 cycles, 46-50 cycles, 96-100 cycles, 196-200 cycles and 296-300 cycles at 1C rate (2 mA cm⁻²) with LiF (**c1**) and without LiF (**d1**). About 9.8μm lithium (charge passed=7.2C cm⁻², about 24.5μm LTO is reacted) is transported from one electrode to the other in each half cycle. Initial, 10th, 100th charge-discharge profiles with LiF (**c2**) and without LiF (**d2**).

In summary, motivated by recent Joint Density Functional Theoretical calculations, which show that the presence of LiF at an electrolyte/lithium metal interface should yield large improvements in stability of Li electrodeposition, we studied physical and electrochemical properties of electrolytes containing lithium halides. Consistent with the theoretical predictions, we report for the first time that simple addition of halogenated lithium salts to a conventional low-mechanical-modulus liquid electrolyte such as PC and EC:DEC, leads to dramatic improvements in lifetime of lithium batteries utilizing metallic lithium as anode. In plate-strip symmetric cell studies, we find that Li-Li symmetric cells employing the Li halide salt reinforced electrolytes and cycled under similar conditions as reported for solid polymer and ceramic electrolytes, except at room temperature, exhibit no evidence of short circuiting. In more aggressive polarization studies, we find that infusing the electrolytes in the pores of a nanoporous ceramic yield lithium metal electrodes that exhibit much larger lifetimes than any previously reported room-temperature battery. Our findings appear significant for at least three reasons. First, they demonstrate that the popular assumption inspired by intuition and supported by continuum modeling, that a high mechanical modulus is a requirement for an electrolyte that can stop growth and proliferation of lithium dendrites is perhaps incorrect. Second, electrolyte reinforcement by lithium halide salts provides an inexpensive easy to use strategy for stabilizing electrodeposition of lithium metal that will enable technological and scientific advances. And, third, the finding underscores the benefits of density functional and other atomistic simulation approaches for guiding materials design for batteries.

Reference

1. Armand, M.; Tarascon, J. M., Building better batteries. *Nature* **2008**, *451* (7179), 652-657.
2. Yang, P.; Tarascon, J.-M., Towards systems materials engineering. *Nature materials* **2012**, *11* (7), 560-563.
3. Xu, K., Nonaqueous liquid electrolytes for lithium-based rechargeable batteries. *Chem. Rev.* **2004**, *104* (10), 4303-4418.
4. Kang, B.; Ceder, G., Battery materials for ultrafast charging and discharging. *Nature* **2009**, *458* (7235), 190-193.
5. Morcrette, M.; Rozier, P.; Dupont, L.; Mugnier, E.; Sannier, L.; Galy, J.; Tarascon, J.-M., A reversible copper extrusion–insertion electrode for rechargeable Li batteries. *Nature materials* **2003**, *2* (11), 755-761.
6. Aricò, A. S.; Bruce, P.; Scrosati, B.; Tarascon, J.-M.; Van Schalkwijk, W., Nanostructured materials for advanced energy conversion and storage devices. *Nature materials* **2005**, *4* (5), 366-377.
7. Whittingham, M. S., Electrical energy storage and intercalation chemistry. *Science* **1976**, *192* (4244), 1126-1127.
8. Bruce, P. G.; Freunberger, S. A.; Hardwick, L. J.; Tarascon, J.-M., Li-O₂ and Li-S batteries with high energy storage. *Nature materials* **2012**, *11* (1), 19.

9. Jayaprakash, N.; Shen, J.; Moganty, S. S.; Corona, A.; Archer, L. A., Porous hollow carbon@ sulfur composites for high-power lithium–sulfur batteries. *Angew. Chem.* **2011**, *123* (26), 6026-6030.
10. Tarascon, J. M.; Armand, M., Issues and challenges facing rechargeable lithium batteries. *Nature* **2001**, *414* (6861), 359-367.
11. Bhattacharyya, R.; Key, B.; Chen, H.; Best, A. S.; Hollenkamp, A. F.; Grey, C. P., In situ NMR observation of the formation of metallic lithium microstructures in lithium batteries. *Nature materials* **2010**, *9* (6), 504-510.
12. Lu, Y.; Das, S. K.; Moganty, S. S.; Archer, L. A., Ionic Liquid-Nanoparticle Hybrid Electrolytes and their Application in Secondary Lithium-Metal Batteries. *Adv. Mater.* **2012**, *24* (32), 4430-4435.
13. Lu, Y.; Korf, K.; Kambe, Y.; Tu, Z.; Archer, L. A., Ionic-Liquid–Nanoparticle Hybrid Electrolytes: Applications in Lithium Metal Batteries. *Angew. Chem.* **2014**, *126* (2), 498-502.
14. Tu, Z.; Kambe, Y.; Lu, Y.; Archer, L. A., Nanoporous Polymer-Ceramic Composite Electrolytes for Lithium Metal Batteries. *Advanced Energy Materials* **2014**, *4* (2), 1300654.
15. Schaefer, J. L.; Yanga, D. A.; Archer, L. A., High Lithium Transference Number Electrolytes via Creation of 3-Dimensional, Charged, Nanoporous Networks from Dense Functionalized Nanoparticle Composites. *Chem. Mater.* **2013**, *25* (6), 834-839.

16. Moganty, S. S.; Srivastava, S.; Lu, Y.; Schaefer, J. L.; Rizvi, S. A.; Archer, L. A., Ionic liquid-tethered nanoparticle suspensions: a novel class of ionogels. *Chem. Mater.* **2012**, *24* (7), 1386-1392.
17. Moganty, S. S.; Jayaprakash, N.; Nugent, J. L.; Shen, J.; Archer, L. A., Ionic-Liquid-Tethered Nanoparticles: Hybrid Electrolytes. *Angew. Chem.* **2010**, *122* (48), 9344-9347.
18. Stone, G.; Mullin, S.; Teran, A.; Hallinan, D.; Minor, A.; Hexemer, A.; Balsara, N., Resolution of the modulus versus adhesion dilemma in solid polymer electrolytes for rechargeable lithium metal batteries. *J. Electrochem. Soc.* **2012**, *159* (3), A222-A227.
19. Monroe, C.; Newman, J., The impact of elastic deformation on deposition kinetics at lithium/polymer interfaces. *J. Electrochem. Soc.* **2005**, *152* (2), A396-A404.
20. Nugent, J. L.; Moganty, S. S.; Archer, L. A., Nanoscale organic hybrid electrolytes. *Adv. Mater.* **2010**, *22* (33), 3677-3680.
21. Croce, F.; Appetecchi, G.; Persi, L.; Scrosati, B., Nanocomposite polymer electrolytes for lithium batteries. *Nature* **1998**, *394* (6692), 456-458.
22. Ding, F.; Xu, W.; Graff, G. L.; Zhang, J.; Sushko, M. L.; Chen, X. L.; Shao, Y. Y.; Engelhard, M. H.; Nie, Z. M.; Xiao, J.; Liu, X. J.; Sushko, P. V.; Liu, J.; Zhang, J. G., Dendrite-Free Lithium Deposition via Self-Healing Electrostatic Shield Mechanism. *J. Am. Chem. Soc.* **2013**, *135* (11), 4450-4456.
23. Chazalviel, J. N., Electrochemical Aspects of the Generation of Ramified Metallic Electrodeposits. *Phys. Rev. A* **1990**, *42* (12), 7355-7367.

24. Rosso, M.; Gobron, T.; Brissot, C.; Chazalviel, J.-N.; Lascaud, S., Onset of dendritic growth in lithium/polymer cells. *J. Power Sources* **2001**, *97*, 804-806.
25. Brissot, C.; Rosso, M.; Chazalviel, J. N.; Lascaud, S., Dendritic growth mechanisms in lithium/polymer cells. *J. Power Sources* **1999**, *81*, 925-929.
26. De Jonghe, L. C.; Feldman, L.; Millett, P., Some geometrical aspects of breakdown of sodium beta alumina. *Mater. Res. Bull.* **1979**, *14* (5), 589-595.
27. Ansell, R., The chemical and electrochemical stability of beta-alumina. *Journal of materials science* **1986**, *21* (2), 365-379.
28. Aurbach, D.; Lu, Z.; Schechter, A.; Gofer, Y.; Gizbar, H.; Turgeman, R.; Cohen, Y.; Moshkovich, M.; Levi, E., Prototype systems for rechargeable magnesium batteries. *Nature* **2000**, *407* (6805), 724-727.
29. Ling, C.; Banerjee, D.; Matsui, M., Study of the electrochemical deposition of Mg in the atomic level: Why it prefers the non-dendritic morphology. *Electrochim. Acta* **2012**, *76*, 270-274.
30. Ozhabes, Y.; Gunceler, D.; Arias, T., Stability and surface diffusion at lithium-electrolyte interphases with connections to dendrite suppression. *arXiv preprint arXiv:1504.05799* **2015**.
31. Lu, Y.; Moganty, S. S.; Schaefer, J. L.; Archer, L. A., Ionic liquid-nanoparticle hybrid electrolytes. *J. Mater. Chem.* **2012**, *22* (9), 4066-4072.
32. Brousse, T.; Fragnaud, P.; Marchand, R.; Schleich, D.; Bohnke, O.; West, K., All oxide solid-state lithium-ion cells. *J. Power Sources* **1997**, *68* (2), 412-415.

33. Nakahara, K.; Nakajima, R.; Matsushima, T.; Majima, H., Preparation of particulate $\text{Li}_4\text{Ti}_5\text{O}_{12}$ having excellent characteristics as an electrode active material for power storage cells. *J. Power Sources* **2003**, *117* (1), 131-136.

CHAPTER 5

DESIGNING ARTIFICIAL SOLID-ELECTROLYTE INTERPHASES FOR SINGLE-ION AND HIGH-EFFICIENCY TRANSPORT IN BATTERIES

Reproduced from Joule (2017)

5.1 Abstract

Substrates able to rectify transport of ions based on their charge and/or size are ubiquitous in biological systems. Electrolytes and interphases that selectively transport electrochemically active ions are likewise of broad interest in all energy storage technologies. In lithium-ion cells, electrolytes that offer single- or near-single-ion conductivity are desired for their ability to reduce internal energy losses caused by ion polarization. In emergent high-energy cells based on metallic lithium or sodium metal anodes, such electrolytes can maintain high ionic conductivity at the anode at all current densities and for this reason are able to stabilize metal deposition at the anode by fundamental mechanisms. Here we report that a thin, 20-300 nanometer-thick, single-ion conducting membrane deposited at a battery anode produces bulk, liquid electrolytes with the highest combination of cation transference number, room-temperature ionic conductivity, and electrochemical stability reported. By means of direct visualization of Li deposition in an optical cell, we find that these single-ion membranes also markedly reduce the propensity of Li to form rough, dendritic deposits in liquid electrolytes. Galvanostatic electrochemical measurements further show that the materials enable long (3mAh) recharge of symmetric lithium/lithium and full lithium/LiNi_{0.8}Co_{0.15}Al_{0.05}O₂ (NCA) cells with relatively high cathode mass loadings (3 mAh cm⁻² or 19.9 mg cm⁻²) and at current densities as high as 3 mA cm⁻².

5.2 Introduction

The high efficiency (> 90%) with which chemical energy is reversibly converted to electrical energy in closed electrochemical systems such as batteries is a principal driver of interest in rechargeable lithium battery technology. Although progress has arguably been slow in developing commercial versions of these batteries that significantly outperform – in terms of energy stored per unit mass or volume – the first lithium-ion batteries (LIBs) introduced in the 1990s, significant strides have been made in improving other performance metrics, including cost, efficiency, lifetime, and battery system power density¹⁻³. As a result LIBs are finding applications in a growing list of technologies, including electrified transportation, grid storage, autonomous aircraft (drones), and robotics⁴⁻⁵. It is understood that the most productive paths forward in designing batteries that offer the high specific energies and power required by these new applications will include development of electrolytes compatible with higher voltage intercalating cathodes. Stable anodes that store more charge per unit mass or volume than the currently used LiC_6 material provide a second pathway. Cathodes based on conversion chemistries (e.g. S_8 , O_2 , CO_2/O_2) also offer potentially large gains in storage capacity. A persistent, fundamental challenge is preserving the high efficiency characteristic of LIB technology in any of these new battery designs. Efficient electrochemical energy storage in batteries requires facile transport of ions in bulk, typically liquid electrolytes and careful management of reactivity and ion transport at explicit interfaces between electrodes and electrolytes. During normal operation, uncontrolled chemical and/or electrochemical reactions of electrolyte components near electrolyte/electrode interfaces produce 10-50 nm thick, ion-conducting membranes composed of organic/inorganic lithium compounds, loosely

termed the solid-electrolyte interphase (SEI)⁶. Under favorable circumstances the SEI passivates the electrode without compromising interfacial ion transport. In lithium-ion batteries, for example, typical liquid electrolytes including carbonates, esters, ethers, etc. with dopant salts such as LiPF₆ or LiTFSI have LUMO levels lower than that of a conventional lithiated graphite anode, which in principle should lead to continuous reductive decomposition of the electrolyte⁷⁻⁸. The fact that these reactions result in minimal loss of efficiency in today's state-of-the art LIBs is believed to be a consequence of transport barriers provided by a well-formed and mechanically stable SEI.

Here we report on *artificial* SEIs created using well-formed and mechanically robust ionomers anchored to the surface of a lithium metal anode and investigate their structure-property-performance characteristics as a function of membrane thickness in the range from 10 μ m to 20 nm. Significantly, we find that *single-ion transport* properties of even a few-nanometer-thick SEI may be imparted to an entire bulk liquid electrolyte that wets the interfacial material without compromising overall ionic conductivity. On this basis we show that by means of SEI design alone it is possible to achieve liquid electrolytes with high room-temperature ionic conductivities and extremely low ion polarization. To our knowledge this is the first direct demonstration of the critical role a well-formed SEI may play in regulating overall ion and mass transport in batteries. By means of direct visualization and electrochemical analysis, we further show that nanometer-thick artificial SEI are able to selectively transport cations to the Li-metal electrode and lead to large improvements in the metals ability to deposit smoothly during battery recharge. Finally, it is shown that the *single-ion*

conducting artificial SEI can be easily integrated with other, previously reported electrolyte design concepts⁹⁻¹⁰ to create synergistic methods to suppress metal dendrite proliferation in liquid electrolytes.

The thickness, chemical composition, transport properties, and mechanical features of the SEI are important determinants of long-term battery stability, but little is known fundamentally about structure-property-performance features of these membranes. A well-established and successful practice in the field has been to introduce sacrificial electrolyte additives, such as vinylene carbonate (VC) and more recently fluoroethylene carbonate (FEC), able to preferentially breakdown and undergo polymerization and ion exchange reactions at the anode/electrolyte interface to produce SEIs with desirable chemical composition and physical properties.⁸ In emergent battery chemistries based on un-hosted reactive metal anodes (such as Li and Na), a stable SEI able to accommodate the cyclic volume changes at the anode during charge (addition) and discharge (removal) of metal atoms to the electrode is known to be a requirement for stable long-term cell operation, but relatively little is known about the design rules for such interphases¹¹.

In a typical liquid electrolyte, disassociated lithium salts in aprotic solvents generate mobile cations and anions. Consequently, the fraction of the ionic conductivity that stems from motion of the electrochemically active ion (Li^+) or lithium transference number t_{Li^+} is typically small. It means that one half or more of the work done in driving ion motion in the cell is wasted work. Unstable mobile anions may also migrate to regions of high potential gradient and breakdown prior to the solvent and

other electrolyte components, contributing to an inhomogeneous SEI and increased interfacial resistance. At current densities above the limiting current, theory predicts that an anion depletion zone (or space charge) can be created in energy battery near the electrode surface, which produces large increases in cell resistance.

Consequences for electrolyte polarization are more severe in emergent battery chemistries such as Li-S, Na-S, Li-O₂/CO₂, Na-O₂/CO₂, Zn-O₂, which use un-hosted metals (e.g. Li, Na, Zn)¹²⁻¹⁶, at the anode for five-to ten-fold improvements in anode storage capacity. In such cells, the existence of a space charge in the electrolyte has been shown to drive unstable electro-convective flows inside the battery, which in turn drives unstable deposition and dendrite formation of the metal during battery recharge¹⁷⁻¹⁸. The fact that the benefits of the metal anodes carry over to cells in which the anode is paired with a conventional intercalating cathode to produce rechargeable batteries with 2-3 times higher specific storage on a gravimetric or volumetric basis, underscores the pressing need for fundamental solutions. Recently, a number of approaches, including using single-ion conducting electrolyte¹⁹⁻²¹, high-modulus separators/electrolyte^{10, 22-23}, SEI protective agents²⁴⁻²⁷, non-carbonaceous hosts for lithium²⁸⁻²⁹ have been proposed to overcome these problems for Li-metal cells. The successes and shortcomings of these approaches are discussed in several comprehensive review articles^{11, 30-31}.

5.3 Experimental Section

Ionomer solution (LITHion™ dispersion, ~ 10 wt% in isopropanol) was purchased from Ion Power Inc. and used as received. The ionomer is composed of a nafion-type

perfluorinated polymer backbone with sulfonic side groups (EW~1100) ion-exchanged with lithium ions, as depicted in **Scheme 5.1**. The ionomer solution was thoroughly dried at 100°C under vacuum for 24 hours, followed by re-dispersed in anhydrous propylene carbonate (PC) (Sigma, 99.7%) at 100°C for 2 days until a homogeneous viscous solution was obtained. Thereafter, the ionomer/PC solution was transferred and stored in an argon-filled glovebox prior to its use. Ionomer/PC solutions with various polymer concentrations were prepared by gradual dilution of the original solution. To prepare coatings on Li metal, the ionomer was solvent casted directly on pre-punched lithium foil electrodes (alfa Aesar), and dried in the glovebox antechamber under vacuum at room temperature. After coating there was no obvious change on the lithium surface, but such coating prevents lithium from rapid oxidation in the ambient environment (**Figure 5.5**). The nanoporous Al₂O₃ (Whatman, 20 nm pore size) membranes used in the study were either placed on top of the wet ionomer layer, with small pores facing down to Li surface, after which the assembly was dried as in the preceding method or placed in the same configuration (small pores facing Li electrode) on dry, ionomer coated Li. We observed no difference in performance of cells prepared using either of the two Al₂O₃ membrane arrangements.

The morphology of the ionomer-coated lithium metal electrodes was characterized using a Leo 1550 Keck Field Emission Scanning Electron Microscopy (FESEM) with a Bruker EDX detector and FEI Strata 400 Focused Ion Beam (FIB) fitted with a Quorum PP3010T Cryo-FIB/SEM Preparation System. To avoid reaction of the lithium sample with O₂ and moisture in ambient air during cryo-FIB experiments, the samples were quickly plunged into a nitrogen slush immediately after treatment or

harvesting from lithium cells. The samples were subsequently maintained -165 °C in the cryo-FIB to preserve their structure. All samples investigated remained under liquid nitrogen or in vacuum for the duration of the experiment. ATR-FTIR was used for confirming coating of the thin ionomer on the lithium surface.

Electrochemical measurements were performed on coin cells assembled in argon-filled glovebox (MBraun, Labmaster). Several types of coin cells were designed to measure different properties. Symmetric cells with two protected/unprotected lithium were used for impedance measurements and lithium plating/stripping experiments. Li/polished Cu asymmetric cells were for evaluating Coulombic efficiency of lithium deposition. Celgard 3501 and 1 M LiPF₆ in ethylene carbonate: dimethyl carbonate (EC:DMC) (v:v = 1:1) with 1 v% vinylene carbonate (VC), and 10 v% fluorinated ethylene carbonate (FEC) additives were used as the separator and electrolyte, respectively. Full cell was composed of protected lithium versus lithium nickel cobalt aluminum oxide (NCA) cathodes provided by CAMP facility at Argonne National Labs with 90% active material loading and area capacity of 3 mAh cm⁻². A piece of glass fiber was added in the full cell to absorb more electrolyte (200 μL) for the full cell.

A Novocontrol dielectric spectrometer with temperature controlling module was used to measure the temperature-dependent conductivity from -5 to 100 °C at a frequency range from 10⁷ to 10⁻¹. The DC ionic conductivity was determined from the real conductivity at the high frequency plateau region based on the previously reported method³²⁻³³. A solartron work station with frequency analyzer was used for obtaining impedance spectra at room temperature. Lithium transference number was determined

by combined impedance and polarization experiments using the same Solartron workstation. Briefly, the first impedance spectra were measured followed by application of a small step voltage (20 mV) that is maintained constant until a steady-state current response is achieved. The steady state impedance was measured again immediately after removal of the constant voltage (CV) step. The lithium transference number can be determined from these measurements using the widely used Bruce-Evans formula³⁴: $t_{Li^+} = \frac{I_{ss}(\Delta V - I_0 R_0)}{I_0(\Delta V - I_{ss} R_{ss})}$, in which I_0 and I_{ss} represent the initial and the steady state current, and R_0 and R_{ss} represent the interfacial resistance before and after the CV step. **Figure 5.1** report typical current response observed for the bare Li as well as for typical ionomer coated Li electrodes in two different electrolytes. It is seen that whereas in the bare Li case the steady-state current falls substantially below the instantaneous value after imposition of the voltage step, the fall off is much smaller for the coated Li electrodes in either electrolyte. It indicates that the ionomer coatings exhibit remarkable ability to limit cell polarization. t_{Li^+} values extracted from the measurements are provided in **Table 5.3** and **5.4**.

X-ray photoelectron spectroscopy SSX-100 was performed on protected lithium surface before and after the cycling. Battery testing was performed on Neware battery testing systems. In situ observation cell was home-made and as illustrated in **Figure 1B**. Two lithium cylinder rods were used as the electrodes connected with tungsten transmission lines to the battery test channels. The snapshots were taken using an Olympus camera and microscope, and adjusted to the size of 1 mm vertically. The ionomer coating was carried out on the lithium rod the same manner as the lithium foil.

To fix a nanoporous Al_2O_3 on the lithium electrode, a solution (30 mg mL^{-1}) of SBS rubber in THF was used as a binder.

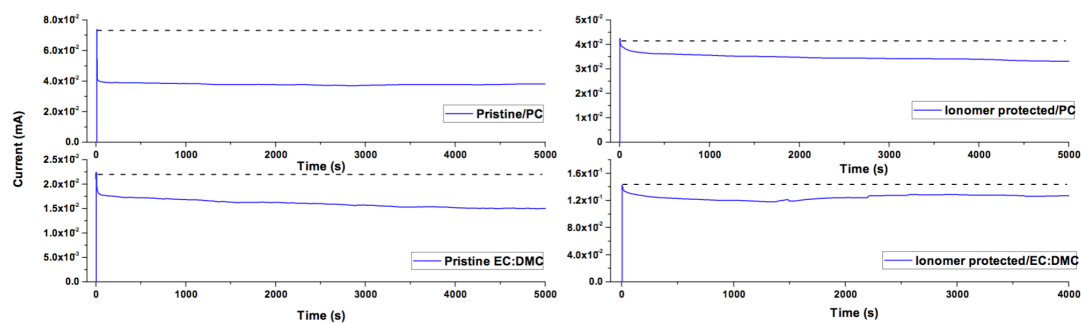


Figure 5.1. Current response to small step change in voltage in symmetric lithium cells. Top row: pristine Li in LiPF_6/PC electrolyte (left) and ionomer protected Li in the same electrolyte (right). Bottom row: pristine Li in $\text{LiPF}_6/\text{EC:DMC}$ electrolyte (left) and ionomer protected Li in the same electrolyte (right).

5.4 Results and discussion

Our specific approach to SEI design focuses on materials that take advantage of synergies identified by recent results from linear stability analysis of electrodeposition of Li.^{30, 35} In so-called structured electrolytes in which a fraction of anions are anchored to a rigid support, this analysis reveals that the growth rate of dendritic nucleates is determined by two dimensionless parameters, $P_1 = JFL/v\sigma t_{Li}G$ and $P_2 = JFL^2/v\sigma t_{Li}S$. Here J is the current density, v is the molar volume of lithium metal, F is the Faraday constant, and L is the distance between the two electrodes. Because the analysis applies to the earliest stages of dendrite growth, P_1 and P_2 are also functions of the electrolyte and SEI properties, including the ionic conductivity σ , the lithium transference number, t_{Li+} , surface tension at the electrode/electrolyte interphase, S , and mechanical modulus, G of the electrolyte and SEI.

Design and Physical Analysis of Ionomer SEIs on Li

Figure 5.1A reports the configuration of the lithium metal anodes used in the study. To create an artificial SEI on Li, a thin conformal layer of a perfluorinated ionomer was formed on the surface by a simple solvent-casting process under an Ar atmosphere (see supporting information). The thickness of the coating layer is easily controlled by repeated application of the casting process or by increasing the concentration of ionomer in the carrier solvent. Removal of the solvent was observed to produce tightly adhered ionomer films on Li that cannot be mechanically peeled off without damaging the Li metal. In order to study the effect of the ionomer on stabilizing lithium deposition, a visualization cell (**Figure 5.1B**) that allows direct

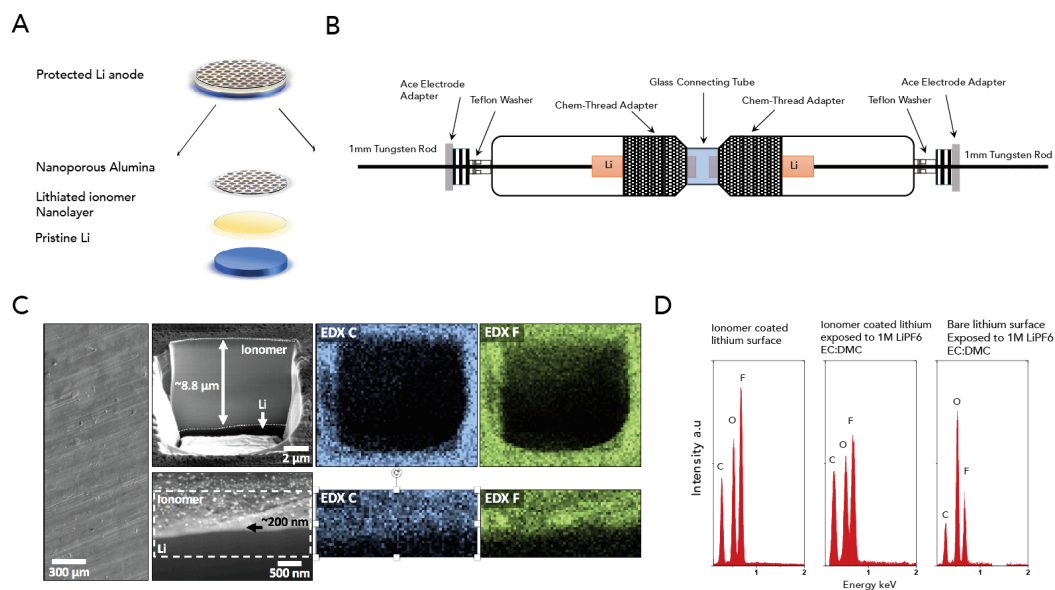
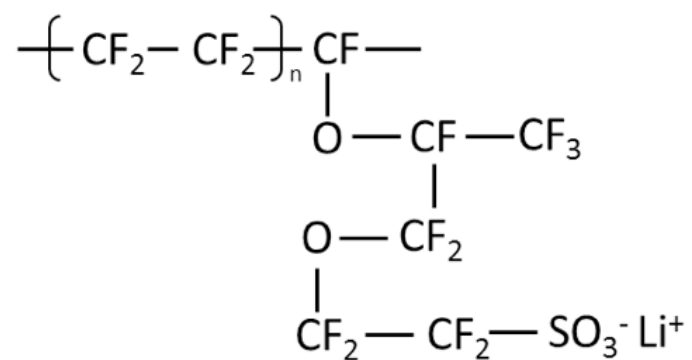


Figure 5.2. Illustration and configuration of the ionomer protected lithium anode. A) Schematic illustration of the protected lithium configuration, see also **Scheme 5.1** and **Figure 5.3**. B) Scheme of the customized visualization setup to observe lithium electrodeposition in situ. C) Cryo-FIB-SEM images of ionomer coating on lithium; the first column is an overview image showing the surface morphology of a ~ 200 nm coating of ionomer. The second column shows cross sections through ~ 9 μm thick (top) and ~ 200 nm thick (bottom) ionomer coatings. Corresponding EDX maps of carbon and fluorine are shown to the right. D) EDX spectra of ionomer coated lithium, ionomer coated lithium exposed to 1 M LiPF_6 EC:DMC overnight, and bare lithium exposed to 1M LiPF_6 EC:DMC overnight.



Scheme 5.1. The structure of the ionomer used as the lithium surface protector as in **Figure 5.1.**

visualization of Li deposition processes in an optical microscope outfitted with extra-long working distance objectives was developed for the study. Briefly, two tungsten rods are used as the circuit connection to lithium metal electrodes, which are sealed in a two-stage non-tapered, high-quality optical glass tube. As discussed later, visualization measurements using the device demonstrate that an ionomeric SEI with the proposed design has an obvious stabilizing effect on Li deposition.

The success of the SEI transfer procedure is readily confirmed using cryo-focused ion beam-scanning electron microscopy (cryo-FIB-SEM), as shown in **Figure 5.1C**. Cryogenic temperatures are necessary to ensure well-behaved lithium milling, as lithium reacts with the gallium ions at room temperature. A homogeneous surface coating can be visually examined from the top-view and its thickness and depth-dependent elemental composition determined by imaging and energy dispersive x-ray (EDX) mapping of cross sections through the coating produced by FIB milling. Our cryo-FIB measurements show that coatings with tunable thicknesses in the range of sub-100 nm up to nearly 10 μm are achieved. FTIR spectra provide additional information about the ionomer coatings, as shown in **Figure 5.3**. Compared with pristine lithium, pronounced broad peaks appear at 1150 cm^{-1} and 1240 cm^{-1} on ionomer coated Li, which can be assigned to the symmetric and asymmetric C-F bond stretching, respectively, a signature of the perfluorinated ionomer backbone³⁶. These features remain even after the ionomer coated lithium being exposed to the electrolyte. **Figure 5.1D** compares EDX spectra of a lithium substrate before and after overnight exposure to 1M LiPF_6 EC:DMC liquid electrolyte. Both spectra exhibit a large fluorine to carbon ratio, compared with the pristine lithium after contacting the

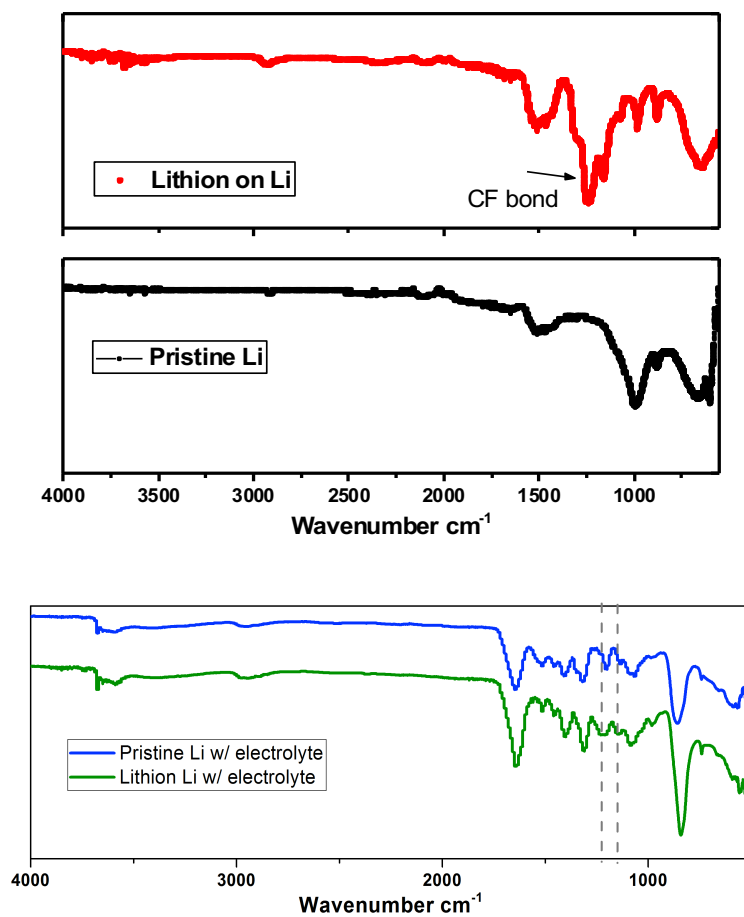


Figure 5.3. FTIR spectra of the ionomer (Lithion) protected Li and the pristine Li before (top) and after (bottom) electrolyte exposal. The dashed lines show the peak position for symmetric and asymmetric carbon-fluorine bond.

electrolyte. The results mean that the ionomer coating on Li is stable in the electrolyte solvent and shows that an ionomer-based SEI created on Li is compatible with the most commonly used carbonate based liquid electrolytes.

A general concern regarding the protection of any anode with an artificial SEI is whether the coating material, usually composed of a moderately ionic-conductive polymer or ceramic, could achieve comparable levels of interfacial ion transport in a spontaneously formed thin SEI film. **Figure 5.4** reports on the ion transport properties of the ionomer SEI on Li in the context of a symmetric lithium battery. The temperature-dependent DC ionic conductivity, as shown in **figure 5.4A**, exhibits a liquid-like, high ionic conductivity within the range of normal battery operation temperatures, and is described well by classic Vogel-Fulcher-Tammann equation for liquid electrolytes. The fact that the overall ionic conductivity of the electrolyte is observed to increase as the ionomer coating thickness is reduced is as expected, but also testifies to the already significant effect the thickness and properties of the SEI have on ion transport in an electrolyte. It is observed further that at coating thickness below 200 nm, the conductivity exceeds $1 \times 10^{-3} \text{ S cm}^{-1}$ at room temperature, comparable to that of a typical liquid electrolyte. Even with the thickest coating studied, the room-temperature conductivity is still high (approximately $5 \times 10^{-4} \text{ S cm}^{-1}$), indicating that an ionomeric SEI provides a promising design for preserving fast interfacial ion transport while other features of a desirable SEI are manipulated. Significantly, it is also seen that when the coatings are co-deposited with a layer of nanoporous Al_2O_3 , shown in earlier work to prohibit dendritic deposition of Li, moderately higher ionic conductivity is observed, simultaneously confirming the

compatibility of the coatings with other electrolyte design concepts and confirming that the coatings do not hinder the high ion mobility within the nanochannels reported in our previous work³⁷.

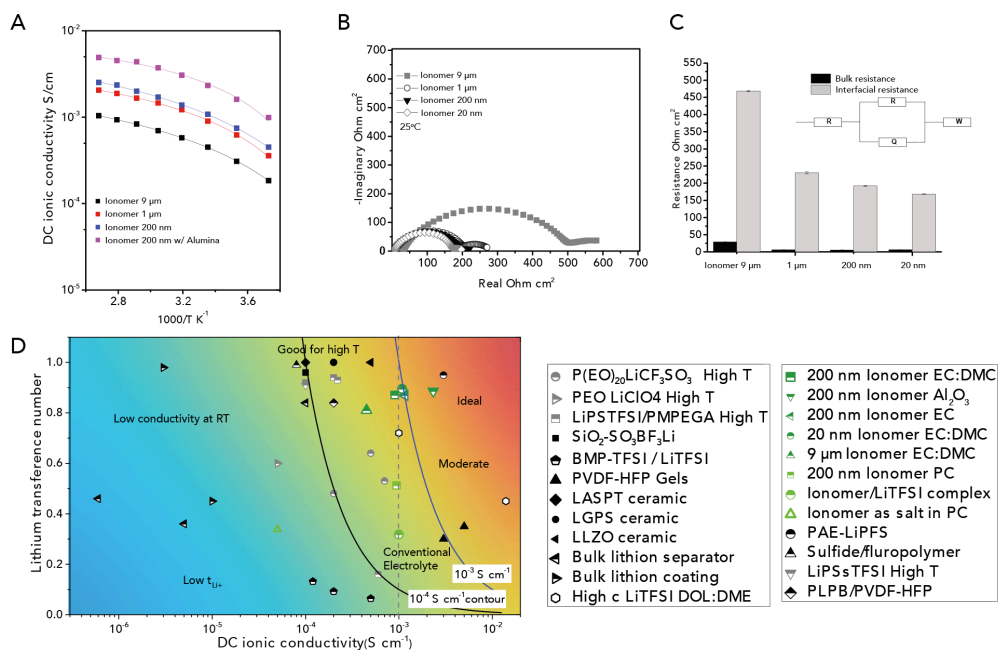


Figure 5.4. Electrochemical property of the ionomer protected lithium anode. A) Temperature-dependent conductivity of symmetric cells with lithium electrodes protected by ionomer coating with different thickness. B) Impedance spectra of symmetric cells with lithium electrodes protected by ionomer coating with different thickness at 25°C, see also **Table 5.1** and S2. C) Fitted bulk and interfacial resistance using the equivalent circuit model (inset). D) A summary figure of the relation between ionic conductivity and lithium transference number of this work and previous works. Gray symbols represent conductivity measured above room temperature. Solid and open symbols represent solid state electrolyte and liquid electrolyte, respectively. Half-filled symbols represent the composite/hybrid of both solid and liquid electrolytes. Conductivity contour lines stand for the value of conductivity contributed

from lithium ions only. Detailed information is included in the supporting information.

See also **Table 5.3** and 5.4.

Table 5.1. Bulk and interfacial resistance of ionomer protected lithium symmetric cells with different coating thickness as reported in **figure 5.4B**.

Thickness of ionomer	Bulk resistance Ohm cm ⁻²	Standard deviation	Interfacial resistance Ohm cm ⁻²	Standard deviation
9 μm	23.11	0.15495	369.6	1.62772
1 μm	4.759	0.24661	181.9	2.73396
200 nm	4.133	0.08006	151.6	1.24448
20 nm	4.99	0.05409	132.8	0.75125

Table 5.2. Resistances fitted from the R(RQ)(RQ)(RQ)W model for **figure 5.4B**.

Unit: Ohm cm ⁻²	9 μm	1 μm	200 nm	20 nm
Liquid electrolyte	23.77	3.442	5.172	4.153
Ionomer liquid interphase	281.4	141.2	144.8	120.9
Li Ionomer interphase	82.9	42.33	20.17	22.98
Ionomer bulk	107.8	17.84	small	small

Table 5.3. Summary of ionic conductivity and lithium transference number of systems plotted in **figure 5.4D**.

	Ionic conductivity S cm⁻¹	t_{Li+}	Reference
P(EO)₂₀LiCF₃SO₃	7e-4 (above RT)	0.48	– 38
PEO composite polymer electrolyte		0.64	
PEO LiClO₄ composite	5e-5 (above RT)	0.6	39
LiPSTFSI/PMPEGA	1-2e-4 (above RT)	0.93	20, 40
lithium poly[(4-styrenesulfonyl) (trifluoromethanesulfonyl)imide-co-methoxy-polyethylene glycol acrylate]			
SiO₂-SO₃BF₃Li	1e-4	0.96	41
Silica nanoparticles functionalized with fixed anion associated with Li			
BMP-TFSI / LiTFSI	1-5e-4	0.064	– 42
N-butyl-N-methyl-pyrrolidinium bis(trifluoromethanesulfonyl)imide & LiTFSI		0.132	
PVDF-HFP Gel electrolyte	0.5-1e-3	0.3-0.5	43-44
LASPT (Li₂Al₂SiP₂TiO₁₃) ceramic	1-4e-4	1	45-46
LGPS (Li₁₀GeP₂S₁₂) ceramic	2e-4	1	
LLZO (Li₇La₃Zr₂O₁₂) ceramic	5e-4	1	
Bulk lithion separator	3e-6	0.98	47
Bulk lithion coating	1e-5	0.45	
Lithiated NafionTM			
High c LiTFSI DOL:DME	1.4e-2	0.45	48
	1e-3	0.72	
200 nm Ionomer EC:DMC	9e-4	0.87	This work
200 nm Ionomer Al₂O₃	2e-3	0.88	
200 nm Ionomer EC	1e-3	0.87	
20 nm Ionomer EC:DMC	1e-3	0.88	
9 μm Ionomer EC:DMC	4e-4	0.81	
200 nm Ionomer PC	9e-4	0.51	
Ionomer/LiTFSI complex	1e-3	0.32	
Ionomer as salt in PC	5e-5	0.31	
PAE-LiPFS	3e-3	0.95	49
Poly(arylene ether) complex			
Sulfide/fluoropolymer	8e-5	0.99	50
LiPSsTFSI High T	1e-4	0.91	51
PEO polymer complex			
PLPB/PVDF-HFP	2e-4	0.84	52
lithium pentaerythrite borate complex			

Table 5.4. Parameters measured for calculating the lithium transference number as reported in figure 5.4D.

Name (t_{Li^+})	R_o (Ohm)	I_o (A)	I_{ss} (A)	R_{ss} (Ohm)
9 μ m Ionomer EC:DMC (0.81)	415	4.00E-05	3.20E-05	520
200 nm Ionomer EC:DMC (0.88)	148	1.16E-04	8.63E-05	204
20 nm Ionomer EC:DMC (0.89)	135	1.23E-04	9.49E-05	180
200 nm Ionomer Al ₂ O ₃ (0.88)	199	8.56E-05	7.32E-05	234
Ionomer/LiTFSI complex (0.32)	258	7.30E-05	5.70E-05	300
Ionomer as salt in PC (0.33)	362	3.09E-05	1.63E-05	386
200 nm Ionomer PC (0.51)	395	4.22E-05	3.31E-05	450
200 nm Ionomer EC (0.87)	1078	1.70E-05	1.61E-05	1129
200 nm Ionomer after 10 cycles at 0.5 mA cm ⁻² , 2 hrs/cycle (0.63)	59	2.61E-04	1.01E-04	170
200 nm Ionomer after 100 cycles at 0.5 mA cm ⁻² , 2 hrs/cycle (0.32)	29	4.31E-04	2.20E-04	36

Electrochemical Analysis of Ionomer SEI on Li

More direct knowledge of how an ionomeric SEI influences interfacial ion transport can be deduced from Electrochemical Impedance Spectroscopy (EIS). **Figure 5.4B** and **5.4C** compare the impedance spectra of ionomer coated lithium/lithium symmetric cells with a coating thickness ranging from 20 nm to 9 μm . Spectra were fit to the equivalent circuit model shown, allowing the bulk and interfacial resistance per area to be determined (**Table 5.1**). Consistent with the results reported in **Figure 5.4A**, a moderately high bulk resistance of about 23 ohm cm^{-2} is observed for the thickest coating (9 μm), which is already bulk-like, in comparison to the interelectrode distance ($\sim 25 \mu\text{m}$). The interfacial resistance, however, is seen to decrease drastically with thickness of the ionomer coating. In particular, it is seen that for thicknesses below 200 nm, the interfacial resistance is about 150 ohm cm^{-2} , close to the value of freshly polished lithium foil. More detailed analysis on impedance spectra involve dissecting interphases individually in the fitting model, as reported in **Table 5.2**. The impedance from the ionomer coating mainly arises from the ionomer/liquid interphase and the bulk ionomer resistance, which supports the hypothesis that the ions are selected transport through the interphase. Additionally, the ionomeric coating makes the protected lithium moderately resistant to oxidation in the ambient air environment, evidenced by a slow build-up of interfacial resistance over 3 hours in a cell allowing air flow through the cap and the current collector (see **figure 5.5**). These observations indicate that ions are efficiently transported from the liquid electrolyte to the Li electrode surface.

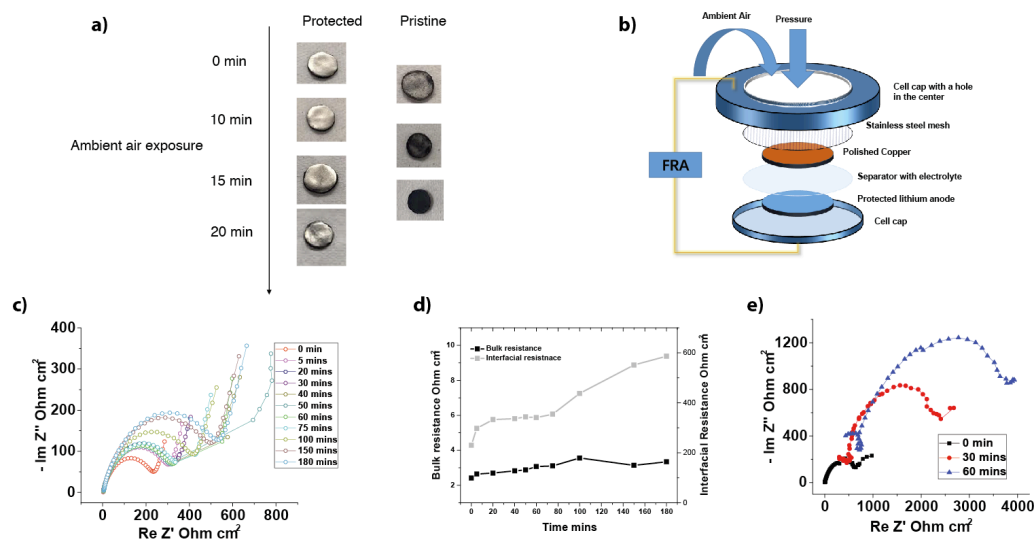


Figure 5.5. a) A visual comparison of protected and unprotected lithium surface in ambient air over 20 mins. b) Illustration of the model cell connected to the frequency analyzer used to quantify impedance involvement of lithium symmetric cell in ambient environment. The cell cap was drilled to allow air flow and a stainless steel mesh was used as the current collector. The model cell was measured at room condition with a relative humidity of 40% c) Impedance spectra of protected lithium cell over time using the model cell described above. d) Fitted bulk and interfacial resistance of protected lithium cell over time. e) Impedance spectra of unprotected lithium cell over time.

An even more interesting finding is the effect an ionomer-based SEI has on more subtle aspects of ion transport and electrolyte polarization. **Figure 5.4D** reports the lithium transference number (t_{Li^+}) measured in Li cells with/without the ionomer SEI. For comparison, the heat-map figure compares the measured values of the t_{Li^+} achieved with those of other materials reported in the literature, in each case benchmarking the results against the ionic conductivity reported for the same materials. In a typical liquid electrolyte with binary lithium salt, the t_{Li^+} usually is between 0.1 – 0.4⁵³. It is apparent from the figure that the Li electrodes coated with an ionomer SEI of arbitrary thickness in the range studied delivers among the highest combination of t_{Li^+} and ionic conductivity of materials reported thus far. More fundamentally interesting is the fact that without the ionomer coating, t_{Li^+} values for the electrolyte used for the measurements - ethylene carbonate (EC): dimethyl carbonate (DMC) with 1 M LiPF₆ salt, are low (~0.3), in agreement with literature reports⁵⁴. It is also apparent that electrolytes fall in several regions as identified by the colors in the figure. Ionic conductivity $> 5 \times 10^{-4}$ S cm⁻¹ are typically required for stable room-temperature battery operation. Conventional liquid electrolytes meet this requirement, but have low t_{Li^+} . As indicated by the materials that fall in the yellow regions, successful efforts aimed at improving the t_{Li^+} for such electrolytes have been reported based on composite salt and polymer/ceramic frameworks. However, these materials are typically limited by their low room-temperature ionic conductivity. Consequently, the fraction of the ion transport contributed by mobile cations is still compromised. The figure also shows contour lines of lithium ion conductivity of 10^{-4} and 10^{-3} S cm⁻¹,

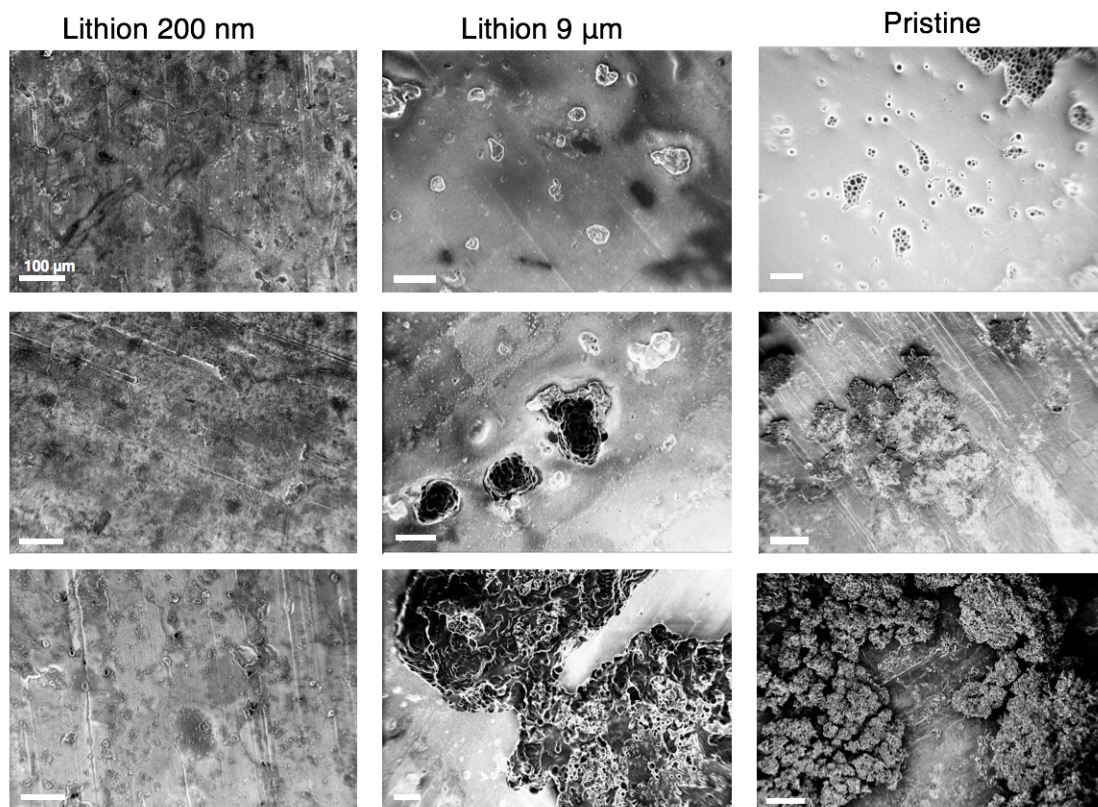


Figure 5.6. Ex situ post-mortem images of 200 nm thick ionomer protected, $\sim 9 \mu\text{m}$ thick ionomer protected, and unprotected lithium electrodes after being deposited 0.1 (first row), 0.5 (second row), and 3 (third row) mAh cm^{-2} of lithium at the current density of 0.5 mA cm^{-2} .

between which most materials targeted for practical battery application must fall. Higher t_{Li^+} can be achieved in lithium ion conducting polymer, ceramics, or other types of composites with immobilized anion species (**Table 5.3**). However, these materials also exhibit moderate or low ambient temperature ionic conductivity and as such are only of practical interest in applications where elevated temperature battery operation is permissible. We've also previously reported on transport properties of bulk perfluorinated lithium conducting ionomer membranes and have shown that these materials offer near single-ion transport and exceptional ability to stabilize Li metal deposition^{19, 55}, yet because of their low ionic conductivity $< 10^{-4} \text{ S cm}^{-1}$, the cells are limited to operating at impractically low current density. In contrast, by incorporating a few-nm thick (e.g. 20 nm) ionomer SEI on the electrode the overall t_{Li^+} for the cell rises to 0.88 and the room ionic conductivity remains high, approximately $1 \times 10^{-3} \text{ S cm}^{-1}$ at room temperature. It is also noted that the ionomer SEI/PC solution does not result in a high t_{Li^+} , likely due to the ability of PC (the ionomer solvent used in the solvent casting step) to dissolve the SEI¹⁹ to produce some unknown fraction of mobile polymer chains in the solvent. This result strengthens the understanding that the immobilized ionomer coating on the lithium/electrolyte interphase does in fact play the dominate role in altering the lithium ion transport behavior. The unusual high ionic conductivity and high lithium transference number imparted by the ionomer SEI is also significant because it defines a straightforward path for breaking the conventional trade-off⁴⁵ between these two important properties in any battery.

Stability of Li electrodeposition on ionomer coated electrodes

In order to further evaluate the effect of the high t_{Li^+} values achieved by means of our ionomer SEI, we investigate the stability of lithium metal deposition on substrates protected by the SEI. Unlike previous studies, where stability was evaluated indirectly from voltage and current measurements during battery cycling, here we employ a customized optical visualization cell (**Figure 5.2B**) that can be mounted on the sampling platform of any optical microscope to monitor the metal interface in real time. Here we first consider changes in the interface structure under unidirectional polarization at constant current density in a symmetric lithium cell constructed from two cylindrical lithium electrodes. **Figure 5.7** shows snapshots of electrodeposition process under a current density of 4 mA cm^{-2} which is above the diffusion limiting current, $J_{OL} = 2zcFD/[L(1-t_{Li^+})] \approx 2.5 \text{ mA cm}^{-2}$, comprised of ions with valency z , concentration c and binary diffusivity D ; L being the inter-electrode distance. It is obvious from the images that the deposition on bare lithium electrode quickly becomes unstable and at a capacity as low as 0.1 mAh cm^{-2} the proliferation of mushroom-like, dendritic structures across the electrode surface occurs. In contrast, electrodes with a 200 nm-thick ionomer SEI are seen to suppress uncontrollable and rough electrodeposition, with compact, smooth electrode surfaces observed at more than ten-times the deposition capacity at which unprotected Li is unstable. A common perspective in the field is that unstable deposition of reactive metals such as Li and Na at moderate current densities is a consequence of the unstable and heterogeneous SEI formed naturally on these metals by spontaneous reaction with electrolyte components¹³. We are able to directly evaluate this hypothesis by depositing thick ($>1 \mu\text{m}$) conformal coatings of the ionomer on Li. Our experiments clearly show that in

the case of a very thick ionomer SEI (9 μm) a Li electrode is as unstable to dendritic deposition as the unmodified Li electrode. It is noted, however, that unlike the pristine Li electrode, the dendrites appear at a few local sites on the electrode, rather than distributed densely over the surface. One possible explanation of this observation is that a thick ionomer coating renders an overall high interfacial resistance so that ions deposit preferentially on defects in the coatings (e.g. at areas where the ionomer coating thickness is low or where poor coverage or pinholes may exist). Our results therefore indicate that an optimal ionomer SEI thickness is essential for achieving uniform electrodeposits at moderate to high current density. We also evaluated the combined effect of an ionomer SEI and nanoporous Al_2O_3 membranes reported in our previous work³⁷ to also stabilize Li deposition. It is seen that smooth deposition is achieved and there is no sign of dendrite penetration through the Al_2O_3 membrane.

Figure 5.7B quantifies the effects observed in **Figure 5.7A** in terms of an effective roughness factor. The roughness here is characterized as ratio between the deposition area deduced using ImageJ image analysis software, to the surface area of a theoretical flat deposit. It is apparent that the surface roughness evolves in two regimes, identified by the green line (flat deposition), and the red line (dendritic growth). In accordance with the visual inspection, the 200 nm-thick ionomer protected symmetric cell with nanoporous Al_2O_3 membranes shows the least roughness, which is close to the trend of flat deposition, underscoring the need to have a strong separator/electrolyte in the lithium cells. Even without the Al_2O_3 membrane, the ionomer coating with 200 nm thickness still retards the proliferation of rough deposits by nearly two times compared with the bare lithium. In both cases, the increase of roughness slows down after

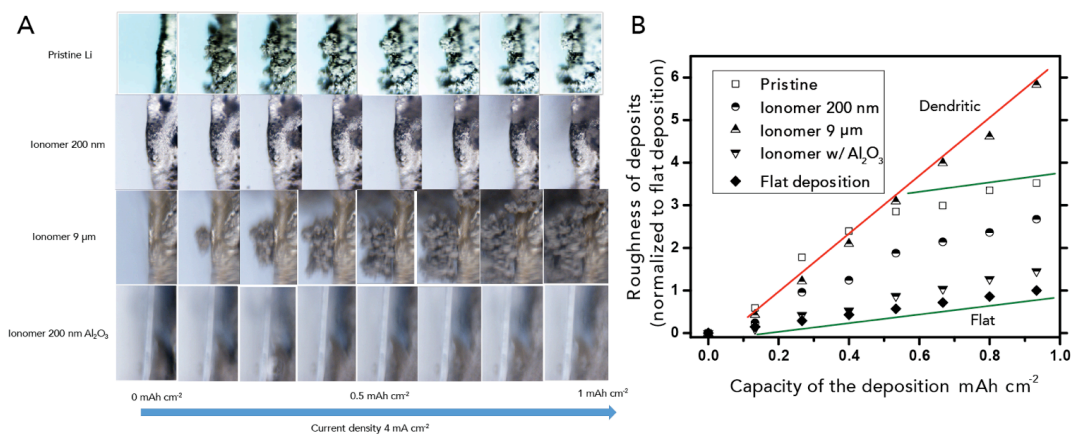


Figure 5.7. Visualization of lithium metal electrodeposition. A) Snapshots of the lithium deposition in a home-made visualization setup using pristine lithium, 200 nm-thick ionomer coated lithium, 9 μm -thick ionomer coated lithium, and 200 nm-thick ionomer coated lithium with nanoporous Al_2O_3 (from top to bottom), during the deposition of 1 mAh cm^{-2} of lithium at a current density of 4 mA cm^{-2} . B) Normalized dimensionless roughness of deposits from above mentioned systems compared with flat deposition. Green line represents the growth of flat deposition and red line represents the growth of dendritic deposition.

depositing 0.3 mAh cm^{-2} of lithium. This may be due to the orphaned lithium ceasing to grow, thus the deposition would happen at other locations which are not captured by the microscope scanning region. However, it is surprising to observe that with $9 \text{ }\mu\text{m}$ -thick ionomer coating, a nearly linear increase of roughness with time is observed, following the red line. This is likely due to the continuous growth of dendrite stems beneath the thick coating, which supports our hypothesis that sparse electrodeposits formed at a few sparse sites as a consequence of conductivity limitation from the thick coating.

Typically, the diffusion-limiting current in a battery is orders of magnitude higher than what can be achieved in our visualization cell due to larger inter-electrode distance in the latter. To understand the effect of an ionomer SEI on battery operation at practical current densities, we performed post-mortem SEM analysis of electrodes harvested from coin cells. As shown in **Figure 5.6**, results from these experiments support the conclusions from the in-situ observation. It is seen for instance that a 200 nm -thick ionomer coating on Li yields a compact, uniform Li deposit morphology even after 3 mAh cm^{-2} of charge. In contrast, electrodes harvested from cells composed of unmodified Li exhibit obviously rougher, mossy dendrites. Consistent with the results from visualization experiments, thicker ionomer SEIs again exhibit larger, rougher electrodeposits sparsely distributed on the electrode surface. Post-mortem FIB-SEM observation (**Figure 5.8**) shows that there are no large lithium deposits above the ionomer layer where FIB cross-sections were taken. FIB-SEM analysis of the electrodes in cells cycled to varying extents (1-100 cycles) indicate that while there is

variation of the ionomer thickness during cycling, the ionomer coatings generally appear to become slightly thicker with cycling. We've tentatively attributed this observation to swelling of the coating as a result of extended exposure to the electrolyte solvent and/or physical deformation induced by repeated lithium plating/stripping cycles.

Figure 5.9 reports galvanostatic cycling experiments in cells that utilize a 200 nm-thick ionomer SEI and a nanoporous Al_2O_3 membrane with 20 nm pore diameter. **Figure 5.9A** compares the Coulombic efficiency (CE) of this lithium/ionomer/ Al_2O_3 /Cu cell with a pristine lithium/Cu cell during a lithium plating/stripping experiment with conventional EC:DMC liquid electrolyte. It is seen that the ionomer has a protective effect on the Li anode against parasitic side reactions with the electrolyte, leading to moderately high ($> 92\%$) and stable Columbic efficiencies in extended cycling. Similar improvements are apparent at a current density of 3 mA cm^{-2} from 3 mAh cm^{-2} plate/strip cycling experiments. The bottom plot in **Figure 5.9A** in fact indicates that an ionomer SEI on Li exhibits moderately high and stable CE profiles. This can be contrasted with cells based on unmodified Li electrodes which show an initial CE of $\sim 86\%$ that deteriorates quickly within 30 cycles, after which the lithium plating/stripping becomes unstable. We note however that while a CE of 92% is an improvement over the pristine Li case, the increase is not large-enough to produce stable cycling of a practical Li cell in which the Li excess is ideally zero. The less than ideal CE values for the ionomer coated Li electrodes are thought to originate from two sources — both having to do with the inherent chemical instability of DMC upon long-term exposure to metallic Li. First, the counter electrode

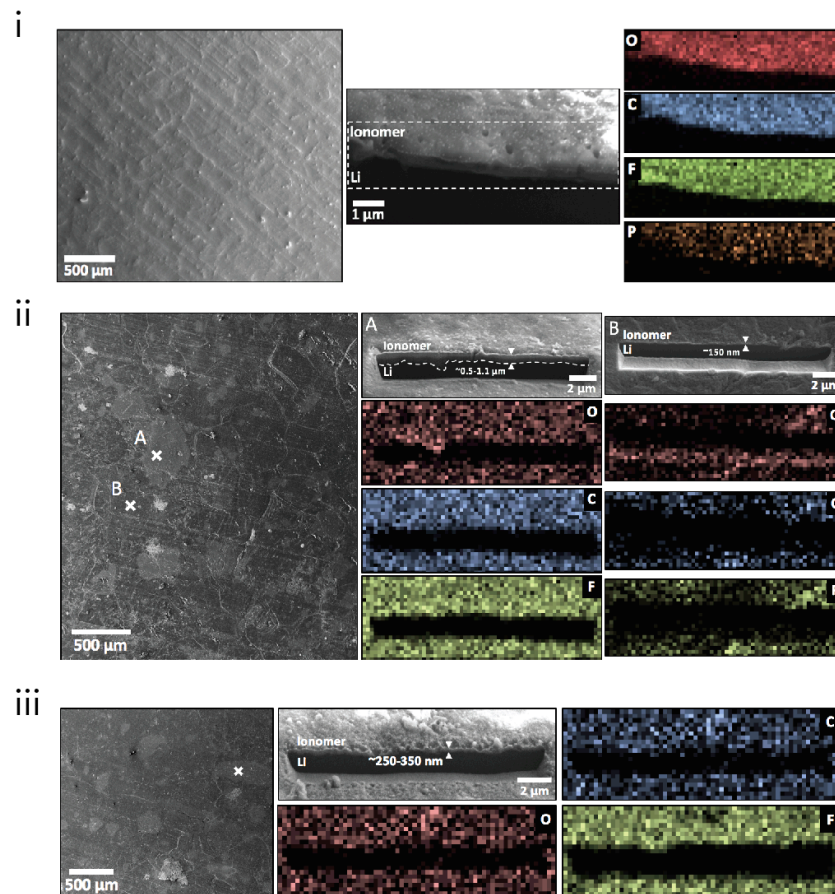


Figure 5.8. Ex situ post-mortem cryo-FIB-SEM overview and cross-sectional images and EDX of 200-300 nm thick ionomer protected lithium after cycling 0.5 mAh cm^{-2} of lithium at the current density of 0.5 mA cm^{-2} . The cross section was obtained by focused ion beam milling perpendicular to the surface of the sample in a predetermined pattern, leaving a vertical surface of the interior of the sample exposed. i) after 1 cycle; ii) after 10 cycles; iii) after 100 cycles.

in the CE experiments is an uncoated copper foil, which means that for at least $\frac{1}{2}$ the duration of a Li plate/stip cycle, freshly deposited Li at the Cu electrode is unprotected and in direct contact with the liquid electrolyte. Second, the ionomer preserves high, liquid-like overall transport of Li ions by absorbing sufficient liquid electrolyte to facilitate fast interfacial transport of Li. This means that freshly deposited Li even at the “protected” Li electrode will also be in direct contact with some volume of liquid electrolyte. The resultant degradation of the electrolyte at both electrodes may be expected to over time change the chemical composition and transport properties of the interphases, which is in fact consistent with our observations (See **Table 5.4**). Our findings mean that in order to simultaneously achieve high transference numbers, stable Li deposition, and high CE values, the ionomer coatings must be used in tandem with a liquid electrolyte with intrinsic chemical stability upon extended contact with metallic Li. Results reported in **Figure 5.10** show that this expectation is indeed met using pure EC as the electrolyte solvent. The figure shows that even without efforts to optimize the electrolyte composition or to protect the Cu counter electrode, CE values as high as 98% can be achieved for ionomer coated Li electrodes cycled in this electrolyte. The results underscore the complementary need for stable artificial interphases and stable electrolytes for enabling lithium metal batteries.

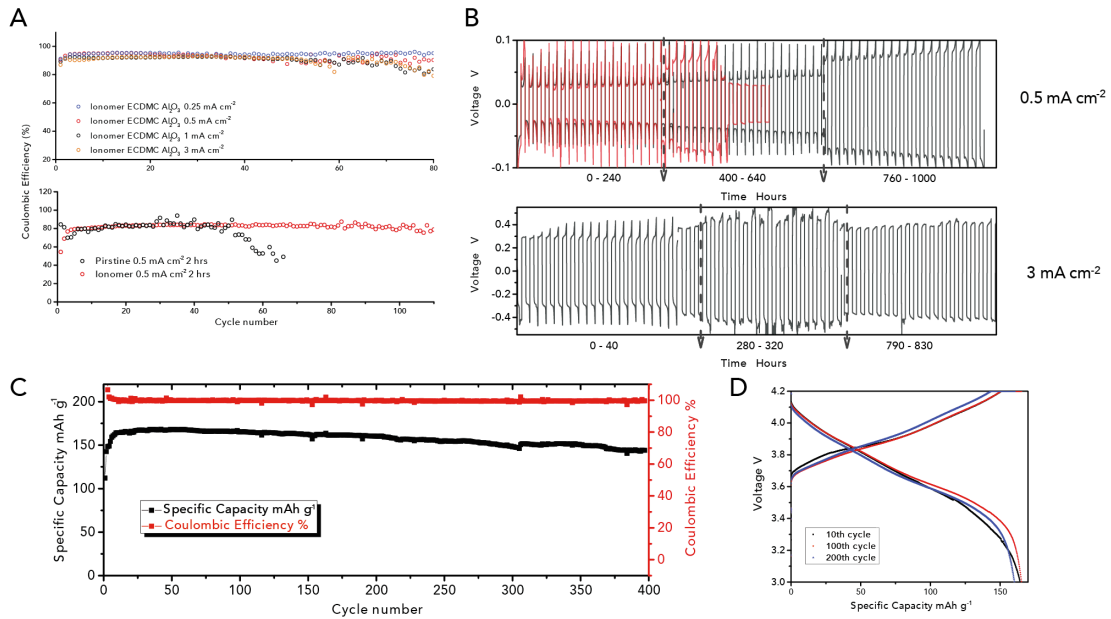


Figure 5.9. Cell cycling performance of the ionomer protected lithium anode. A) Coulombic efficiency (CE) measurements of 200 nm-thick ionomer and nanoporous Al₂O₃ protected lithium/Cu cells at current densities of 0.25, 0.5, and 1 mA cm⁻² for 1 mAh cm⁻² per plating/stripping, and 3 mA cm⁻² for 3 mAh cm⁻² per plating/stripping, using a 1 M LiPF₆ EC:DMC electrolyte with 10% FEC and 1%VC. The bottom figure compares the CE of 200 nm-thick ionomer protected lithium with unprotected lithium in the same electrolyte with no additives. B) Lithium plating/stripping voltage profile of ionomer and nanoporous Al₂O₃ protected lithium at 0.5 and 3 mA cm⁻² for 3 mAh cm⁻² per plating/stripping, with red line representing the bare lithium. C) 200 nm-thick ionomer and nanoporous Al₂O₃ protected versus NCA cathode with 3 mAh cm⁻² areal capacity operated at 0.5 C. D) Voltage – specific capacity profile of the 200 nm-thick ionomer and nanoporous Al₂O₃ protected lithium/NCA cell.

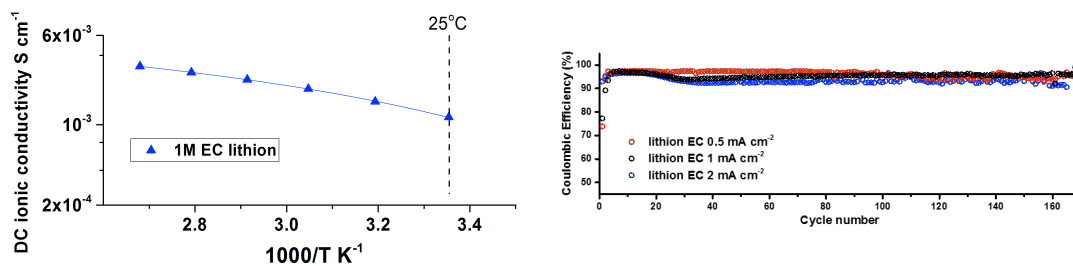


Figure 5.10. Left: Temperature-dependent DC ionic conductivity of the symmetric cell with 200 nm ionomer protected lithium electrodes and 1 M LiPF₆ in EC as the electrolyte. Right: the CE measurement of the 200 nm ionomer protected lithium with 1 M LiPF₆ in EC as the electrolyte at various current densities for 1 mAh cm⁻² plating/stripping.

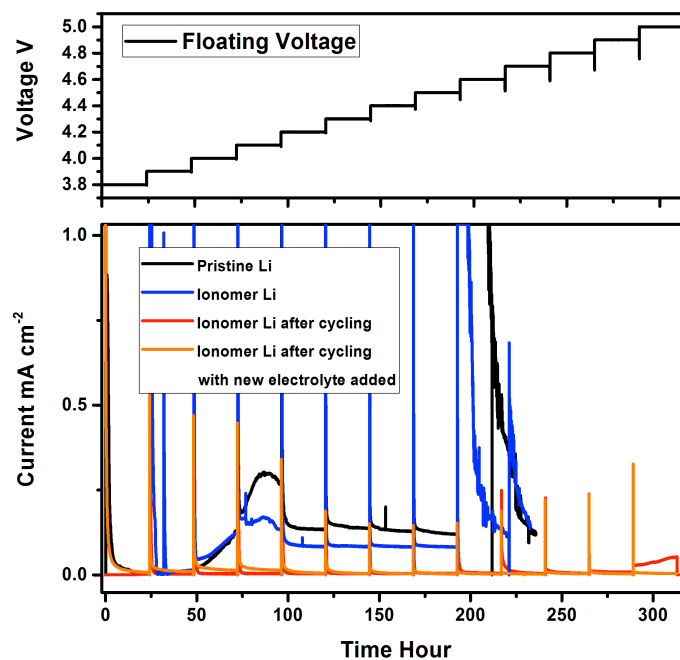


Figure 5.11. Floating test of ionomer protected lithium vs. NCA cathode from 3.8 V to 5 V, with each step lasts for 24 hours. The black line and the blue line represent the current profiles of pristine Li and ionomer protected lithium, respectively. The red line represents the current profile of the ionomer protected lithium cell after initial 50 cycles of cycling. The orange line represents the current profile of the ionomer protected lithium cell after 50 cycles of cycling, and then added fresh electrolyte.

The long-term lithium plating/stripping performance in the baseline EC:DMC electrolyte was evaluated in lithium/lithium symmetric cells (**Figure 5.9B**), with both electrodes protected by ionomer coating. At a moderate current density of 0.5 mA cm^{-2} and 6 hours per charge/discharge step, the lifetime is at least doubled, relative to cells based on unmodified Li electrodes, which are seen to exhibit sudden drop in voltage (red line) after a small number of cycles. Similar results are seen when cells are cycled at a higher, more practical current density of 3 mA cm^{-2} for 1 hour per charge/discharge. It is noted that in this case, even after 800-hours of continuous testing, the voltage profile displays no signs of failure by dendrite-induced short circuits. It is noted, nonetheless, that at intermediate cycles, occasional voltage spikes are observed during cycling at the higher rates. We tentatively attribute these spikes to side reactions associated with the ionomer SEI.

Analysis in half-cell -> full-cell LMBs based on intercalating cathodes

As a final assessment of the ionomer SEI, we investigated galvanostatic cycling of what we loosely term a *half-cell -> full cell* in which a conventional intercalating $\text{LiNi}_{0.8}\text{Co}_{0.15}\text{Al}_{0.05}\text{O}_2$ (NCA) cathode with high active material mass loading (3 mA cm^{-2} or 19.9 mg cm^{-2}) is paired with a metallic lithium anode. **Figure 5.9C and D** report the specific capacity and CE of these Li-NCA cells operated at 0.5C. It is seen that within 400 cycles of charge and discharge there is at most a 6% loss of capacity and the CE remains close to unity. The voltage profiles show there is minimal

overpotential increase during extended cycling, which is attributed to the stable interfacial resistance the ionomer SEI provides the Li electrode. **Figure 5.12** reports results from post-mortem analysis of an ionomer/ Al_2O_3 protected lithium surface after extensive full-cell cycling. A uniform lithium surface is observed and there is no sign of clogging of the Al_2O_3 . EDX analysis reveals a strong fluorine signal from primary fluorinated compounds, which is confirmed by XPS analysis (**Figure 5.13**). This indicates that in addition to the stabilizing effect of the single- or near-single ion transport enabled by the ionomer SEI, spontaneous formation of species such as LiF at the anode may play a role in the exceptional stability the ionomer SEI imparts to $\text{Li}^{25-26, 56}$. **Figure 5.11** reports results from floating experiments using protected/unprotected Li as anode and NCA as cathode. Voltages in the range 3.8 to 5 V were used for the experiments with each voltage step lasting for 24 hours. Cells based on the ionomer protected Li are seen to exhibit much lower leakage currents above 4.1 V, compared with those based on pristine Li anodes. This observation is consistent with the existence of a stable SEI that stabilizes the electrolyte against electrochemical decomposition at potentials beyond its stability limit. Even smaller leakage currents are seen after initial battery cycling, where for floating voltages up to 5 V, a leakage current $< 10 \mu\text{A cm}^{-2}$ is measured. To further evaluate the stability of the interphase, fresh electrolyte ($>100 \mu\text{L}$) was added to some of the pre-cycled cells and the floating voltage reinstated. It is seen the leak current remains quite low, indicating that the ionomer interphase remains robust and strong.

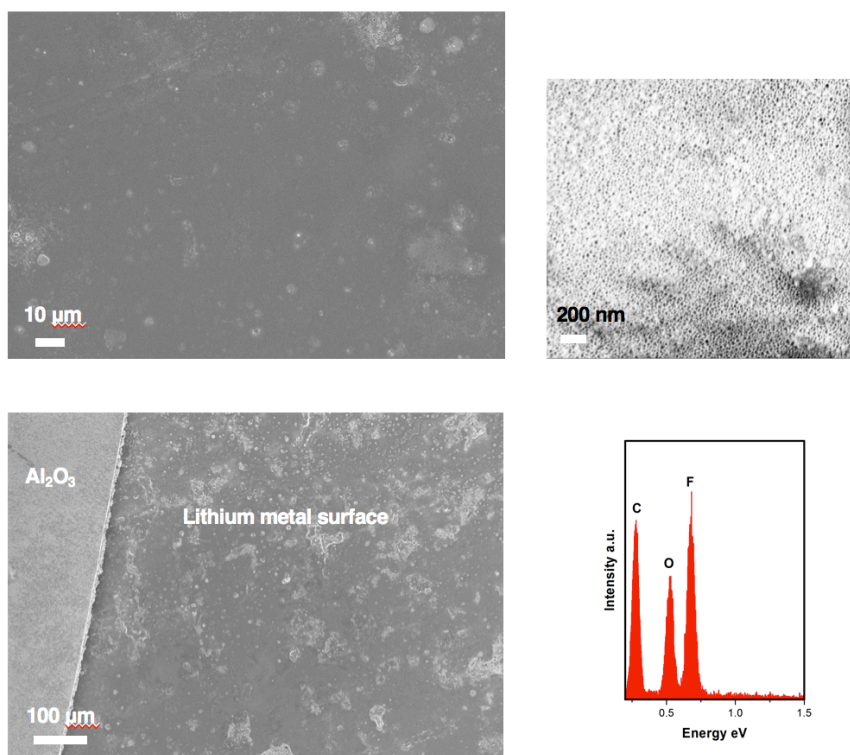


Figure 5.12. Ex situ post-mortem SEM images of 200 nm thick ionomer and nanoporous Al₂O₃ protected lithium surface after cycling in a lithium/NCA cell at 0.5 C. The loading of NCA electrode is 3 mAh cm⁻². Top left: overall image of the lithium surface; top right: image of the nanoporous Al₂O₃ that was facing the lithium; bottom left: Boundary between a broken part of nanoporous Al₂O₃ on top of the protected lithium metal surface; bottom right: EDX spectra of the protected lithium surface after cycling.

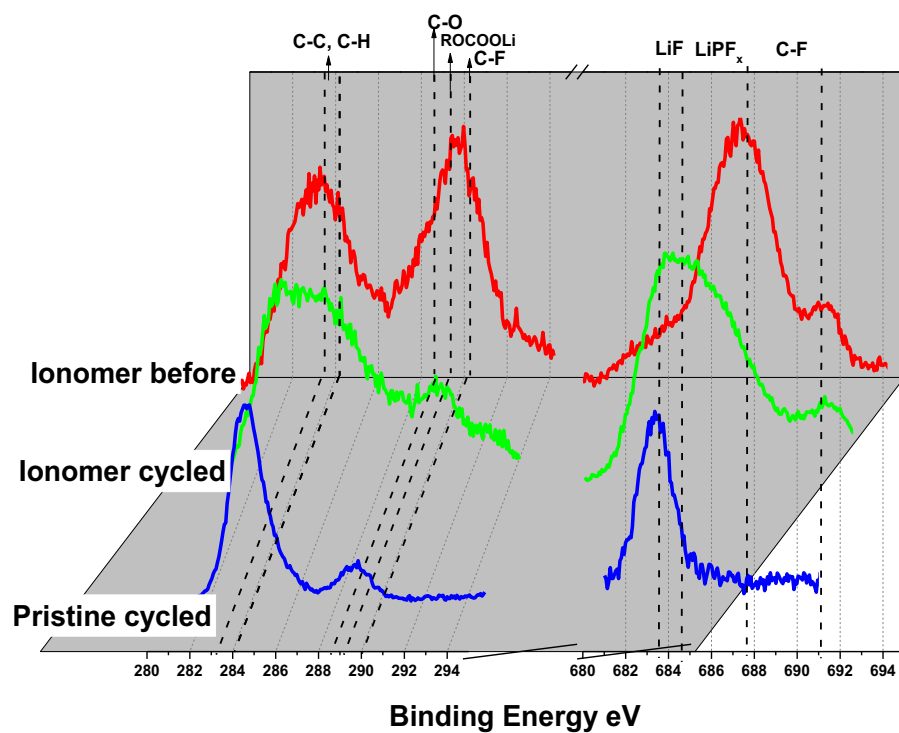


Figure 5.13. XPS spectra of carbon and fluorine of ionomer coated lithium metal before and after cycling at 0.5 mA cm^{-2} for two cycles, and pristine lithium after cycling in $1 \text{ M LiPF}_6 \text{ EC:DMC}$ electrolyte

To summarize, we have demonstrated that artificial SEI based on nanometer-thick ionomer coatings on Li metal electrodes stabilize the electrodes in long-term cycling studies performed in both over-limiting current and diffusion-allowed regimes. The SEIs appear to protect Li from direct contact with liquid electrolyte, but do not compromise interfacial mobility of Li^+ at the electrolyte/Li interface. Significantly, we also find that even a few nanometer-thick ionomer coating on Li fundamentally alters ion transport behavior in the entire cell, achieving a high lithium transference number close to 0.9 even in generic carbonate-based electrolytes doped with standard salts. Direct visualization studies show that an ionomer SEI on Li leads to a flatter, more uniform deposition of the metal, but that the effect disappears when the SEI thickness becomes too large. When integrated in lithium metal batteries (LMBs) that employ nanoporous membranes as separators, and either copper, metallic lithium, or a NCA as the counter electrode, we find that the protected Li anodes exhibit long-term failure-free lithium plating/stripping in a carbonate based electrolyte at high current density of 3 mA cm^{-2} for over 800 hours for 3 mAh cm^{-2} capacity per cycle. Similar highly stable and efficient full cell operation with less than 11% capacity fade over 400 cycles is also reported in Li/NCA cells, in which the active material loading in the cathode is high (3 mAh cm^{-2}). Our results provide a path towards SEI design that enables high energy and safe lithium metal batteries. They also provide a path for achieving higher efficiency charge transport in rechargeable batteries of all types through regulated ion transport in artificial SEIs tethered to the electrodes.

Reference

1. Tarascon, J. M.; Armand, M., Issues and challenges facing rechargeable lithium batteries. *Nature* **2001**, *414* (6861), 359-367.
2. Armand, M.; Tarascon, J. M., Building better batteries. *Nature* **2008**, *451* (7179), 652-657.
3. Yoshino, A., The Birth of the Lithium-Ion Battery. *Angewandte Chemie-International Edition* **2012**, *51* (24), 5798-5800.
4. Etacheri, V.; Marom, R.; Elazari, R.; Salitra, G.; Aurbach, D., Challenges in the development of advanced Li-ion batteries: a review. *Energy Environ. Sci.* **2011**, *4* (9), 3243-3262.
5. Dunn, B.; Kamath, H.; Tarascon, J.-M., Electrical energy storage for the grid: a battery of choices. *Science* **2011**, *334* (6058), 928-935.
6. Xu, K., Electrolytes and interphases in Li-ion batteries and beyond. *Chem. Rev.* **2014**, *114* (23), 11503-11618.
7. Aurbach, D.; Talyosef, Y.; Markovsky, B.; Markevich, E.; Zinigrad, E.; Asraf, L.; Gnanaraj, J. S.; Kim, H.-J., Design of electrolyte solutions for Li and Li-ion batteries: a review. *Electrochim. Acta* **2004**, *50* (2), 247-254.
8. Goodenough, J. B.; Kim, Y., Challenges for rechargeable Li batteries. *Chem. Mater.* **2009**, *22* (3), 587-603.
9. Tu, Z.; Lu, Y.; Archer, L., A Dendrite-Free Lithium Metal Battery Model Based on Nanoporous Polymer/Ceramic Composite Electrolytes and High-Energy Electrodes. *Small* **2015**.

10. Tu, Z.; Kambe, Y.; Lu, Y.; Archer, L. A., Nanoporous Polymer-Ceramic Composite Electrolytes for Lithium Metal Batteries. *Advanced Energy Materials* **2014**, *4* (2).
11. Cheng, X. B.; Zhang, R.; Zhao, C. Z.; Wei, F.; Zhang, J. G.; Zhang, Q., A review of solid electrolyte interphases on lithium metal anode. *Advanced Science* **2015**.
12. Tu, Z.; Nath, P.; Lu, Y.; Tikekar, M. D.; Archer, L. A., Nanostructured electrolytes for stable lithium electrodeposition in secondary batteries. *Acc. Chem. Res.* **2015**, *48* (11), 2947-2956.
13. Lin, D.; Liu, Y.; Cui, Y., Reviving the lithium metal anode for high-energy batteries. *Nature Nanotechnology* **2017**, *12* (3), 194-206.
14. Aurbach, D.; McCloskey, B. D.; Nazar, L. F.; Bruce, P. G., Advances in understanding mechanisms underpinning lithium–air batteries. *Nature Energy* **2016**, *1*, 16128.
15. Pang, Q.; Liang, X.; Kwok, C. Y.; Nazar, L. F., Advances in lithium–sulfur batteries based on multifunctional cathodes and electrolytes. *Nature Energy* **2016**, *1*, 16132.
16. Li, Y.; Dai, H., Recent advances in zinc–air batteries. *Chem. Soc. Rev.* **2014**, *43* (15), 5257-5275.
17. Chazalviel, J. N., Electrochemical Aspects of the Generation of Ramified Metallic Electrodeposits. *Phys. Rev. A* **1990**, *42* (12), 7355-7367.
18. Rosso, M.; Gobron, T.; Brissot, C.; Chazalviel, J.-N.; Lascaud, S., Onset of dendritic growth in lithium/polymer cells. *J. Power Sources* **2001**, *97*, 804-806.

19. Lu, Y.; Tikekar, M.; Mohanty, R.; Hendrickson, K.; Ma, L.; Archer, L. A., Stable Cycling of Lithium Metal Batteries Using High Transference Number Electrolytes. *Advanced Energy Materials* **2015**.
20. Bouchet, R.; Maria, S.; Meziane, R.; Aboulaich, A.; Lienafa, L.; Bonnet, J.-P.; Phan, T. N.; Bertin, D.; Gigmes, D.; Devaux, D., Single-ion BAB triblock copolymers as highly efficient electrolytes for lithium-metal batteries. *Nature materials* **2013**, *12* (5), 452-457.
21. Srivastava, S.; Schaefer, J. L.; Yang, Z.; Tu, Z.; Archer, L. A., 25th anniversary article: polymer–particle composites: phase stability and applications in electrochemical energy storage. *Adv. Mater.* **2014**, *26* (2), 201-234.
22. Khurana, R.; Schaefer, J. L.; Archer, L. A.; Coates, G. W., Suppression of lithium dendrite growth using cross-linked polyethylene/poly (ethylene oxide) electrolytes: a new approach for practical lithium-metal polymer batteries. *J. Am. Chem. Soc.* **2014**, *136* (20), 7395-7402.
23. Tung, S.-O.; Ho, S.; Yang, M.; Zhang, R.; Kotov, N. A., A dendrite-suppressing composite ion conductor from aramid nanofibres. *Nature communications* **2015**, *6*.
24. Ding, F.; Xu, W.; Graff, G. L.; Zhang, J.; Sushko, M. L.; Chen, X. L.; Shao, Y. Y.; Engelhard, M. H.; Nie, Z. M.; Xiao, J.; Liu, X. J.; Sushko, P. V.; Liu, J.; Zhang, J. G., Dendrite-Free Lithium Deposition via Self-Healing Electrostatic Shield Mechanism. *J. Am. Chem. Soc.* **2013**, *135* (11), 4450-4456.
25. Lu, Y.; Tu, Z.; Archer, L. A., Stable lithium electrodeposition in liquid and nanoporous solid electrolytes. *Nature materials* **2014**.

26. Zhang, X. Q.; Cheng, X. B.; Chen, X.; Yan, C.; Zhang, Q., Fluoroethylene Carbonate Additives to Render Uniform Li Deposits in Lithium Metal Batteries. *Adv. Funct. Mater.* **2017**.
27. Li, W.; Yao, H.; Yan, K.; Zheng, G.; Liang, Z.; Chiang, Y.-M.; Cui, Y., The synergetic effect of lithium polysulfide and lithium nitrate to prevent lithium dendrite growth. *Nature communications* **2015**, *6*.
28. Lin, D.; Liu, Y.; Liang, Z.; Lee, H.-W.; Sun, J.; Wang, H.; Yan, K.; Xie, J.; Cui, Y., Layered reduced graphene oxide with nanoscale interlayer gaps as a stable host for lithium metal anodes. *Nature nanotechnology* **2016**, *11* (7), 626-632.
29. Liang, Z.; Lin, D.; Zhao, J.; Lu, Z.; Liu, Y.; Liu, C.; Lu, Y.; Wang, H.; Yan, K.; Tao, X., Composite lithium metal anode by melt infusion of lithium into a 3D conducting scaffold with lithiophilic coating. *Proceedings of the National Academy of Sciences* **2016**, *113* (11), 2862-2867.
30. Tikekar, M. D.; Choudhury, S.; Tu, Z.; Archer, L. A., Design principles for electrolytes and interfaces for stable lithium-metal batteries. *Nature Energy* **2016**, *1*, 16114.
31. Xu, W.; Wang, J. L.; Ding, F.; Chen, X. L.; Nasybutin, E.; Zhang, Y. H.; Zhang, J. G., Lithium metal anodes for rechargeable batteries. *Energy Environ. Sci.* **2014**, *7* (2), 513-537.
32. Jonscher, A. K., The universal dielectric response. *Nature* **1977**, *267*, 673-679.
33. Nugent, J. L.; Moganty, S. S.; Archer, L. A., Nanoscale organic hybrid electrolytes. *Adv. Mater.* **2010**, *22* (33), 3677-3680.

34. Evans, J.; Vincent, C. A.; Bruce, P. G., Electrochemical measurement of transference numbers in polymer electrolytes. *Polymer* **1987**, 28 (13), 2324-2328.
35. Tikekar, M. D.; Archer, L. A.; Koch, D. L., Stabilizing electrodeposition in elastic solid electrolytes containing immobilized anions. *Science Advances* **2016**, 2 (7), e1600320.
36. Liang, Z.; Chen, W.; Liu, J.; Wang, S.; Zhou, Z.; Li, W.; Sun, G.; Xin, Q., FT-IR study of the microstructure of Nafion® membrane. *Journal of membrane science* **2004**, 233 (1), 39-44.
37. Tu, Z.; Zachman, M. J.; Choudhury, S.; Wei, S.; Ma, L.; Yang, Y.; Kourkoutis, L. F.; Archer, L. A., Nanoporous Hybrid Electrolytes for High-Energy Batteries Based on Reactive Metal Anodes. *Advanced Energy Materials* **2017**.
38. Croce, F.; Persi, L.; Scrosati, B.; Serraino-Fiory, F.; Plichta, E.; Hendrickson, M., Role of the ceramic fillers in enhancing the transport properties of composite polymer electrolytes. *Electrochim. Acta* **2001**, 46 (16), 2457-2461.
39. Croce, F.; Appetecchi, G.; Persi, L.; Scrosati, B., Nanocomposite polymer electrolytes for lithium batteries. *Nature* **1998**, 394 (6692), 456-458.
40. Feng, S.; Shi, D.; Liu, F.; Zheng, L.; Nie, J.; Feng, W.; Huang, X.; Armand, M.; Zhou, Z., Single lithium-ion conducting polymer electrolytes based on poly [(4-styrenesulfonyl)(trifluoromethanesulfonyl) imide] anions. *Electrochim. Acta* **2013**, 93, 254-263.
41. Schaefer, J. L.; Yanga, D. A.; Archer, L. A., High Lithium Transference Number Electrolytes via Creation of 3-Dimensional, Charged, Nanoporous Networks

- from Dense Functionalized Nanoparticle Composites. *Chem. Mater.* **2013**, *25* (6), 834-839.
42. Fromling, T.; Kunze, M.; Schonhoff, M.; Sundermeyer, J.; Roling, B., Enhanced lithium transference numbers in ionic liquid electrolytes. *The Journal of Physical Chemistry B* **2008**, *112* (41), 12985-12990.
43. Stolarska, M.; Niedzicki, L.; Borkowska, R.; Zalewska, A.; Wieczorek, W., Structure, transport properties and interfacial stability of PVdF/HFP electrolytes containing modified inorganic filler. *Electrochim. Acta* **2007**, *53* (4), 1512-1517.
44. Du Pasquier, A.; Warren, P.; Culver, D.; Gozdz, A.; Amatucci, G.; Tarascon, J.-M., Plastic PVDF-HFP electrolyte laminates prepared by a phase-inversion process. *Solid State Ionics* **2000**, *135* (1), 249-257.
45. Fergus, J. W., Ceramic and polymeric solid electrolytes for lithium-ion batteries. *J. Power Sources* **2010**, *195* (15), 4554-4569.
46. Agrawal, R. C.; Pandey, G. P., Solid polymer electrolytes: materials designing and all-solid-state battery applications: an overview. *Journal of Physics D-Applied Physics* **2008**, *41* (22).
47. Song, J.; Lee, H.; Choo, M.-J.; Park, J.-K.; Kim, H.-T., Ionomer-liquid electrolyte hybrid ionic conductor for high cycling stability of lithium metal electrodes. *Scientific reports* **2015**, *5*, 14458.
48. Suo, L. M.; Hu, Y. S.; Li, H.; Armand, M.; Chen, L. Q., A new class of Solvent-in-Salt electrolyte for high-energy rechargeable metallic lithium batteries. *Nature Communications* **2013**, *4*.

49. Oh, H.; Xu, K.; Yoo, H. D.; Kim, D. S.; Chanthad, C.; Yang, G.; Jin, J.; Ayhan, I. A.; Oh, S. M.; Wang, Q., Poly (arylene ether)-based single-ion conductors for lithium-ion batteries. *Chem. Mater.* **2015**, *28* (1), 188-196.
50. Villaluenga, I.; Wujcik, K. H.; Tong, W.; Devaux, D.; Wong, D. H.; DeSimone, J. M.; Balsara, N. P., Compliant glass-polymer hybrid single ion-conducting electrolytes for lithium batteries. *Proceedings of the National Academy of Sciences* **2016**, *113* (1), 52-57.
51. Ma, Q.; Zhang, H.; Zhou, C.; Zheng, L.; Cheng, P.; Nie, J.; Feng, W.; Hu, Y. S.; Li, H.; Huang, X., Single Lithium-Ion Conducting Polymer Electrolytes Based on a Super-Delocalized Polyanion. *Angew. Chem. Int. Ed.* **2016**, *55* (7), 2521-2525.
52. Qin, B.; Liu, Z.; Zheng, J.; Hu, P.; Ding, G.; Zhang, C.; Zhao, J.; Kong, D.; Cui, G., Single-ion dominantly conducting polyborates towards high performance electrolytes in lithium batteries. *Journal of Materials Chemistry A* **2015**, *3* (15), 7773-7779.
53. Zhao, J.; Wang, L.; He, X.; Wan, C.; Jiang, C., Determination of lithium-ion transference numbers in LiPF₆-PC solutions based on electrochemical polarization and NMR measurements. *J. Electrochem. Soc.* **2008**, *155* (4), A292-A296.
54. Zugmann, S.; Fleischmann, M.; Amereller, M.; Gschwind, R. M.; Wiemhöfer, H.; Gores, H., Measurement of transference numbers for lithium ion electrolytes via four different methods, a comparative study. *Electrochim. Acta* **2011**, *56* (11), 3926-3933.

55. Cai, Z.; Liu, Y.; Liu, S.; Li, L.; Zhang, Y., High performance of lithium-ion polymer battery based on non-aqueous lithiated perfluorinated sulfonic ion-exchange membranes. *Energy Environ. Sci.* **2012**, *5* (2), 5690-5693.
56. Lu, Y.; Tu, Z.; Shu, J.; Archer, L. A., Stable lithium electrodeposition in salt-reinforced electrolytes. *J. Power Sources* **2015**, *279*, 413-418.

CHAPTER 6

SOLID-SOLID INTERPHASES FOR HYBRID RECHARGEABLE BATTERY ANODES

Reproduced from Nature Energy in revision

6.1 Abstract

Carefully designed solid electrolyte interphases (SEI) play a key role in achieving stable, reversible and efficient energy storage in batteries. In high energy metal-based rechargeable batteries, the poorly formed natural SEI on anodes is now understood to pose a crucial barrier preventing their large-scale implementation. We herein report that hybrid battery anodes created by depositing a second electrochemically active metal (e.g. Sn) on a reactive alkali metal electrode in a facile ion-exchange process leads to drastically higher exchange currents and stable long term performance of cells based on Li and Na electrodes. Sn-Li anodes are shown to present long-term cycling stability at 3 mA cm^{-2} and 3 mAh cm^{-2} with a regulated surface morphology, evidenced in both direct visualization and ex-situ electrodeposition studies. Prototype full cells that pair the hybrid Li anodes with high loading LiNiCoAlO (NCA) cathodes are also reported based on the Sn-Li anode design. We further show that Na anodes, notorious for their chemical and morphological instability, can be cycled stably for over 1700 hours with minimal voltage divergence. The Sn-Li and Sn-Na anodes appear to benefit from a combination of alloying and electrodeposition storage reactions and, in so doing, open the way for new hybrid alkali metal battery technology that takes advantage of ion exchange chemistry to achieve stable long-term storage.

6.2 Introduction

Rechargeable batteries can efficiently store and convert chemical energy to electricity and thus are of increasing interest in a growing set of practices, including consumer electronics, advanced robotics, grid storage and electrified transportation¹⁻⁴. To keep pace with constantly increasing performance demands, progress is required to design energy storage systems able to safely and reversibly store electrical energy with high energy density, high efficiency, and long lifetime⁵⁻⁷. While conventional rechargeable batteries, such as those based on lead-acid, nickel-cadmium, lithium ion or flow redox continue to receive attention as platforms for meeting emerging storage needs, progress has been mostly incremental with the greatest advances centered on improving performance to cost ratio⁸⁻⁹. It has been commonly understood that the exploration of other electrochemically active materials which undergo efficient reduction/oxidation chemistry and possess considerably higher energy per unit mass/volume than those used in state-of-the-art batteries, represent an important direction towards the energy storage breakthroughs sought in applications¹⁰⁻¹².

The carbonaceous anode of a lithium ion battery (LIB) can be replaced by a metallic lithium anode with ten-times the specific energy (3860 mAh/g vs. 360 mAh/g), which in principle should enable advanced high energy non-lithiated cathodes such as sulfur or oxygen, so that the energy storage density of the whole cell can be significantly improved (from ca. 0.3 kWh/kg in LIB to 2.5 kWh/kg for Li-S or 10 kWh/kg in Li-O₂ batteries). Even more exciting cost and performance profiles are possible with room temperature versions of these batteries that utilize metallic sodium or aluminum as anode¹³⁻¹⁴. Challenges associated with developing reversible, safe and cost-effective high energy rechargeable batteries based on any of these chemistries have become

increasingly well-known^{6, 15}. The most difficult issues stem from the fact that the highly electrochemically active materials at the anode are either naturally unstable against commonly used electrolytes or promote uncontrolled formation of rough, fragile solid electrolyte interphases (SEI). Although the concept of using spontaneously formed SEI on the anode to regulate these events is not unfamiliar to the field, as it has long been discovered on lithiated graphite anodes in LIBs, information regarding its formation mechanism and detailed methods for controlling its structure/composition remain lacking¹⁶⁻¹⁷. The fact that the state-of-the-art LIBs render very high Coulombic efficiency and thus minimal energy loss during cycling underscores the criticalness of a well-defined, stable SEI¹⁸.

Unfortunately, these benefits are not easily realized in anodes based on energetic metals such as aluminum, lithium, or sodium, as well as silicon and tin because their naturally grown SEIs are fragile, non-homogeneous (in terms of both morphology and composition), and the electrodes undergo substantial volume change during charge-discharge cycling. Thus, whether the charge storage reaction relies on alloy formation, intercalation, or plating of the active metal at the battery anode, the SEI formed naturally at any of these anodes undergoes repeated breakage and reformation processes during battery cycling, which is a parasitic cycle that consumes electrolyte and salt¹⁹. Additionally, if the electrode process requires metal plating, even at moderate current densities the conductivity inhomogeneity promotes selective electrodeposition on sparse local sites where bulky, mossy dendrites can grow and proliferate.

Here we show that through creation of artificial interphases composed of a metal that stores charge by alloying reactions on one that utilizes plating processes for charge storage, it is possible to create hybrid anodes that utilize both storage mechanisms to overcome the most serious challenges with both sodium and lithium electrodes. In particular, we report that a facile ion exchange chemistry performed in a conventional carbonate electrolyte can be used to rapidly deposit conformal coatings of metals such as tin onto sodium or lithium electrodes. By controlling the thickness of these coatings to nanometer dimensions, we further show that they are able to perform multiple beneficial functions, including protecting the underlying metal electrode against parasitic reactions with liquid electrolytes, providing a compliant interphase that is able to accommodate volume changes associated with both the alloying and plating processes at the electrode, and suppressing dendrite formation at a Li or Na metal anode. The resultant hybrid lithium-metal/lithium-ion energy storage mode achieved in cells where the alloying and plating reactions occur at similar potentials also facilitates fast, unhindered ion transport across the interphase. By these means, we find that the reported hybrid anodes enable high-capacity, dendrite-free long-term battery cycling in both symmetric cells and prototype full cells with high loading $\text{LiNi}_{0.8}\text{Co}_{0.15}\text{Al}_{0.05}\text{O}_2$ (NCA) electrodes with a nominal specific capacity of about 190 mAh g^{-1} . The approach is particularly promising for sodium electrodes, notorious for their reactivity and propensity to form large, fragile dendritic deposits²⁰ that easily break and become electrically disconnected from the electrode mass even at low current rates. It is observed that hybrid Sn/Na electrodes cycle stably for over 1000 hours in normally reactive carbonate-based liquid electrolytes.

6.3 Experimental Section

Lithium metal foil was purchased from MTI (99.9%) and stored in the sub-ppm Argon filled glovebox (Inert Inc.) before usage without additional treatment. Tin bis(trifluoromethanesulfonyl) imide (SnTFSI, Alfa Aesar) was dissolved in ethylene carbonate: dimethyl carbonate (EC:DMC, 1:1 v:v) with different concentrations and the resultant clear solution was used to pretreat lithium metal foil to form surface protection. 100 μ L SnTFSI solution was dropped on the lithium surface and the reaction was allowed for 30 mins. Treated lithium metal appears dark gray on the surface and was dried in the glovebox antechamber before usage. The Sn coating can also be transferred to an inert stainless steel by gently pressing the treated lithium metal on the stainless steel. As-obtained Sn/stainless steel electrodes could be directly used for characterization. Sodium cubes (Sigma-Aldrich) were stored in mineral oil and sliced with fresh inner exposed for the same surface treatment.

A Leo 1550 Keck Field Emission Scanning Electron Microscopy (FESEM) with a Bruker EDX detector and a FEI Strata 400 DualBeam Focused Ion Beam (FIB) fitted with a Quorum PP3010T Cryo-FIB/SEM Preparation System were used to characterize the surface morphology and cross section morphology of the tin-protected alkali metal. To avoid reaction of the lithium sample with O₂ and moisture in ambient air during cryo-FIB experiments, the samples were quickly plunged into a nitrogen slush immediately after treatment or harvesting from lithium cells. To confirm the chemical stability of lithium in liquid nitrogen, a scan of EDX spectrum of a pristine lithium frozen undergoing the same treatment was conducted which showed no

detectable nitrogen signal (**Figure 6.1**). The samples were subsequently maintained -165 °C in the cryo-FIB to preserve their structure. After cooling, all samples investigated remained under liquid nitrogen or in vacuum for the duration of the experiment. The crystal structure of the tin-protected lithium/sodium was investigated using a Rigaku X-Ray diffractometer (XRD) from 20 to 80 degree (two theta). Tin-protected sodium metal was wrapped in Kapton tape during the experiment to avoid oxidation in air. Tin-protected lithium metal was measured directly to gain the best resolution, since the surface treatment significantly slows down the oxidation. X-ray photoelectron spectroscopy SSX-100 (XPS) was used to study the detailed chemistry information on the tin-protected lithium surface. To avoid surface contamination, a vacuum puck was used to transfer samples from the argon filled glovebox to the high-vacuum XPS chamber without exposure to atmosphere.

Electrochemical studies were performed using CR2032 coin cells with symmetric and asymmetric design. Symmetric lithium cells were assembled with two tin treated lithium metal anodes (SnLi/SnLi), Celgard 3501 polypropylene separator, and electrolyte containing 1 M LiPF₆ in EC:DMC (1:1) with 10 v% fluorinated ethylene carbonate (FEC) and 1 v% vinylene carbonate (VC). For cyclic voltammetry measurement, symmetric lithium cells with pristine lithium and tin treated lithium (Li/SnLi) were used. Symmetric sodium cells were assembled with two tin treated sodium metal anodes (SnNa/SnNa), Celgard 3501 polypropylene separator, and electrolyte containing 1 M NaPF₆ in EC: propylene carbonate (PC) (1:1 v%). Asymmetric lithium cells composed of tin treated lithium metal anode with a thickness of 450 μm and lithium nickel cobalt aluminum oxide (NCA) cathodes (SnLi/NCA)

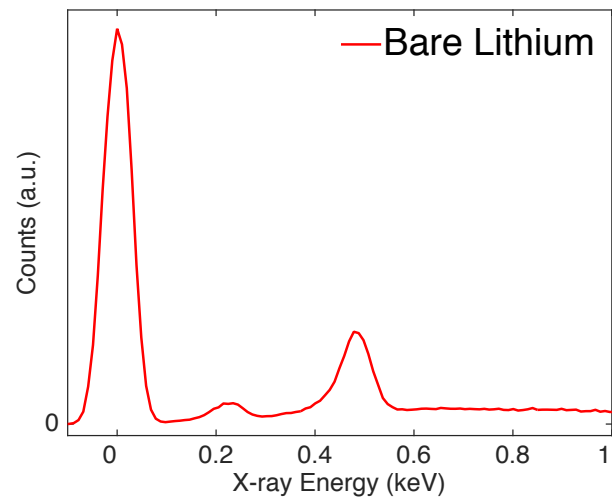


Figure 6.1. EDX profile of a bare lithium immersed in liquid nitrogen. Data was harvested using the cryo-FIB-SEM at -165 °C.

provided by CAMP facility at Argonne National Labs with 90% active material loading and area capacity of 3 mAh cm⁻². A piece of glass fiber was added in the prototype full cell to absorb sufficient electrolyte (200 μL, about 110 μL remained in the cell after the cell crimping). For 3:1 anode to cathode capacity ratio SnLi/NCA cells, lithium was firstly deposited on a stainless steel with the predetermined capacity (9 mAh cm⁻² ~ 45 cm) in 1 M LiTFSI DOL:DME (1:1), whose surface was thoroughly cleaned with DOL solvent and dried. Then the same Sn ion exchange process was applied to achieve the SnLi anode, as described previously.

Temperature-dependent ionic conductivity and impedance spectra were measured from 10⁷ Hz to 10⁻¹ Hz at a temperature range of -5 to 100 °C using Novocontrol dielectric/impedance spectrometer coupled with the temperature-controlling chamber. Cyclic voltammetry (CV) was performed on a CH 600E potentiostat with lithium being the pseudo-reference electrode at a sweep rate of 1 mV s⁻¹. Galvanostatic plating/stripping of symmetric cells was studied on Neware battery testers at room temperature. SnLi/NCA prototype full cells were cycled using a constant current-constant voltage charge and constant current discharge from 3 to 4.2 V.

In situ observation cell was home-made and as illustrated in the previous chapter. Two lithium cylinder rods with a diameter of half inch were used as the electrodes connected with stainless steel transmission lines to the battery test channels. The snapshots were taken using an Olympus camera and microscope with 100x magnification. Images analysis was performed using the ImageJ software.

6.4 Results and discussion

A successful SEI for a reactive metal anode must have several properties. First, it must maintain conformal contact with the metal to prevent reductive decomposition of the electrolyte, and such contact needs to be maintained when metal anodes undergo volume expansion during multiple charge-discharge cycles. Second, it should facilitate fast transport of ions at both the interface formed with the liquid electrolyte and with the metal anode. Third, it must remain mechanically and electrochemically stable in a dynamic environment during extensive cycling. The results reported in this study build on recent progress addressing electrolyte consumption and dendritic electrodeposition at reactive metal anodes⁶⁻⁷. Previous studies have shown that a broad range of materials, including crosslinked polymers²¹⁻²², ceramic conductors²³, and hybrid composites²⁴⁻²⁷ prevent dendrite proliferation by fundamentally slowing the deposition kinetics at rough regions on an electrode²⁸. An equally important body of work has emerged, which shows that carefully tuning ion transport in liquid electrolytes can provide an effective method for suppressing electroconvective instabilities that accelerate dendrite growth at currents above the limiting current. For example, the application of various single-ion conductors have been shown to be effective at suppressing rough electrodeposition and minimizing ionic polarization²⁹⁻³¹. For related reasons, the use of supporting electrolytes, such as ionic liquids^{13, 20, 32}, has also emerged as an effective way of preventing dendrite proliferation at Li and Na electrodes.

SEI additives, such as vinylene carbonate, fluorinated ethylene carbonate, and others that breakdown prior to natural SEI precursors to build interphases with preferable electrochemical stability and mechanical robustness³³⁻³⁵ have also emerged as

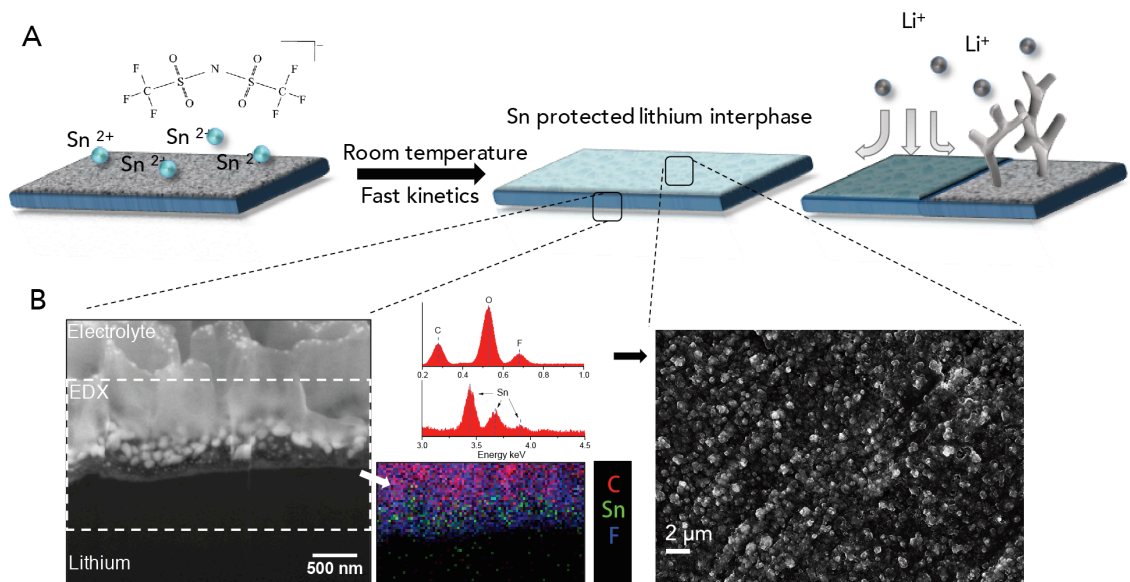


Figure 6.2. Hybrid anodes based on facile and fast Sn deposition on reactive metals produced by ion exchange. A) Schematic illustration of the tin protection on lithium metal electrode. B) Left: Cryo-FIB-SEM image of the cross-section from the tin-protected lithium and the EDX elemental mapping of fluorine (red) and tin (green) in the dashed rectangular region; right: Room-temperature field emission-SEM image of surface morphology of the tin-protected lithium and corresponding EDX spectra.

effective in promoting SEI layers with desired mechanical and transport properties. Artificial SEI composed of polymers³⁶⁻³⁷, inorganic conductive compounds³⁸⁻³⁹, nanoparticles⁴⁰⁻⁴¹, thin film⁴²⁻⁴³, carbon materials⁴⁴⁻⁴⁵ etc., produced either in-situ or ex-situ on reactive metal electrodes have also been reported to isolate the electrodes from parasitic side reactions with unstable anions or solvent components in liquid electrolytes. The success of such coatings has in turn lead to adaptation of methods such as Langmuir-Blodgett, vapor deposition to transfer preformed coatings onto electrodes.

The hybrid anodes used in the study were prepared by means of a simple surface ion-exchange reaction in a commonly used aprotic liquid lithium electrolyte, 1M LiPF₆ in an ethylene carbonate-dimethyl carbonate (EC:DMC) solvent blend containing a second salt (see **Figure 6.2A**)⁴⁶. For this first study, we focus on Sn because much is known about the electrochemical behavior of the metal and its oxides⁴⁷⁻⁴⁸, including the fast interdiffusion of Li in Sn and the < 500mV separation between electrochemical alloy formation and Li plating. The treatment process is also fast and spontaneous due to the large electronegativity difference between alkali metals and metallic tin. Depending on the concentration of Sn salt employed, the appearance of the lithium surface after the treatment ranges from dark brown to dark gray in color. The surface and the cross-sectional morphology of tin-protected lithium can be obtained without surface contamination using a cryo-FIB-SEM (also see experimental section). **Figure 6.2B** shows a cross-sectional image captured at -165°C of Sn-Li created using a 10 mM tin salt in the electrolyte, in which a clearly tri-layer structure can be observed. The top layer is the frozen electrolyte used for the treatment,

followed by a tin-rich layer with thickness on the order of 500 nm that is seen to be composed of nanoparticles with average size around 200 nm. EDX mapping confirms Sn is present in the nanoparticles of the protection layer. Note that no Sn signal is observed in the electrolyte region, which testifies to the fast and thorough interfacial reaction used to create the Sn overlayer. The bird's eye view of the Sn-Li hybrid anode without electrolyte by room-temperature SEM reveals a uniform distribution of Sn nanoparticles on the surface of Li, a morphology quite distinctive from the pristine lithium.

To confirm the structure and chemistry of the Sn-Li hybrid electrode surface, an X-ray diffractometer (XRD) is employed to understand the crystal structure and phase information. **Figure 6.5A** exhibits the XRD spectra of lithium metal with its surface treated with electrolytes containing 1, 10 and 100 mM Sn salt. At the lowest concentration, only lithium metal signals and a minor lithium oxide peak at 32.6 degree are observed, which indicates the reaction is inhibited likely due to the low activity of Sn ions. Peaks at 31.1, 32.4, 44.1 and 45.2 degrees start to appear when the concentration is increased to 10 mM, suggesting metallic tin with structure following the R3m space group is formed. Increasing the tin salt concentration to 100 mM, the metallic Sn layer alloys with Li, evidenced by peaks labeled with asterisks which correspond to a Li_5Sn_2 phase. The Sn overlayer generated from the high concentration (100 mM) electrolyte exhibits an increased thickness to about 2 μm with a compact, solid-like structure, as shown in **Figure 6.3** and **6.4**. The surface morphology is glassy in appearance with grain gaps among alloy terraces, possibly due to the formation of zintl phase that is naturally ionic and brittle⁴⁹⁻⁵⁰. Because of their more uniform

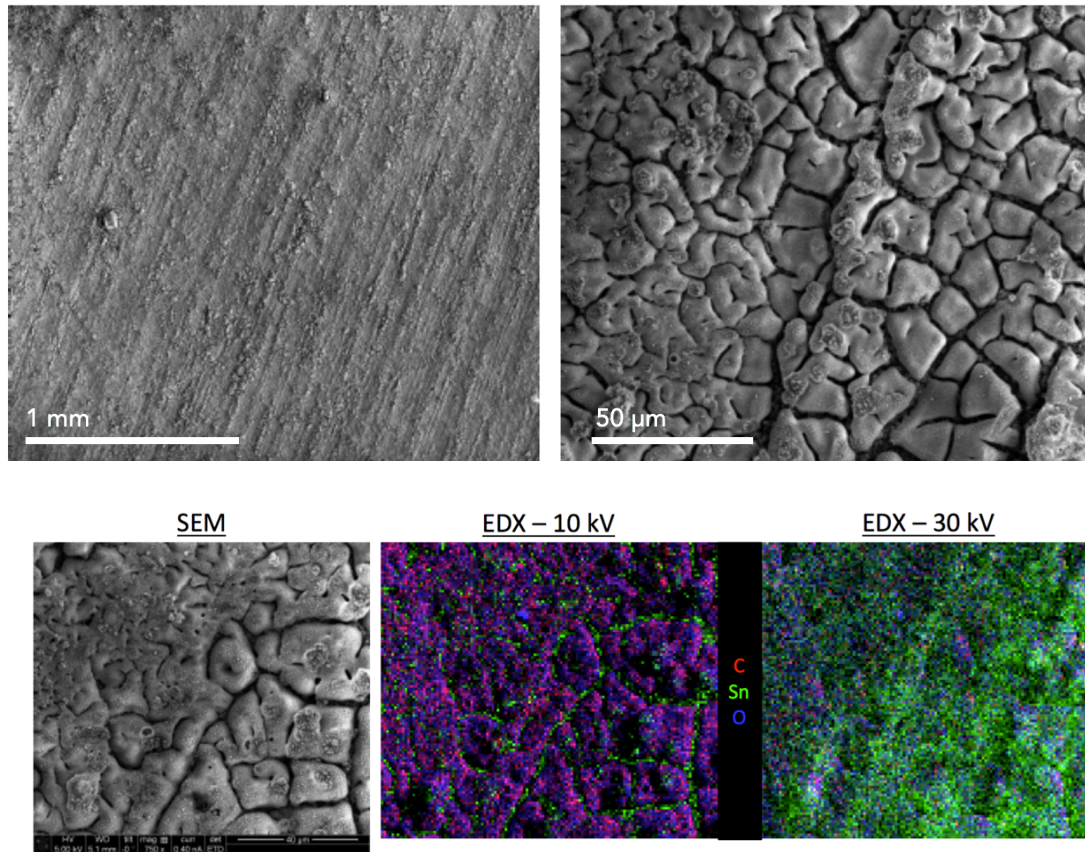


Figure 6.3. Cryo-SEM images and EDX elemental mapping of the tin-protected lithium surface treated with 100 mM tin-bearing electrolyte. The 10 kV electrons don't penetrate the electrolyte so the Sn signal is only observed in the cracks. The 30 kV electrons penetrate the electrolyte and reveal the Sn layer covering the surface below.

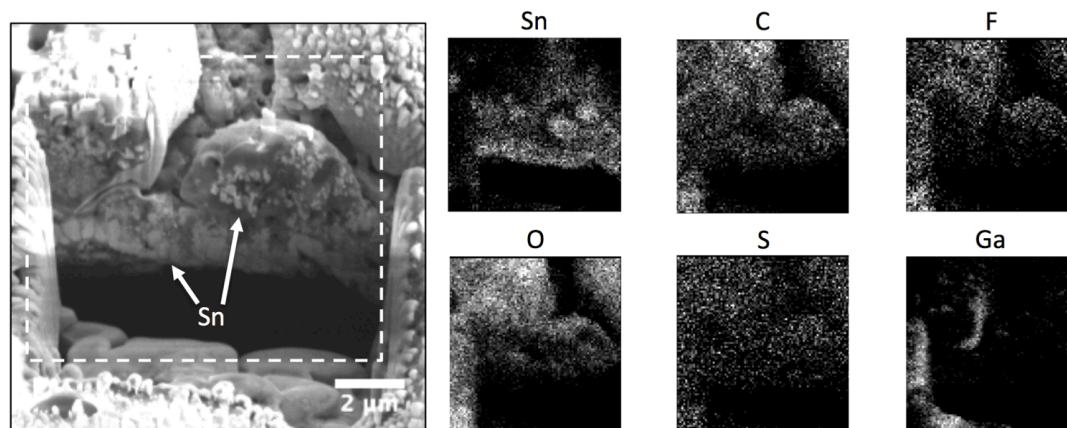


Figure 6.4. Cryo-FIB-SEM and EDX elemental mapping of the tin-protected lithium surface cross section (100 mM tin-bearing electrolyte).

morphologies, electrochemical properties of Sn-Li hybrid anodes created using the 10 mM electrolyte (corresponding to 500 nm coating thickness) are evaluated in detail. Compared to the overall thickness of the lithium electrode (450 μm for bulk lithium or 45 μm for thin lithium studied later), the Sn coating only takes a small fraction of volume and thus the high-energy advantage of lithium metal can be maintained. Of particular interest in such studies is the fact that because both the Sn and Li components in such electrodes are able to reversibly store Li by alloying and plating processes, respectively, lithium batteries that rely on mixed storage mechanisms are possible. The thin Sn layers on the hand do not alloy with a significant quantity of lithium ions and thus avoid possible irreversibility typically observed in Sn anodes. The binary lithium plating/alloying energy storage modes on the interphase between the anode and the electrolyte are expected to work in synergy with the surface protection feature provided by the Sn SEI to achieve both high energy density and high stability.

Knowledge of the charge transport processes at Sn-based electrode/electrolyte interphase can be deduced from impedance spectroscopy. **Figure 6.5B** compares the temperature-dependent Nyquist plots of symmetric cells equipped with the Sn-Li electrodes and the pristine lithium in a commonly used EC:DMC electrolyte. Each spectrum can be fitted into the equivalent circuit model to decouple the interfacial transport resistance from other processes. As expected, the interfacial resistance decreases with increasing temperature, with detailed information presented in **Figure 6.6**. The change as a function of temperatures follows a quasi-Arrhenius form in the intermediate temperature region which approximately indicates the interfacial

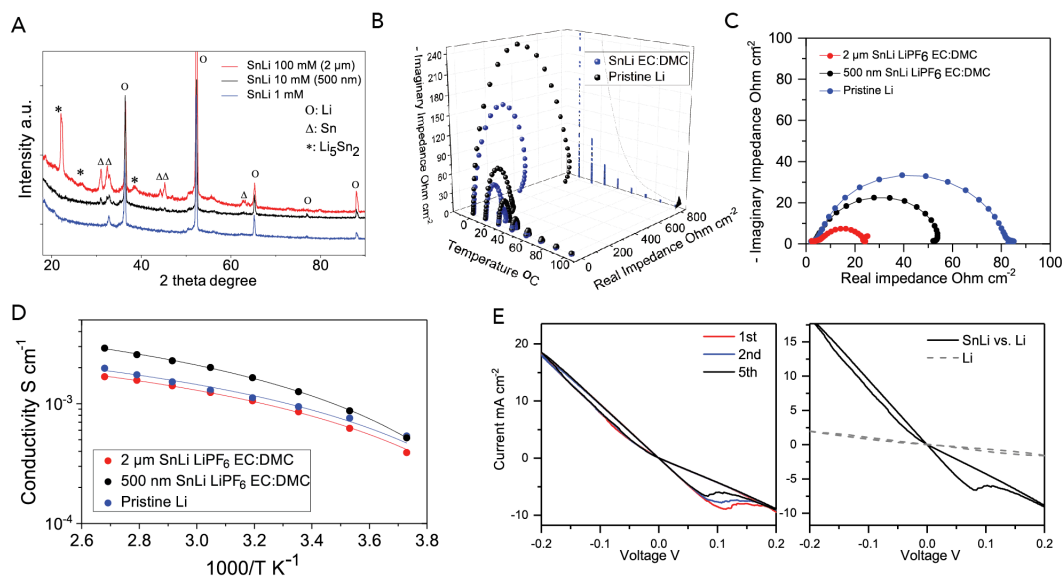


Figure 6.5. Physical and electrochemical analysis of Sn-Li hybrid electrodes. A) XRD profiles of tin-protected lithium prepared from the tin-bearing electrolyte with concentrations of 1 mM, 10 mM and 100 mM. B) Impedance spectra of symmetric lithium cells with tin-protected lithium and pristine lithium at a range of temperatures from -5 to 100 °C. C) A comparison of impedance spectra of symmetric lithium cells with tin-protected lithium and pristine lithium at room temperature. D) Temperature-dependent ionic conductivity of symmetric lithium cells with tin-protected lithium and pristine lithium. E) Cyclic voltammogram of cells with lithium/tin-protected lithium and lithium/lithium electrodes scanned with 1 mV s⁻¹.

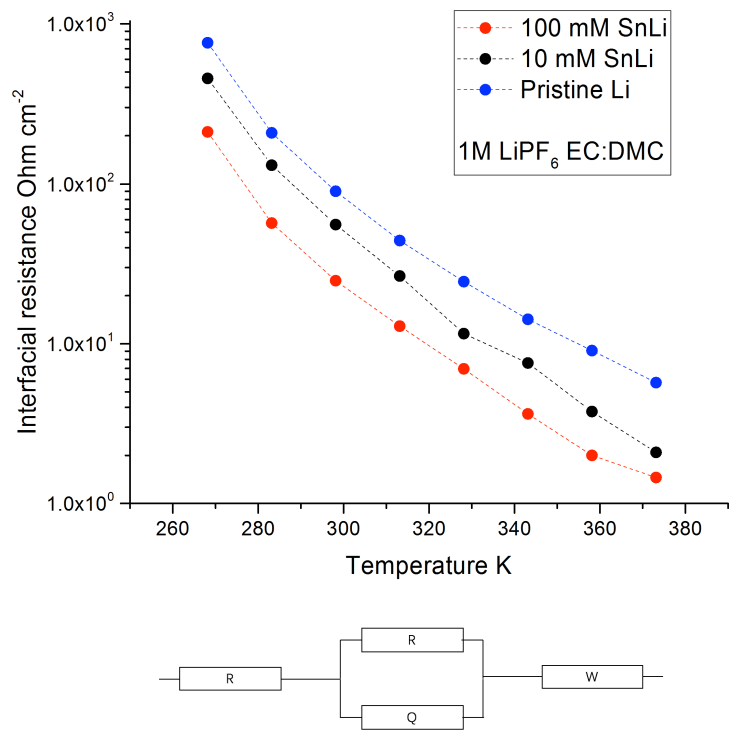


Figure 6.6. Temperature-dependent Interfacial resistance fitted from the equivalent circuit model: R(RQ)W, in which R is the resistance, Q is the constant phase element and the W is the Warburg element.

transport being a thermally activated procedure. Only one semicircle appears in the spectra which indicates that the tin protection introduces no additional interfacial transport resistance. In fact, the interfacial resistance of cells using Sn-Li anodes are gradually lowered with increasing concentration of tin-bearing electrolyte compared with that of the pristine lithium, as presented in **Figure 6.5C**. A nearly threefold decrease (from approximately 80 Ohm cm^{-2} (pristine) to 25 Ohm cm^{-2} ($2 \text{ }\mu\text{m}$ tin protection)) of the interfacial resistance is observed. This result demonstrates that ion transport through the Sn SEI is unhindered and perhaps even promoted, which we suspect comes from fast charge transfer kinetics at the Sn/Li interface. In particular, it is well known that because of its reactivity with oxygen, lithium metal foil usually forms an insulating oxidized layer on its surface even when stored in an Ar filled glovebox. By treating the lithium with tin-bearing electrolyte, the oxidized layer is replaced by electrochemically active Sn nanostructures, which significantly facilitate ion transport through the SEI. Evidence in support of this point is presented in **Figure 6.7** where the interfacial impedance of Sn-Li anodes exposed to air is reported as a function of time. It is clearly seen that the Sn overlayer leads to enhanced chemical stability of the interface, which would enable integration of such electrodes in conventional dry-room manufacturing processes. The temperature-dependent ionic conductivity of electrolytes in contact with the Sn-Li anodes is reported in **Figure 6.5D** for various Sn coating thicknesses. The conductivity is seen to exhibit a Vogel–Fulcher–Tamman (VFT) temperature dependence in all cases and cells based on the 500 nm Sn layer exhibit the highest ionic conductivity (1.3 mS cm^{-1} at room temperature) compared with the pristine Li and SnLi with thicker Sn layer.

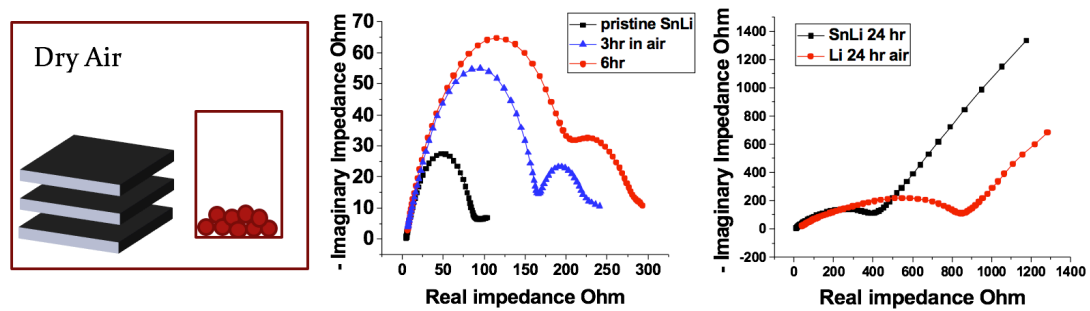


Figure 6.7. Dry air stability of the tin-protected lithium. Left: illustration of the dry air chamber composed of a desiccator filled with molecular sieves in which the relative humidity was kept $< 10\%$. Middle and right: impedance spectra of the tin-protected lithium after different amounts of exposure time, compared with the pristine lithium.

Considering essentially the same electrolyte is used in the measurement, the slight variation of the conductivity may come from the increased actual surface area of the 500 nm thick-SnLi with a particle-covering surface, in contrast to the flat pristine Li or glassy 2 μm -thick SnLi surface. To further understand the electrochemical features of a Sn-Li anode, symmetric cells composed of a pristine Li electrode and a Sn-Li working electrode were evaluated using cyclic voltammetry (**Figure 6.5E**). The broad peak near 100 mV corresponding to tin lithiation/delithiation has been observed during multiples cycles in addition to the typical Li/Li⁺ polarization curves, which corroborates the understanding that the Sn layer on Li is electrochemically active along with lithium plating/stripping. XPS analysis on the cycled Sn-Li anode (**Figure 6.8**) reveals a SEI composed of typical materials including lithium carbonate, lithium alcohonate, and fluorinated species. High-resolution scanning in the Sn 3d region shows completely attenuated peaks due to a SEI formed during the surface treatment. These peaks become more pronounced and only slightly attenuated after multiple cycles, which testifies to the stable lithium-tin interaction without obvious SEI buildup, a result in agreement with the previous study⁵¹. The right figure in 2E compares the cyclic voltammogram of Li/Li cell and Li/Sn-Li cells. The drastic slope difference is the most significant feature. Fitting the small overpotential region of the I- η curve to Tafel equation the exchange current density can be obtained, as presented in **Figure 6.9**. The results show that the exchange current (7.5 mA cm^{-2}) for the Sn-Li anode is substantially higher than the corresponding value for Li/Li⁺ on pristine lithium⁵². The fast charge transfer kinetics obtained from the exchange current density reinforces our conclusions from the impedance results that the Sn-rich SEI on lithium facilitates

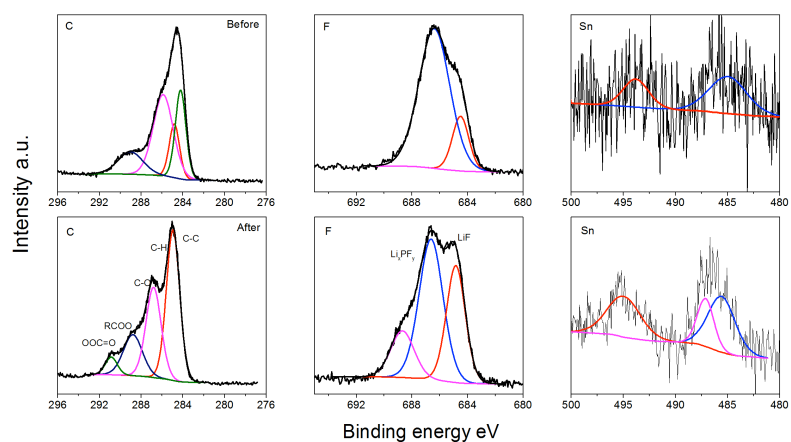


Figure 6.8. XPS profiles of the tin-protected lithium before and after cycling at 0.5 mA cm^{-2} , 0.5 mAh cm^{-2} for 10 cycles. High-resolution carbon, fluorine, and tin elements are presented. Sample transferring was accomplished in an inert sample transfer puck directly from the argon-filled glovebox to the high vacuum chamber.

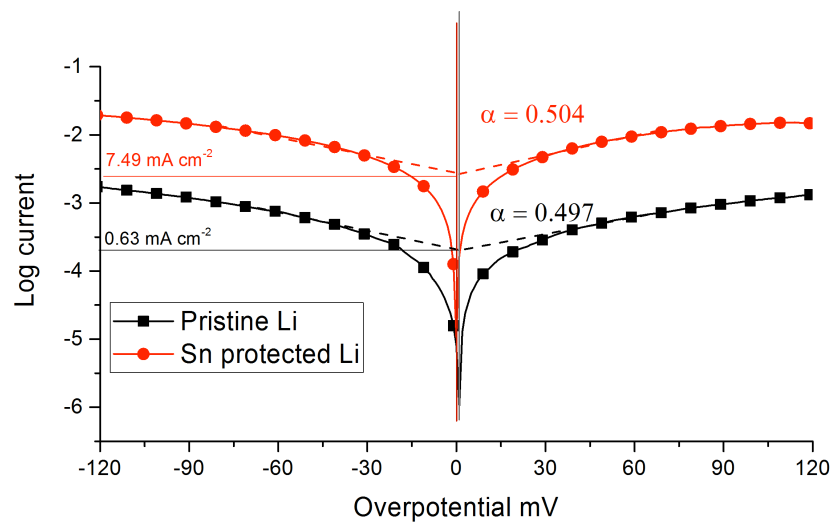


Figure 6.9. Tafel plot of the pristine lithium cell and the tin-protected lithium cell.

faster charge transfer at the electrode. Further investigations have been conducted on understanding the properties of the Sn coating alone using cells with inert stainless steel(SS) electrodes. To ensure a direct comparison, the same Sn coating on the SnLi electrode has been transferred on the stainless steel, as described in the experimental section. **Figure 6.10** compare the impedance spectra of the SnSS cell with the SnLi. Similar low interfacial impedance compared to the pristine lithium (**Figure 6.5C**) has been observed which confirms the effectiveness of the Sn coating on improving interfacial ion transport. The electrochemical activity of the Sn coating can be straightforwardly examined by the cyclic voltammetry, as shown in **Figure 6.11**. Pronounced peaks in the range of 0.3 – 0.8 V represent ions intercalating into Sn[cite], along with the lithium plating/stripping peaks at lower voltage. Similar electrochemical response can be observed from the galvanostatic cycling of the cell as reported in **Figure 6.12**. A plateau at in the range of 0.3 -0.4 V during the cell discharge at the low current can be attributed to the lithiation of Sn. Post-mortem SEM images have also been harvested to understand the structural change after the cycling. **Figure 6.13** compare the images of SnSS surface before and after cycling, which shows the full retaining of the Sn particle morphology despite slight agglomeration is observed (**Figure 6.14**). The Sn coating further facilitates to form flat lithium electrodeposits possibly by forming a SnLi/Li composite.

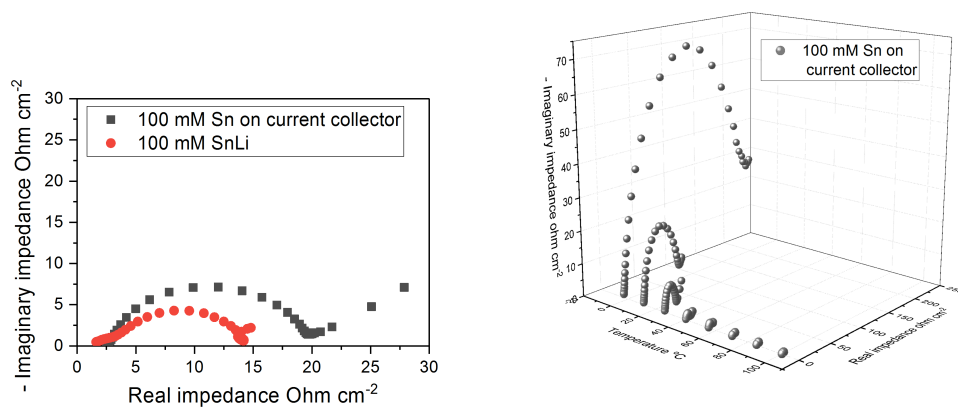


Figure 6.10. Left: a comparison of impedance spectra of cell with Sn coating on Li and cell with Sn coating on stainless steel. Right: temperature-dependent impedance spectra of cell with Sn coating on stainless steel

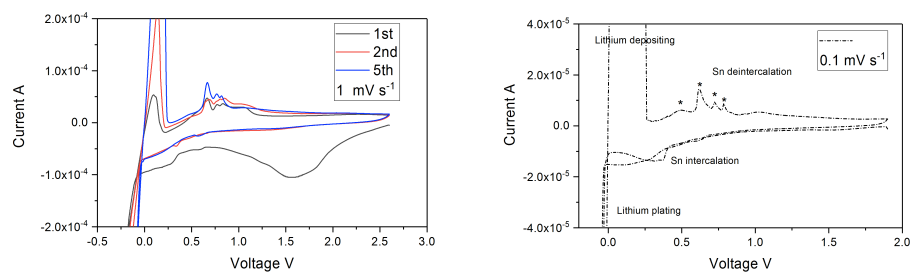


Figure 6.11. Cyclic voltammogram of Li – Sn/stainless steel cell scanned at 1 mV s⁻¹ and 0.1 mV s⁻¹, respectively.

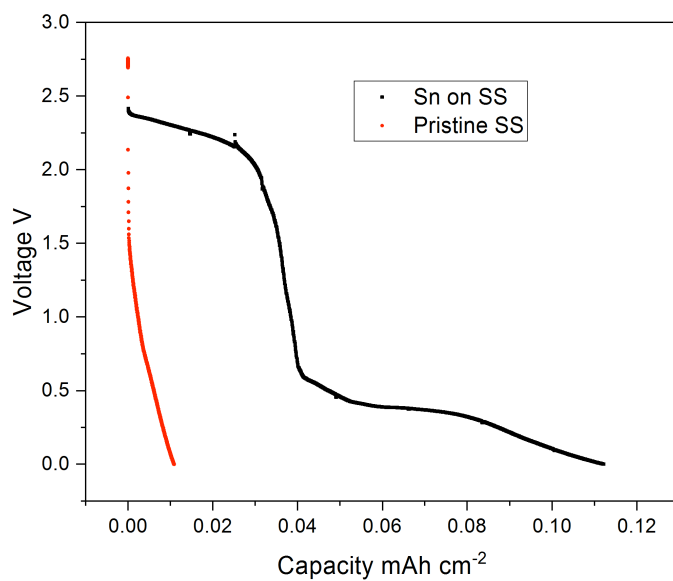


Figure 6.12. Galvanostatic discharge of Li-stainless steel (SS) cell and Li-Sn/SS cell at 0.01 mA cm⁻².

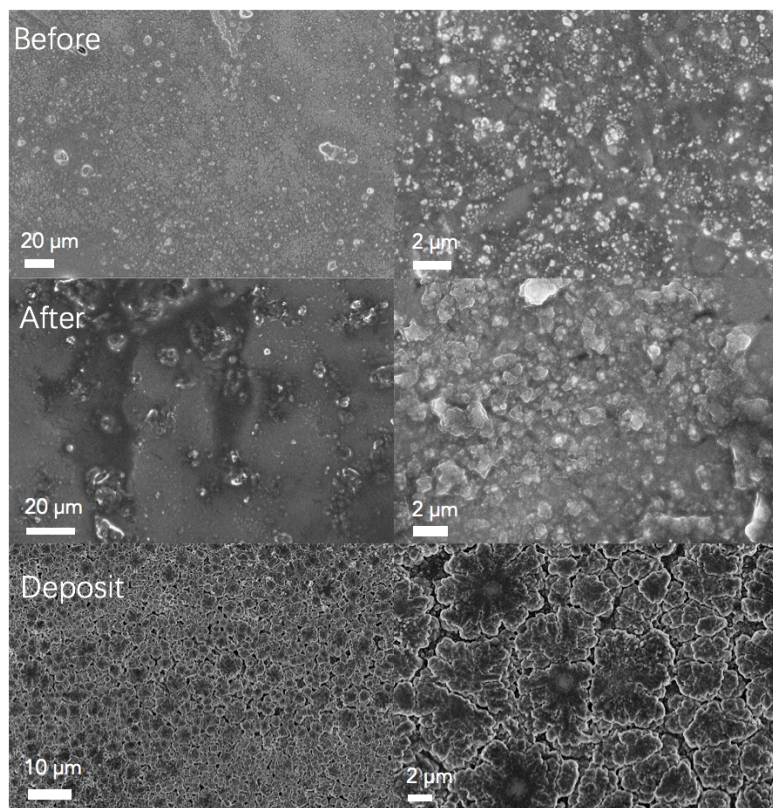


Figure 6.13. SEM images of the Sn coating on the stainless steel before and after 50 cycles at 1 mA cm^{-2} , 1 mAh cm^{-2} , and the morphology of the deposits shown in the bottom figures.

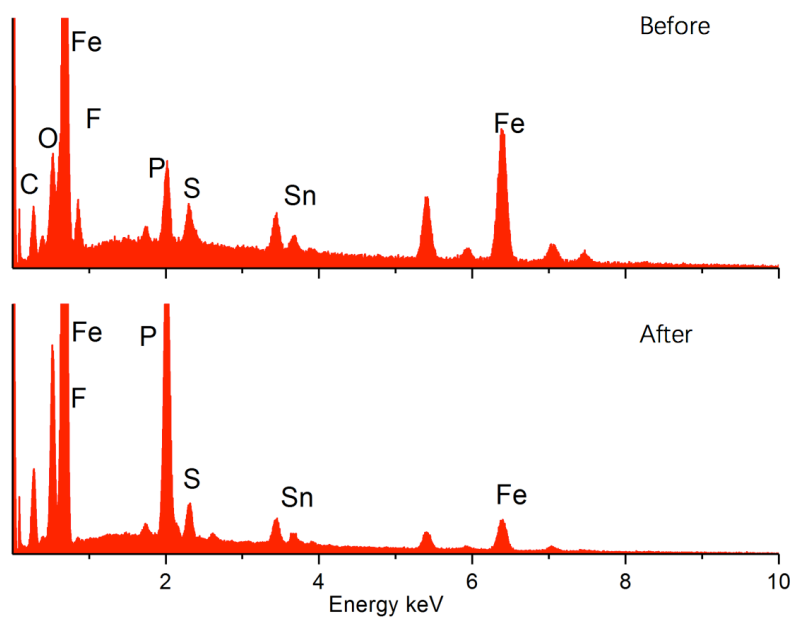


Figure 6.14. EDX spectra of the Sn coating on the stainless steel before and after 50 cycles at 1 mA cm^{-2} , 1 mAh cm^{-2} .

In addition to the desired electrochemical properties, a suitable artificial SEI on lithium is expected to suppress dendrite proliferation, especially during long-term battery operation. Lithium electrodeposition at a 500 nm Sn-Li electrode was visualized using a custom-built optical cell used previously that fits in the stage of an up-right optical microscope (Nikon Optiphot) equipped with extra-long working distance objectives. For these experiments, Sn coatings were applied on two cylinder-shape lithium surfaces, which are connected to the battery tester by stainless steel transmission wires. Real-time images of the electrolyte/Sn interface can be captured at all stages of electrodeposition using the optical microscope. **Figure 6.15A** (top) shows the evolution of the interface profile during the initial electrodeposition at a current density of 4 mA cm^{-2} . It is seen that the electrode substrate has a smooth morphology and is essentially dendrite-free, with a visually slower growth rate compared with the pristine lithium shown in the lower panel of the same figure. Semi-quantitative analysis can be performed on images using ImageJ software to obtain deposition thickness and roughness (here defined as the ratio between the 2D image area from the measurement and the theoretical value assuming a dense, flat deposit) as a function of capacity, as presented in **Figure 6.15B**. Drastic morphology and roughness differences are apparent during the initial deposition of $0.5 - 1 \text{ mAh cm}^{-2}$, a capacity roughly equivalent to the lithium ion capacity of the tin coating. Electrodeposition of more lithium on the Sn-Li electrode is seen to produce a slightly rougher surface morphology, which is within expectations considering the above diffusion limiting current applied. The overall roughness is the Sn-Li electrodes are nonetheless

remarkably reduced relative to the rapid and uncontrollable mossy deposits observed for a pristine Li electrode. These results further imply the electrochemically active Sn overlayer on the Li electrode is able to stabilize electrodeposition of Li likely by alloying with Li and facilitating fast interfacial transport. Similar results have been obtained in the ex situ post-mortem SEM study on Sn-Li electrodes with different amount of deposits (**Figure 6.16**). The non-dendritic morphology retains after multiple cycles (**Figure 6.17**), which along with the XPS results confirm the stability of the Sn coating during the lithium plating/stripping. Both in situ and ex situ studies clearly demonstrate that tin-protection is effective on achieving dendrite free deposition of lithium even at the high current density.

The SEI formed on an electrode is understood to be dynamic, varying with time and in space. A requirement for interface stability is that artificial interphases must be able to survive extensive cycling. Here we show in **Figure 6.15C** that the Sn-Li anode can be steadily operated in a symmetric cell configuration at a practical current density of 3 mA cm^{-2} and a capacity of 3 mAh cm^{-2} per cycle. No short-circuit has been observed during a 500-hour period of continuous measurement, as opposed to the control which exhibits a permanent failure evidenced by the sudden voltage drop occurring at about 55 hours, as compared in **Figure 6.15D** and **Figure 6.18**. The stability of the Sn-Li anode makes it a promising candidate for new types of Li batteries that rely on a combination of plating and alloying processes for achieving stable, long-term operation. **Figure 6.15E** shows that such cells can be operated in prototype full cell configurations paired with state-of-the art intercalating cathodes (NCA) with high loading (19.9 mg cm^{-2} ; 3 mAh cm^{-2}); the inset reports the voltage-capacity profile. A

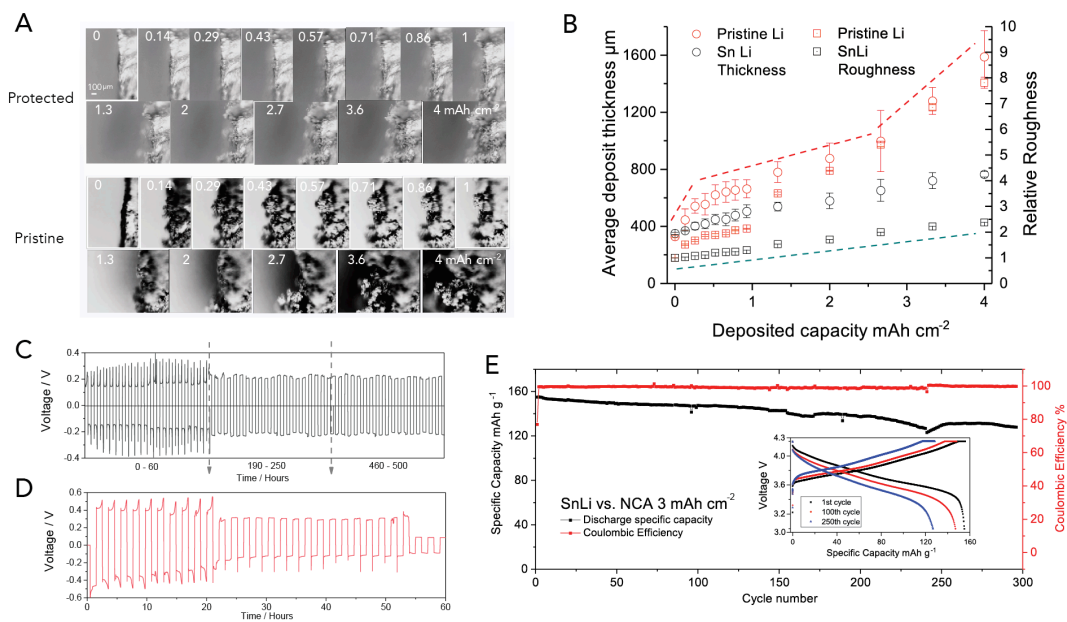


Figure 6.15. Direct and indirect demonstrations of stability of Sn-Li hybrid anodes. A) Capacity-sequenced optical microscopy images of the electrolyte-electrode interface during electrodeposition on Sn-Li (top) and pristine lithium (bottom) electrodes at a current density of 4 mA cm⁻². B) Quantitative analysis of average deposition thickness (red) and relative roughness (black) during the deposition observed in fig. 3A. C) Voltage profile of galvanostatic lithium plating/stripping on the symmetric tin-protected lithium cell at a current density of 3 mA cm⁻² for one hour each step. D) The same experiment applied on the symmetric pristine lithium cell. E) Cycling profile of the tin-protected lithium vs. NCA with 3 mAh cm⁻² areal capacity operated from 3 to 4.2 V at 0.5C. The inset shows the voltage profile of the 1st, 100th, and 200th cycle.

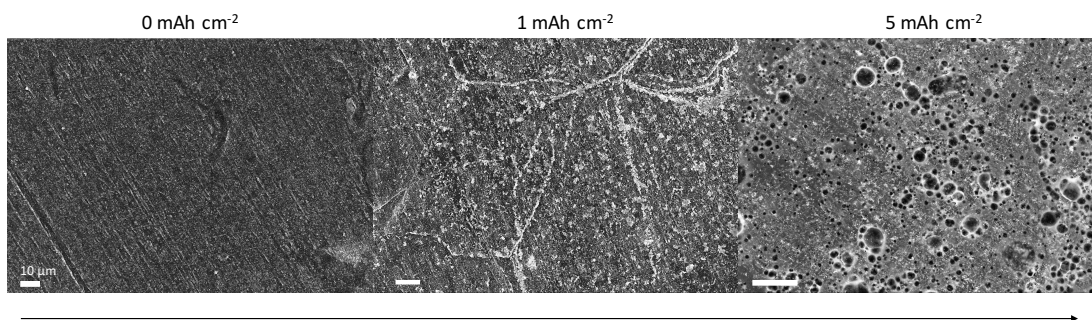


Figure 6.16. Post-mortem SEM images of tin-protected lithium after being initially electrodeposited with different amounts of lithium.

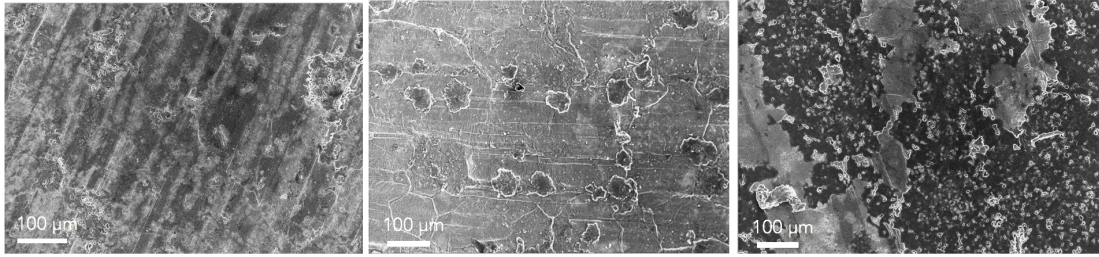


Figure 6.17. SEM images of the Sn coating on the lithium before and after 10 cycles at left: 0.5 mA cm^{-2} , 0.1 mAh cm^{-2} , middle: 0.5 mA cm^{-2} , 0.5 mAh cm^{-2} , and right: 0.5 mA cm^{-2} , 3 mAh cm^{-2} .

capacity retention > 80% is observed over 300 cycles of operation at a rate of 0.5 C with Coulombic efficiency close to unity (**Figure 6.19**). Similar stable battery operation has also been observed in cells equipped with LiCoO₂ cathodes (**Figure 6.20**), which testifies to the broad compatibility of the Sn-Li hybrid anode configuration studied here. Considering the high specific capacity of the lithium and saving from the copper current collector, an anode/cathode capacity ratio of 30 to 1 offers comparable gravimetric energy density to the lithium ion batteries at materials level. To further reduce the lithium amount in the cell, the potential application of the hybrid anodes in cells where the anode:cathode capacity ratio is fixed at 3:1 is illustrated in **Figure 6.21**. A pre-determined capacity of lithium has been firstly deposited on a stainless steel and treated with tin-bearing electrolyte to serve as the anode. In contrast to the pristine lithium, which fails quickly within 30 cycles, Sn-Li||NCA cells cycle stably for over 100 cycles as a result of alleviated lithium loss. Post-mortem analysis (figure S20) reveals that thickened SEI forms as a result of electrolyte decomposition, despite the surface morphology remains flat. This in principle leads to an increased impedance which underscores the necessary efforts to optimize the electrolyte composition for Sn-Li anodes that are expected to yield further improvements in cell performance.

The success of the Sn-Li hybrid electrodes leads one to wonder if the same concept might be applied to achieve stability of sodium anodes, notorious for their reactivity with carbonate electrolytes and propensity to form rough, dendritic deposits during battery recharge. To evaluate this, Sn-Na hybrid electrodes were prepared in a similar manner based on ion exchange with a Sn salt additive. **Figure 6.22A** compares the

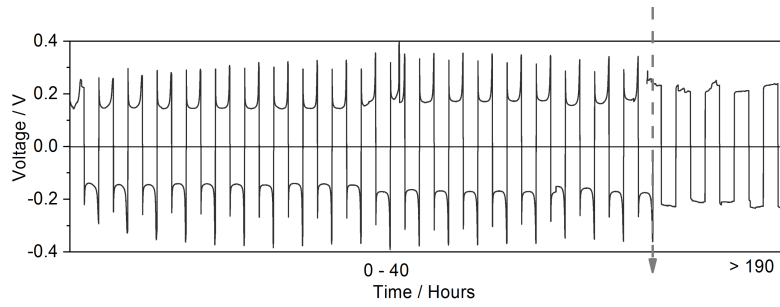


Figure 6.18. Zoom-in initial voltage profile as in Figure 6.15C, the abnormal spike in the middle of the cycling is associated with an unexpected software error.

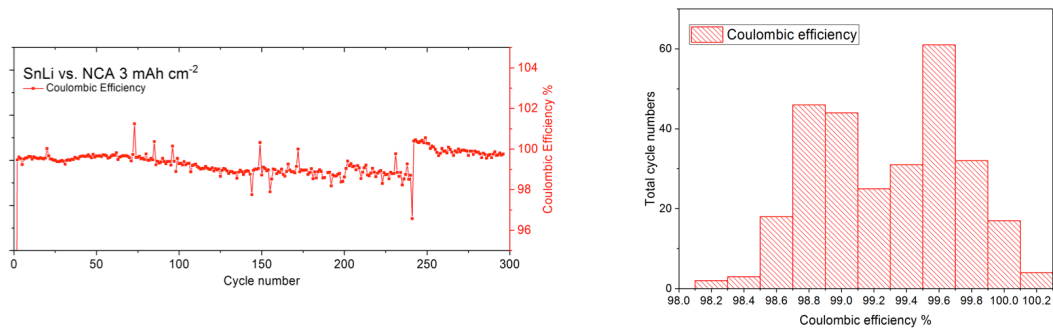


Figure 6.19. Left: zoom in image of the Coulombic efficiency profile of the SnLi – NCA cell. Right: analysis of the Coulombic efficiency in all cycles.

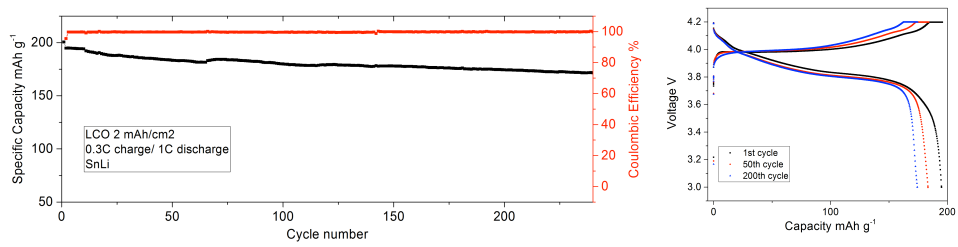


Figure 6.20. Capacity and voltage profile of the tin-protected lithium vs. LCO cathode (2 mAh cm⁻²). The cycling was operated at 0.3C/1C charge/discharge condition.

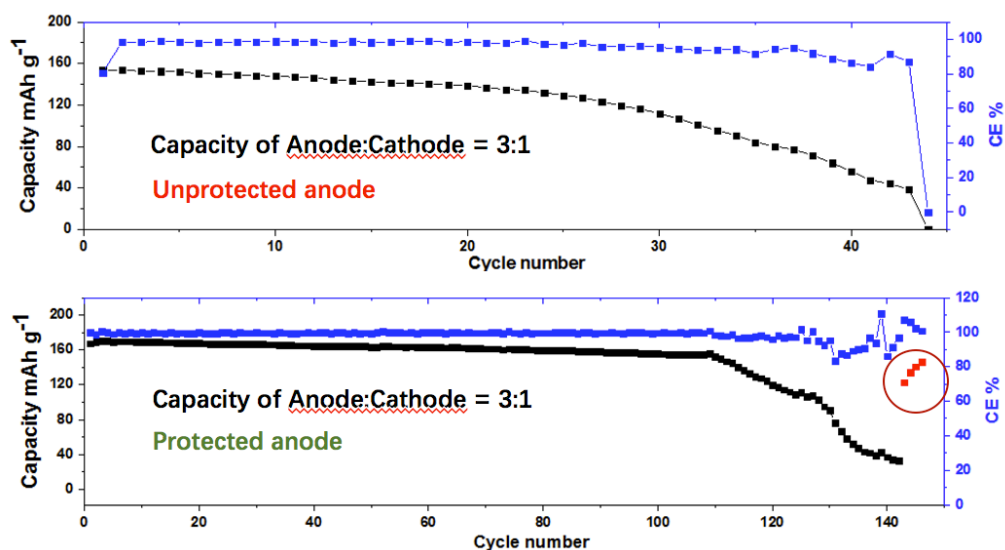


Figure 6.21. Capacity and efficiency profile of the tin-protected lithium vs. NCA cathode (3 mAh cm^{-2}) operated at 0.5C with anode to cathode capacity ratio of 3:1. The pre-determining amount of lithium was electrodeposited in 1M LiTFSI DOL:DME on a stainless steel electrode, followed by cleaning with DOL and the tin-bearing electrolyte treatment. The red points in the end represents the battery cycled at 0.1C , which shows a significant capacity recovery indicating the loss of capacity largely arises from the increased resistance.

impedance spectra measured at room temperature for the pristine symmetric sodium cell and symmetric Sn-Na cells, both in a 1M NaPF₆ EC: propylene carbonate (PC) based electrolyte. The interfacial resistance of the Sn-Na cells is evidently significantly reduced compared with the pristine case. In contrast to lithium, the Sn layer on sodium is mostly in the form of a sodium-rich alloy instead of the elemental metal as evidenced by XRD profile (**Figure 6.23**). Some oxide peaks are observed as a result of swift reaction of sodium in the environment. This can be attributed to the high reactivity of the sodium. After cycling symmetric cells for 10 cycles at a current density of 0.5 mA cm⁻², both pristine and Sn-Na electrodes were harvested and observed using SEM (**Figure 6.22B**). The pristine sodium forms irregular bumps covering the surface likely due to the non-uniform, fragile SEI formation because of the electrolyte decomposition. On the other hand, the surface of the Sn-Na electrode maintains a flat, uniform morphology. A protected electrode surface is particularly critical for long-term battery operation. As a proof-of-concept, the symmetric sodium cells were subjected to repeated charge/discharge cycles at moderate current densities of 0.25 and 0.5 mA cm⁻², as shown in **Figure 6.22C** and **D**. Sodium metal batteries typically fail quickly due to the resistive SEI formed by uncontrolled side reactions between sodium and the electrolyte, which manifests in a tell-tale voltage divergence at the end of life. In contrast, the Sn-Na symmetric cells exhibit drastically improved voltage profiles over 1700 hours at 0.25 mA cm⁻² and 1000 hours at 0.5 mA cm⁻² of operation, with only slight increase of overpotential. Whereas the pristine sodium cell exhibits a quick voltage divergence to 1V after merely 250 hours even at the low current density, presented in **Figure 6.22E** and **F**. These results evidently suggest that

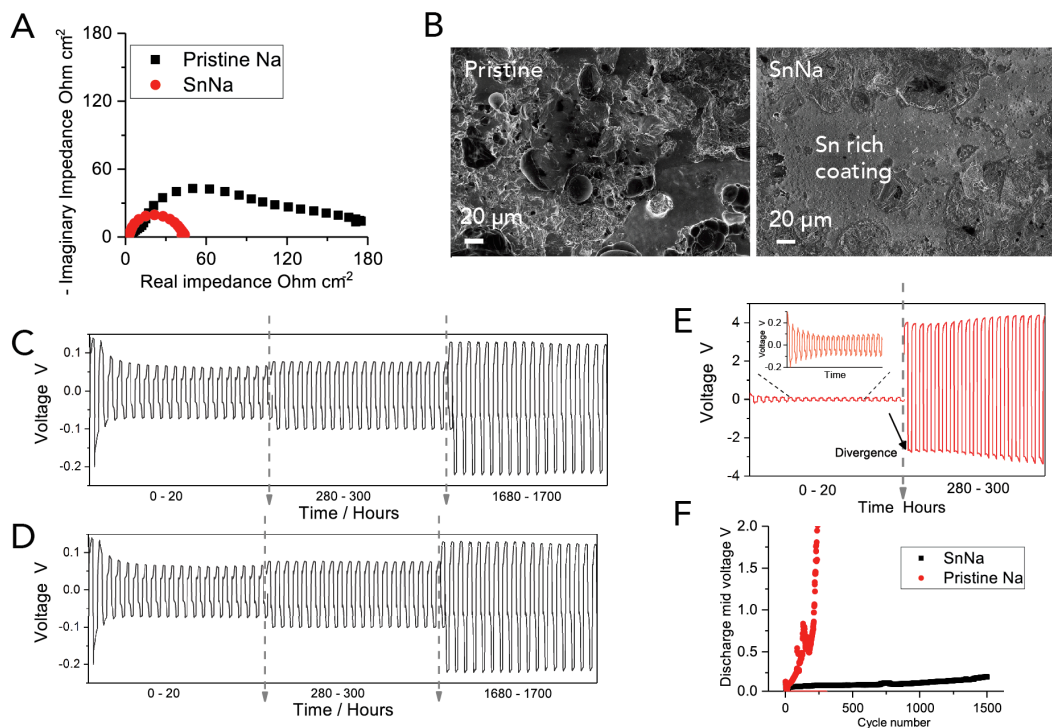


Figure 6.22. Hybrid Sn-Na anodes offer a route to stable deposition at reactive sodium electrodes. A) Impedance spectra of the tin-protected sodium symmetric cell and pristine sodium symmetric cell measured at room temperature. B) Post-mortem SEM images on the pristine sodium electrode (left) and tin-protected sodium electrode (right) after being cycled at 0.5 mA cm^{-2} and 0.25 mAh cm^{-2} for 10 cycles. C) Voltage profile of sodium plating/stripping on the symmetric tin-protected sodium cell at a current density of 0.25 mA cm^{-2} for one hour each step. D) Voltage profile of sodium plating/stripping on the symmetric tin-protected sodium cell at a current density of 0.5 mA cm^{-2} for half an hour each step. E) Voltage profile of sodium plating/stripping on the symmetric pristine sodium cell at a current density of 0.25 mA cm^{-2} for one hour each step, with the inset showing the first 20-hour plot. F) Average discharge voltage at different cycles for the tin-protected sodium and the pristine sodium from **Figure 6.22C** and **6.22E**.

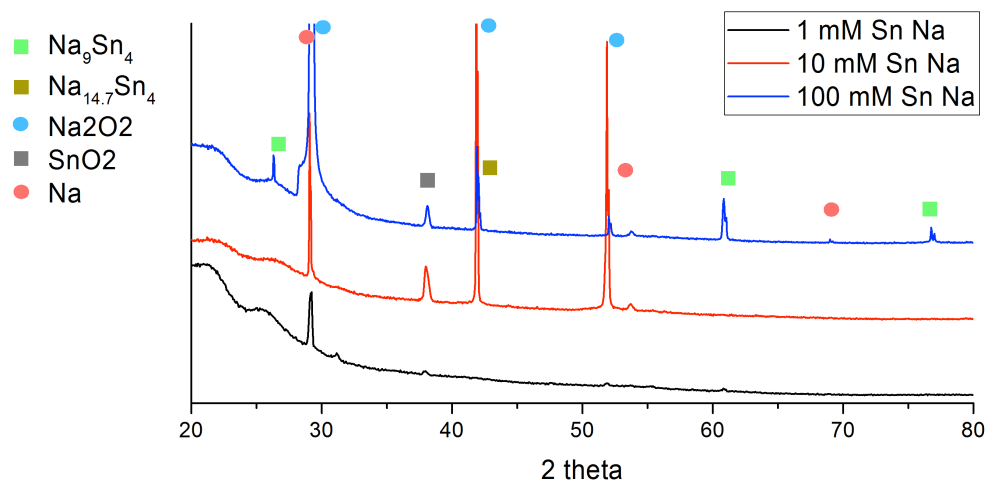


Figure 6.23. XRD profile of the tin-protected sodium treated with different tin-bearing electrolytes measured in Kapton tape envelopes.

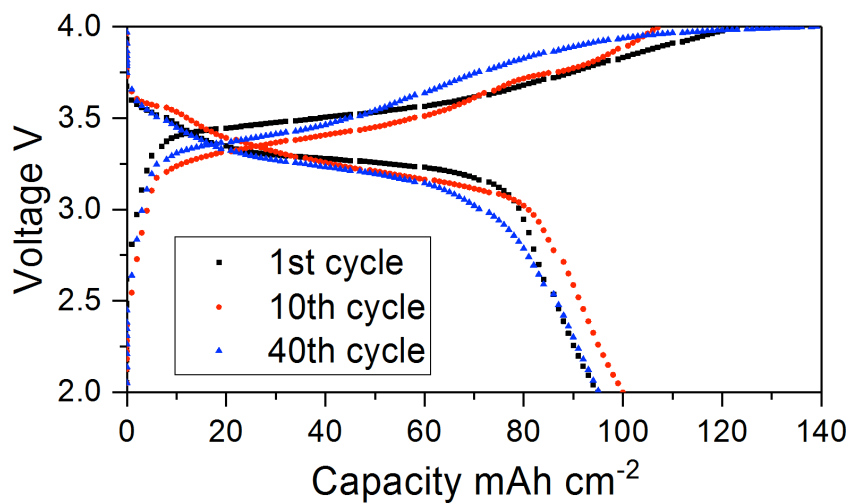


Figure 6.24. Voltage-capacity profile of SnNa / Sodium manganese hexacyanoferrates cell at different cycle numbers operated at 2C. The Prussian blue electrode was prepared as previously reported. The electrode contains 50 wt% active material, 40% super P, and 10% PVDF binder.

Sn protection of reactive metal anodes provides a versatile route towards hybrid anodes that take advantage of alloying and plating process for stable, high-energy electrochemical storage.

In summary, we report that hybrid anodes created by depositing Sn on the surface of reactive metals such as Li and Na via a facile ion-exchange reaction provides a mechanism for protecting the anode and at the same time facilitate fast charge transfer kinetics at the electrode. We find that Sn-Li and Sn-Na anodes exhibit vastly reduced interfacial impedance and much higher exchange current in liquid electrolytes, which is attributed to a hybrid ion storage mechanism including both metal electrodeposition and alloying. Sn-Li anodes are also reported by means of direct visualization studies in an optical microscope and ex-situ electron microscopy measurements to exhibit stable long-term galvanostatic cycling without forming dendrites. The excellent stability of Sn-Li is further demonstrated in studies utilizing the material as the anode for lithium metal batteries where it is paired with a high loading (19.9 mg cm^{-2} , 3 mAh cm^{-2}) NCA cathode. Motivated by these observations, we show that Sn-Na anodes exhibit an impressive ability to facilitate stable electrodeposition sodium, which is known to be intrinsically more reactive. Over 1600 hours of steady operation of symmetric protected sodium batteries can be achieved at moderate current densities with no signs of voltage divergence typically observed in Na cells.

Reference

1. Armand, M.; Tarascon, J. M., Building better batteries. *Nature* **2008**, *451* (7179), 652-657.
2. Goodenough, J. B.; Kim, Y., Challenges for rechargeable Li batteries. *Chem. Mater.* **2009**, *22* (3), 587-603.
3. Bruce, P. G., Energy storage beyond the horizon: Rechargeable lithium batteries. *Solid State Ionics* **2008**, *179* (21-26), 752-760.
4. Whittingham, M. S., Electrical energy storage and intercalation chemistry. *Science* **1976**, *192* (4244), 1126-1127.
5. Xu, W.; Wang, J. L.; Ding, F.; Chen, X. L.; Nasybutin, E.; Zhang, Y. H.; Zhang, J. G., Lithium metal anodes for rechargeable batteries. *Energy Environ. Sci.* **2014**, *7* (2), 513-537.
6. Tikekar, M. D.; Choudhury, S.; Tu, Z.; Archer, L. A., Design principles for electrolytes and interfaces for stable lithium-metal batteries. *Nature Energy* **2016**, *1*, 16114.
7. Lin, D.; Liu, Y.; Cui, Y., Reviving the lithium metal anode for high-energy batteries. *Nature Nanotechnology* **2017**, *12* (3), 194-206.
8. Etacheri, V.; Marom, R.; Elazari, R.; Salitra, G.; Aurbach, D., Challenges in the development of advanced Li-ion batteries: a review. *Energy Environ. Sci.* **2011**, *4* (9), 3243-3262.
9. Tarascon, J. M.; Armand, M., Issues and challenges facing rechargeable lithium batteries. *Nature* **2001**, *414* (6861), 359-367.

10. Aurbach, D.; McCloskey, B. D.; Nazar, L. F.; Bruce, P. G., Advances in understanding mechanisms underpinning lithium–air batteries. *Nature Energy* **2016**, *1*, 16128.
11. Ma, L.; Hendrickson, K. E.; Wei, S.; Archer, L. A., Nanomaterials: Science and applications in the lithium–sulfur battery. *Nano Today* **2015**, *10* (3), 315-338.
12. Li, Y.; Dai, H., Recent advances in zinc–air batteries. *Chem. Soc. Rev.* **2014**, *43* (15), 5257-5275.
13. Wei, S.; Xu, S.; Agrawal, A.; Choudhury, S.; Lu, Y.; Tu, Z.; Ma, L.; Archer, L. A., A stable room-temperature sodium-sulfur battery. *Nature communications* **2016**, *7*.
14. Al Sadat, W. I.; Archer, L. A., The O₂-assisted Al/CO₂ electrochemical cell: A system for CO₂ capture/conversion and electric power generation. *Science advances* **2016**, *2* (7), e1600968.
15. Tu, Z.; Nath, P.; Lu, Y.; Tikekar, M. D.; Archer, L. A., Nanostructured electrolytes for stable lithium electrodeposition in secondary batteries. *Acc. Chem. Res.* **2015**, *48* (11), 2947-2956.
16. Cheng, X. B.; Zhang, R.; Zhao, C. Z.; Wei, F.; Zhang, J. G.; Zhang, Q., A review of solid electrolyte interphases on lithium metal anode. *Advanced Science* **2015**.
17. Xu, K., Electrolytes and interphases in Li-ion batteries and beyond. *Chem. Rev.* **2014**, *114* (23), 11503-11618.
18. Verma, P.; Maire, P.; Novák, P., A review of the features and analyses of the solid electrolyte interphase in Li-ion batteries. *Electrochim. Acta* **2010**, *55* (22), 6332-6341.

19. Ji, L.; Lin, Z.; Alcoutlabi, M.; Zhang, X., Recent developments in nanostructured anode materials for rechargeable lithium-ion batteries. *Energy Environ. Sci.* **2011**, *4* (8), 2682-2699.
20. Wei, S.; Choudhury, S.; Xu, J.; Nath, P.; Tu, Z.; Archer, L. A., Highly Stable Sodium Batteries Enabled by Functional Ionic Polymer Membranes. *Adv. Mater.* **2017**, *29* (12).
21. Khurana, R.; Schaefer, J. L.; Archer, L. A.; Coates, G. W., Suppression of lithium dendrite growth using cross-linked polyethylene/poly (ethylene oxide) electrolytes: a new approach for practical lithium-metal polymer batteries. *J. Am. Chem. Soc.* **2014**, *136* (20), 7395-7402.
22. Tung, S.-O.; Ho, S.; Yang, M.; Zhang, R.; Kotov, N. A., A dendrite-suppressing composite ion conductor from aramid nanofibres. *Nature communications* **2015**, *6*.
23. Fergus, J. W., Ceramic and polymeric solid electrolytes for lithium-ion batteries. *J. Power Sources* **2010**, *195* (15), 4554-4569.
24. Lu, Y.; Korf, K.; Kambe, Y.; Tu, Z.; Archer, L. A., Ionic-Liquid–Nanoparticle Hybrid Electrolytes: Applications in Lithium Metal Batteries. *Angew. Chem. Int. Ed.* **2014**, *53* (2), 488-492.
25. Villaluenga, I.; Wujcik, K. H.; Tong, W.; Devaux, D.; Wong, D. H.; DeSimone, J. M.; Balsara, N. P., Compliant glass–polymer hybrid single ion-conducting electrolytes for lithium batteries. *Proceedings of the National Academy of Sciences* **2016**, *113* (1), 52-57.

26. Tu, Z.; Lu, Y.; Archer, L., A Dendrite-Free Lithium Metal Battery Model Based on Nanoporous Polymer/Ceramic Composite Electrolytes and High-Energy Electrodes. *Small* **2015**.
27. Tu, Z.; Zachman, M. J.; Choudhury, S.; Wei, S.; Ma, L.; Yang, Y.; Kourkoutis, L. F.; Archer, L. A., Nanoporous Hybrid Electrolytes for High-Energy Batteries Based on Reactive Metal Anodes. *Advanced Energy Materials* **2017**.
28. Monroe, C.; Newman, J., The impact of elastic deformation on deposition kinetics at lithium/polymer interfaces. *J. Electrochem. Soc.* **2005**, *152* (2), A396-A404.
29. Bouchet, R.; Maria, S.; Meziane, R.; Aboulaich, A.; Lienafa, L.; Bonnet, J.-P.; Phan, T. N.; Bertin, D.; Gigmes, D.; Devaux, D., Single-ion BAB triblock copolymers as highly efficient electrolytes for lithium-metal batteries. *Nature materials* **2013**, *12* (5), 452-457.
30. Ma, Q.; Zhang, H.; Zhou, C.; Zheng, L.; Cheng, P.; Nie, J.; Feng, W.; Hu, Y. S.; Li, H.; Huang, X., Single Lithium-Ion Conducting Polymer Electrolytes Based on a Super-Delocalized Polyanion. *Angew. Chem. Int. Ed.* **2016**, *55* (7), 2521-2525.
31. Lu, Y.; Tikekar, M.; Mohanty, R.; Hendrickson, K.; Ma, L.; Archer, L. A., Stable Cycling of Lithium Metal Batteries Using High Transference Number Electrolytes. *Advanced Energy Materials* **2015**.
32. Korf, K. S.; Lu, Y.; Kambe, Y.; Archer, L. A., Piperidinium tethered nanoparticle-hybrid electrolyte for lithium metal batteries. *Journal of Materials Chemistry A* **2014**, *2* (30), 11866-11873.
33. Lee, Y. M.; Seo, J. E.; Lee, Y.-G.; Lee, S. H.; Cho, K. Y.; Park, J.-K., Effects of triacetoxymethylsilane as SEI layer additive on electrochemical performance of

lithium metal secondary battery. *Electrochem. Solid-State Lett.* **2007**, *10* (9), A216-A219.

34. Ota, H.; Shima, K.; Ue, M.; Yamaki, J.-i., Effect of vinylene carbonate as additive to electrolyte for lithium metal anode. *Electrochim. Acta* **2004**, *49* (4), 565-572.

35. Zhang, X. Q.; Cheng, X. B.; Chen, X.; Yan, C.; Zhang, Q., Fluoroethylene Carbonate Additives to Render Uniform Li Deposits in Lithium Metal Batteries. *Adv. Funct. Mater.* **2017**.

36. Zheng, G.; Wang, C.; Pei, A.; Lopez, J.; Shi, F.; Chen, Z.; Sendek, A. D.; Lee, H.-W.; Lu, Z.; Schneider, H., High-performance lithium metal negative electrode with a soft and flowable polymer coating. *ACS Energy Letters* **2016**, *1* (6), 1247-1255.

37. Ma, L.; Kim, M. S.; Archer, L. A., Stable artificial solid electrolyte interphases for lithium batteries. *Chem. Mater.* **2017**, *29* (10), 4181-4189.

38. Liu, Y.; Lin, D.; Yuen, P. Y.; Liu, K.; Xie, J.; Dauskardt, R. H.; Cui, Y., An Artificial Solid Electrolyte Interphase with High Li-Ion Conductivity, Mechanical Strength, and Flexibility for Stable Lithium Metal Anodes. *Adv. Mater.* **2017**, *29* (10).

39. Li, J.; Dudney, N. J.; Nanda, J.; Liang, C., Artificial solid electrolyte interphase to address the electrochemical degradation of silicon electrodes. *ACS applied materials & interfaces* **2014**, *6* (13), 10083-10088.

40. Choudhury, S.; Agrawal, A.; Wei, S.; Jeng, E.; Archer, L. A., Hybrid hairy nanoparticle electrolytes stabilizing lithium metal batteries. *Chem. Mater.* **2016**, *28* (7), 2147-2157.

41. Kim, M. S.; Ma, L.; Choudhury, S.; Archer, L. A., Multifunctional Separator Coatings for High-Performance Lithium–Sulfur Batteries. *Advanced Materials Interfaces* **2016**, *3* (22).
42. Kozen, A. C.; Lin, C.-F.; Pearse, A. J.; Schroeder, M. A.; Han, X.; Hu, L.; Lee, S.-B.; Rubloff, G. W.; Noked, M., Next-generation lithium metal anode engineering via atomic layer deposition. *ACS nano* **2015**, *9* (6), 5884-5892.
43. Han, X.; Gong, Y.; Fu, K. K.; He, X.; Hitz, G. T.; Dai, J.; Pearse, A.; Liu, B.; Wang, H.; Rubloff, G., Negating interfacial impedance in garnet-based solid-state Li metal batteries. *Nature materials* **2017**, *16* (5), 572-579.
44. Lin, D.; Liu, Y.; Liang, Z.; Lee, H.-W.; Sun, J.; Wang, H.; Yan, K.; Xie, J.; Cui, Y., Layered reduced graphene oxide with nanoscale interlayer gaps as a stable host for lithium metal anodes. *Nature nanotechnology* **2016**, *11* (7), 626-632.
45. Liang, Z.; Lin, D.; Zhao, J.; Lu, Z.; Liu, Y.; Liu, C.; Lu, Y.; Wang, H.; Yan, K.; Tao, X., Composite lithium metal anode by melt infusion of lithium into a 3D conducting scaffold with lithiophilic coating. *Proceedings of the National Academy of Sciences* **2016**, *113* (11), 2862-2867.
46. Tu, Z.; Choudhury, S.; Wei, S.; Archer, L., Surface Protected Active Metal Electrodes for Rechargeable Batteries. *Cornell Invention Disclosure 7607* **2017**.
47. Lou, X. W.; Wang, Y.; Yuan, C.; Lee, J. Y.; Archer, L. A., Template-free synthesis of SnO₂ hollow nanostructures with high lithium storage capacity. *Adv. Mater.* **2006**, *18* (17), 2325-2329.
48. Winter, M.; Besenhard, J. O., Electrochemical lithiation of tin and tin-based intermetallics and composites. *Electrochim. Acta* **1999**, *45* (1), 31-50.

49. Choi, Y.-S.; Byeon, Y.-W.; Ahn, J.-P.; Lee, J.-C., Formation of Zintl Ions and Their Configurational Change during Sodiation in Na–Sn Battery. *Nano Lett.* **2017**, *17* (2), 679-686.
50. Nesper, R., Structure and chemical bonding in Zintl-phases containing lithium. *Prog. Solid State Chem.* **1990**, *20* (1), 1-45.
51. Li, J.-T.; Swiatowska, J.; Seyeux, A.; Huang, L.; Maurice, V.; Sun, S.-G.; Marcus, P., XPS and ToF-SIMS study of Sn–Co alloy thin films as anode for lithium ion battery. *J. Power Sources* **2010**, *195* (24), 8251-8257.
52. Munichandraiah, N.; Scanlon, L.; Marsh, R., Surface films of lithium: an overview of electrochemical studies. *J. Power Sources* **1998**, *72* (2), 203-210.

CHAPTER 7

STABILIZING PROTIC AND APROTIC LIQUID ELECTROLYTES AND LI METAL ELECTRODES USING ULTRATHIN ARTIFICIAL SOLID ELECTROLYTE INTERPHASES

7.1 Abstract

Regulating solid electrolyte interphases has long been regarded as a critical practice to achieve efficient and reversible electrical energy storage by improving electrochemical stability window and reducing the parasitic side reactions. Here we report that a rationally engineered ceramic interphase at nanometer scale can broaden the oxidative stability limit by 1.5 V for both conventional aprotic and protic electrolytes used in lithium batteries. Such interphase further facilitates stable lithium metal electrodeposition and exhibits high Coulombic efficiency over extensive cycling at a high current density of 3 mA cm^{-2} and a capacity of 3 mAh cm^{-2} . With the high-resolution cryo-FIB-SEM characterization, the solid/compact lithium electrodeposits anchored by the ceramic interphase are understood to contribute to the stable lithium plating/stripping. The results directly enable a proof-of-concept ‘anode-free’ battery with all lithium initially provided in the cathode which in situ form a metallic anode for the long-term cycling.

7.2 Introduction

Rechargeable batteries reversibly convert stored chemical energy to electricity and are of interest in a growing family of practices, including portable electronics, electric vehicles, and renewable energy storage, etc¹⁻⁴. To meet increasing demands for more reliable, safer, and more energy dense storage, increasing attention has turned to understanding and controlling nanoscale physical and chemical processes at the solid electrode/liquid electrolyte and solid electrode/solid electrolyte interphases that normally form spontaneously during the first cycles of battery operation.⁵⁻⁶ The

chemical composition, thickness, structure, and transport properties of these interphases are now understood to be key determinants of battery performance and lifetime, but because of the complexity of spontaneously formed interphases, little is known about how and why each of these variables impact cell-level performance and even less is known about how they might be rationally designed to achieve a desired electrochemical function. It is remarkable, for example, that although the chemical potential (Fermi level) of the graphitic carbon anode in a Lithium-ion battery (LIB) lies well above the Lowest Unoccupied Molecular Orbital (LUMO) levels of the most successful aprotic liquid electrolytes, LIBs can be operated stably for hundreds to thousands of cycles of charge and discharge at high Coulombic efficiencies. The expectation that widely used alkyl carbonate electrolytes in contact with the graphitic anode would undergo continuous reduction is disproved in state-of-the-art LIBs largely as a result of the robust, electrochemically stable, and self-limiting solid electrolyte interphase (SEI) layer formed spontaneously on the anode by electrochemical breakdown of electrolyte components.⁷ We note that these issues are as pronounced at the interfaces formed between solid-state electrolytes and battery anodes⁸, as well as between emerging high voltage, Nickel-rich intercalating cathodes and liquid electrolytes⁹.

A well-formed and stable SEI is even more critical for emergent metal-based rechargeable batteries in which the graphitic carbon anode of LIBs is replaced by more electrochemically active metals such as Li, Na, Si, and Sn to achieve higher energy density¹⁰⁻¹¹. In addition to the electrochemical stability of the electrolyte at the anode working potential, the intrinsic reactivity of Li and Na means that even in the

discharged state, there is a thermodynamic driving force that favors continuous reduction of electrolyte in contact with the metals. Further, these parasitic reactions between the active metal anodes and electrolyte are now understood to be the root cause of many failure modes, including voltage divergence, dendrite formation, and active electrode material loss¹². Even more problematic is the fact that the electroplating and alloying reactions these metals undergo during battery charge result in rather large volume changes (as high as 250% for a Sn anode)¹³. It means that a spontaneously formed SEI must not only possess the traits theorized for the success of the SEI in LIBs — self-limiting formation process, electronically insulating, and ionically conductive, but it must also be able to flex and stretch to accommodate volume changes at the electrode without cracking or structural breakdown.

Herein, we report on physical properties, electrochemical features, and stability of model artificial solid-electrolyte interphases (ASEI) created from ultra-thin conformal ceramic coatings that allow us to interrogate electrochemical stability of liquid electrolytes at both high and low potentials. **Figure 7.1a** illustrates the configuration of the electrodes and ASEI used in the study. A key finding is that even at thicknesses as low as 15nm, liquid electrolytes in contact with such interphases display very large increases in anodic and cathodic stability. As illustrated in **figures 7.1b-1d**, the improvements in electrolyte stability are as impressive in protic and aprotic liquids. Results reported in **figure 7.1b**, for example, show that an ASEI composed of a 15 nm thick Al₂O₃ ALD coating on stainless steel electrodes increases the electrochemical stability window of an aqueous 1M LiTFSI electrolyte by more than 1.5V. Adopting a Li/Li⁺ reference reveals that the stability achieved is 1.1 to 4.2 V (Li/Li⁺), which is

comparable to results reported in recent pioneering studies using so-called water-in-salt electrolytes composed of 21M LiTFSI¹⁴. Application to aprotic liquid electrolytes composed of 1M LiPF₆ in propylene carbonate (PC) shows that both the electrochemical stability and ability of the electrolyte to sustain stable and reversible electrodeposition of Li metal are enhanced significantly, underscoring the importance of the anode/electrolyte interphase in stabilizing Li and other reactive metal anodes prone to fail by rough, dendritic deposition and parasitic reaction with liquid electrolytes. By combining the Al₂O₃ ASEI with a suitable liquid electrolyte we further show that it is possible to achieve high-Coulombic efficiency (> 98%) and stable lithium cycling at a current density as high as 3 mA cm⁻². Building on these observations, we investigate long-term stability in lithium cells in which the only source of Li is in the cathode.

7.3 Experimental Section

Polished copper plates were purchased from McMaster Carr and cut into 1 cm by 1 cm square electrodes. Plasmon Enhanced Atomic layer deposition (PEALD) of Al₂O₃ was accomplished in the clean room of Cornell NanoScale Science & Technology Facility (CNF) using Oxford ALD FlexAL with trimethylaluminum (TMA) as the precursor at 110 °C. CR2032 coin cells were assembled for electrochemical measurements with Celgard 3501 as the separator. 1 M LiPF₆ in PC was purchased from Sigma Aldrich and stored in the Argon filled glovebox before usage. 1 M LiPF₆ EC:DOL (v% 9:1)

was prepared and stored in the glovebox as well. Lithium titanate (LTO) electrode using copper as the current collector with 3 mAh cm⁻² areal loading was from NEI Corp.

A Novocontrol dielectric spectrometer was used to measure the impedance spectra at a frequency range from 10⁷ to 10⁻¹ Hz. X-ray photoelectron spectroscopy SSX-100 was performed on protected lithium surface before and after the cycling. The electrochemical measurements were performed using CH Instrument 600E and Neware multichannel battery testers on coin cells. Specifically, the anode free cell was constructed using the Al₂O₃ coated as the anode current collector. A thin film of lithium with predetermined amount of capacity was pressed on the LTO electrode serving as the over-lithiated cathode.

The morphology of the Al₂O₃ coated electrodes before and after the cycling were characterized using a Leo 1550 Keck Field Emission Scanning Electron Microscopy (FESEM) with a Bruker EDX detector and FEI Strata 400 Focused Ion Beam (FIB) fitted with a Quorum PP3010T Cryo-FIB/SEM Preparation System. The samples were subsequently maintained -165 °C in the cryo-FIB to preserve their structure during the ion milling.

7.4 Results and discussion

A variety of approaches have been proposed in the literature for fabricating electrolyte/electrode interphases that achieve a specific electrochemical function, e.g. extended electrochemical stability¹⁵⁻¹⁶, passivating a reactive anode against parasitic

chemical reactions with an electrolyte¹⁷⁻¹⁸, producing compact dendrite-free deposition of metals such as Li and Na during battery recharge¹⁹⁻²⁰, and so forth). The vast majority of these designs rely on preferential degradation of so-called SEI additives such as ethylene carbonate, vinylene carbonate, fluorinated compounds, etc. that are introduced as sacrificial agents in an electrolyte.²¹⁻²⁴ Achieving interphases with favorable composition, structure, and physical properties therefore requires extensive amounts of trial-and-error experimentation²⁵⁻²⁶. While these approaches have been successful in creating intermediate voltage LIBs with exceptional stability and efficiency, their effectiveness in achieving stability of electrochemically active metal electrodes has been less impressive. A more promising approach is to select the electrolyte solvent itself for its ability to produce mechanically robust interphases. In this regard, ether and ester-based electrolytes have been actively investigated for their ability to form stable and conductive SEI that facilitates reversible lithium plating/stripping during extended cycling²⁷. Concerns about the narrow electrochemical stability window of such solvents and their potential for gas formation during battery cycling has until recently been a major drawback⁶. These concerns have been partially alleviated by recent demonstrations of markedly enhanced electrochemical stability windows of liquid electrolytes containing large concentrations of soluble salts²⁸. Unfortunately salts with the required levels of stability and solubility are expensive, which raises additional concerns about the practicality of the proposed solutions²⁸.

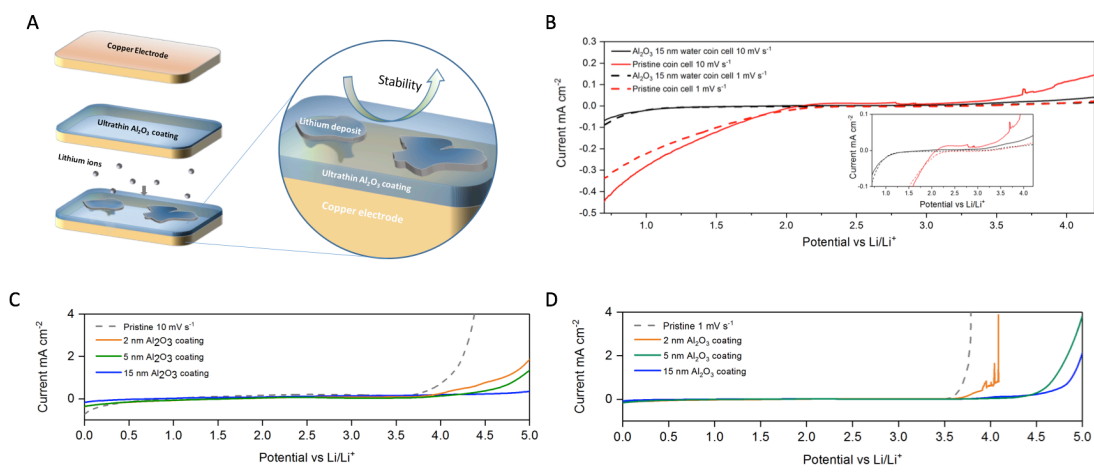


Figure 7.1. A) Schematic illustration of the ultrathin oxide (eg. Al_2O_3) artificial SEI on a conductive substrate. B) The electrochemical stability test of the Al_2O_3 coated interphase from -1.8 to 1.8 V vs. stainless steel at various potential sweeping rates in 1M LiTFSI/water. C) The electrochemical stability test Li- Al_2O_3 Cu cells with 2, 5, and 15 nm thickness and control from 0 to 5 V vs. Li/Li⁺ at 10 mV s⁻¹ in 1M LiPF₆/PC. D) The electrochemical stability test Li- Al_2O_3 Cu cells with 2, 5, and 15 nm thickness and control from 0 to 5 V vs. Li/Li⁺ at 1 mV s⁻¹ in 1M LiPF₆/PC.

ASEI based on pre-formed materials, including polymer thin films, particles of various sorts, solid-state electrolytes, two-dimensional materials, and so on present a viable alternative to solution based methods. Interphases based on these materials have been prepared by casting, vapor deposition, layer-by-layer assembly or direct reaction of components on metal electrodes^{15, 19, 29}. With few exceptions^{18, 30}, achieving conformal coatings of uniform thickness at the electrode/electrolyte interfaces where they are needed is challenging and success is largely determined on a case-by-case basis. Solid state electrolytes including various ion conductive polymers and ceramics are known to maintain stability in metal-based rechargeable batteries. However, the poor contact between solid electrode and electrolyte has emerged as a serious limitation to progress and strategies for lowering the interfacial resistance in order to facilitate room temperature cell operation is an area of significant recent activity⁸. Here we find that atom-by-atom deposition of the ASEI by means of Atomic Layer Deposition (ALD) provides a straightforward strategy for creating ultrathin ceramic coatings on metals that overcome these limitations.

The results in Figures 1b-1d show that the improved stability observed upon application of the ASEI is insensitive to the voltage scan rate (linear scan measurements at 10 mV s^{-1} and 1 mV s^{-1} reveal at most minor changes in stability), confirming that the effect is not merely the result of impeded ion transport to the interface. For a 1M LiPF₆-PC electrolyte between Li and Al₂O₃/Cu electrodes with various Al₂O₃ coating thickness, results in Fig. 1c & 1d further show that there is a

progressive increase of the cathodic stability as the thickness of the Al₂O₃ coating increases. Specifically, whereas the control cell without the Al₂O₃ ASEI is seen to exhibit a current divergence at around 3.6 V, possibly due to the known Cu corrosion at this range of voltage. Even at a slow scan rate of 1 mV s⁻¹ when ample time is allowed for transport and decomposition reactions at solid/liquid interfaces, Li – 15 nm-thick Al₂O₃/Cu cells manifest negligible current until around 4.7V, clearly demonstrating that a Al₂O₃ ASEI with desirable thickness can profoundly extend the high voltage stability of all components (solvent and salt) in a liquid electrolyte.

Figure 7.2A compares cyclic voltammograms of Li –Cu and Li – Al₂O₃/Cu from 2.5 V to -0.2 V at a scan rate of 0.1 mV s⁻¹. In both cases, the peaks from -0.2 to 0.2 V show typical metal deposition and stripping characteristics, indicating that reversible lithium cycling is not hindered by the Al₂O₃ coating (**figure 7.3**). Cathodic peaks between 0.5 V and 0.7 V are also observed in cells with and without Al₂O₃ coating along with their corresponding anodic peaks starting from 1 V, indicating a reversible process likely related to the non-specific surface layer charge/discharge. However, a pronounced difference can be observed during the first discharge: prior to the lithium plating, a broad peak in the range 1 - 1.5 V is observed, which is typically associated with decomposition of the electrolyte³ and impurities is completely prevented with the application of a 15 nm thick Al₂O₃ coating. In other words, the result shows that the natural formation of poor quality SEI can be arrested by reforming the interphase without changing the conventionally used liquid electrolytes. The Al₂O₃ ASEI is also found to drastically improve lithium deposition morphology, as reported in **figure 7.2B** and **7.2C**. Propylene carbonate has been known to form insulating and fragile

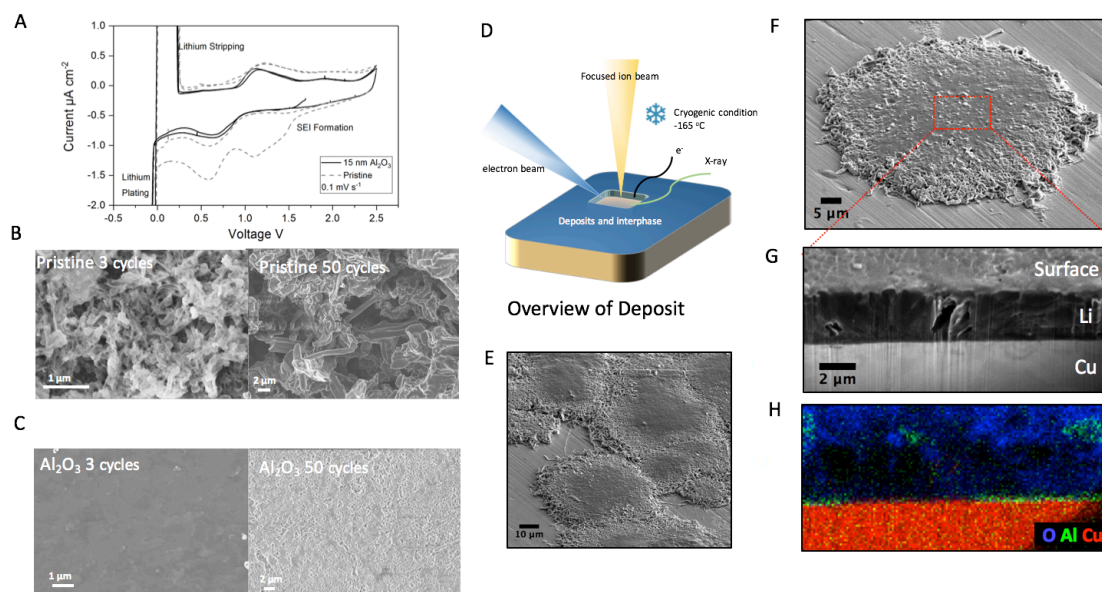


Figure 7.2. A) Cyclic voltammogram of the Li-Cu asymmetric cell with/without 15 nm thick Al_2O_3 coating in 1M LiPF_6/PC scanned at 0.1 mV s^{-1} . B) Post-mortem SEM images of the bare interphase after 3 and 100 cycles in 1M LiPF_6/PC . C) Post-mortem SEM images of the 15 nm thick Al_2O_3 interphase after 3 and 100 cycles in 1M LiPF_6/PC . D) A illustration of the cryo-FIB-SEM study under liquid nitrogen cooling. E) The overview of the deposit on the 15 nm-thick Al_2O_3 coated interphase. F) The zoom-in view of the deposit, with red rectangle highlighting the location for ion milling. G) The cross-section image of the electrodeposit on 15 nm-thick Al_2O_3 coated interphase. H) The EDX elemental mapping of the cross-section of the 15 nm-thick Al_2O_3 coated interphase.

SEI, which produces low Coulombic efficiency in rechargeable lithium batteries that utilize PC³¹. **Figure 7.2B** shows that the poor SEI also adversely affects electrode morphology by promoting uneven electrodeposition of lithium, which evolves to a dendritic structure after multiple cycles. Contrarily, as seen in **figure 7.2C**, a 15 nm thick Al₂O₃ coating yields compact and dendrite-free Li electrodeposits.

To determine the mechanism by which the Al₂O₃ ASEI enhances interfacial stability, we employed cryo-focused ion beam (FIB) – scanning electron microscopy (SEM) (**figure 7.2D**) to characterize the morphology and structure of the lithium deposits. Cryo-FIB-SEM is an important tool in this component of the study because the sharp edges of the sectioned materials possible with the method enables high-quality cross-section images of the lithium deposit that are not achievable with conventional approaches that rely on room temperature sectioning. **Figure 7.2E** reports a typical cryo-FIB-SEM image of a 15 nm thick Al₂O₃/Cu electrode in 1 M LiPF₆/PC after 3 cycles of charge and discharge. It is apparent that the lithium deposits form a complex structure in which very large island-like satellites are connected to a compact, flat center by fibrous edges. **Figures 7.F, 7.2G, and 7.2H** allow the morphology of the deposits to be scrutinized more carefully. It is seen that a dense layer of lithium with thickness of 3 μm exists as distinct deposits and that the edges of the deposit is composed of Li of relatively loose rougher structure. These results are to our knowledge the first demonstration that Li can form solid dense electrodeposits in liquid electrolytes. EDX mapping was employed to elucidate the chemistry of the cross-section of the material. The results clearly show that the central region is devoid of oxygen signals confirming that it is pure elemental lithium, which is not detectable

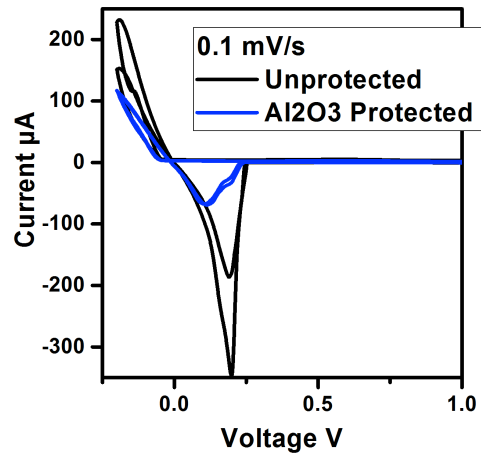


Figure 7.3. Cyclic voltammogram of the Li-Cu asymmetric cell with/without 15 nm thick Al₂O₃ coating in 1M LiPF₆/PC scanned at 0.1 mV s⁻¹.

by EDX. A portion of Al_2O_3 in the middle of the image appears to be lifted out of the plane, allowing Li deposition beneath the Al_2O_3 ASEI, yet the adjacent region show stronger aluminum signal (green dots), which suggests the majority of the Li mass is actually on top of the Al_2O_3 coating. Considering the Al_2O_3 being an electron insulator, this unorthodox result may be explained by the radial growth of lithium deposit under the strained ASEI from the center of the island outwards, as confirmed by further cryo-FIB-SEM images and EDX mapping of multiple electrodeposits formed at a low current density (**figure 7.4 and 7.5**). We conclude, therefore, that the Al_2O_3 layer essentially serves to anchor the Li deposit to the current collector, which ensures good adhesion between the lithium deposit mass and current collector, facilitating good electronic transport through the Li mass and facilitating uniform deposition.

Impedance spectroscopy provides additional insights on the behavior of the Al_2O_3 surface layer in an electrochemical system. **Figure 7.7A** reports the impedance spectra of the Li – $\text{Al}_2\text{O}_3/\text{Cu}$ asymmetric cell as a function of Al_2O_3 coating thickness in the range 2 nm to 15 nm. Results in the figure show that the interfacial impedance increases with coating thickness. This trend continues with further increases in the coating thickness, as demonstrated in **figure 7.6**. **Figure 7.7C** shows that while the trend of increasing interfacial impedance with increasing Al_2O_3 thickness is preserved after cycling the Li – $\text{Al}_2\text{O}_3/\text{Cu}$ asymmetric cells, the interfacial impedance of cells with higher Al_2O_3 thickness decreases by several orders of magnitude, with the result that the Area Specific Resistance (ASR) at all coating thicknesses is low. This large reduction in interfacial resistance could arise from lithiation of the Al_2O_3 coatings and/or from stress-induced cracks in the coating, which would facilitate direct contact

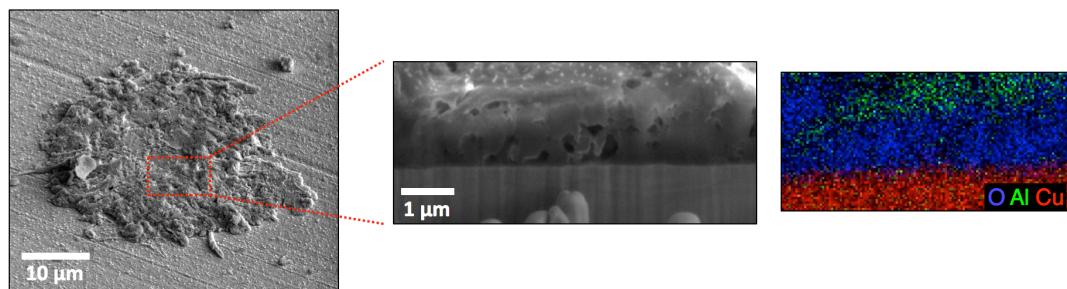


Figure 7.4. Cryo-FIB-SEM image of a location deposited at a current density of 0.1 mA cm^{-2} for 0.05 mAh cm^{-2} after 3 cycles.

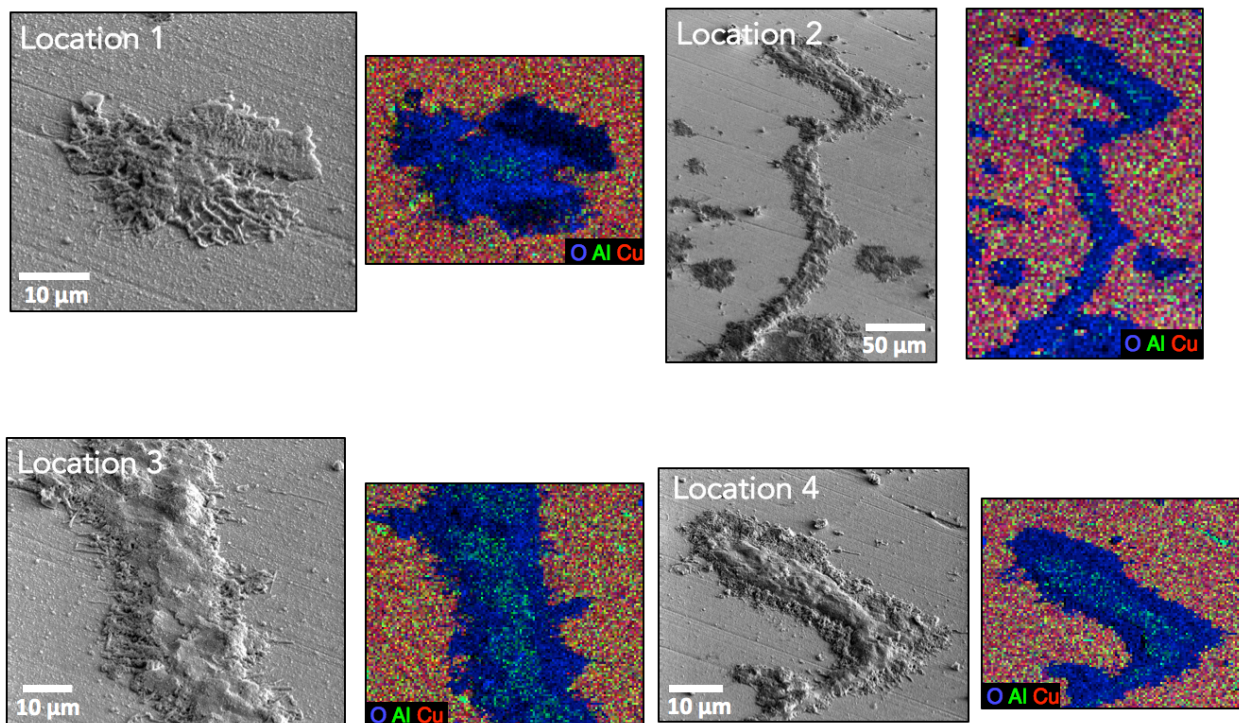


Figure 7.5. Multiple locations of deposits at a current density of 0.1 mA cm^{-2} for 0.05 mAh cm^{-2} and their corresponding EDX mapping.

with the liquid electrolyte. The latter hypothesis can be partially ruled out by the fact that the interfacial impedance remains a strong function of coating thickness. To more thoroughly evaluate the two hypotheses, X-ray photoelectron spectroscopy (XPS) was employed to elucidate the surface chemistry of Al₂O₃/Cu electrode before and after lithium electrodeposition, as reported in **figure 7.7B**. The carbon spectra and their decoupled components (C-H 284.1 eV, C-O 285.5 eV, and C=O 288.3 eV) remain virtually unchanged after lithium electrodeposition, confirming that minimal decomposition of the PC based electrolyte occurs, which is inconsistent with expectations for the ASEI cracking mechanism. A slight variation of the fluorinated species is observed as indicated by the forming LiP_xF_y and LiF, likely from the breakdown of the salt. The aluminum signal remains pronounced after cycling, yet exhibiting a negative shift in the binding energy from 74.4 eV which is typical for Al₂O₃ to 73.5 eV. Such change is believed to be associated with the lithiation and the reduction of the Al₂O₃ upon the interaction of lithium, as also confirmed by the slight negative shift from the oxygen peaks³².

The Al₂O₃ coating has a major influence on the Coulombic efficiency (CE) of lithium plating/stripping. **Figure 7.7C** compares the CE of Li-Cu and Li – Al₂O₃ Cu asymmetric cells cycled in 1M LiPF₆ PC at a current density of 1 mA cm⁻² for 0.5 mAh cm⁻² capacity, with different Al₂O₃ coating thicknesses. The lithium electrodeposition on the bare Cu is observed to occur at low CE, which quickly decreases in the first 50 cycles, a result within our expectation as PC is known to form poor SEI and results in low efficiency stripping and plating of Li. In contrast, both CE values and the lifetime before failure are markedly improved with thicker Al₂O₃

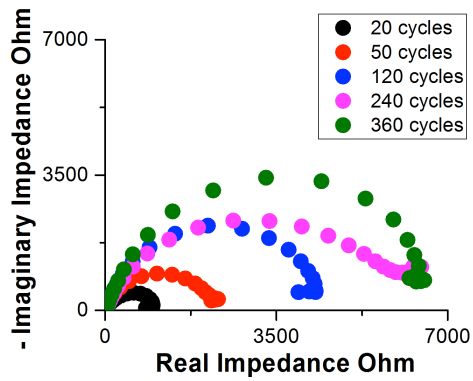


Figure 7.6. Impedance spectra of Li-Cu asymmetric cell with different Al₂O₃ coating thickness.

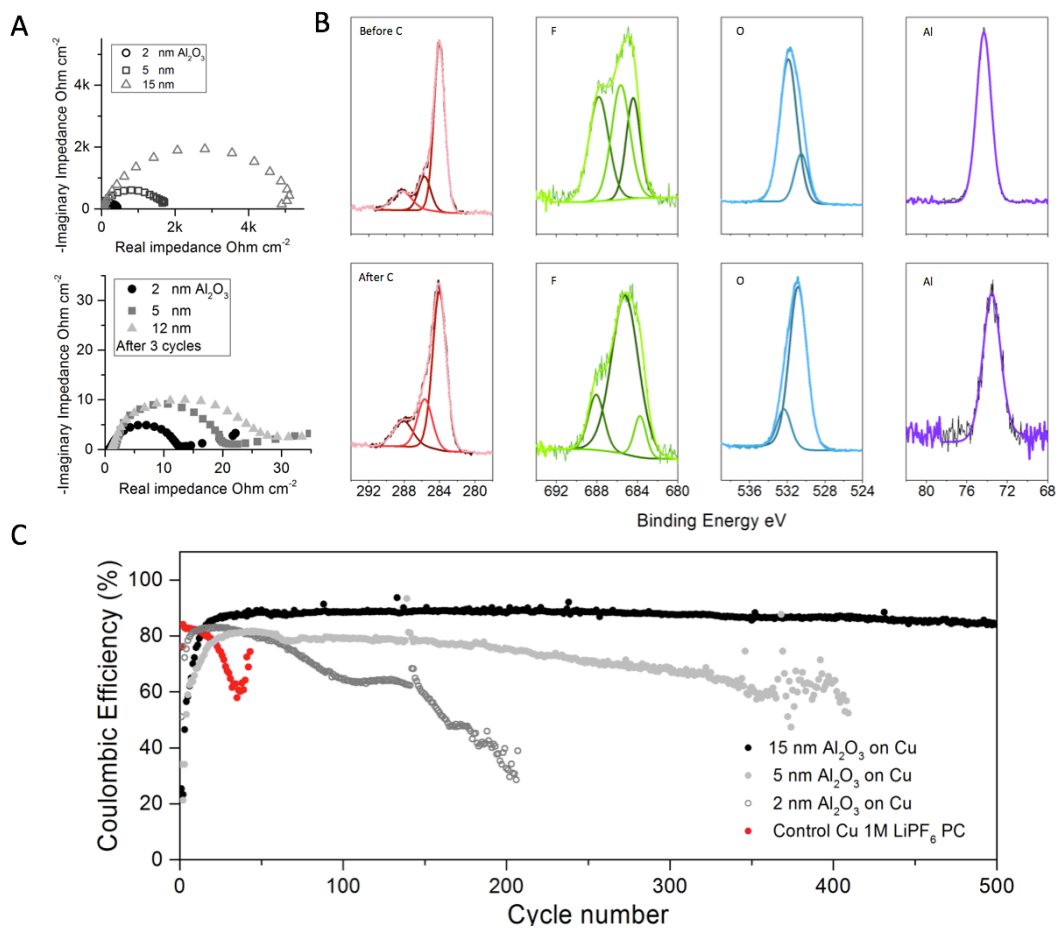


Figure 7.7. A) Top: Impedance spectra of the Al_2O_3 coated interphase with different thicknesses in 1M LiPF_6/PC ; bottom: Impedance spectra of the Al_2O_3 coated interphase with different thicknesses in 1M LiPF_6/PC after 3 cycles. B) High-resolution XPS spectra of the 15 nm-thick Al_2O_3 coated interphase before and after cycling. C) Coulombic efficiency measurement of the Al_2O_3 coated interphase with different thicknesses operated at 1 mA cm^{-2} for 0.5 mAh cm^{-2} capacity per cycle.

coating with the same liquid electrolyte used in all cells. The 15 nm thick Al_2O_3 coating provides what appears to be the optimal CE $\approx 90\%$ over 500 cycles with only small increase in overpotential (**Figure 7.8**); an impressive result for a PC-based electrolyte. The result can be trivially explained in terms of the Al_2O_3 ASEI protection of Li against parasitic side reactions. More detailed investigation of the lithium electrodeposition process, however, suggests that this explanation is incomplete. Specifically, by combining the morphological and electrochemical analytical studies, we believe that a ‘lifting-expanding-jointing’ process is involved during the electrodeposition, which exposes the edge of the deposits to the electrolyte. The enhanced stability provided by the Al_2O_3 coating therefore appears to stem primarily from the protection provided by the Al_2O_3 overlayer and the strong adhesion achieved near the deposit nucleus (root) and the current collector, which also limits the formation of electronically disconnected or ‘dead’ lithium.

Additional support for this mechanism comes from electrochemical studies in a EC:DOL-based electrolyte that exhibits greater chemical stability in contact with Li. **Figure 7.10**, 7.9A and 7.9C report results from CE measurements using control Li-Cu and Li – 15 nm Al_2O_3 Cu asymmetric cells cycled in a 1M LiPF_6 EC:DOL electrolyte at different current densities and capacities. The control cells exhibit initial CE $> 95\%$, but the values quickly decrease, with clear signs of interphase failure after 200 cycles at 1 mA cm^{-2} for 0.5 mAh cm^{-2} and 50 cycles at 3 mA cm^{-2} for 3 mAh cm^{-2} , respectively. In contrast the Li – 15 nm Al_2O_3 Cu cell exhibit high and stable eCE $> 98\%$ even at a high current density and capacity for over 250 cycles without any obvious signs of failure. Voltage-capacity profiles provided in **figure 7.9B** and 7.9D

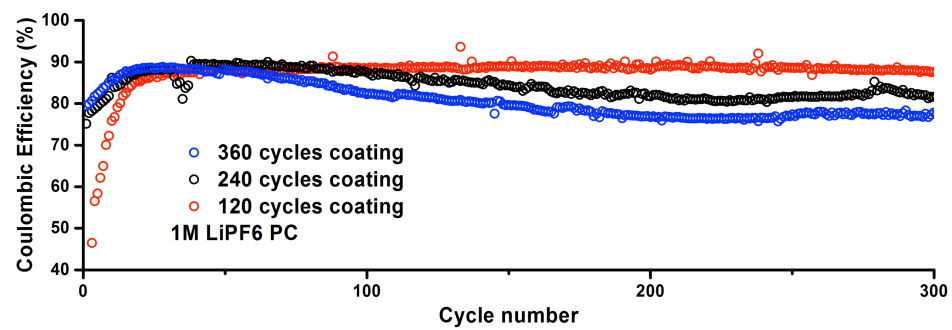


Figure 7.8. Coulombic efficiency of Li-Cu asymmetric cell with Al_2O_3 coating thickness of 120, 240 and 360 cycles.

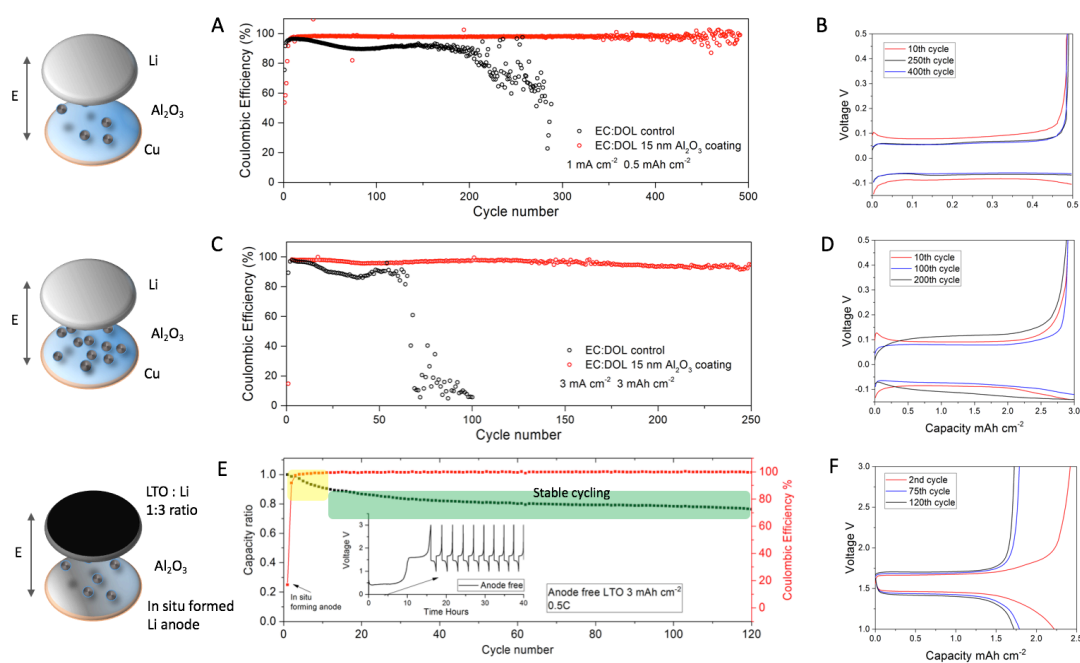


Figure 7.9. A) Coulombic efficiency measurement of the 15 nm-thick Al₂O₃ coated interphase and bare interphase in 1 M LiPF₆/EC:DOL (9:1 v%) at a current density of 1 mA cm⁻² and capacity of 0.5 mAh cm⁻², with the illustration on the left. B) Voltage-area capacity profile at different cycles for A. C) Coulombic efficiency measurement of the 15 nm-thick Al₂O₃ coated interphase and bare interphase in 1 M LiPF₆/EC:DOL (9:1 v%) at a current density of 3 mA cm⁻² and capacity of 3 mAh cm⁻². D) Voltage-area capacity profile at different cycles for C. E) Anode-free model cell with lithium originated in the LTO counter electrode (capacity of LTO:Li = 1:3) operated at 0.5C with lithium anode formed in situ during the first cycle (inset). F) Voltage-area capacity profile at different cycles for E.

show that the cells cycle with minimal overpotential buildup, indicative that the interface is stable. The high CE achieved with this combination of ASEI and electrolyte, can be tested more rigorously in a so-called *anode-free* lithium battery, in which an over-lithiated or thick cathode is the only source of Li in the cell and the anode used in the cycling studies is formed in-situ by lithium deposition on a Al_2O_3 Cu current collector during the first cycle. As a demonstration of the concept, cells with a 15 nm thick Al_2O_3 Cu-LTO (areal capacity 3 mAh cm^{-2}) configuration were constructed with a thin lithium foil placed on the LTO electrode to mimic an over-lithiated cathode. The capacity ratio between the Li in the overlayer and Li in the LTO electrode was maintained as 3 to 1. The initial voltage profile measured in the first charge cycle is illustrated in the inset figure of **figure 7.9E**. A clear long first charge step with two voltage plateaus represent the lithium deposition under low potential ($\sim 0.4 \text{ V}$ for Li-Li) and high potential (1.5 V for LTO-Li) is observed. At the point of transition, it can be seen from the voltage profiles that the cell performs identical to a typical Li-LTO cell. Stable, high CE charge-discharge cycling is achieved for over 100 cycles, which compares well to what is observed for the Cu-LTO control cell in the same electrolyte, where by the 10th cycle (**figure 7.11 and 7.12**), the initial capacity is already below 80% of the initial value. The stable battery cycling performance is attributed to the high Coulombic efficiency of Al_2O_3 Cu-LTO cell, as directly calculated from the equation $R_{\text{np}} (\text{CE})^n = 80\%$, in which the R_{np} represents the N/P capacity ratio, CE being the average Coulombic efficiency and n as the cycle number before 80% capacity retention. Al_2O_3 Cu-LTO cell thus exhibits an average CE of 98.9%, whereas the cell without artificial SEI shows a CE of about 91%.

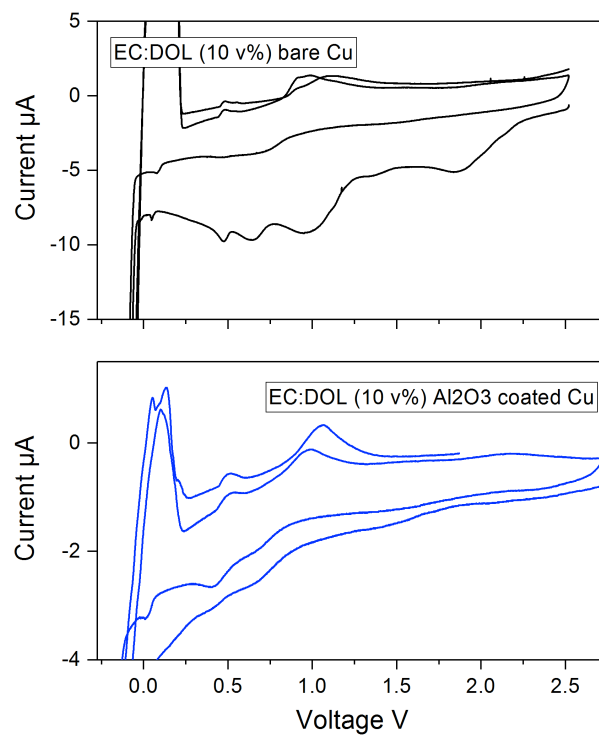


Figure 7.10. Cyclic voltammogram of the Li-Cu asymmetric cell with/without 15 nm thick Al₂O₃ coating in 1M LiPF₆ in EC:DOL (9:1 v%) scanned at 0.1 mV s⁻¹.

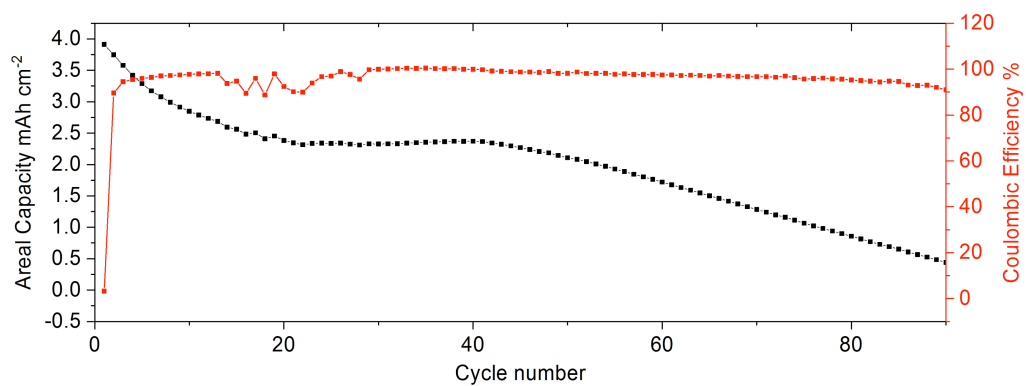


Figure 7.11. Cycling profile of the anode free cell with bare Cu in 1M LiPF₆ in EC:DOL (9:1 v%) operated at 0.5C.

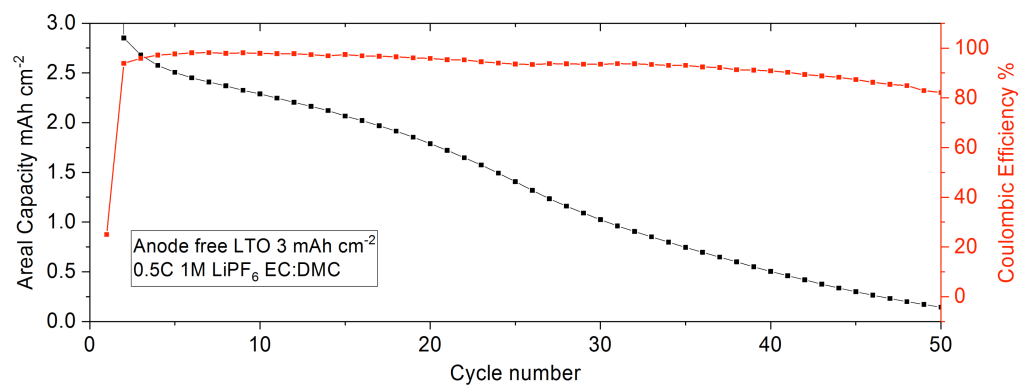


Figure 7.12. Cycling profile of the anode free cell with bare Cu in 1M LiPF₆ in EC:DMC operated at 0.5C.

To summarize, we show that by carefully engineering the electrode/electrolyte interphase with a pin-hole free few-nm thick Al_2O_3 coating it is possible to dramatically improve the electrochemical stability of protic and aprotic liquid electrolytes. At low voltages, the Al_2O_3 layer also serves as an effective artificial SEI which enables long-term reversible and efficient lithium cycling even in a poor SEI-forming propylene carbonate electrolyte. The ASEI is shown to promote formation of flat, compact Li electrodeposits that maintain strong attachment to the Cu current collector and appear to grow by a ‘lifting-expanding-jointing’ process. By incorporating a new, high-efficiency (EC-DOL) electrolyte design, the Al_2O_3 ASEI is reported to yield stable high-efficiency lithium plating/stripping with a CE > 98% at a current density of 3 mA cm^{-2} and a capacity of 3 mAh cm^{-2} for over 250 cycles. We take advantage of these results to demonstrate in-situ formation of Li anodes and stable charge/discharge cycling of so-called anode-free lithium metal cells in which an over-lithiated LTO cathode with a 3 to 1 lithium-cathode capacity ratio is the only source of Li in the cell.

Reference

1. Tarascon, J. M.; Armand, M., Issues and challenges facing rechargeable lithium batteries. *Nature* **2001**, *414* (6861), 359-367.
2. Armand, M.; Tarascon, J. M., Building better batteries. *Nature* **2008**, *451* (7179), 652-657.
3. Etacheri, V.; Marom, R.; Elazari, R.; Salitra, G.; Aurbach, D., Challenges in the development of advanced Li-ion batteries: a review. *Energy Environ. Sci.* **2011**, *4* (9), 3243-3262.
4. Yoshino, A., The Birth of the Lithium-Ion Battery. *Angewandte Chemie-International Edition* **2012**, *51* (24), 5798-5800.
5. Cheng, X. B.; Zhang, R.; Zhao, C. Z.; Wei, F.; Zhang, J. G.; Zhang, Q., A review of solid electrolyte interphases on lithium metal anode. *Advanced Science* **2015**.
6. Xu, K., Electrolytes and interphases in Li-ion batteries and beyond. *Chem. Rev.* **2014**, *114* (23), 11503-11618.
7. Verma, P.; Maire, P.; Novák, P., A review of the features and analyses of the solid electrolyte interphase in Li-ion batteries. *Electrochim. Acta* **2010**, *55* (22), 6332-6341.
8. Manthiram, A.; Yu, X.; Wang, S., Lithium battery chemistries enabled by solid-state electrolytes. *Nature Reviews Materials* **2017**, *2*, 16103.
9. Edström, K.; Gustafsson, T.; Thomas, J. O., The cathode–electrolyte interface in the Li-ion battery. *Electrochim. Acta* **2004**, *50* (2), 397-403.
10. Lin, D.; Liu, Y.; Cui, Y., Reviving the lithium metal anode for high-energy batteries. *Nature Nanotechnology* **2017**, *12* (3), 194-206.

11. Tu, Z.; Nath, P.; Lu, Y.; Tikekar, M. D.; Archer, L. A., Nanostructured electrolytes for stable lithium electrodeposition in secondary batteries. *Acc. Chem. Res.* **2015**, *48* (11), 2947-2956.
12. Tikekar, M. D.; Choudhury, S.; Tu, Z.; Archer, L. A., Design principles for electrolytes and interfaces for stable lithium-metal batteries. *Nature Energy* **2016**, *1*, 16114.
13. Hu, R.; Zhu, M., Sn-Based Alloy Anode Materials for Lithium-Ion Batteries: Preparation, Multi-scale Structure, and Performance. In *Nanomaterials in Advanced Batteries and Supercapacitors*, Springer: 2016; pp 93-125.
14. Suo, L.; Borodin, O.; Gao, T.; Olguin, M.; Ho, J.; Fan, X.; Luo, C.; Wang, C.; Xu, K., “Water-in-salt” electrolyte enables high-voltage aqueous lithium-ion chemistries. *Science* **2015**, *350* (6263), 938-943.
15. Li, J.; Dudney, N. J.; Nanda, J.; Liang, C., Artificial solid electrolyte interphase to address the electrochemical degradation of silicon electrodes. *ACS applied materials & interfaces* **2014**, *6* (13), 10083-10088.
16. Park, J. S.; Meng, X.; Elam, J. W.; Hao, S.; Wolverton, C.; Kim, C.; Cabana, J., Ultrathin lithium-ion conducting coatings for increased interfacial stability in high voltage lithium-ion batteries. *Chem. Mater.* **2014**, *26* (10), 3128-3134.
17. Li, N. W.; Yin, Y. X.; Yang, C. P.; Guo, Y. G., An artificial solid electrolyte interphase layer for stable lithium metal anodes. *Adv. Mater.* **2016**, *28* (9), 1853-1858.
18. Tu, Z.; Choudhury, S.; Zachman, M. J.; Wei, S.; Zhang, K.; Kourkoutis, L. F.; Archer, L. A., Designing Artificial Solid-Electrolyte Interphases for Single-Ion and High-Efficiency Transport in Batteries. *Joule* **2017**.

19. Ma, L.; Kim, M. S.; Archer, L. A., Stable artificial solid electrolyte interphases for lithium batteries. *Chem. Mater.* **2017**, *29* (10), 4181-4189.
20. Wei, S.; Choudhury, S.; Xu, J.; Nath, P.; Tu, Z.; Archer, L. A., Highly Stable Sodium Batteries Enabled by Functional Ionic Polymer Membranes. *Adv. Mater.* **2017**, *29* (12).
21. Lu, Y.; Tu, Z.; Archer, L. A., Stable lithium electrodeposition in liquid and nanoporous solid electrolytes. *Nature materials* **2014**.
22. Lu, Y.; Tu, Z.; Shu, J.; Archer, L. A., Stable lithium electrodeposition in salt-reinforced electrolytes. *J. Power Sources* **2015**, *279*, 413-418.
23. Ding, F.; Xu, W.; Graff, G. L.; Zhang, J.; Sushko, M. L.; Chen, X.; Shao, Y.; Engelhard, M. H.; Nie, Z.; Xiao, J., Dendrite-free lithium deposition via self-healing electrostatic shield mechanism. *J. Am. Chem. Soc.* **2013**, *135* (11), 4450-4456.
24. Lee, Y. M.; Seo, J. E.; Lee, Y.-G.; Lee, S. H.; Cho, K. Y.; Park, J.-K., Effects of triacetoxymethylsilane as SEI layer additive on electrochemical performance of lithium metal secondary battery. *Electrochim. Solid-State Lett.* **2007**, *10* (9), A216-A219.
25. Ota, H.; Shima, K.; Ue, M.; Yamaki, J.-i., Effect of vinylene carbonate as additive to electrolyte for lithium metal anode. *Electrochim. Acta* **2004**, *49* (4), 565-572.
26. Zhang, X. Q.; Cheng, X. B.; Chen, X.; Yan, C.; Zhang, Q., Fluoroethylene Carbonate Additives to Render Uniform Li Deposits in Lithium Metal Batteries. *Adv. Funct. Mater.* **2017**.

27. Xu, W.; Wang, J. L.; Ding, F.; Chen, X. L.; Nasybutin, E.; Zhang, Y. H.; Zhang, J. G., Lithium metal anodes for rechargeable batteries. *Energy Environ. Sci.* **2014**, *7* (2), 513-537.
28. Suo, L. M.; Hu, Y. S.; Li, H.; Armand, M.; Chen, L. Q., A new class of Solvent-in-Salt electrolyte for high-energy rechargeable metallic lithium batteries. *Nature Communications* **2013**, *4*.
29. Liu, Y.; Lin, D.; Yuen, P. Y.; Liu, K.; Xie, J.; Dauskardt, R. H.; Cui, Y., An Artificial Solid Electrolyte Interphase with High Li-Ion Conductivity, Mechanical Strength, and Flexibility for Stable Lithium Metal Anodes. *Adv. Mater.* **2017**, *29* (10).
30. Han, X.; Gong, Y.; Fu, K. K.; He, X.; Hitz, G. T.; Dai, J.; Pearse, A.; Liu, B.; Wang, H.; Rubloff, G., Negating interfacial impedance in garnet-based solid-state Li metal batteries. *Nature materials* **2017**, *16* (5), 572-579.
31. Dey, A.; Sullivan, B., The electrochemical decomposition of propylene carbonate on graphite. *J. Electrochem. Soc.* **1970**, *117* (2), 222-224.
32. Kozen, A. C.; Lin, C.-F.; Pearse, A. J.; Schroeder, M. A.; Han, X.; Hu, L.; Lee, S.-B.; Rubloff, G. W.; Noked, M., Next-generation lithium metal anode engineering via atomic layer deposition. *ACS nano* **2015**, *9* (6), 5884-5892.